Static and Dynamic Homogenization Analyses of Discrete Granular and Atomistic Structures on Different Time and Length Scales

Joachim Peter Dettmar

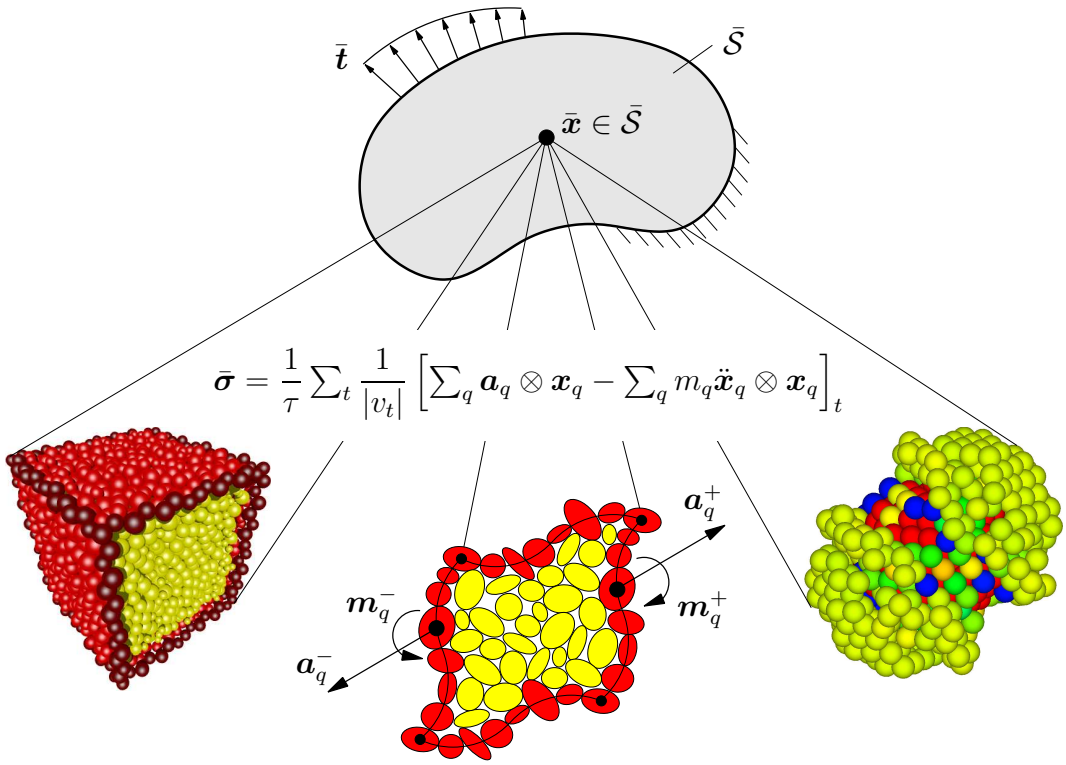

Bericht Nr.: I-17 (2006)
Institut für Mechanik (Bauwesen), Lehrstuhl I
Professor Dr.-Ing. C. Miehe
Stuttgart 2006

Static and Dynamic Homogenization Analyses of Discrete Granular and Atomistic Systems on Different Time and Length Scales

Von der Fakultät Bau- und Umweltingenieurwissenschaften
der Universität Stuttgart zur Erlangung der Würde
eines Doktor-Ingenieurs (Dr.-Ing.)
genehmigte Abhandlung

von

Joachim Peter Dettmar

aus Köln

Hauptberichter: Prof. Dr.-Ing. Christian Miehe
Mitberichter: Prof. Dr. rer. nat. Hans J. Herrmann

Tag der mündlichen Prüfung: 13. Oktober 2005

Institut für Mechanik (Bauwesen) der Universität Stuttgart
2006

Herausgeber:
Prof. Dr.-Ing. habil. C. Miehe

Organisation und Verwaltung:

Anja Zimmermann
Institut für Mechanik (Bauwesen)
Lehrstuhl I
Universität Stuttgart
Pfaffenwaldring 7
D-70550 Stuttgart
Tel.: ++49–(0)711/685–66378
Fax : ++49–(0)711/685–66347

ISBN 3-937859-05-5 (D 93 Stuttgart)

Abstract

This work deals with scale bridging methods for discrete microscopic granular and nanoscopic atomistic aggregates of particles between different length and time scales. The bridging between the scales is achieved by direct homogenization of micro- and nanoscopic physical quantities. In the first part of the work, *static* homogenization techniques for granular materials are developed where a distinct definition of a granular microstructure serves as the starting point for the development of homogenization definitions. Three new boundary constraints are consistently derived from classical continuous definitions and implemented in a strain-driven environment. The finite-sized character of the particles is accounted for in the formulation. With regard to stiffness, it is shown that the periodic surface constraints are bounded by the linear deformation- and uniform traction constraints. Additionally, true dual-scale analyses of granular structures at large strains are performed. The continuum approach on the coarse scale employs the finite element method which serves as a numerical tool without any constitutive assumptions as the physical input is solely governed by the granular microstructures. The second part of the work covers *dynamic* homogenization techniques in connection with the classical molecular dynamics method for atomistic simulations. A uniform traction constraint is developed and it is shown that this formulation is the only suitable choice as it allows for a computational modeling of defects and cracks in a nanosystem. The constraint is implemented in a deformation-controlled environment allowing for computational treatments in coarse scale continuum methods. The dynamic homogenization incorporates the kinetics of all atoms in the aggregate. Several numerical examples in all sections of the thesis round off the discussion of the static and dynamic homogenization techniques for discrete structures.

Zusammenfassung

In der vorliegenden Arbeit werden Methoden für Skalenübergänge für diskrete mikroskopisch-granulare sowie nanoskopisch-atomistische Partikelaggregate zwischen verschiedenen Längen- und Zeitskalen entwickelt. Im ersten Teil werden zunächst *statische* Homogenisierungsmethoden für granulare Materialien behandelt. Beruhend auf einer eindeutigen Definition einer granularen Mikrostruktur werden Formulierungen für drei neue Randbedingungen entwickelt. Die drei diskreten Randbedingungen werden, auf klassischen Kontinuumsformulierungen basierend, konsistent hergeleitet, wobei der diskrete Charakter der Partikel besonders berücksichtigt wird. Es wird gezeigt, dass die Steifigkeit bei periodischen Randbedingungen durch die zwei weiteren Bedingungen beschränkt ist. Zusätzlich werden Mehrskalenanalysen granularer Materialen bei großen Deformationen gezeigt, bei denen die Simulationen auf zwei Skalen simultan durchgeführt werden. Auf der großen Skale wird die Finite-Elemente-Methode als numerisches Werkzeug verwendet. Dabei liefern die granularen Mikrostrukturen den physikalisch-konstitutiven Input. Im zweiten Teil der Arbeit werden *dynamische* Homogenisierungsmethoden im Rahmen der klassischen Molekulardynamik für atomistische Simulationen diskutiert. Es wird eine diskrete Spannungsrandbedingung entwickelt, mit der Defekt- und Rissbildungen in Nanostrukturen simuliert werden können. Die dynamische Homogenisierung schließt die Kinetik aller Atome im System mit ein. Im Hinblick auf die Nutzung mit Kontinuumsmethoden wird die Einbettung der Randbedingung in deformationsgesteuerte Umgebungen betrachtet. Zahlreiche numerische Beispiele runden die Diskussion statischer und dynamischer Homogenisierungstechniken für diskrete Strukturen ab.

Preface

The work for this thesis was completed between 2001 and 2005 while I was an assistant lecturer at chair I of the Institute of Applied Mechanics (Civil Engineering) at the University of Stuttgart.

Firstly, I offer my sincerest thanks to my academic teacher Professor Christian Miehe for his encouragement and the freedom he provided me to prepare this thesis as a member of his research group over the period of more than four years. Our unbiased discussions as well as his support, especially during the final months when I was preparing to leave university, are greatly appreciated. I would also like to thank Professor Hans J. Herrmann of the Institute for Computational Physics at the University of Stuttgart for assuming the responsibility of co-chair and composing the second report on my thesis, despite being on sabbatical in South America.

In addition, I would like to thank all my former colleagues from both chairs of the institute for the amicable collaboration. In particular, I am very much indebted to Dr. Claus Bayreuther and Jan Schotte for all the fruitful discussions and friendly atmosphere; their willingness to share their experience and knowledge as well as upfront support comprised a cornerstone of my work. Moreover, I am much obliged to Ingrid Bruss for having been a very reliable and thorough student assistant during my entire time at the institute. The early completion of my thesis would not have been possible without her continued assistance.

Furthermore, I thank my Canadian friend Richard G. Thiessen for proof-reading the chapters of my manuscript, and Anja Zimmermann for the cordial and always smooth cooperation in all administrative matters at the institute.

Last but not least, the continuing support of my parents and grandparents over the years, whose backing has rendered my work possible in the first place, is truly appreciated and will never be forgotten.

München, May 2006 Joachim Peter Dettmar

Contents

1. Introduction **1**
1.1. Background 2
1.2. Goals and Outline 5

2. Principles of Nonlinear Continuum Mechanics **9**
2.1. Kinematics of Finite Deformations 9
2.1.1. Lagrangian and Eulerian Descriptions of Motion 10
2.1.2. Velocity and Acceleration. Material Time Derivatives 10
2.1.3. Fundamental Geometric Mappings 11
2.1.4. Metric Tensors. Stretch and Stretch Vectors 14
2.1.5. Basic Strain Tensors 16
2.1.6. Polar Decomposition. Spectral Representation 17
2.1.7. Velocity Gradients and Lie Time Derivative 19
2.2. Concept of Stress 20
2.2.1. Representation of Stress Tensors 20
2.2.2. 'Pull-Back' and 'Push-Forward' Operations. Piola Identity 22
2.2.3. Stress Power and Material Work of Deformation 23
2.3. Physical Balance Principles 24

3. Static Homogenization of Discrete Granular Materials **27**
3.1. Current State of Research 27
3.2. Micro-Macro Modeling of Granular Materials 28
3.2.1. Distinct Definition of a Periodic Microstructure 30
3.3. Micro-Macro Transitions for Continuous Microstructures 32
3.3.1. Equilibrium Conditions for Continuous Microstructures 32
3.3.2. Homogenized Macroscopic Stresses of Continuous Microstructures . 32
3.3.3. Linear Deformations on the Boundary of the Microstructure 33
3.3.4. Periodic Deformations on Opposite Boundaries 33
3.3.5. Uniform Tractions on the Boundary of the Microstructure 33
3.4. Micro-Macro Transitions for Particle Microstructures 34
3.4.1. Equilibrium Conditions for Particle Microstructures 34
3.4.2. Homogenized Macroscopic Stresses of Particle Microstructures 36
3.4.3. Linear Deformations on the Boundary of the Microstructure 38
3.4.4. Periodic Particle Deformations/Rotations on Opposite Boundaries . 38

3.4.5. Uniform Tractions on the Boundary of the Microstructure 40
3.5. Penalty-type Implementation of the Boundary Constraints 40
3.5.1. Potential Functions for Particle Interaction Forces 40
3.5.2. Penalty Forces for the New Class of Boundary Constraints 41

4. Micromechanical Modeling of Granular Materials 45
4.1. Classical Contact Force-Displacement Laws 45
4.1.1. Elastic Contact Normal Law of Hertz 45
4.1.2. Elastoplastic Contact Normal Law of Walton & Brown 46
4.1.3. Elastic-Perfectly Plastic Contact Normal Law of Thornton 47
4.1.4. Tangential Contact Tangential Law of Cattaneo and Mindlin . . 47
4.2. Interparticle Contact between Arbitrary-Shaped Plane Granules 48
4.2.1. Contact Properties 49
4.2.2. Elastic Contact-Normal Force Mechanism 50
4.2.3. Frictional-Cohesive Contact-Tangential Force Mechanism 51
4.3. Interparticle Contact between 3D Spherical Granules 54
4.3.1. Elastic Contact-Normal Force Mechanism 54
4.3.2. Frictional-Cohesive Contact-Tangential Force Mechanism 55
4.4. Contact Detection Algorithms 57
4.5. Surface Meshing and Current Volume of the Granular Microstructure 59
4.5.1. Definitions of Surface and Volume of the Granular Microstructure . 59
4.5.2. Computation of the Actual Volume 59
4.5.3. Surface Meshing 60
4.6. Time Discretization and Explicit Integration 61
4.6.1. Equation of Motion 61
4.6.2. Global Damping Mechanism 62
4.6.3. Local Interparticle Damping Mechanism 63
4.6.4. Particle Force Vectors 63

5. Numerical Simulations of Granular Microstructures 65
5.1. Computational Setup 65
5.1.1. Constitutive Force-Potential Functions 65
5.1.2. Fabric Measures in Rigid Particle Structures 66
5.2. Numerical Examples in 2D: Key Characteristics 66
5.2.1. Elliptical Particle under Gravity onto an Inclined Plane 66
5.2.2. Free Gravitational Motion of a Heap of Particles 67

5.3. Numerical Examples in 2D: Microstructures with Elliptical Particles 68
5.3.1. Compression-Shear for a Rectangular, Periodic Microstructure 68
5.3.2. Compression followed by Cyclic Shear Loading 73
5.3.3. Compression-Shear for Circular, Nonperiodic Microstructures 73
5.3.4. Compression-Shear for Non-Standard, Periodic Microstructure 75
5.4. Numerical Examples in 3D: Microstructures with Spherical Particles 78
5.4.1. Compression-Shear Mode for Two Cubic Microstructures 79

6. Multiscale Analyses of Granular Materials at Finite Strains 87
6.1. Finite Element Formulations at Finite Deformations 87
6.1.1. Spatial Discretization 88
6.1.2. Time Discretization 89
6.1.3. Mass Lumping 90
6.1.4. Adaptive Global Damping 90
6.1.5. Linear and Quadratic Triangular Elements 92
6.1.6. Element nodal loads 92
6.2. Solution Procedure of the Coupled Boundary-Value Problems 93
6.3. Applications of Multiscale Analyses 95
6.3.1. Example: Compression Test of a Quadratic Specimen 96
6.3.2. Application: Simulation of a Biaxial Compression Test 99

7. Atomistic Simulations on the Nano Scale 105
7.1. Current State of Research 105
7.2. Molecular Dynamics Technique 107
7.3. Restrictions of Atomistic Simulations 108
7.4. Lagrangian of Second Kind and Energy Contributions 108
7.5. Molecular Dynamics at Finite Temperatures 109
7.6. Time Discretization: Verlet Integration 110

8. Empirical Interatomic Potentials 111
8.1. Interatomic Bonding 111
8.2. Empirical Interatomic Potentials and Forces 114
8.3. Two-Body (Pair) Potentials 115
8.3.1. Lennard-Jones 12-6 Potential 115
8.3.2. Morse Potential 117
8.4. Multi-Body Atom Interactions for Metals 118

8.4.1. Embedded Atom Method (EAM) . . . 119
8.4.2. A Finnis-Sinclair Potential: The Sutton & Chen Model . . . 121
8.5. A Note on Unit Conversions . . . 122

9. Dynamic Homogenization of Atomistic Nanostructures . . . 125
9.1. A Statistical Mechanics Approach to Homogenization . . . 125
9.1.1. Statistical Ensembles . . . 125
9.1.2. Ensemble Averages versus Time Averages . . . 126
9.1.3. The Ergodic Hypothesis . . . 127
9.2. Dynamic Equilibrium of Atomistic Systems . . . 128
9.3. Dynamic Homogenization of Nanostructural Quantities . . . 129
9.3.1. Mesoscopic Mechanical Cauchy Stress . . . 130
9.3.2. A Note on the Classical Virial Stress . . . 131
9.4. Boundary Conditions for Atomistic Nanostructures . . . 132
9.4.1. Periodic Boundary Constraints . . . 133
9.4.2. Linear or Constant Displacement Boundary Constraints . . . 133
9.4.3. Uniform Stress Boundary Constraints . . . 134
9.5. Deformation-Controlled Uniform Stress Boundary Constraints . . . 135

10. Molecular Dynamics Applications . . . 137
10.1. Elastic Deformations in Metallic Structures . . . 137
10.1.1. 3D Elastic Shear Deformation of an fcc Crystal . . . 137
10.2. Plastic Deformations in Metallic Structures . . . 138
10.2.1. 2D Point Defect in Triangular Single Crystal Lattice . . . 139
10.2.2. 2D Annihilation of Two Point Defects in a Triangular Lattice . . . 141
10.2.3. 3D Nanovoid Deformation in Copper under Shear . . . 141
10.2.4. 2D Fracture Study of a Triangular Al Lattice with Nanovoid . . . 143

11. Conclusion and Outlook . . . 147

References . . . 149

List of Figures . . . 159

1. Introduction

Modeling of materials can be performed on different length- and time scales. In classical mechanics, the theoretical and computational framework is the continuum where the constitutive behavior is independent of the size of the body of interest. Therein, the true physical matter of the body of interest is assumed to be "smeared" into some continuously distributed material. Within this classical setting of large-strain continuum mechanics, phenomenological macroscopic material models are developed with locally defined constitutive equations where the material parameters are fit according to experimental observations. In recent years however, attention has been shifted to analyses of materials on multiple scales where the real microscopic or even nanoscopic structures at each point of the macroscopic continuum are accounted for. This is due to the phenomenological assumptions associated with classical material models giving rise to many uncertainties in the accuracy of the simulations. Theoretical developments and computational simulations usually include formulations of governing field equations, geometrical, material and loading data, spatial and temporal discretizations as well as material models. Every one of these formulations contains assumptions that influence the accuracy of the solution and the ability to correctly predict the true material behavior. The aim of the consideration of deformation mechanisms on multiple scales is the reduction or even elimination of uncertainties and empirical assumptions associated with the above building blocks. The main sources of errors in engineering computations can be classified into uncertainties in experimental data (are the fitted parameters accurate enough?), discretization errors (is the solution mesh-independent?) and finally empirism (how physically accurate is the phenomenological constitutive model?). For example, conventional plasticity models fail to predict the formation of ears in deep drawing processes of metals. More recent models, see for example Miehe & Schotte [81], account for the micro- and crystal structures of such materials and are able to predict the earing correctly. Fully empirical models fail because they do not account for the evolution of the particular microstructures properly. These models do not eliminate uncertainties, but rather add to them as more material parameters need to be determined when the material model becomes more intricate. The goal of the computation of materials on multiple scales is the identification of deformation mechanisms at *all* relevant length scales. The ultimate aim hereby is a predictive simulation of materials and structures based on first principles and therefore completely free of any phenomenological parameters. Such a calculation is said to be *ab initio* if it relies on basic and well established laws of nature without any additional assumptions or special models. Experimental input in ab initio computations is limited to the determination of values of fundamental physical constants. The simulations would specifically get their constitutive input solely from the subatomic scale. The author is aware of the fact that at the moment such computations which bridge many orders of length- and time scales are far too complex to be achieved with today's computational power. Today's multiple scale techniques are rather aimed at providing efficient and exact methods to bridge neighboring length scales such that the physics at lower scales influence or even determine the mechanical behavior on the next higher scale.

Many materials show discrete microstructures such as granular media like soil and sand or even metallic materials with discrete particulate-like atomistic structures on the nano scale. Figure 1 depicts the structures of granulates and metals on several time- and length scales. On the subatomic or quantum scale, the theoretical and computational modeling

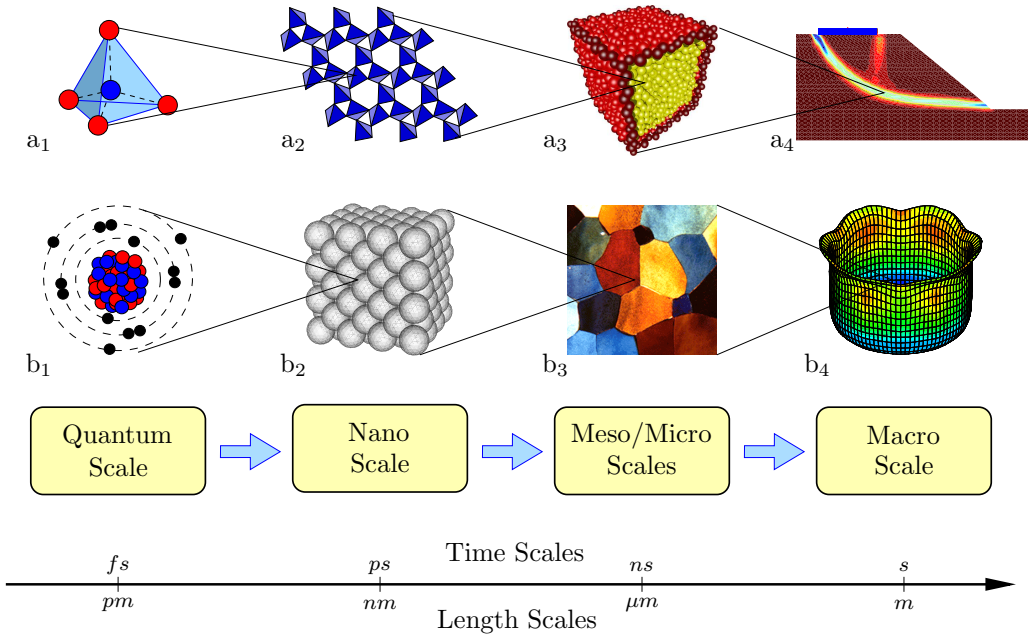

Figure 1: Multiscale modeling is concerned with simulations of materials on different length- and time scales: a. Visualization of several scales for the simulation of granulates, here specifically for sands with SiO_4 crystal structure. In b. the primary scales for simulations of metallic materials are shown. Both scale subdivisions start from a subatomic scale and end up at some macroscopically observed problems. Whereas macroscopic problems are mostly tackled with phenomenological continuum mechanics approaches, lower scales frequently exhibit particulate structures and other more physically-based approaches must be favored.

is concerned with the behavior of protons, neutrons and electrons that represent what is known as an atom or, more complex, a molecule. Simulations at the quantum scale are performed on picometer length- and femtosecond time scales. The next higher scale is known as the nano scale. Here, the interaction of atoms or molecules is investigated at nanometer length- and picosecond time scales. The modeling of materials on meso- and microscopic scales, which for the sake of clarity are not further resolved into separate scales in the figure, focuses on a broad spectrum of length- and time scales. Among them are examples such as micromechanically-motivated subgrain, single and polycrystal structures, dislocation dynamics and discrete element techniques. Finally, classical engineering computations are performed on the macroscopic scale which cover everything above the millimeter range. Materials and structures on this macroscopic scale are usually assumed to possess a continuous structure. However, the deformation of materials is a phenomenon which has ramifications at all length scales, with different physical mechanisms on each of these scales. The physics that determine the deformation behavior change from one scale to another; it is the physics that provide the basis for the constitutive and governing equations that are formulated on every scale. Thus, the connection between the length scales, known as *scale bridging*, poses a mathematical or computational problem, not a physical one.

1.1. Background

Microstructures of discrete character cover a wide spectrum of materials. If one views materials on different scales, eventually some kind of particulate structure on some scale will be observed. Examples are granulates like sand, gravel, rocks, powder and grains that

on the *microscopic level* exhibit strongly discontinuous structures, see Figure 2. Here, typical micro-to-macro simulations, i.e. simulations that bridge different scales, are performed on length scales from micro- ($10^{-6}m$) to the meter (m) scales. Other materials

Figure 2: Particle aggregates can be represented by a wide variety of materials like for example powder, gravel, flint and rocks (source: internet).

such as metals, polymers and ceramics show distinctive particulate structures on the *nano level* with length scales of nanometers ($10^{-9}m$). Metallic materials are made of atomic crystalline structures, so-called lattice structures. From nature, 14 different such unit cell structures are known, but most metals possess either body center cubic (bcc), face centered cubic (fcc) or hexagonal closed packed (hcp) structures. Computational simulations of these structures are termed *atomistic simulations*. In contrast to highly structured systems, polymers and synthetic materials which are composed of many simple molecules can be considered. The backbone of such organic materials are carbon chains. The carbon atoms can have up to three common bonds and are still able to form bonds with other atoms. The ability for molecules to form long such chains is crucial for polymeric materials. Under stress, these chains unfold resulting in an elongation of the polymer, which can be much greater than in materials with crystalline structures. Polymer structures can also be reinforced by carbon nanotubes altering the polymer into a light weight, high strength material with considerable potential for aerospace and other applications. In Figure 3, exemplary nanostructures of monomer and polymer chains, an fcc unit cell and a Lomer dislocation core in an fcc metal are shown. In addition to the very small length scales, the different time scales also need to be taken into account when analyses are performed on multiple scales. In atomistic simulations for example, nano scale deformation mechanisms occur in time frames of femtoseconds ($10^{-15}s$). Therefore, discrete structures occur on many different scales and in many different materials. A unified approach to the modeling, simulation and homogenization of discrete structures is therefore highly desired.

So far, in the modeling of discrete microstructures, attention has mostly been paid to the simulation of the *evolution* of single microstructures associated with macroscopic point values, but not their embedding into large, higher-scale meso- and macroscopic simulations. With the advent of powerful computers, coupled analyses of these problems on several scales is only the next logical step. Obviously, macroscopic materials and structures of our daily life can not be modeled by tracking each and every molecule in the simulation. The number of atoms in such structures exceeds 10^{23}, whereas with today's most powerful computers and parallel implementations, simulations with up to only 10^9 atoms can be modeled, see for example Abraham, Walkup et al. [1]. Even with the steady increase in computational power, it is not foreseeable when the computational resources will be powerful enough to track each and every atom in an engineering computation. Instead, solution techniques on the macroscopic level such as the finite or the bound-

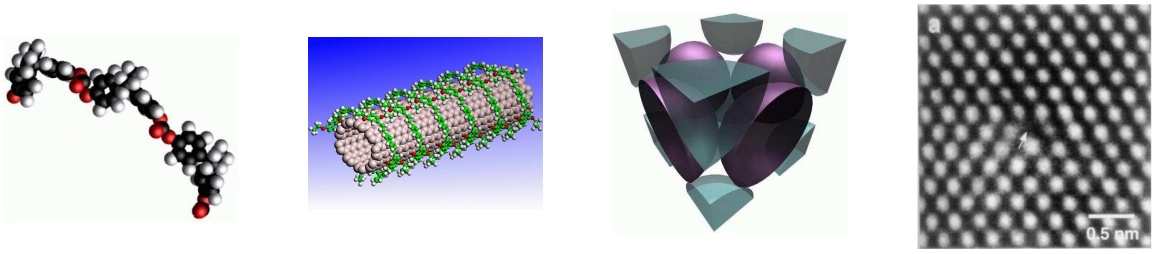

Figure 3: Nanoscopic structures of a monomer chain, polymer chains surrounding a carbon nanotube, an fcc unit cell (sources: internet) and a Lomer dislocation core as seen through electron microscopy (source: Mills, Daw & Foiles [86]).

ary element methods are among the most powerful methods. These techniques employ a phenomenological approach which, at least in standard formulations, do not incorporate true physically-based material formulations. Instead, constitutive material models are formulated that govern the phenomenology of the material. More advanced and recently developed techniques split up the modeling ointo several time- and length scales. Specifically, the loading and deformation of a structure is still macroscopically tracked, but the material models no longer possess the above introduced local phenomenology. Instead, finer and possibly more heterogeneous or even discrete models of the underlying microscopic structure are invoked. The transfer between scales is termed *micro-macro transition*, and the concept of the averaging of microscopic variables towards those that are macroscopically observable is known as *homogenization*. Thus, one problem that arises in such multiple scale analyses is the definition of the overall response of macroscopically driven microstructures.

The topic of multiscale modeling of materials describes a broad field in mechanics where a vast amount of research has been done over recent years. Generally, microstructures can be distinguished into two classes, namely *deformation induced* and *initially present* microstructures. The first class refers to the kinds of microstructures that are not initially present in the material. These microstructures develop and evolve in response to the applied deformation. During the applied deformation, the initially well-posed macroscopic problem may become ill-posed due to strain-softening behavior, localization or damage in the material, accompanied by a loss of ellipticity. To replace these ill-posed problems, multiple phase microstructures are introduced in analogy to phase decomposition problems in elasticity which can be resolved, for example, by relaxation methods. The relaxation analysis then yields well-posed mesh-objective boundary-value problems for objective simulations, see the references Miehe, Lambrecht & Gürses [80], Ortiz & Repetto [95], Lambrecht, Miehe & Gürses [66], Lambrecht, Miehe & Dettmar [65] and Gürses, Lambrecht & Miehe [44]. This class of microstructures is tackled starting from the macroscopic scale towards smaller scales. The other class covers microstructures that are initially and always present in the material, like the kind investigated in this work. The direction of the scale bridging is performed in the opposite direction than that of the deformation induced microstructures, i.e. the macroscopic structures are influenced starting from the lower scales. The second class represents the true microscopic or even nanoscopic structures of the particular material. The term *homogenization* is usually acquainted with such microstructures. The aim hereby is to develop expressions that average microscopic quantities into overall homogenized macroscopic observables and thus bridge two length scales by computational exploitation of certain average theorems.

These microscopic quantities can be for example the local physical forces between particles in granular media, interatomic forces in atomistic systems or nodal quantities in heterogeneous continuous microstructures. The averaged value then represents a quantity that can be used in the simulation on the larger scale. Nonlinear homogenization methods for heterogeneous microstructures from various viewpoints are discussed in the recent works Miehe [76, 75], Bayreuther [12], Miehe, Schröder & Schotte [84], Miehe, Schotte & Lambrecht [82] and Miehe, Schröder & Becker [83]. A key feature of all micro-macro transitions is the particular definition of boundary constraints. These constraints strongly influence the behavior, deformation and, most importantly, the stiffness of the microstructure. Many different definitions of boundary constraints can be found in literature. Three classical definitions are described in this work and are consistently transfered to their discrete counterparts.

1.2. Goals and Outline

This work deals with scale bridging techniques starting from the microscopic and the nanoscopic scales at large-strain deformations. Two classes of materials are investigated, namely the behavior of granular media on the microscopic scale and that of atomistic systems on the nanoscopic scale, see Figure 1. Both classes of materials have highly discontinuous structures in common. Each particle, either an atom or a granule, can be regarded as a discrete body that interacts with other discrete bodies through some constitutive or physical law. For both classes of materials and structures, domain averaging techniques are developed that yield superior overall ("smeared") variables which in turn are computed solely based on physical quantities on the granular or atomistic scales. Specifically, these techniques are developed for deformation-controlled microstructures with distinct definitions of both the unit cells and the surface constraints that govern the stiffness of the aggregates. These averaging methods that yield quantities associated with superior scales are commonly known as *direct homogenization* or *direct micro-macro techniques*. In order to distinguish the different length scales on which the formulations and simulations in this work are performed, granular structures on the microscopic scale are usually termed *microstructures*, whereas such atomistic systems on the nanoscopic scale are consequently called *nanostructures* or *nanosystems*. For such micro- and nanostructures, it is assumed that the micro-/ nanoscopic and the superior meso-/ macroscopic length scales differ by an order of magnitude ($l_{micro}/l_{macro} \ll 1$) and ($l_{nano}/l_{meso} \ll 1$), respectively, such that boundary-layer effects are negligible. This assumed large-scale difference also motivates the negligence of inertial forces with respect to contact forces on the boundary of the particulate aggregates.

First of all, in **chapter 2** some fundamental principles of nonlinear continuum mechanics are outlined which are needed in the further developments. Therein, the kinematics of finite deformations, the concept of stresses and the physical balance principles that hold for every body regardless of the material are outlined. A distinct geometric approach based on modern terminologies of differential geometry for the description of nonlinear material behavior is employed.

Considering the microstructure as representing the material model or constitutive input of some superordinate macroscopic finite element problem, it is highly desired that the deformation of the discrete microstructure is controlled in a deformation-driven sense. That is, not some external force, stress or other form of loading, but some prescribed defor-

mation is imposed, governs the micromechanical deformation and finally determines the mechanical response of the structure. In **chapter 3** a direct homogenization technique for *granular* materials at finite strains within the context of deformation-controlled systems is presented. The focus is put on quasistatic problems. For such granular microstructures, three new boundary constraints for both particle displacements and rotations of the finite-sized particles are developed based on a classical homogenization theory for continuous structures. To achieve this, a new and distinct definition of the granular microstructure based on a true periodic boundary frame is introduced. It will be shown that the *linear deformation-* and the *uniform traction* constraints yield upper and lower bounds for *periodic* constraints with regard to the stiffness of the microscopic granular aggregate. Subsequently, the micro-macro transitions that yield macroscopic observables such as the homogenized stresses are consistently derived from classical continuous formulations. A unique homogeneous stress formulation for these granular aggregates is outlined. In this context, the dependence of the symmetry of the stress tensor on the choice of the boundary conditions is addressed. Recently, this latter topic has been quite controversely discussed in literature on granular media, see for example Bardet & Vardoulakis [9], Ehlers, Ramm et al. [38] and references cited therein. Eventually, the algorithmic treatment by means of a penalty-type implementation is discussed. In **chapter 4** the micromechanical modeling of granular media is introduced, starting with a review of classical constitutive interparticle contact-interaction laws. Then the interparticle contact formulations for two dimensional circular and elliptical as well as three dimensional spherical particles used henceforth are presented. Some contact detection algorithms found in literature are outlined. The computation of the actual volume of three dimensional granular structures by means of a surface meshing is described. Finally, the explicit integration scheme of the equation of motion, coupled with global and local damping mechanisms in order to achieve quasistatic solutions is specified. **Chapter 5** comprises numerical examples of deformation-controlled simulations of granular microstructures. The constitutive force-potential functions are specified and several fabric measures, which will be investigated later, are introduced. The numerical examples deal with periodic granular microstructures in both two and three dimensions. It is shown that the linear displacement and uniform traction constraints for particles on the boundaries yield upper and lower bound characteristics for periodic boundary conditions with regard to the stiffness of the aggregate. A comparative study of these three new constraints is performed, since such a discussion for discrete structures is not present in literature. Several shapes of such microstructures and loading modes are investigated. The results cover discussions of the homogenized macroscopic quantities such as stresses and some fabric measures that characterize the granular microstructures. Subsequently, **chapter 6** extends the purely micromechanical simulations to true two scale analyses of granular materials based on directly evaluated micro-macro transitions, where the granular microstructures with the new periodic boundary constraints are embedded into a macroscopic "smeared" finite element code. On the macroscopic scale, the finite element method is employed in the context of finite strains. Its methodology is described and the solution procedure of the coupled boundary value problems on the two scales is outlined. For the macro level structure, the physical input (material model) comes solely from the microstructure, and a fully coupled concurrent computation is performed of boundary-value problems on two different length scales. Two examples are discussed where several technical and physical issues are investigated. The last example is a computer simulation of a biaxial test that was performed in a labora-

tory in Grenoble and published in the work Desrues & Viggiani [35]. Eventually, such studies should build the framework or a numerical laboratory for a subsequent parameter identification for proper macroscopic phenomenological equations. With chapter 6, the discussion of granular microstructures closes.

In the next step, the focus shifts to several length scales below the previous. The modeling of atomistic structures on the nano scale possesses many parallels to that of granulates on the micro scale. **Chapter 7** contains an introduction to computer simulations on the atomistic scale. The classical molecular dynamics (MD) technique at finite thermodynamic temperatures is outlined and its restrictions are addressed. The Verlet integration algorithm of Newton's first law is presented and some energetic issues, which are inevitably embodied in molecular dynamics formulations, are outlined. **Chapter 8** focuses on empirical interatomic potentials with an accent on the physics behind the functionals. An introduction to interatomic bonding is given, the derivation of the interatomic forces from the interatomic potentials is outlined and some frequently used interatomic potentials, simple and more advanced formulations, are described. The chapter closes with a note on unit conversions since when dealing with mechanical structures on such very small scales, units are often the root of errors in such simulations. In **chapter 9** a dynamic homogenization technique for discrete atomistic nanostructures is developed. A brief introduction to statistical mechanics is given. The different boundary conditions, as in chapter 3, are discussed, followed by the presentation of both the theory and the algorithms of the uniform stress surface constraint in the fully dynamic context. It is shown that only the constraint which yields uniform stresses on the surfaces of atomistic nanosystems provides a framework able to capture all relevant atomistic deformation mechanisms such as dislocations. The dynamic homogenization technique of nanostructural quantities to meso- or macroscopically observables is outlined. The ergodic hypothesis is described and the connection between ensemble and time averages explained. This hypothesis is then used to define the time averaged Cauchy stress tensor as the physically relevant measure of stress in an atomistic system. As a contrast to the Cauchy stresses, the virial stresses are briefly outlined and their physical relevance addressed. Finally, **chapter 10** covers applications of the molecular dynamics techniques to nanosystems in the context of the newly developed deformation-driven implementation. Therein, atomistic simulations of nanoscopic crystalline structures of metallic materials are performed. It splits up into an introductory part where the elastic deformations of several monoatomic metals are comparatively studied. The second part comprises plastic deformations with both ductile behavior and fracture processes. The examples cover both two and three dimensional atomistic nanostructures.

In summary, the first part of the thesis deals with simulations between the micro- and macroscopic scales shown in Figure $1a_3$-a_4. Here, due to the larger time scale and assumed slow rate of deformation, the mechanical homogenization of microscopic quantities is performed in a quasistatic setting. The second part of the thesis deals with atomistic simulations at the nano scale, shown in Figure $1b_2$. The time scales considered here are very small such that the dynamics, which essentially represent the thermodynamic temperature of such systems, must be accounted for when nanoscopic quantities are homogenized. All boundary constraints are implemented by a unified penalty method that proves to be a convenient computational tool for both quasistatic and fully dynamic micro- and nanostructure simulations. All homogenization and simulation techniques are presented in two and three dimensions suitable for large strain applications.

2. Principles of Nonlinear Continuum Mechanics

The mechanics of continuous solids and fluids is a fundamental field of knowledge and lays the groundwork for all advanced fields of applied mechanics. For a proper understanding of the relations developed in the next chapters, a sound understanding of the fundamental geometry of linear and nonlinear continuum mechanics is necessary. The mechanics of solid bodies can be described on different scales. On approach is the micromechanical description of matter. Therein, a discrete character of the material is assumed that might for example be an atomistic lattice structure. In this work the concept of a continuous medium is considered as the physically macroscopic formulation. The relevance of this approach depends on the kind of problem and the scale of the phenomenons to be described.

In the common mathematical sense, a continuum is understood to be a domain filled with particles of some kind. These particles, seen as material points, are geometrically solely described by their positions in space. It is then assumed that points which are initially close together, remain so in subsequent considerations. This observation builds the framework for the assumption of a continuum. This mathematical idealization as a continuum is suitable for the description of solid bodies on large scales. In what follows, the finite kinematics of deformations of solid bodies is discussed. Then, stress tensors and fundamental balance equations are introduced. The notation and modern differential-geometric terminologies are mainly adopted from representations in Miehe [74].

2.1. Kinematics of Finite Deformations

The geometric description of deformations of solids and fluids without reference to the cause of deformation is termed *kinematics*. In this work, focus is put on solid bodies, such a body is defined as a physical object with a macroscopically idealized continuous structure and certain physical properties such as density and color. The possibly discrete micro- or nanostructure is left out at this stage of the description. At a time $\tau = 0$, the physical body B occupies a domain $\mathcal{B}$ in the Euclidean space, see Figure 4. This physical

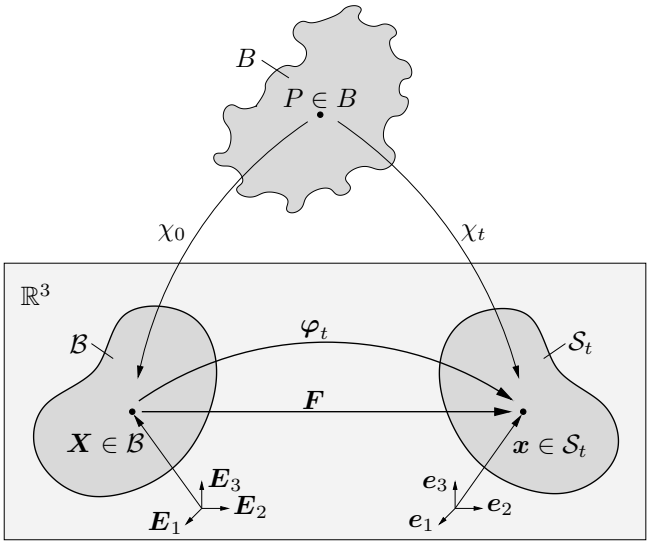

Figure 4: Placements $\mathcal{B}$ and $\mathcal{S}_t$ of the physical body B in the Euclidean space $\mathbb{R}^3$ at times $\tau = 0$ ($\mathcal{B}$) and $\tau = t$ ($\mathcal{S}_t$).

body B is a continuous assemblage of material particles $P \in B$, which stand in a bijective relation to a domain $\mathcal{B} \subset \mathbb{R}^3$ of the Euclidean space $\mathbb{R}^3$. A position $\boldsymbol{X} \in \mathcal{B}$ characterizes the point that is occupied by the material particle P.

2.1.1. Lagrangian and Eulerian Descriptions of Motion. Figure 4 visualizes the placements and general motion of a physical body B. This motion is described by configurations χ_t parameterized in time τ,

$$\chi_t : \left\{ \begin{array}{lcl} B & \rightarrow & \mathcal{S}_t \subset \mathbb{R}^3 \\ P & \mapsto & \boldsymbol{x} = \chi_t(P) \end{array} \right. \tag{2.1}$$

Therefore, particle P of the moving material body occupies a series of locations in space $\mathbb{R}^3$, see again Figure 4. In the Euclidean space $\mathbb{R}^3$ two differential manifolds $\mathcal{B}$ and $\mathcal{S}_t$ are introduced where a reference position $\boldsymbol{X}$ and an actual position $\boldsymbol{x}$ are assigned to a material particle P. The two configurations are parameterized in the neighborhoods $\mathcal{N}_{\boldsymbol{X}}$ and $\mathcal{N}_{\boldsymbol{x}}$ of a material point by $\boldsymbol{X} = X^A$ and $\boldsymbol{x} = x^a$, respectively. The reference configuration is also termed *material* or *Lagrangian* configuration. In contrast, a dual *current, spatial* or *Eulerian* configuration exists that represents the actual configuration of the body under consideration, see Figure 5. For the reference or Lagrangian configuration the relation

$$\boldsymbol{X} = \chi_0(P) \quad \Longrightarrow \quad P = \chi_0^{-1}(\boldsymbol{X}) \tag{2.2}$$

holds and denotes the Lagrangian placement $\boldsymbol{X}$ of the material point P. A dual counterparts on the Eulerian manifold exists which is termed Eulerian placement $\boldsymbol{x}$. The mapping χ_0 is not time-dependent, whereas the Eulerian configuration $\boldsymbol{x} = \chi_t(P) =: \boldsymbol{\varphi}(\boldsymbol{X}, t)$ depends on time t. The nonlinear mapping

$$\boldsymbol{\varphi}_t : \left\{ \begin{array}{lcl} \mathcal{B} & \rightarrow & \mathcal{S}_t \\ \boldsymbol{X} & \mapsto & \boldsymbol{x} = \boldsymbol{\varphi}_t(\boldsymbol{X}) \end{array} \right. \tag{2.3}$$

is termed the *deformation map* or point map of the material body at time $t \in \mathbb{R}_+$. It describes the nonlinear motion of the material point P with respect to its reference position $\boldsymbol{X}$. The reference configuration can be chosen arbitrarily. It is not required to be the undeformed configuration, but in solid mechanics this unloaded, stress-free initial configuration is mostly taken to be the reference configuration.

2.1.2. Velocity and Acceleration. Material Time Derivatives. The material velocities and accelerations $\boldsymbol{V}$ and $\boldsymbol{A}$ of material particles are understood to be vector fields on the current configuration of the body, but they are parameterized in Lagrangian coordinates $\boldsymbol{X}$ of the referential configuration,

$$\begin{array}{rclcl} \boldsymbol{V}(\boldsymbol{X}, t) & = & \dfrac{\partial}{\partial t}\boldsymbol{\varphi}(\boldsymbol{X}, t) & = & \dfrac{d}{dt}\boldsymbol{\varphi}_{\boldsymbol{X}}(t) \ , \\ \boldsymbol{A}(\boldsymbol{X}, t) & = & \dfrac{\partial}{\partial t}\boldsymbol{V}(\boldsymbol{X}, t) & = & \dfrac{d^2}{dt^2}\boldsymbol{\varphi}_{\boldsymbol{X}}(t) \ . \end{array} \tag{2.4}$$

The term *material velocity* follows from the parametrization in Lagrangian coordinates $\boldsymbol{X}$. The notation $\boldsymbol{\varphi}_X(t)$ with index $\boldsymbol{X}$ describes the path of point P, whereas $\boldsymbol{\varphi}_t(\boldsymbol{X})$ with index t depicts the deformation at a 'frozen' time t. In analogy to the material

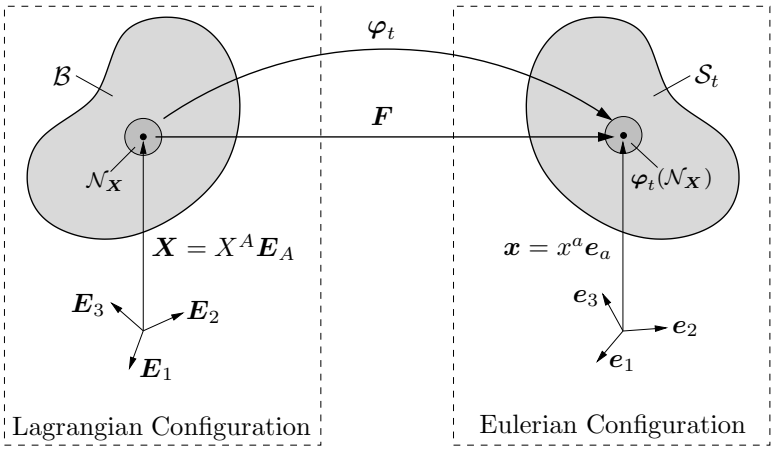

Figure 5: $\mathcal{B}$ and $\mathcal{S}_t$ parameterized in the neighborhood $\mathcal{N}_{\boldsymbol{X}}$ of a material point $\boldsymbol{X}$ by Lagrangian and Eulerian coordinate charts X^A and x^a

representations just introduced, spatial velocity and acceleration are parameterized in Eulerian coordinates $\boldsymbol{x} = \boldsymbol{\varphi}_t(\boldsymbol{X})$ with referential position $\boldsymbol{X}_t = \boldsymbol{\varphi}^{-1}(\boldsymbol{x})$. This leads to the definitions for the spatial velocity $\boldsymbol{v}$ and acceleration $\boldsymbol{a}$

$$\begin{aligned} \boldsymbol{v}(\boldsymbol{x},t) &= \boldsymbol{V}(\boldsymbol{\varphi}_t^{-1}(\boldsymbol{x}),t) \ , \\ \boldsymbol{a}(\boldsymbol{x},t) &= \boldsymbol{A}(\boldsymbol{\varphi}_t^{-1}(\boldsymbol{x}),t) \ , \end{aligned} \tag{2.5}$$

which are understood as vector fields on the current configuration $\mathcal{S}_t$. They are parameterized in the Eulerian coordinates $\boldsymbol{x}$. The material time derivatives of spatial objects like for example the velocity field $\boldsymbol{v}$ can be derived based on the representations of material and spatial velocities and accelerations previously introduced. For example, the material velocity follows as

$$\boldsymbol{A}(\boldsymbol{X},t) = \frac{\partial}{\partial t}\boldsymbol{v}(\boldsymbol{\varphi}_t(\boldsymbol{X}),t) + \nabla_{\boldsymbol{x}}\boldsymbol{v}(\boldsymbol{\varphi}_t(\boldsymbol{X}),t) \cdot \boldsymbol{V}(\boldsymbol{X},t) \ . \tag{2.6}$$

The tensor object $\nabla_{\boldsymbol{x}}\boldsymbol{v}$ is commonly termed *spatial velocity gradient*. The velocity field of the spatial acceleration then follows as the composition $\boldsymbol{a} = \boldsymbol{A} \circ \boldsymbol{\varphi}_t^{-1}$ and thus the material time derivative of the spatial velocity field follows as

$$\boldsymbol{a}(\boldsymbol{X},t) = \frac{\partial}{\partial t}\boldsymbol{v}(\boldsymbol{x},t) + \nabla_{\boldsymbol{x}}\boldsymbol{v}(\boldsymbol{x},t) \cdot \boldsymbol{v}(\boldsymbol{x},t) \ . \tag{2.7}$$

The first term in equation (2.7) describes the local time derivative where $\boldsymbol{x}$ is kept fixed, the second term describes the convective part due to a change of position $\boldsymbol{x}$. In short, the derivative can be written as $\boldsymbol{a} = \dot{\boldsymbol{v}} = \partial_t \boldsymbol{v} + \nabla_{\boldsymbol{x}}\boldsymbol{v} \cdot \boldsymbol{v}$ with the material time derivation operator $(\dot{\bullet}) = \frac{d}{dt}(\bullet)$ of the general spatial object $(\bullet)$. This time derivation rule is valid for all spatial variables parameterized in the time-dependent position $\boldsymbol{x}$. It is always additively composed of a local and a convective time derivative.

2.1.3. Fundamental Geometric Mappings. Deformation Gradient and Tangential Map. With the aid of point map (2.3), material points $\boldsymbol{X}$ of the Lagrangian configuration $\mathcal{B}$ can be mapped onto spatial Eulerian configurations $\mathcal{S}_t$. In what follows, the mathematical descriptions of the deformations of material curves and associated tangent vectors is summarized. The deformation gradient $\boldsymbol{F}$ is defined as the Frechet derivative,

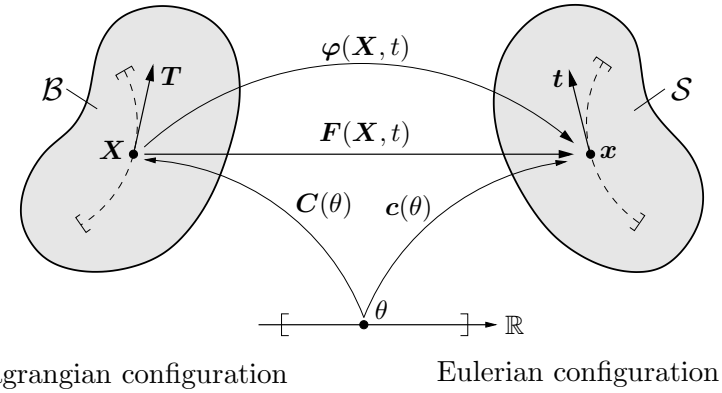

Figure 6: The deformation gradient $\boldsymbol{F} = F^a{}_A$ maps material tangent vectors at Lagrangian curves onto spatial tangent vectors at deformed material curves.

also called the directional derivative, of the deformation map $\boldsymbol{\varphi}$ defined as

$$\boxed{\boldsymbol{F}(\boldsymbol{X},t) := \frac{\partial}{\partial \boldsymbol{X}}\boldsymbol{\varphi}(\boldsymbol{X},t) = \nabla_{\boldsymbol{X}}\boldsymbol{\varphi}(\boldsymbol{X},t)\ .} \tag{2.8}$$

The deformation gradient $\boldsymbol{F}(\boldsymbol{X},t)$ plays the central role in the description of finite deformations of solid bodies. The deformation gradient maps tangent vectors at material curves onto tangent vectors at the associated spatial curves. In contrast to the *nonlinear* point map $\boldsymbol{\varphi}(\boldsymbol{X},t)$, the deformation gradient $\boldsymbol{F}_t : \mathbb{R}^3 \to \mathbb{R}^3$ is understood to operate *linearly*. As an example, a curve is considered that is described by a scalar parameter θ. The material representation is denoted by the nonlinear relation $\boldsymbol{C}(\theta) : \theta \mapsto \boldsymbol{X} = \boldsymbol{C}(\theta)$ and its associated spatial counterpart by $\boldsymbol{c}(\theta) : \theta \mapsto \boldsymbol{x} = \boldsymbol{c}(\theta)$. Both parametrizations $\boldsymbol{C}(\theta)$ and $\boldsymbol{c}(\theta)$ describe the same matter and are therefore related. With the deformation map $\boldsymbol{\varphi}(\boldsymbol{X},t)$, the relation is established as

$$\boldsymbol{x} = \boldsymbol{\varphi}(\boldsymbol{X},t) \quad \Rightarrow \quad \boldsymbol{c}(\theta) = \boldsymbol{\varphi}(\boldsymbol{C}(\theta),t)\ . \tag{2.9}$$

The deformed tangent vector $\boldsymbol{t}(\theta)$ on the Eulerian configuration can be connected to the material tangent vector $\boldsymbol{T}(\theta)$ with the aid of the deformation gradient $\boldsymbol{F}(\boldsymbol{X},t)$. By use of the chain rule, $\boldsymbol{t}(\theta) = \frac{d}{d\theta}\boldsymbol{c}(\theta) = \nabla_{\boldsymbol{X}}\boldsymbol{\varphi} \cdot \frac{d}{dt}\boldsymbol{C}(\theta)$ and therefore

$$\boldsymbol{t}(\theta) = \boldsymbol{F}(\boldsymbol{X},t)\boldsymbol{T}(\theta)\ . \tag{2.10}$$

The deformed tangent vector $\boldsymbol{t}(\theta)$ is a geometric object of the tangential space $T_{\boldsymbol{x}}\mathcal{S}_t$ of the Eulerian configuration. In analogy, the material tangent vector $\boldsymbol{T}(\theta)$ is a geometric object of the tangential space $T_{\boldsymbol{X}}\mathcal{B}$ of the Lagrangian configuration. Both tangential spaces are connected by the deformation gradient $\boldsymbol{F}(\boldsymbol{X},t)$. This linear tangent map is expressed as

$$\boldsymbol{F}(\boldsymbol{X},t) : \left\{ \begin{array}{lcl} T_{\boldsymbol{X}}\mathcal{B} & \to & T_{\boldsymbol{x}}\mathcal{S}_t \\ \boldsymbol{T}(\theta) & \mapsto & \boldsymbol{t}(\theta) = \boldsymbol{F}(\boldsymbol{X},t)\boldsymbol{T}(\theta)\ . \end{array} \right. \tag{2.11}$$

$T_{\boldsymbol{X}}\mathcal{B}$ represents the tangential space (vector space) of $\mathcal{B}$ at position $\boldsymbol{X} \in \mathcal{B}$, and $T_{\boldsymbol{x}}\mathcal{S}_t$ represents the tangential space of $\mathcal{S}_t$ at position $\boldsymbol{x} \in \mathcal{S}_t$. In the normal three dimensional case the deformation gradient possesses nine independent coordinates at each time t. It describes the deformation of a solid body in the neighborhood $\mathcal{N}_{\boldsymbol{X}}$ of a material point $\boldsymbol{X}$.

From a material object the transformation generates its dual spatial counterpart. Observe that the deformation gradient $\boldsymbol{F}$ is considered to be a two-point tensor $\boldsymbol{F} = F^a{}_A$.

Adjoint Transformation and Normal Map. In the following section the transformation of area vectors from Lagrangian to Eulerian spaces and vice versa is discussed. The cross product of two tangent vectors, which span up an area, gives an area vector object embedded into the solid body. These two vectors are tangent vectors at material curves, see last section. The required transformation $\boldsymbol{N}(\boldsymbol{X}, t)$ maps a material area vector $\boldsymbol{A}_{\boldsymbol{X}}$ onto its spatial counterpart $\boldsymbol{a}_{\boldsymbol{x}}$ in the form $\boldsymbol{a}_{\boldsymbol{x}} = \boldsymbol{N}(\boldsymbol{X}, t)\boldsymbol{A}_{\boldsymbol{x}}$, therefore $\boldsymbol{N}(\boldsymbol{T}_{\boldsymbol{X}} \times \bar{\boldsymbol{T}}_{\boldsymbol{X}}) = \boldsymbol{t}_{\boldsymbol{x}} \times \bar{\boldsymbol{t}}_{\boldsymbol{x}}$. With the tangent map $\boldsymbol{F}$ and the elementary definition of the determinant of a tensor, the transformation of the area normal is expressed as

$$\boldsymbol{N}(\boldsymbol{X}, t) = \det[\boldsymbol{F}]\boldsymbol{F}^{-T} = J\boldsymbol{F}^{-T} =: \operatorname{cof}[\boldsymbol{F}] \tag{2.12}$$

with the transpose $\boldsymbol{F}^{-T}$ of the deformation gradient and the *Jacobian* $J = \det[\boldsymbol{F}]$. Also, $\operatorname{cof}[\bullet]$ denotes the cofactor of $[\bullet]$. Based on the relation $\boldsymbol{a}_{\boldsymbol{x}} = \det[\boldsymbol{F}]\boldsymbol{F}^T\ \boldsymbol{A}_{\boldsymbol{X}}$ between two area normals, the normal map is defined as

$$\boldsymbol{F}^{-T}(\boldsymbol{X}, t) : \left\{ \begin{array}{lcl} T^*_{\boldsymbol{X}}\mathcal{B} & \rightarrow & T^*_{\boldsymbol{x}}\mathcal{S}_t \\ \boldsymbol{N}_{\boldsymbol{X}} & \mapsto & \boldsymbol{n}_{\boldsymbol{x}} = \boldsymbol{F}^{-T}\boldsymbol{N}_{\boldsymbol{X}} \ . \end{array} \right. \tag{2.13}$$

The normal map $\boldsymbol{F}^{-T}$ maps normal vectors that are perpendicular to area elements of the material configuration onto normal vectors of the associated deformed area elements. The *cofactor* $\operatorname{cof}[\boldsymbol{F}] := J\boldsymbol{F}^{-T}$ of the deformation gradient $\boldsymbol{F}$ also takes into account the magnitude of the mapped vector of the form $\boldsymbol{a} = \operatorname{cof}[\boldsymbol{F}]\boldsymbol{A} = J\boldsymbol{F}^{-T}\boldsymbol{A}$. The symbol $T^*_{\boldsymbol{X}}\mathcal{B}$ represents the so-called cotangential space of $\mathcal{B}$ at position $\boldsymbol{X} \in \mathcal{B}$, and $T^*_{\boldsymbol{x}}\mathcal{S}_t$ represents the cotangential space of $\mathcal{S}_t$ at position $\boldsymbol{x} \in \mathcal{S}_t$.

Change of Volume. Jacobian Map. Now the deformation of volume elements of the body is investigated. The material and spatial volume elements $V_{\boldsymbol{X}}$ and $v_{\boldsymbol{x}}$ are formed by triple scalar products of the tangent vectors associated with the curves on the respective configurations

$$V_{\boldsymbol{X}} = \boldsymbol{T}_{\boldsymbol{X}} \cdot (\bar{\boldsymbol{T}}_{\boldsymbol{X}} \times \bar{\bar{\boldsymbol{T}}}_{\boldsymbol{X}}) \quad \text{and} \quad v_{\boldsymbol{x}} = \boldsymbol{t}_{\boldsymbol{x}} \cdot (\bar{\boldsymbol{t}}_{\boldsymbol{x}} \times \bar{\bar{\boldsymbol{t}}}_{\boldsymbol{x}}) \ . \tag{2.14}$$

The required mapping $V_t(\boldsymbol{T} \cdot (\bar{\boldsymbol{T}} \times \bar{\bar{\boldsymbol{T}}})) = \boldsymbol{t} \cdot (\bar{\boldsymbol{t}} \times \bar{\bar{\boldsymbol{t}}})$ maps a Lagrangian volume element $V_{\boldsymbol{X}}$ onto its Eulerian counterpart $v_{\boldsymbol{x}}$. With the tangential mapping and the definition of the determinant, the volume map is identified as

$$V_t = \det[\boldsymbol{F}] =: J \ . \tag{2.15}$$

This determinant is commonly known as the Jacobian $J := \det[\boldsymbol{F}]$ and is formally understood as a mapping of the form

$$J : \left\{ \begin{array}{lcl} \mathbb{R}_+ & \rightarrow & \mathbb{R}_+ \\ V_{\boldsymbol{X}} & \mapsto & v_{\boldsymbol{x}} = JV_{\boldsymbol{X}} \ . \end{array} \right. \tag{2.16}$$

The linear scalar-valued Jacobian J maps material volume elements onto deformed volume elements. Interpenetrations of matter are not permitted, therefore the important property $J > 0$ holds. Figure 7 summarizes the three fundamental geometric mappings.

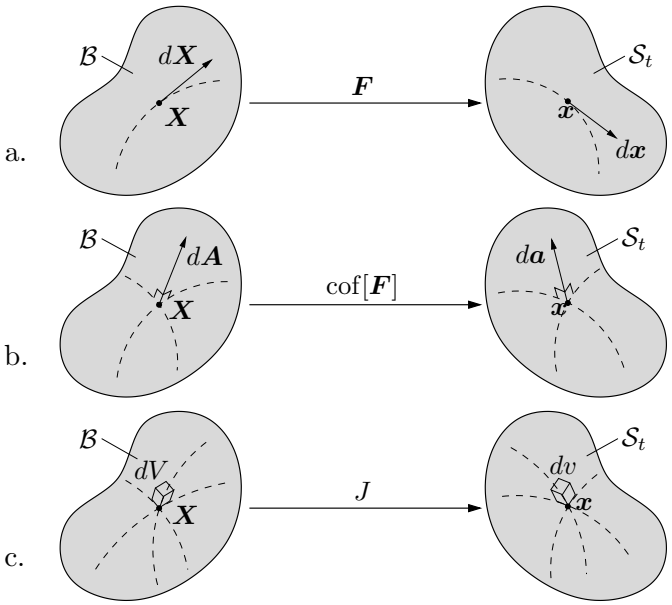

Figure 7: Three basic mappings, a. tangent map $\boldsymbol{F}$, b. normal map cof[$\boldsymbol{F}$] and c. volume map J.

2.1.4. Metric Tensors. Stretch and Stretch Vectors. The computation of the magnitudes of vectors is performed with the aid of the scalar product. Therefore, metric tensors are required and will become apparent in this section. The magnitudes, absolute values or lengths of tangent vectors are defined by

$$\left.\begin{array}{rcccl} |\boldsymbol{T}|_{\boldsymbol{G}} & = & \sqrt{\boldsymbol{T}\cdot(\boldsymbol{G}\boldsymbol{T})} & = & \sqrt{T^A(T^B\delta_{AB})} \\ |\boldsymbol{t}|_{\boldsymbol{g}} & = & \sqrt{\boldsymbol{t}\cdot(\boldsymbol{g}\boldsymbol{t})} & = & \sqrt{T^a(T^b\delta_{ab})} \end{array}\right\} . \tag{2.17}$$

Due to the positions of the indices, the inner product between two tangent vectors can only be calculated with the aid of the Lagrangian and Eulerian metric tensors $\boldsymbol{G}$ and $\boldsymbol{g}$, respectively. In orthonormal cartesian basis systems, $\boldsymbol{E}_A = \boldsymbol{E}^A$ and $\boldsymbol{e}_a = \boldsymbol{e}^a$ with $\boldsymbol{E}_i \cdot \boldsymbol{E}_j = \delta_{ij}$ and $\boldsymbol{e}_i \cdot \boldsymbol{e}_j = \delta_{ij}$. Applied in this work, the Kronecker symbols are used as natural metrics. The Lagrangian metric $\boldsymbol{G} = \delta_{AB}\boldsymbol{E}^A \otimes \boldsymbol{E}^B$ and the Eulerian counterpart $\boldsymbol{g} = \delta_{ab}\boldsymbol{e}^a \otimes \boldsymbol{e}^b$ are considered to be mappings of tangent vectors between tangential- and cotangential spaces. They generate their respective normal vectors in the cotangential spaces in the form

$$\boldsymbol{G} : \left\{\begin{array}{lcl} T_{\boldsymbol{X}}\mathcal{B} & \rightarrow & T^*_{\boldsymbol{X}}\mathcal{B} \\ \boldsymbol{T} & \mapsto & \boldsymbol{N} = \boldsymbol{G}\boldsymbol{T} \end{array}\right. ; \qquad \boldsymbol{g} : \left\{\begin{array}{lcl} T_{\boldsymbol{X}}\mathcal{S}_t & \rightarrow & T^*_{\boldsymbol{x}}\mathcal{S}_t \\ \boldsymbol{t} & \mapsto & \boldsymbol{n} = \boldsymbol{g}\boldsymbol{t}. \end{array}\right. . \tag{2.18}$$

The geometrical mappings between the tangential and cotangential spaces of the Lagrangian and Eulerian configurations are depicted in Figure 8. So far the mappings between all tangential spaces of both configurations have been introduced. In what follows, the finite deformations of material curves are discussed. In order to describe this, the stretch vector $\boldsymbol{\lambda}$ is defined and desribes the change of deformation by progression on the material curve in the direction of the tangential vector $\boldsymbol{T}$. The tangent vector follows as the directional derivative $\boldsymbol{\lambda} = \frac{d}{d\epsilon}|_{\epsilon=0}\boldsymbol{\varphi}_t(\boldsymbol{X} + \epsilon\boldsymbol{T})$ and therefore

$$\boldsymbol{\lambda} = \boldsymbol{F}_t\boldsymbol{T} . \tag{2.19}$$

If the Lagrangian vector $\boldsymbol{T}$ is normalized to the so-called tangent unit vector, e.g. $|\boldsymbol{T}|_{\boldsymbol{G}} = 1$, then the scalar stretch of the material curve follows by definition as $\lambda = |\boldsymbol{\lambda}|_{\boldsymbol{g}} = \sqrt{\boldsymbol{\lambda} \cdot (\boldsymbol{g}\boldsymbol{\lambda})}$. The stretch λ can mathematically be derived in two different ways. On the one hand, it can be derived in the material configuration based on a given material direction $\boldsymbol{T}$, or alternatively in the spatial configuration based on an a priori known spatial direction $\boldsymbol{t}$.

Material Description of the Stretch. If the deformation gradient $\boldsymbol{F}$ and the material tangent unit vector $\boldsymbol{T}$ are given, the spatial stretch vector follows as $\boldsymbol{\lambda} = \boldsymbol{F}\boldsymbol{T}$ and thus the stretch as the norm of the stretch vector as $\lambda = |\boldsymbol{\lambda}|_{\boldsymbol{g}} = \sqrt{\boldsymbol{T} \cdot (\boldsymbol{F}^T \boldsymbol{g} \boldsymbol{F})\boldsymbol{T}}$. Based on this representation, the *right Cauchy-Green tensor* $\boldsymbol{C}$ can be defined as

$$\boldsymbol{C} = \boldsymbol{F}^T \boldsymbol{g} \boldsymbol{F} \qquad \text{or} \qquad C_{AB} = F^a{}_A F^b{}_B \delta_{ab} \ . \tag{2.20}$$

The right Cauchy-Green tensor $\boldsymbol{C}$ is a positive definite symmetric tensor field on the material configuration $\mathcal{B}$ with the property of a metric. Therefore, in analogy to $\boldsymbol{G}$, the right Cauchy-Green tensor $\boldsymbol{C}$ can be regarded as a mapping from the tangential to the cotangential spaces of the Lagrangian configuration,

$$\boldsymbol{C} : \left\{ \begin{array}{lcl} T_{\boldsymbol{X}}\mathcal{B} & \rightarrow & T^*_{\boldsymbol{X}}\mathcal{B} \\ \boldsymbol{T} & \mapsto & \boldsymbol{N} = \boldsymbol{C}\boldsymbol{T} \end{array} \right. . \tag{2.21}$$

An important coherence follows from the observation that the right Cauchy-Green tensor represents the Eulerian metric $\boldsymbol{g}$ in the Lagrangian configuration. It is the so-called *Pull-Back* $\boldsymbol{C} = \boldsymbol{\varphi}_t^*(\boldsymbol{g})$ of the Eulerian metric $\boldsymbol{g}$. In order to describe the deformation comprehensively, in addition to stretches, changes of angles need to be computed. With given material directions, the shearing strains ϑ are determined using the right Cauchy-Green metric. At first, two initially perpendicular tangent vectors $\boldsymbol{T}$ and $\bar{\boldsymbol{T}}$ are considered. The actual angle in the deformed configuration is calculated with the expression

$$\cos\vartheta = \frac{\boldsymbol{T} \cdot (\boldsymbol{C}\bar{\boldsymbol{T}})}{|\boldsymbol{T} \cdot \boldsymbol{C}\boldsymbol{T}|} \ . \tag{2.22}$$

Spatial Description of the Stretch. If the normal mapping $\boldsymbol{F}^{-T}$ and the spatial direction $\boldsymbol{t}$ with $|\boldsymbol{t}|_{\boldsymbol{g}} = 1$ are given, then the Lagrangian stretch vector is expressed on the material configuration as $\boldsymbol{\Lambda} := \boldsymbol{T}/\lambda$. The scalar-valued stretch then follows as $\frac{1}{\lambda} = |\boldsymbol{\Lambda}|_{\boldsymbol{G}} = \sqrt{\boldsymbol{t} \cdot (\boldsymbol{F}^{-T} \boldsymbol{G} \boldsymbol{F}^{-1})\boldsymbol{t}}$. Based on this representation, the *left Cauchy-Green tensor* can be defined as

$$\boldsymbol{c} = \boldsymbol{F}^{-T} \boldsymbol{G} \boldsymbol{F}^{-1} \qquad \text{or} \qquad c_{AB} = (F^A{}_a)^{-1} (F^B{}_b)^{-1} \delta_{AB} \ . \tag{2.23}$$

The left Cauchy-Green tensor also bears the properties of a metric, because it is understood as a mapping from the tangential to the cotangential spaces of the Eulerian configuration,

$$\boldsymbol{c} : \left\{ \begin{array}{lcl} T_{\boldsymbol{x}}\mathcal{S}_t & \rightarrow & T^*_{\boldsymbol{x}}\mathcal{S}_t \\ \boldsymbol{t} & \mapsto & \boldsymbol{n} = \boldsymbol{c}\boldsymbol{t} \ . \end{array} \right. \tag{2.24}$$

Instead of the left Cauchy-Green tensor $\boldsymbol{c}$, its inverse is frequently used. This tensor $\boldsymbol{b} = \boldsymbol{c}^{-1}$ is commonly known as the *Finger tensor*. As the inverse, it maps elements

of the Eulerian cotangential space to the Eulerian tangential space. From a geometrical point of view, the left Cauchy-Green tensor $\boldsymbol{c}$ represents the Lagrangian metric $\boldsymbol{G}$ in the Eulerian description. It is characterized by the so-called *Push-Forward* $\boldsymbol{c} = \boldsymbol{\varphi}_{t*}(\boldsymbol{G})$ of the Lagrangian metric $\boldsymbol{G}$. The change of the angle between two tangential vectors $\boldsymbol{t}$ und $\bar{\boldsymbol{t}}$, which are perpendicular in the deformed structure, with respect to the initial configuration is defined as the angle θ between the two material stretch vectors $\boldsymbol{\Lambda}$ and $\bar{\boldsymbol{\lambda}}$,

$$\cos\theta = \frac{\boldsymbol{t} \cdot (\boldsymbol{c}\bar{\boldsymbol{t}})}{|\boldsymbol{t} \cdot (\boldsymbol{c}\boldsymbol{t})|} \ . \tag{2.25}$$

Thus it is determined using the left Cauchy-Green metric $\boldsymbol{c}$. Figure 8 summarizes the dual commuting mappings between the tangential and cotangential spaces of the Lagrangian and Eulerian configurations. The definitions of the deformation-dependent metric tensors can easily be gathered. The metric tensors $(\boldsymbol{G}, \boldsymbol{c})$ and $(\boldsymbol{C}, \boldsymbol{g})$ are dual geometric

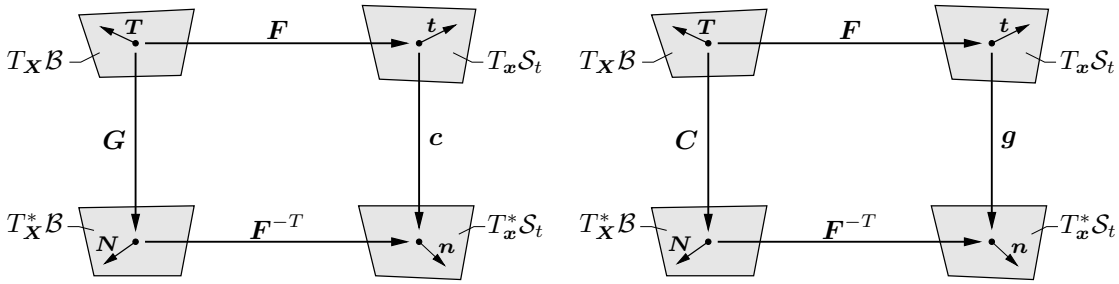

Figure 8: Definition of the dual reference $(\boldsymbol{G}, \boldsymbol{c})$ and current $(\boldsymbol{C}, \boldsymbol{g})$ metric tensors as mappings.

objects that commute, connected by the Pull-Back-/ Push-Forward operations with the tangential- and normal mappings. It must be noted that the representations of the metric tensors as constant Kronecker symbols hold in cartesian basis systems only.

2.1.5. Basic Strain Tensors. So far the deformation gradient $\boldsymbol{F}$ and some more derived basic geometric objects have been introduced as fundamental measures of deformation of large strain kinematics. In order to further characterize the local deformation, in what follows several elementary strain tensors are presented. These strain tensors describe the deformation of infinitesimal volume elements with reference to either the Lagrangian or the Eulerian manifolds.

Lagrangian Description. Green Strain Tensor. At first a material tangent unit vector $\boldsymbol{T}$ is considered. In the deformed structure the magnitude follows as $\lambda = |\boldsymbol{T}|_{\boldsymbol{g}}$. Comparison of the squares of the lengths of material and spatial line elements $\epsilon_{Green} = (\lambda^2 - 1)/2$ defines the so-called *Green strain tensor* $\boldsymbol{E}$ as

$$\hat{\boldsymbol{E}}(\boldsymbol{C}) = \frac{1}{2}(\boldsymbol{C} - \boldsymbol{G}) \ . \tag{2.26}$$

The Green strain tensor $\boldsymbol{E}$ additively compares the spatial metric (in the Lagrangian representation) $\boldsymbol{C}$ with the material one $\boldsymbol{G}$ with respect to the Lagrangian manifold. In the initial configuration, it follows that $\boldsymbol{E}_0 = \boldsymbol{0}$, in contrast to the right Cauchy-Green tensor that in the initial configuration equals the unit tensor $\boldsymbol{C}_0 = \boldsymbol{1}$.

Eulerian Description, Almansi Strain Tensor. In analogy to the material description, in the Eulerian approach a spatial tangent unit vector $\boldsymbol{t}$ is considered. For the

spatial configuration with $|\boldsymbol{t}|_{\boldsymbol{g}} = 1$, the material length of the vector follows as $|\boldsymbol{t}|_{\boldsymbol{C}} = 1/\lambda$. A comparison of the squares of the lengths of both line elements $\epsilon_{Almansi} = (1 - \lambda^{-2})/2$ yields the representation of the *Almansi strain tensor* $\boldsymbol{e}$ as

$$\hat{\boldsymbol{e}}(\boldsymbol{c}) = \frac{1}{2}(\boldsymbol{g} - \boldsymbol{c}) \ . \tag{2.27}$$

The Almansi strain tensor additively compares the spatial metric $\boldsymbol{g}$ with the material one (in the Eulerian description) $\boldsymbol{c}$ with respect to the Eulerian manifold. In the initial configuration the Almansi strain tensor is zero, $\boldsymbol{e}_0 = \boldsymbol{0}$, whereas the material metric follows as $\boldsymbol{c}_0 = \boldsymbol{1}$. In literature, many different strain measures are defined, for an overview see for example the books Bonet & Wood [15] or Holzapfel [49].

2.1.6. Polar Decomposition. Spectral Representation. The fundamental tangential mapping $\boldsymbol{F} : T_{\boldsymbol{X}}\mathcal{B} \to T_{\boldsymbol{x}}\mathcal{S}$ can, in a multiplicative sense, unambiguously be understood as a composition of a rotation and a stretch,

$$\boldsymbol{F} = \boldsymbol{R}\boldsymbol{U} = \boldsymbol{v}\boldsymbol{R} \ . \tag{2.28}$$

Here, the rotation tensor $\boldsymbol{R} = R^a{}_A \in SO(3)$ represents a proper orthogonal tensor of the special group $SO(3)$ with the two properties $\boldsymbol{R}^T = \boldsymbol{R}^{-1}$ and $\det[\boldsymbol{R}] = +1$. Again, $\boldsymbol{R}$ is understood as a mapping, it maps elements of the Lagrangian tangential space onto the Eulerian tangential space, $\boldsymbol{R} : T_{\boldsymbol{X}}\mathcal{B} \to T_{\boldsymbol{x}}\mathcal{S}_t$. The geometric object $\boldsymbol{U} = U^A{}_B \in \mathrm{Sym}_+(3)$ is termed the *right stretch tensor*. It maps elements of the Lagrangian tangential space onto the same Lagrangian tangential space, $\boldsymbol{U} : T_{\boldsymbol{X}}\mathcal{B} \to T_{\boldsymbol{X}}\mathcal{B}$. The right stretch tensor $\boldsymbol{U}$ is symmetric and positively definit. As a dual object, the *left stretch tensor* $\boldsymbol{v} = v^a{}_b \in \mathrm{Sym}_+(3)$ can be introduced that is also symmetric and positively definite. It maps elements of the Eulerian tangential space onto the same Eulerian tangential space, $\boldsymbol{v} : T_{\boldsymbol{x}}\mathcal{S}_t \to T_{\boldsymbol{x}}\mathcal{S}_t$. Figure 9 graphically depicts the rotation and stretch tensors as mappings. The symmetry properties of the stretch tensors $\boldsymbol{U}$ and $\boldsymbol{v}$ can only be defined

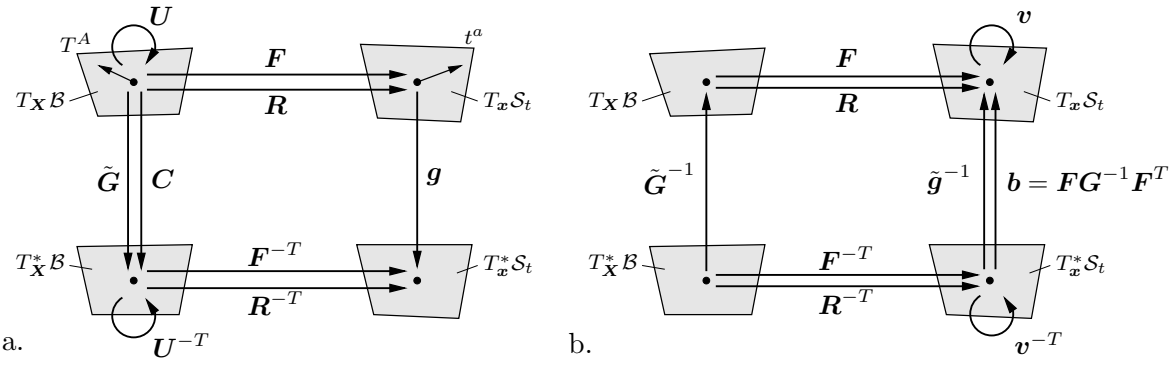

Figure 9: The right and left stretch tensors $\boldsymbol{U}$ and $\boldsymbol{v}$, respectively, are interpreted as mappings on the Lagrangian and Eulerian configurations.

with the aid of metric tensors since symmetry conditions only make sense for geometric objects with coequal indices which therefore represent mappings from the tangential into the cotangential spaces and vice versa, respectively. Thus one has $(\boldsymbol{G}\boldsymbol{U})^T = (\boldsymbol{G}\boldsymbol{U})$ and $(\boldsymbol{v}\boldsymbol{g}^{-1})^T = (\boldsymbol{v}\boldsymbol{g}^{-1})$ and the expressions of the Lagrangian and Eulerian metric tensors $\boldsymbol{C}$ and $\boldsymbol{c}$ in terms of the stretch tensors follow as

$$\boldsymbol{C} = \boldsymbol{U}^T\boldsymbol{R}^T\boldsymbol{g}\boldsymbol{R}\boldsymbol{U} = \boldsymbol{U}^T\boldsymbol{G}\boldsymbol{U} \quad \text{and} \quad \boldsymbol{c}^{-1} = \boldsymbol{v}\boldsymbol{R}\boldsymbol{G}^{-1}\boldsymbol{R}^T\boldsymbol{v}^T = \boldsymbol{v}^{-T}\boldsymbol{g}\boldsymbol{v}^{-1} \ . \tag{2.29}$$

From these relations the Lagrangian and Eulerian metric tensors can be identified as $\boldsymbol{G} = \boldsymbol{R}^T\boldsymbol{g}\boldsymbol{R}$ and $\boldsymbol{g}^{-1} = \boldsymbol{R}\boldsymbol{G}^{-1}\boldsymbol{R}^T$. They characterize the orthogonality $\boldsymbol{g}\boldsymbol{R}\boldsymbol{G}^{-1} = \boldsymbol{R}^{-T} = \boldsymbol{R}^{-1} = \boldsymbol{G}^{-1}\boldsymbol{R}^T\boldsymbol{g}$ of the rotation tensor $\boldsymbol{R}$. The right and left stretch tensors $\boldsymbol{U}$ and $\boldsymbol{v}$ are computed from the definitions of the right and left Cauchy-Green tensors in the material and spatial descriptions as

$$\boldsymbol{U} = \sqrt{\boldsymbol{G}^{-1}\boldsymbol{C}} \qquad \text{and} \qquad \boldsymbol{v} = \sqrt{\boldsymbol{c}^{-1}\boldsymbol{g}} \; . \tag{2.30}$$

From these expressions and with a known deformation gradient $\boldsymbol{F}$, the rotation tensor can be computed as $\boldsymbol{R} = \boldsymbol{F}\boldsymbol{U}^{-1}$ and $\boldsymbol{R} = \boldsymbol{v}^{-1}\boldsymbol{F}$, respectively. These equations yield the dual eigenvalue problems

$$\left.\begin{aligned} (\boldsymbol{G}^{-1}\boldsymbol{C})\boldsymbol{N}^i &= \lambda_i^2\boldsymbol{N}^i \\ \boldsymbol{N}_i(\boldsymbol{G}^{-1}\boldsymbol{C}) &= \lambda_i^2\boldsymbol{N}_i \end{aligned}\right\} \qquad \left.\begin{aligned} (\boldsymbol{c}^{-1}\boldsymbol{g})\boldsymbol{n}^i &= \lambda_i^2\boldsymbol{n}^i \\ \boldsymbol{n}_i(\boldsymbol{c}^{-1}\boldsymbol{g}) &= \lambda_i^2\boldsymbol{n}_i \end{aligned}\right\} \; . \tag{2.31}$$

Here the eigenvalues λ_i characterize the main stretches. Due to the symmetry of the tensors $\boldsymbol{C}$ and $\boldsymbol{G}$, these eigenvalues are real. $\boldsymbol{N}^i$, $\boldsymbol{N}_i$ and $\boldsymbol{n}^i$, $\boldsymbol{n}_i$ are dual, contra- and covariant Lagrangian and Eulerian eigenvector triads with properties $\boldsymbol{N}^i \cdot \boldsymbol{N}_j = \delta^i{}_j$ and $\boldsymbol{n}^i \cdot \boldsymbol{n}_j = \delta^i{}_j$. As basis systems, they naturally span the tangential and cotangential spaces. With the aid of the metric tensors, the co- and contravariant vector triads can be connected in their respective configurations,

$$\boldsymbol{N}_i = \boldsymbol{G}\boldsymbol{N}^i \quad \text{and} \quad \boldsymbol{n}_i = \boldsymbol{g}\boldsymbol{n}^i \; . \tag{2.32}$$

In analogy, the triads of the respective tangential- and cotangential spaces are connected by the rotation tensor,

$$\boldsymbol{n}^i = \boldsymbol{R}\boldsymbol{N}^i \quad \text{and} \quad \boldsymbol{n}_i = \boldsymbol{R}^{-T}\boldsymbol{N}^i \; . \tag{2.33}$$

The rotation tensor $\boldsymbol{R}$ rotates the Lagrangian eigenvector triads $\boldsymbol{N}^i$ and $\boldsymbol{N}_i$ into the Eulerian representations $\boldsymbol{n}^i$ and $\boldsymbol{n}_i$. With these recent relations, the spectral representations $(\boldsymbol{G}^{-1}\boldsymbol{C}) = \sum_{i=1}^{3} \lambda_i^2 \boldsymbol{N}^i \otimes \boldsymbol{N}_i$ and $(\boldsymbol{c}^{-1}\boldsymbol{g}) = \sum_{i=1}^{3} \lambda_i^2 \boldsymbol{n}^i \otimes \boldsymbol{n}_i$ can be transformed with equations (2.31). This yields the spectral representations of the two stretch tensors and the rotation tensor as

$$\boldsymbol{U} = \sum_{i=1}^{3} \lambda_i \boldsymbol{N}^i \otimes \boldsymbol{N}_i \; , \qquad \boldsymbol{v} = \sum_{i=1}^{3} \lambda_i \boldsymbol{n}^i \otimes \boldsymbol{n}_i \quad \text{and} \quad \boldsymbol{R} = \sum_{i=1}^{3} \boldsymbol{n}^i \otimes \boldsymbol{N}_i \; . \tag{2.34}$$

In this work only cartesian basis systems are employed, thus there is no difference between the Lagrangian and Eulerian co- and contravariant eigenvector triads. The relations $\boldsymbol{N}^i = \boldsymbol{N}_i$ and $\boldsymbol{n}^i = \boldsymbol{n}_i$ hold. Thus the spectral representations of the metric tensors in the eigenvectors can be given as

$$\left.\begin{aligned} \boldsymbol{C} &= \sum_{i=1}^{3} \lambda_i^2 \boldsymbol{N}_i \otimes \boldsymbol{N}_i \\ \boldsymbol{G} &= \sum_{i=1}^{3} 1 \boldsymbol{N}_i \otimes \boldsymbol{N}_i \end{aligned}\right\} \qquad \left.\begin{aligned} \boldsymbol{g} &= \sum_{i=1}^{3} 1 \boldsymbol{n}_i \otimes \boldsymbol{n}_i \\ \boldsymbol{c} &= \sum_{i=1}^{3} \lambda_i^2 \boldsymbol{n}_i \otimes \boldsymbol{n}_i \; . \end{aligned}\right\} \tag{2.35}$$

The deformation gradient $\boldsymbol{F}$ is a two-field tensor and can alternatively be built by the dyadic product of the Eulerian and Lagrangian principal stretch directions,

$$\boldsymbol{F} = \sum_{i=1}^{3} \lambda_i \boldsymbol{n}^i \otimes \boldsymbol{N}_i \; . \tag{2.36}$$

2.1.7. Velocity Gradients and Lie Time Derivative. Now the decription of the temporal change of spatial objects relative to the actual configuration is discussed. These relative time derivatives are related to the material time derivatives of Lagrangian objects. The time derivation of spatial objects $\dot{\boldsymbol{w}} = \frac{\partial}{\partial t}\boldsymbol{w} + \operatorname{grad}_{\boldsymbol{x}} \boldsymbol{w} \cdot \boldsymbol{w}$ is described as the sum of local and convective parts of the time derivatives. It yields the total temporal change of a spatial object $\boldsymbol{w}(\boldsymbol{x}, t)$. In what follows, this relative change is discussed in more detail. If the stretch of a material line element $\boldsymbol{\lambda} = \boldsymbol{FT}$ is considered, its time derivative follows as $\dot{\boldsymbol{\lambda}} = \dot{\boldsymbol{F}}\boldsymbol{T}$. The time derivative of the deformation gradient $\dot{\boldsymbol{F}}$ is termed *material velocity gradient*, it is the gradient of the material velocity field,

$$\dot{\boldsymbol{F}} = \nabla_{\boldsymbol{X}} \boldsymbol{V} \ . \tag{2.37}$$

In order to represent the change of the stretch $\dot{\boldsymbol{\lambda}}$ exclusively in terms of *spatial* tensor fields, from $\boldsymbol{T} = \boldsymbol{F}^{-1}\boldsymbol{\lambda}$ the time derivative can be deduced as

$$\dot{\boldsymbol{\lambda}} = \dot{\boldsymbol{F}}\boldsymbol{F}^{-1}\boldsymbol{\lambda} = \boldsymbol{l}\boldsymbol{\lambda} \ . \tag{2.38}$$

This equation defines the *spatial velocity gradient* $\boldsymbol{l} = \nabla_{\boldsymbol{x}} \boldsymbol{v} = \dot{\boldsymbol{F}}\boldsymbol{F}^{-1}$ that represents a spatial mixed-variant tensor field. A Lie time derivative $\mathcal{L}_{\boldsymbol{v}}\boldsymbol{w}$ of a spatial Eulerian object $\boldsymbol{w}$ describes its relative change with respect to time and is generated in three steps. At first, a 'Pull-Back' operation of the Eulerian object $\boldsymbol{w}$ onto its material representation $\boldsymbol{W} = \boldsymbol{\varphi}_t^*(\boldsymbol{w})$ is performed. This Lagrangian object $\boldsymbol{W}$ can now be derived with respect to time, $\dot{\boldsymbol{W}} = \frac{\partial}{\partial t}\boldsymbol{W}$. Finally, the newly derived material object is then transformed by a 'Push-Forward' operation onto the spatial configuration,

$$\mathcal{L}_{\boldsymbol{v}}\boldsymbol{w} = \boldsymbol{\varphi}_{t*}(\dot{\boldsymbol{W}}) \ .$$

This procedure is known as the *Lie time derivative* of the spatial object $\boldsymbol{w}$. In summary, the three-step algorithm to compute the Lie time derivative can be written in one expression as

$$\mathcal{L}_{\boldsymbol{v}}\boldsymbol{w} = \boldsymbol{\varphi}_{t*}\left[\frac{\partial}{\partial t}\left[\boldsymbol{\varphi}_t^*(\boldsymbol{w})\right]\right] \ . \tag{2.39}$$

As an example, the Lie time derivation of the spatial metric $\boldsymbol{g} = \delta_{ab}$, the constant Kronecker symbol, is considered:

1. 'Pull-Back' of $\boldsymbol{g}$,

$$\boldsymbol{\varphi}_t^*(\boldsymbol{g}) = \boldsymbol{F}^T\boldsymbol{g}\boldsymbol{F} = \boldsymbol{C}$$

   yields the right Cauchy-Green tensor as the dual material object.
2. Time derivation of the material object $\boldsymbol{C}$,

$$\dot{\boldsymbol{C}} = \frac{\partial}{\partial t}\boldsymbol{C} = \overline{\boldsymbol{F}^T\boldsymbol{g}\boldsymbol{F}} = \dot{\boldsymbol{F}}^T\boldsymbol{g}\boldsymbol{F} + \boldsymbol{F}^T\boldsymbol{g}\dot{\boldsymbol{F}} \ .$$

3. 'Push-Forward' of the material object $\dot{\boldsymbol{C}}$,

$$\mathcal{L}_{\boldsymbol{v}}\boldsymbol{g} = \boldsymbol{F}^{-T}\dot{\boldsymbol{C}}\boldsymbol{F}^{-1} = \boldsymbol{F}^{-T}\dot{\boldsymbol{F}}^T\boldsymbol{g} + \boldsymbol{g}\dot{\boldsymbol{F}}\boldsymbol{F}^{-1} =: \boldsymbol{l}^T\boldsymbol{g} + \boldsymbol{g}\boldsymbol{l} = 2\boldsymbol{d} \ .$$

An important result is that the Lie time derivative of the spatial metric $\boldsymbol{g}$ corresponds to the deformation velocity tensor $\boldsymbol{d}$. The associated rates of the deformations in the material and spatial configurations are expressed as

$$\dot{\boldsymbol{E}} = \frac{1}{2}\dot{\boldsymbol{C}} \quad \longleftrightarrow \quad \boldsymbol{d} = \frac{1}{2}\mathcal{L}_{\boldsymbol{v}}\boldsymbol{g} \ . \tag{2.40}$$

Note that the Lie time derivative a priori yields objective rates of tensors, i.e. they are invariant under superimposed rigid body motions.

2.2. Concept of Stress

In the following sections general physical statements of continuum mechanics are discussed which base on *Euler's cut principle* An introduction of *phenomenological* quantities such as the stresses is presented as well as conservation laws of *physical* quantities such as mass and momentum. At first, a part $\mathcal{B}_P$ of the continuous body $\mathcal{B}$ is cut out of the rest of the solid. A key idea now is to replace the mechanical (and possible thermal) influences of the remaining part of the body by contact stresses (and heat flux expressions), see Figure 10. Then mass, momentum and angular momentum for the cut body are accounted for and balanced. The Eulerian traction (stress) vector $\boldsymbol{t}$ on the spatial deformed surface $\partial\mathcal{S}_P$

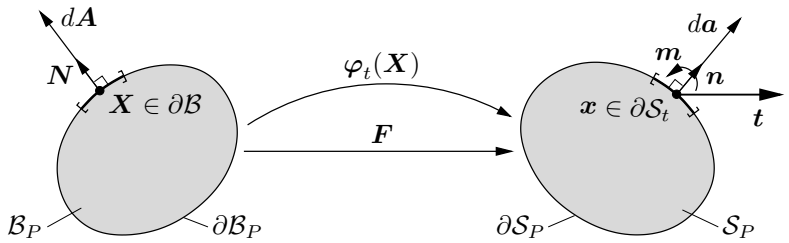

Figure 10: Parts $\mathcal{B}_P$ and $\mathcal{S}_t$ cut out from the whole body $\mathcal{B}$. At a point $\boldsymbol{x} \in \partial\mathcal{S}_P$, the mechanical action of the remaining part of $\mathcal{S}_t$ is replaced by tractions $\boldsymbol{t}$ and couple tractions $\boldsymbol{m}$.

replaces the mechanical influence of the part that is cut off.

2.2.1. Representation of Stress Tensors. Cauchy Stress Tensor. The stress vector $\boldsymbol{t}$ is assumed to be a linear function of the direction of the cut, characterized by the normal direction $\boldsymbol{n}$ on the Eulerian surface $\partial\mathcal{S}_P$,

$$\boldsymbol{t}(\boldsymbol{x}, t; \boldsymbol{n}) = \boldsymbol{\sigma}(\boldsymbol{x}, t) \cdot \boldsymbol{n} \ . \tag{2.41}$$

This equation is commonly known as the *theorem of Cauchy*, it defines the *Cauchy stress tensor* $\boldsymbol{\sigma} = \sigma^{ab}$. From a geometrical point of view and since the normal is an element of the cotangential space of the Eulerian manifold, $\boldsymbol{n} \in T^*_{\boldsymbol{x}}\mathcal{S}$, and the traction vector being an element of the tangential space, $\boldsymbol{t} \in T_{\boldsymbol{x}}\mathcal{S}_t$, the Cauchy stress tensor is understood as a mapping of the form

$$\boldsymbol{\sigma} : \left\{ \begin{array}{lcl} T^*_{\boldsymbol{x}}\mathcal{S}_t & \rightarrow & T_{\boldsymbol{x}}\mathcal{S}_t \\ \boldsymbol{n} & \mapsto & \boldsymbol{t} = \boldsymbol{\sigma} \cdot \boldsymbol{n} \end{array} \right. . \tag{2.42}$$

Sometimes, not only surface tractions but also surface couple stresses are introduced to replace the mechanical action of the remaining part, see Figure 10. Therein, a Cauchy-like

theorem of the form $\boldsymbol{m} = \tilde{\boldsymbol{\sigma}}\boldsymbol{n}$ is assumed, where $\tilde{\boldsymbol{\sigma}}$ is the couple stress tensor. The Cauchy stresses relate the force that locally acts at the cut surface $\partial\mathcal{S}_P$ to the deformed surface, see Figure 10. Therefore, the Cauchy stresses are also termed *true stresses*. If body- and surface couple tractions are neglected, the Cauchy stress tensor becomes symmetric. A proof follows in the discussion of the balance of angular momentum.

Kirchhoff Stress Tensor. The *Kirchhoff stress tensor* $\boldsymbol{\tau}$ follows by multiplying the Cauchy stress tensor with the Jacobian $J = \det[\boldsymbol{F}]$ as

$$\boldsymbol{\tau} = J\boldsymbol{\sigma} \ . \tag{2.43}$$

Recall that the Jacobian J characterizes the volume ratio of infinitesimal volume elements of the form $dv = J\ dV$. The Kirchhoff stress tensor $\boldsymbol{\tau} = \tau^{ab}$ is a contravariant Eulerian object and is therefore understood as a mapping,

$$\boldsymbol{\tau} : \left\{ \begin{array}{lcl} T^*_{\boldsymbol{x}}\mathcal{S}_t & \rightarrow & T_{\boldsymbol{x}}\mathcal{S}_t \\ \boldsymbol{n} & \mapsto & J\boldsymbol{t} = \boldsymbol{\tau}\cdot\boldsymbol{n} \end{array} \right. . \tag{2.44}$$

In contrast to the true Cauchy stress tensor, the Kirchhoff stress tensor can be understood as the dual geometrical Eulerian object to the purely Lagrangian second Piola-Kirchhoff stress tensor $\boldsymbol{S}$, see below. Observe furthermore that in countless problems in continuum mechanics, an important rate is the Lie time derivative of the Kirchhoff stresses that appears as $\mathcal{L}_{\boldsymbol{v}}\boldsymbol{\tau} = \dot{\boldsymbol{\tau}} - \boldsymbol{l}\boldsymbol{\tau} - \boldsymbol{\tau}\boldsymbol{l}^T$.

First Piola-Kirchhoff Stress Tensor. The Cauchy theorem $\boldsymbol{t} = \boldsymbol{\sigma}\boldsymbol{n}$ is completely an Eulerian operation. A Lagrangian counterpart is constructed by the Cauchy-type theorem as

$$\boldsymbol{T}(\boldsymbol{X}, t; \boldsymbol{N}) = \tilde{\boldsymbol{P}}(\boldsymbol{X}, t)\boldsymbol{N} \ , \tag{2.45}$$

where $\boldsymbol{N}$ characterizes the unit normal associated with the undeformed cut surface $\partial\mathcal{B}_P$. Observe that $\boldsymbol{T} = T^a$ represents an *Eulerian* object, see Figure 10. $\boldsymbol{T}$ relates the current contact force to the initial surface, whereas the Cauchy object $\boldsymbol{t}$ relates it to the deformed cut surface. Both formulations must be equivalent,

$$\boldsymbol{T}\cdot dA = \boldsymbol{t}\cdot da \ . \tag{2.46}$$

The two infinitesimal area elements $d\boldsymbol{a} = \boldsymbol{n}da$ and $d\boldsymbol{A} = \boldsymbol{N}dA$ are transformed based on a normal mapping. With $d\boldsymbol{a} = J\boldsymbol{F}^{-T}d\boldsymbol{A}$, using equation (2.46) and the transformation of the two associated area elements, the definition of the *First Piola-Kirchhoff stress tensor* arises as

$$\tilde{\boldsymbol{P}} = J\boldsymbol{\sigma}\boldsymbol{F}^{-T} = \boldsymbol{\tau}\boldsymbol{F}^{-T} \ . \tag{2.47}$$

This is known as the *Piola transformation* of the Cauchy stress tensor $\boldsymbol{\sigma}$. Due to $\boldsymbol{T} \in T_{\boldsymbol{x}}\mathcal{S}_t$ and $\boldsymbol{N} \in T^*_{\boldsymbol{X}}\mathcal{B}$, the first Piola-Kirchhoff stress tensor is also understood as a mapping,

$$\tilde{\boldsymbol{P}} : \left\{ \begin{array}{lcl} T^*_{\boldsymbol{x}}\mathcal{B} & \rightarrow & T_{\boldsymbol{x}}\mathcal{S}_t \\ \boldsymbol{N} & \mapsto & \boldsymbol{T} = \boldsymbol{P}\boldsymbol{N} \end{array} \right. . \tag{2.48}$$

This stress tensor $\tilde{\boldsymbol{P}} = \tilde{P}^{aA}$ measures the stresses with regard to the undeformed, initial cut surface $\partial\mathcal{B}_P$. These stresses are therefore fictitious and frequently called nominal

stresses. In contrast to the other, one-field stress tensors, $\tilde{\boldsymbol{P}} = \tilde{P}^{aA}$ is an unsymmetric two-point stress tensor field. A modified first Piola-Kirchhoff tensor $\boldsymbol{P} = \boldsymbol{g}\tilde{\boldsymbol{P}}$ with $P_a{}^A = \delta_{ab}\tilde{P}^{bA}$ is often used, see Figure 11, as for example in variational two-point formulations in elastostatics. Therein, the work done on a solid in deformation is expressed by the dual form $\mathcal{P} := \boldsymbol{P} : \dot{\boldsymbol{F}}$.

Second Piola-Kirchhoff Stress Tensor. From a formal point of view, a purely Lagrangian stress tensor as the Lagrangian counterpart to the Eulerian stress tensors is required. It can be constructed by transforming the nominal stress vector $\boldsymbol{T} \in T_{\boldsymbol{x}}\mathcal{S}_t$ with $\boldsymbol{F}^{-1}$ back onto the associated Lagrangian object, $\tilde{\boldsymbol{T}} = \boldsymbol{F}^{-1}\boldsymbol{T} \in T_{\boldsymbol{X}}\mathcal{B}$. This leads to the definition of a new stress tensor that is characterized by a theorem similar to Cauchy's law, $\tilde{\boldsymbol{T}} = \boldsymbol{S}\boldsymbol{N}$. This finally gives the definition of the *second Piola-Kirchhoff stress tensor* $\boldsymbol{S} = S^{AB}$,

$$\boldsymbol{S} = \boldsymbol{F}^{-1}\tilde{\boldsymbol{P}} = \boldsymbol{F}^{-1}\boldsymbol{\tau}\boldsymbol{F}^{-T} \ . \tag{2.49}$$

The second Piola-Kirchhoff stress tensor $\boldsymbol{S} = S^{AB}$ is a purely Lagrangian symmetric object. As a mapping it reads

$$\boldsymbol{S} : \left\{ \begin{array}{lcl} T^*_{\boldsymbol{X}}\mathcal{B} & \rightarrow & T_{\boldsymbol{X}}\mathcal{B} \\ \boldsymbol{N} & \mapsto & \tilde{\boldsymbol{T}} = \boldsymbol{S}\boldsymbol{N} \end{array} \right. . \tag{2.50}$$

Figure 11 summarizes the stress tensors as mappings between the tangential and cotangential spaces of the Lagrangian and Eulerian manifolds. The relations between the particular formulations can easily be constructed by using the proper mappings between the tangential and co-tangential spaces.

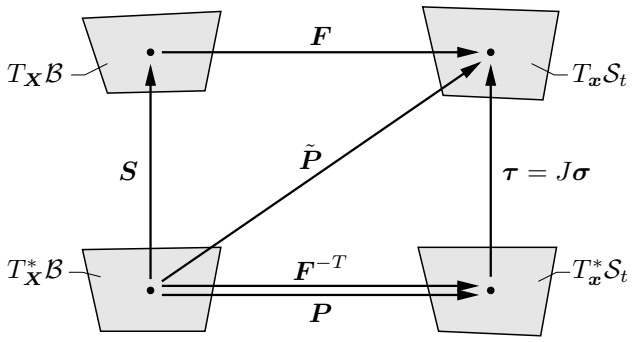

Figure 11: Definition of stress tensors as mappings.

2.2.2. 'Pull-Back' and 'Push-Forward' Operations. Piola Identity. Similar to the dual Eulerian metrics $\boldsymbol{g}$ and $\boldsymbol{C}$, the Kirchhoff stress tensor $\boldsymbol{\tau}$ and the second Piola-Kirchhoff stress tensor $\boldsymbol{S}$ can be regarded as dual objects,

$$\boldsymbol{S} = \boldsymbol{\varphi}_t^*(\boldsymbol{\tau}) \qquad \boldsymbol{\tau} = \boldsymbol{\varphi}_{t*}(\boldsymbol{S}) \ . \tag{2.51}$$

Thus, $(\boldsymbol{C}, \boldsymbol{S})$ as well as $(\boldsymbol{g}, \boldsymbol{\tau})$ are dual geometric objects which in the Lagrangian and Eulerian configurations characterize strains and stresses. This duality is also emphasized by the fact that these quantities in the stress power appear as work-conform objects. If in

the referential configuration the stress power per unit volume $\dot{\mathcal{P}} := \boldsymbol{S} : \dot{\boldsymbol{E}}$ is considered, then the stress power follows by reformulation with $\dot{\boldsymbol{E}} = \overline{\frac{1}{2}(\boldsymbol{C} - \boldsymbol{G})}^{\cdot} = \frac{1}{2}\dot{\boldsymbol{C}}$ as

$$\mathcal{P} = \boldsymbol{S} : \frac{1}{2}\dot{\boldsymbol{C}} \ . \tag{2.52}$$

This expression can be transformed into the other configurations by $\mathcal{P} = \frac{1}{2}\,\mathrm{tr}[\boldsymbol{S}\dot{\boldsymbol{C}}^T] = \frac{1}{2}[\boldsymbol{F}^{-1}\boldsymbol{F}\boldsymbol{S}\boldsymbol{F}^T\boldsymbol{F}^{-T}\dot{\boldsymbol{C}}] = \frac{1}{2}\,\mathrm{tr}[(\boldsymbol{F}\boldsymbol{S}\boldsymbol{F}^T)(\boldsymbol{F}^{-T}\dot{B}C\boldsymbol{F}^{-1})]$.With the definitions of the Kirchhoff stresses $\boldsymbol{\tau}$ and its Lie time derivative $\mathcal{L}_{\boldsymbol{v}}\boldsymbol{g}$ of the Eulerian metric $\boldsymbol{g}$, the transformation reads $\mathcal{P} = \boldsymbol{\tau} : \frac{1}{2}\mathcal{L}_{\boldsymbol{v}}\boldsymbol{g}$. With the identity $\frac{1}{2}\mathcal{L}_{\boldsymbol{v}}\boldsymbol{g} = \mathrm{sym}[\boldsymbol{g}\boldsymbol{l}] = \boldsymbol{d}$, the purely Eulerian counterpart to (2.52) arises the as

$$\mathcal{P} = \boldsymbol{\tau} : \boldsymbol{d} \ . \tag{2.53}$$

The total stress power of the entire solid under consideration follows by integration of the local stress powers of the Lagrangian and Eulerian volumes, respectively. The Piola identity states that $\mathrm{DIV}[J\boldsymbol{F}^{-T}] = 0$ (the proof is given below). As divergence operators in the subsequent discussions the symbols

$$\mathrm{DIV}[\bullet] = \mathrm{DIV}_{\boldsymbol{X}}[\bullet] = [\bullet] \cdot \nabla_{\boldsymbol{X}} \quad \text{and} \quad \mathrm{div}[\bullet] = \mathrm{div}_{\boldsymbol{x}}[\bullet] = [\bullet] \cdot \nabla_{\boldsymbol{x}} \tag{2.54}$$

are used. The integral $\int_{\partial \mathcal{S}_P} = \int_{\partial \mathcal{S}_P} \boldsymbol{n}\ da = 0$ of $d\boldsymbol{a}$ over the actual cut surface $\partial \mathcal{S}_P$ is zero, with the area transformation it is mapped to the material configuration by $\int_{\partial \mathcal{S}_P} d\boldsymbol{a} = \int_{\partial \mathcal{B}_P} J\boldsymbol{F}^{-T} d\boldsymbol{A} = \int_{\partial \mathcal{B}_P} (J\boldsymbol{F}^{-T})\boldsymbol{N}\ dA = 0$. Application of the theorem of Gauss $\int_{\partial \mathcal{S}_P} d\boldsymbol{a} = \int_{\mathcal{B}_P} \mathrm{DIV}[J\boldsymbol{F}^{-T}] dV$ and the localization law, stating that $\mathcal{B}_P \subset \mathcal{B}$ can be arbitrary small, yields the local form

$$\mathrm{DIV}[J\boldsymbol{F}^{-T}] = 0 \ , \tag{2.55}$$

as given at the beginning of this section. The Piola identity possesses the following consequences with regard to the stress tensors. The first Piola-Kirchhoff and the Cauchy stress tensors are connected by the Piola transformation $\boldsymbol{P} = J\boldsymbol{\sigma}\boldsymbol{F}^{-T}$. Then the Piola identity yields

$$\mathrm{DIV}[\boldsymbol{P}] = J\,\mathrm{div}[\boldsymbol{\sigma}] \ . \tag{2.56}$$

2.2.3. Stress Power and Material Work of Deformation. With the geometric objects defined above, the stress power with respect to unit area of the reference configuration can be expresses in three different geometric settings in the form

$$\mathcal{P} := \boldsymbol{P} : \dot{\boldsymbol{F}} \ = \ \boldsymbol{S} : \frac{1}{2}\dot{\boldsymbol{C}} \ = \ \boldsymbol{\tau} : \frac{1}{2}\mathcal{L}_{\boldsymbol{v}}\boldsymbol{g}. \tag{2.57}$$

$\mathcal{P}$ represents the stress power, $\boldsymbol{P} : \dot{\boldsymbol{F}}$ denotes its two-point formulation, $\boldsymbol{S} : \frac{1}{2}\dot{\boldsymbol{C}}$ the Lagrangian and $\boldsymbol{\tau} : \frac{1}{2}\mathcal{L}_{\boldsymbol{v}}\boldsymbol{g}$ the Eulerian ones. $(\boldsymbol{F}, \boldsymbol{P})$, $(\boldsymbol{C}, \boldsymbol{S})$ and $(\boldsymbol{g}, \boldsymbol{\tau})$ are called dual kinematic/ kinetic objects. With the local stress power at hand, the full work needed by an (in)elastic continuum to deform from the reference to the current configuration can be computed for applied Dirichlet (essential) boundary conditions,

$$W = \int_{\mathcal{B}} w\ dV \quad \text{with} \quad w = \int_0^t \mathcal{P} d\tau \ . \tag{2.58}$$

$\mathcal{P}, w$ and W are input objects for a constitutive formulation based on the second axiom of thermodynamics. Observe that all subsequent treatments can be performed in the three basic and equivalent geometric settings, *1. the two-point formulation* $(\boldsymbol{P}, \boldsymbol{F})$, *2. the Lagrangian formulation* $(\boldsymbol{S}, \boldsymbol{C})$ and *3. the Eulerian formulation* $(\boldsymbol{\tau}, \boldsymbol{g})$.

2.3. Physical Balance Principles

In the present section, the classical fundamental balances equations for mass, linear momentum and angular momentum are discussed, as well as their consequences in the context of continuum mechanics. The balance principles apply to all branches of solid mechanics. They are valid for the whole or arbitrary parts of a continuum body $\mathcal{B}$, for every material and they do not depend on any material parameters. These fundamental balance principles must be satisfied at all times. Two further balance principles, the balances of energy and entropy, are omitted here since the text focuses on isothermal processes.

Balance of Mass. A fundamental physical property of any material is its mass, frequently denoted by the scalar m. Usually, it is defined to be a measure of the amount of material that a body $\mathcal{B}$ consists of. The density of the referential configuration is denoted by $\varrho_0(\boldsymbol{X})$, whereas the density of the spatial configuration is given by $\varrho(\boldsymbol{x}, t)$. The mass $M_{\mathcal{S}_P}$ of a particle $\mathcal{S}_P \subset \mathcal{S}_t$ follows as the integral $M_{\mathcal{S}_P} = \int_{\mathcal{S}_P} \varrho dV$. The *conservation of mass* is postulated as

$$\frac{d}{dt} M_{\mathcal{S}_P} = 0 \ , \tag{2.59}$$

stating that the mass $M_{\mathcal{S}_p}$ of a subset $\mathcal{S}_P \subset \mathcal{S}_t$ is constant in time. In some fields of continuum mechanics, the balance of mass is not continuous. For example, in biological growth processes, where mass production is time-dependent. In this thesis however, the mass is conserved in time. However, the Eulerian integration boundaries are time-dependent. In order to perform the integration, a transformation into integrals over the time-independent Lagrangian configuration is needed and is of the form $\frac{d}{dt} M_{\mathcal{S}_P} = \frac{d}{dt} \int_{\mathcal{S}_P(t)} \varrho \ dv = \frac{d}{dt} \int_{\mathcal{B}_P} \varrho_0 \ dV =: \frac{d}{dt} M_{\mathcal{B}_P} = 0$. This yields the local relation

$$\varrho = \frac{1}{J} \varrho_0 \ . \tag{2.60}$$

Equation (2.60) represents the local form of the balance of mass and is based on a comparison of the actual density ϱ with the material density ϱ_0. An alternative definition of the balance of mass follows from $\frac{d}{dt} \int_{\mathcal{B}_P} \varrho J dV = \int_{\mathcal{B}_P} \frac{d}{dt}(\varrho J) dV = 0$. Application of the localization theorem $\mathcal{B}_P \to dV$ and the chain rule gives $\dot{\varrho} J + \varrho \dot{J} = 0$. Note, the time derivative of the Jacobian calls for the chain rule, therefore

$$\dot{J} = \partial_{\boldsymbol{F}} \det[\boldsymbol{F}] : \dot{\boldsymbol{F}} = \operatorname{cof}[\boldsymbol{F}] : \dot{\boldsymbol{F}} \ , \tag{2.61}$$

with the cofactor $\operatorname{cof}[\boldsymbol{F}] := J \boldsymbol{F}^{-T}$ of the deformation gradient $\boldsymbol{F}$. Transformation with the aid of the trace operator yields an expression in terms of the spatial velocity gradient of the form $\operatorname{cof}[\boldsymbol{F}] : \dot{\boldsymbol{F}} = J \operatorname{tr}[\boldsymbol{F}^{-1} \dot{\boldsymbol{F}}] = J \operatorname{tr}[\boldsymbol{l}]$ and finally the local Eulerian form

$$\dot{\varrho} + \varrho \operatorname{div}[\boldsymbol{v}] = 0 \ , \tag{2.62}$$

where $\boldsymbol{v}$ represents the actual velocity field of the structure.

Balance of Linear Momentum. The balance of linear momentum is an essential principle in continuum mechanics. The linear momentum of a subset $\mathcal{S}_P \subset \mathcal{S}_t$ is given by $\boldsymbol{I}_{\mathcal{S}_P} = \int_{\mathcal{S}_P} \boldsymbol{v} \ dm = \int_{\mathcal{S}_P} \boldsymbol{v} \varrho \ dv$ and the resulting forces $\boldsymbol{F}_{\mathcal{S}_P} = \int_{\mathcal{S}_P} \boldsymbol{\gamma} \ dm + \int_{\partial \mathcal{S}_P} \boldsymbol{t} \ da$. Here, the first term defines body forces. The second term considers forces on the surface of the

body. *dm* represents an infinitesimal mass element associated with a point $\boldsymbol{x} \in \mathcal{S}_P$. The *conservation of linear momentum* is postulated as

$$\frac{d}{dt}\boldsymbol{I}_{\mathcal{S}_P} = \boldsymbol{F}_{\mathcal{S}_P} \ , \tag{2.63}$$

stating that the temporal change of momentum $\frac{d}{dt}\boldsymbol{I}_{\mathcal{S}_P}$ of $\mathcal{S}_P \subset \mathcal{S}_t$ equals the sum of all forces acting on $\mathcal{S}_P$. Transformation back to the Lagrangian configuration, application of the localization theorem and time derivation finally yields the *local form of the balance of linear momentum* as

$$\varrho_0 \dot{\boldsymbol{V}} = \varrho_0 \boldsymbol{\gamma} + \mathrm{DIV}[\boldsymbol{P}] \tag{2.64}$$

in the Lagrangian configuration. This equation can be mapped to the Eulerian configuration, the actual spatial form of the local balance of linear momentum then reads

$$\varrho \dot{\boldsymbol{v}} = \varrho \boldsymbol{\gamma} + \mathrm{div}[\boldsymbol{\sigma}] \quad \text{in } \mathcal{S} \ . \tag{2.65}$$

Balance of Angular Momentum. Another fundamental principle of continuum mechanics is the balance of angular momentum or moment of momentum. The most widely used continua are those without distributed couples in the interior of the body or on its boundary. They are referred to as *non-polar continua*. In the absence of these distributed resultant couples, the symmetry of the Cauchy stress tensor is derived. In view to further developments in this work, *polar continua* are considered with distributed couples on the boundary $\partial\mathcal{S}_P$ of the domain $\mathcal{S}_P$. However, body couples in analogy to body forces within the body are neglected. In analogy to the definitions of the previous section, the angular momentum of a subset $\mathcal{S}_P \subset \mathcal{S}$ with respect to a fixed position $'0'$ in space is defined as $\boldsymbol{D}_0 = \int_{\mathcal{S}_P} \boldsymbol{x} \times \boldsymbol{v} \ dm = \int_{\mathcal{S}_P} \boldsymbol{x} \times \boldsymbol{v}\varrho \ dv$. The resultant moment of the forces (torque) acting on $\mathcal{S}_P$ with respect to $'0'$ is given by

$$\boldsymbol{M}_0 = \int_{\mathcal{S}_P} \boldsymbol{x} \times \boldsymbol{\gamma}\varrho \ dv + \int_{\partial\mathcal{S}_P} \boldsymbol{x} \times \boldsymbol{t} \ da + \int_{\partial\mathcal{S}_P} \boldsymbol{m} \ da \ . \tag{2.66}$$

Here, $\boldsymbol{m}$ represents the distributed *couple traction vector* on the boundary $\partial\mathcal{S}_P$ of the domain $\mathcal{S}_P$. The *conservation of angular momentum* is postulated as

$$\frac{d}{dt}\boldsymbol{D}_0 = \boldsymbol{M}_0 \ , \tag{2.67}$$

stating that the change in time of the angular momentum $\boldsymbol{D}_0$ with respect to $'0'$ of the body part $\mathcal{S}_P \subset \mathcal{S}_t$ equals the couple $\boldsymbol{M}_0$ with respect to $'0'$ acting on $\mathcal{S}_P$. Again, time derivation can only be performed over a time-independent domain, therefore the above expressions need at first to be transformed back into their reference configurations. With the relations $dv = J \ dV$ and $\varrho_0 = J\varrho$, the transformation becomes

$$\frac{d}{dt}\boldsymbol{D}_0 = \int_{\mathcal{B}_P} \boldsymbol{x} \times \dot{\boldsymbol{v}}\varrho_0 \ dV \ . \tag{2.68}$$

In the same manner, the resultant couple of the body forces transforms as $\int_{\mathcal{P}_S} \boldsymbol{x} \times \boldsymbol{\gamma}\varrho \ dv = \int_{\mathcal{B}_P} \boldsymbol{x} \times \boldsymbol{\gamma}\varrho_0 \ dV$. The resultant of the traction forces then transforms with

$$\int_{\partial\mathcal{S}_P} \boldsymbol{x} \times \boldsymbol{t} \ da = \int_{\mathcal{B}_P} \boldsymbol{x} \times \mathrm{DIV}[\boldsymbol{P}] \ dV + \int_{\mathcal{B}_P} \frac{1}{2}\mathcal{E}_{ijk}(\sigma_{ji} - \sigma_{ij})J \ dV \ , \tag{2.69}$$

where $\boldsymbol{\mathcal{E}} = \mathcal{E}_{ijk}$ is the third-order permutation tensor. In analogy to considerations for linear forces, a Cauchy-type theorem is applied to the couple tractions of the form $\boldsymbol{m} = \tilde{\boldsymbol{\sigma}}\boldsymbol{n}$ where $\tilde{\boldsymbol{\sigma}}$ is the so-called *couple stress tensor*. It is a linear operator that acts on the Eulerian outward unit vector field $\boldsymbol{n}$. With the application of the theorem of Gauss, the transformation becomes

$$\int_{\partial\mathcal{S}_P} \boldsymbol{m}\ da = \int_{\partial\mathcal{S}_P} \tilde{\boldsymbol{\sigma}}\boldsymbol{n}\ da = \int_{\mathcal{S}_P} \operatorname{div}[\tilde{\boldsymbol{\sigma}}]\ dv = \int_{\mathcal{B}_P} \operatorname{div}[\tilde{\boldsymbol{\sigma}}] J\ dV\ . \tag{2.70}$$

Insertion of the above transformation expressions into the conservation equation for the angular momentum (2.67) gives

$$\int_{\mathcal{B}_P} \boldsymbol{x} \times (\dot{\boldsymbol{v}}\varrho_0 - \boldsymbol{\gamma}\varrho_0 - \operatorname{DIV}[\boldsymbol{P}])\ dV = \int_{\mathcal{B}_P} \mathcal{E}_{ijk}\frac{1}{2}(\sigma_{ji} - \sigma_{ij}) J\ dV + \int_{\mathcal{B}_P} J \operatorname{div}[\tilde{\boldsymbol{\sigma}}]\ dV\ . \tag{2.71}$$

The left side contains the global form of the equation of motion that equals zero. This term drops out and the equation becomes $\int_{\mathcal{B}_P} \mathcal{E}_{ijk}\frac{1}{2}(\sigma_{ji} - \sigma_{ij})\ dV = \int_{\mathcal{B}_P} J \operatorname{div}[\tilde{\boldsymbol{\sigma}}]\ dV$. Application of the localization theorem and noting that the integrand on the left side denotes the axial vector of the *skew part* of $\boldsymbol{\sigma}$ yields

$$\boldsymbol{w}_{\boldsymbol{\sigma}-\boldsymbol{\sigma}^T} = J \operatorname{div}[\tilde{\boldsymbol{\sigma}}]\ . \tag{2.72}$$

Clearly, in the absence of resultant distributed couples the right side would be zero. Therefore, the axial vector field of the skew part of $\boldsymbol{\sigma}$ would be zero, confirming the symmetry of the Cauchy stress tensor for non-polar continua. For polar continua, these Cauchy stresses are not necessarily symmetric. If the Cauchy stresses are symmetric, then some simple transformations give rise to symmetry definitions for the second Piola-Kirchhoff and the Kirchhoff stress tensors,

$$\boxed{\boldsymbol{S}^T = \boldsymbol{S} \quad \text{and} \quad \boldsymbol{\tau}^T = \boldsymbol{\tau}\ .} \tag{2.73}$$

Observe that in contrast, the first Piola-Kirchhoff stress tensor $\tilde{\boldsymbol{P}}$ is generally unsymmetric, even if couple tractions are considered.

3. Static Homogenization of Discrete Granular Materials

Granular materials represent a wide spectrum of engineering materials. Their dimensions range from micrometers, e.g. powder materials and flour, over sand and rocks in the millimeter- and meter ranges up to even asteroids and planets with dimensions as large or even larger than kilometers, as shown in Figure 12. On the very small scales, that is, below about $80\mu m$, the interparticle behavior is mainly governed by van der Waals-, electrostatic- and cohesive forces. For particles with larger sizes, the behavior is primarily determined by mechanical forces due to interparticle contacts where attractive forces do not enter the theoretical formulation. In physics, such media are frequently termed *dry granulates*, whereas the smaller sized ones are consequently called *wet granulates*.

3.1. Current State of Research

For the modeling of granular materials, either continuum or micromechanically-based methods can be chosen. Pure continuum theories focus on the phenomenological modeling of such structures. In the papers Haff [45] and Jenkins & Savage [54] for example, such continuum approaches are developed where the evolution of the particles is considered as a fluid-mechanical problem. For micromechanically-based descriptions, literature provides two fundamentally different approaches to the description of the homogenized macroscopic behavior of such granular aggregates: analytical and discrete modeling techniques. In the analytical approach, analytic macroscopic constitutive equations are formulated where the micromechanical information enters in terms of either structural or fabric tensors obtained from analytical homogenization, see for example Deresiewicz [34], Thornton [112], Christoffersen, Mehrabadi & Nemat-Nasser [25], Bathurst & Rothenburg [11], Mehrabadi, Loret & Nemat-Nasser [73], Kruyt & Rothenburg [62, 63], Cambou, Dubujet, Emeriault & Sidoroff [20], Emeriault, Cambou & Mahboudi [39] and Cambou [19]. In the second micromechanically-based approach covering purely discrete modeling techniques, every granule is explicitly treated and its evolution followed throughout the total deformation process. Therein, constitutive equations are introduced on the microscopic level that define the interparticle mechanical behavior, and the macroscopic response is governed by a computational exploitation of averaging theorems. Computational treatments of granular matter in various formulations and approaches are for example outlined in the works Cundall & Strack [29], Cundall [28], Herrmann & Luding [47], Kun & Herrmann [64], Tillemans & Herrmann [114], Bardet & Proubet [8], Rothenburg & Bathurst [104], Ting, Khwaja, Meachum & Rowell [115], Moreau [89], Bardet [7], Borja & Wren [16, 124] and the references cited therein. Although, this list is by no means exhaustive. Analytical modeling techniques often apply rigorous simplifications to the microstructural behavior. In contrast, the discrete modeling methods provide straightforward insight into the local micromechanical response of complex particle aggregates, for example with regard to the analysis of material instabilities. An event-driven approach to the modeling of the mechanical evolution of such particulate aggregates is known as *inelastic hydrodynamics*. Therein, the instantaneous collisions between particles are understood to be short but high impacts which lead to sudden jumps in the velocity of the particles affected. The impact is defined as the time integral over the impact force, with the time period of the impact being very small. In connection with the so-called restitution coefficient that distinguishes between elastic, elastoplastic and plastic impacts, the change of momentum

of both particles follows from the conservation law of total momentum and finally gives the new translational and rotational velocities after the collision. In this formulation, the restitution and the friction coefficients can be regarded as the constitutive input since they determine the interparticle mechanical behavior. A review is given in the paper LUDING [68]. However, the formulation is only valid for sliding contacts and not for sticking ones. Also, the method is completely dynamic, obtaining static solutions is complicated and can only be possible using artificial methods. A different approach for micromechanical simulations of discrete granulates is the discrete element method (DEM), which has become a popular tool. It essentially goes back to the work of CUNDALL & STRACK [29]. In the following sections, this method is employed and specified for the simulation of granular microstructures, and a consistent method for micro-macro transitions of periodic granular aggregates is developed. Therewith, the new developments in this part of the work on granulates can be summarized into

- a consistent formulation of micro-macro transitions for granular microstructures at large strains, based on a distinct definition of a periodic particle unit cell,
- a novel set of boundary constraints for periodic particle aggregates that account for finite particle displacements and rotations on the surfaces of the microstructures,
- a deformation-controlled implementation of the constraints, suitable for use in higher scale finite element simulations,
- a bound characterization of the linear deformation- and uniform traction constraints for periodic definitions with regard to the stiffness of the microstructure and
- full two scale concurrent micro-macro simulations of granulate media with coupled boundary value problems on both the micro- and macroscopic scales.

3.2. Micro-Macro Modeling of Granular Materials

Figure 13 shows a "smeared" macroscopic continuum where a microstructure of elliptically-shaped granules is attached locally at a point $\bar{\boldsymbol{x}} \in \mathcal{S}$ of the macrostructure and deformed in a compression-shear mode. A micro-macro transition of such a discrete aggregate is concerned with the definition of homogenized overall properties such as strains, stresses and powers. The length scales of the macro- and microscales are assumed to differ considerably such that boundary-layer effects are of low order. The constitutive micromechanical material response is governed by a Coulomb-type elastic-plastic friction interaction law for the particles. A main difference compared to other works on granular microstructures is a distinct definition of the aggregate volume and its boundary conditions which govern the representation of the macro-stresses. A well-defined periodic cell allows a consistent transfer of overall definitions for continuous microstructures of heterogeneous materials to discrete particle microstructures. Recall from classical homogenization theory that periodicity conditions reflect exact results with regard to the aggregate stiffness for periodic structures, while linear deformation and uniform traction constraints yield upper and lower bound characteristics, respectively. It will be shown that these statements also hold true for granular materials. Consequently, the proposed periodicity conditions are considered to be an optimal choice for particle aggregates and will thus be used for the proposed *two-scale micro-macro simulations*, where boundary-value

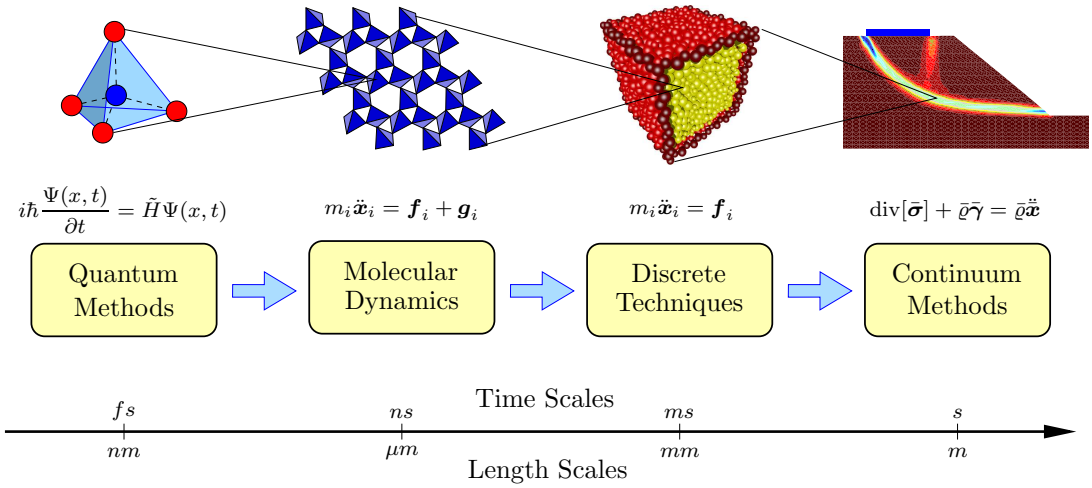

Figure 12: Time and length scales associated with the modeling of granular materials on different scales. Phenomenological continuum models are usually employed on the macro scale that describe the macroscopic behavior. On the micro scale, discrete element methods can be used to model the mechanical behavior of the microstructures. Here, as an example, a silica sand with silicon dioxide SiO_4 molecules is shown. It possesses a complicated trigonal-trapezohedral crystal lattice structure on the nano level.

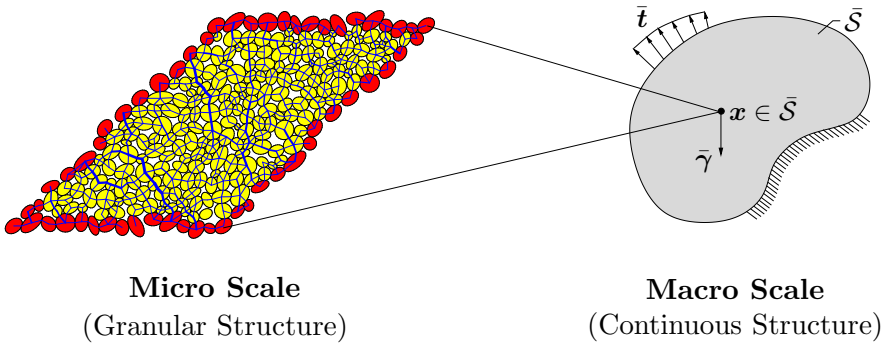

Figure 13: Eulerian deformed configuration of a continuous macrostructure with a granular microstructure locally attached at a point $\bar{\boldsymbol{x}} \in \bar{\mathcal{S}}$ with periodic displacement/ rotation constraints on the surface of the representative volume element.

problems on both the micro- and macroscales will be linked and solved simultaneously. A key development here is the consistent derivation of new compact statements for micro-macro transitions that define the overall stresses of granular assemblies for a new class of three different types of boundary conditions. Following the works Miehe [77], Miehe & Dettmar [78, 79], Dettmar & Miehe [36, 37] and the first approach in Schröder [105], in this section at first continuous formulations for the overall properties of continuous microstructures for the three classical boundary constraints (D) linear displacements on the boundary, (P) periodic deformations on opposite boundaries and (S) uniform tractions on the surface of the representative volume are outlined. Therein, the constraints and overall macroscopic averaged quantities are solely formulated in terms of microscopic, discrete surface data. In the subsequent chapter, these continuous formulations are consistently transferred to their discrete counterparts for discontinuous granular structures in both two and three spatial dimensions. For the discrete finite-sized granules, the effect of particle rotations must also be included because it has an impact on the periodicity of the microstructure and hence on the macroscopic stresses. Finally, the algorithmic im-

plementation by a penalty method with quadratic penalty terms is developed. This will later prove to be a convenient computational tool in discrete element formulations. For all subsequent considerations, special attention is paid to the definition of the periodic unit cell of granular particles which leads to specific constraints for both particle displacements and rotations of the granules on the well-defined boundary frame of the microstructure.

3.2.1. Distinct Definition of a Periodic Microstructure. Figure 14 shows two portions of arbitrary two dimensional assemblies of elliptical particles where two different shapes of periodic granular microstructures are highlighted. In 14a, a standard rect-

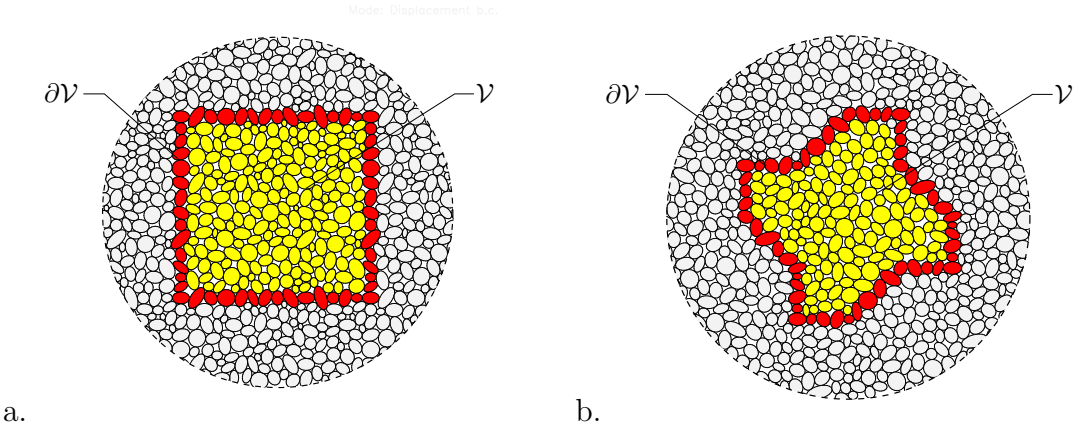

a. b.

Figure 14: Examples of two periodic granular microstructures cut out from random particle assemblies: a. rectangular and b. arbitrarily-shaped periodic microstructures are possible. Note that the elementary granular volume splits up into particles in the interior domain $\mathcal{V}$ and those that define the boundary frame $\partial\mathcal{V}$, dark shaded in the picture.

angular periodic microstructure is defined, whereas in 14b an arbitrary-shaped periodic representative volume element is shown. Such a microstructure $\mathcal{B} \subset \mathbb{R}^3$ characterizes a representative elementary aggregate of granular particles. The definition of the representative volume is not restricted to rectangular shapes or a shape with straight edges. In the formulation at hand, any arbitrary definitions are possible. The aggregate of particles as depicted in Figure 16c is defined as a granular microstructure. The total number of particles of the representative volume $|\mathcal{V}|$ is decomposed into M particles that represent the boundary frame of the assembly and the remaining N particles in the interior domain. The centroids of the particles $\mathcal{P}_p, p = 1...N$ in the bulk (the interior domain) are elements of the domain of the microstructure, that is

$$\boldsymbol{X}_p \in \mathcal{V} \quad \text{for} \quad p = 1...N \ . \tag{3.1}$$

Here, the *boundary frame* consists of the M particles $\mathcal{P}_q, q = 1...M$ (those that are red/ dark shaded in Figures 14 and 16). The centroids $\boldsymbol{X}_q \in \mathcal{P}_q$ of these particles define the surface of the microstructure, namely

$$\boldsymbol{X}_q \in \partial\mathcal{V} \quad \text{for} \quad q = 1...M \ . \tag{3.2}$$

The particles $\mathcal{P}_q, q = 1...M$ provide a frame for the macroscopic driving of the granular aggregate in the interior domain of the representative elementary volume. Figure 15 shows the assembly of some periodically deformed continuous und particle microstructures. The periodicity of the material can be defined in terms of a Lagrangian positively orientated

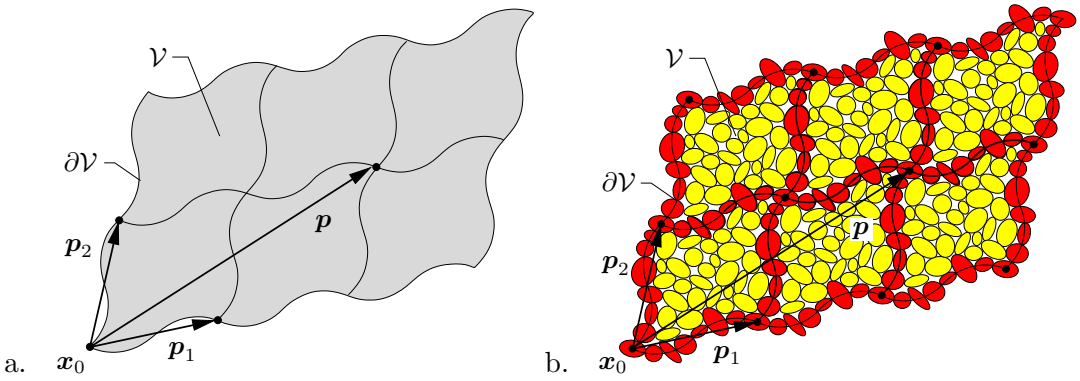

Figure 15: Periodic structure of matter in the deformed configuration for two-dimensional a. continuous and b. granular microstructures. The periodic cell structure is defined by the current periodicity frame $\{\boldsymbol{p}_\alpha\}_{\alpha=1,\dots,d}$. The mechanical characteristics of the material are invariant with respect to a translation of the unit cell along the vector $\boldsymbol{p} = \sum_{\alpha=1}^{d} m_\alpha \boldsymbol{p}_\alpha$ with $m_\alpha \in \mathcal{N}$.

periodicity frame $\{\boldsymbol{p}_\alpha\}_{\alpha=1\dots d}$, with its origin at $\boldsymbol{x}_0 \in \mathcal{R}^3$. Greek indices loop over the space dimension, i.e. $d = 2$ for two dimensional plane and $d = 3$ for three dimensional microstructures. The periodicity in the Lagrangian reference configuration is expressed by possible translations of the microstructure along the vector

$$\boldsymbol{p} = \sum_{\alpha=1}^{d} m_\alpha \boldsymbol{p}_\alpha \quad \text{with} \quad m_\alpha \in \mathcal{N} \tag{3.3}$$

with integers $\{m_\alpha\}_{\alpha=1\dots d}$. The assumed characteristic structure of the material is invariant with respect to this translation. As a consequence, it is sufficient to define the material properties of the medium in a small domain $\mathcal{V} \subset \mathcal{R}^3$, called the *unit cell of a periodic medium*. This cell can be repeated by the translation vector $\boldsymbol{p}$. As pointed out in Anthoine [4], neither the periodicity frame nor the associated cell of a periodic medium are uniquely defined. However, the most natural cell is the parallelogram spanned by the vectors $\boldsymbol{p}_\alpha$ of the periodicity frame as indicated in Figure 15. For a given reference frame, all possible cells have the same volume in the actual configuration specified by

$$|v| = \boldsymbol{p}_1 \cdot (\boldsymbol{p}_2 \times \boldsymbol{p}_3) > 0 \ , \tag{3.4}$$

and with the Lagrangian vectors $\boldsymbol{P}_i$, the reference volume $|\mathcal{V}|$ can similarly be computed. As shown in Figure 17(P), the boundary $\partial\mathcal{V}$ of a periodically-shaped cell $\mathcal{V}$ can always be divided

$$\partial\mathcal{V} = \bigcup_{\alpha=1}^{d} (\partial\mathcal{V}_\alpha^+ + \partial\mathcal{V}_\alpha^-) \tag{3.5}$$

into d pairs $\{\partial\mathcal{V}_\alpha^+, \partial\mathcal{V}_\alpha^-\}_{\alpha=1\dots d}$ of identical sides corresponding to each other through translations along the periodicity vectors $\boldsymbol{P}_\alpha$ or $\boldsymbol{p}_\alpha$ in the Lagrangian and Eulerian reference frames, respectively. The two corresponding sides, $\partial\mathcal{V}_\alpha^+$ and $\partial\mathcal{V}_\alpha^-$, are said to be opposite. The distance of corresponding points $\boldsymbol{X}_\alpha^+ \in \partial\mathcal{V}_\alpha^+$ and $\boldsymbol{X}_\alpha^- \in \partial\mathcal{V}_\alpha^-$ is given by the vectors of the periodicity frame, that is

$$\boldsymbol{X}_\alpha^+ - \boldsymbol{X}_\alpha^- = \boldsymbol{P}_\alpha \ . \tag{3.6}$$

Outward normals at corresponding points $\boldsymbol{X}_\alpha^+$ and $\boldsymbol{X}_\alpha^-$ are opposite, namely $\boldsymbol{N}_\alpha^- = -\boldsymbol{N}_\alpha^+$.

3.3. Micro-Macro Transitions for Continuous Microstructures

To start this subchapter, equilibrium definitions for the overall properties of continuous periodic microstructures in terms of surface data in a spatial geometric setting with respect to the Eulerian configuration are outlined. This treatment follows the work MIEHE [77] and is necessary for the following introduction of equilibrium conditions for the discrete granular microstructures.

3.3.1. Equilibrium Conditions for Continuous Microstructures. A static equilibrium state of a continuous microstructure can be expressed by conservation of linear and angular momenta which — with the negligence of body forces, couples and kinetic quantities — in terms of the microscopic Cauchy stresses $\boldsymbol{\sigma}$ read

$$\operatorname{div}[\boldsymbol{\sigma}] = \boldsymbol{0} \quad \text{and} \quad \boldsymbol{\sigma}^T - \boldsymbol{\sigma} = \boldsymbol{0} \quad \text{in } \boldsymbol{\varphi}_t(\mathcal{V}) \ . \tag{3.7}$$

Therein, the Cauchy stress tensor $\boldsymbol{\sigma}$ is assumed to be related to the current metric $\boldsymbol{g}$ by some solid material model. Note that equation $(3.7)_2$ is only valid for structures without couple tractions on the surface and body couples in the interior domain. It confirms the symmetry of the Cauchy stress tensor. Integration of (3.7) over the current domain $\boldsymbol{\varphi}_t(\mathcal{V})$ and application of the Gauss theorem then yields the global conditions of equilibrium

$$\int_{\boldsymbol{\varphi}_t(\partial\mathcal{V})} \boldsymbol{t} \ da = \boldsymbol{0} \quad \text{and} \quad \int_{\boldsymbol{\varphi}_t(\partial\mathcal{V})} (\boldsymbol{t} \otimes \boldsymbol{x} - \boldsymbol{x} \otimes \boldsymbol{t}) \ da = \boldsymbol{0} \ , \tag{3.8}$$

where $\boldsymbol{t}$ represents the traction vector on a point $\boldsymbol{x}$ on the deformed continuous microstructure under consideration.

3.3.2. Homogenized Macroscopic Stresses of Continuous Microstructures. The overall Kirchhoff macroscopic stress tensor $\bar{\boldsymbol{\tau}}$ associated with the continuous microstructure under consideration is defined by the volume average of the microscopic Kirchhoff stresses $\boldsymbol{\tau}$ as

$$\bar{\boldsymbol{\tau}} := \frac{1}{|\mathcal{V}|} \int_{\mathcal{V}} \boldsymbol{\tau} \ dV \ . \tag{3.9}$$

From the equilibrium state (3.7) it can be recast into a form solely defined in terms of surface quantities

$$\bar{\boldsymbol{\tau}} = \frac{1}{|\mathcal{V}|} \int_{\boldsymbol{\varphi}_t(\partial\mathcal{V})} \boldsymbol{t} \otimes \boldsymbol{x} \ da \ . \tag{3.10}$$

In order to compute the macroscopic homogenized Cauchy stresses $\bar{\boldsymbol{\sigma}}$, the current volume $|v| := \det[\bar{\boldsymbol{F}}]|\mathcal{V}|$ of the deformed microstructure in terms of the macroscopic deformation gradient $\bar{\boldsymbol{F}}(t)$ is introduced. This volume drives the microstructure. With the macroscopic Kirchhoff stress tensor $\bar{\boldsymbol{\tau}}$ at hand, the macroscopic Cauchy stresses $\bar{\boldsymbol{\sigma}}$ of the microstructure follow as

$$\bar{\boldsymbol{\sigma}} := \frac{|\mathcal{V}|}{|v|} \bar{\boldsymbol{\tau}} \ . \tag{3.11}$$

With these macroscopic homogenized stress definitions at hand, the three classical boundary constraints for (D) linear deformations on the whole boundary, (P) periodic deformations on opposite boundaries and (S) uniform tractions on the surface of the microstructure can now be outlined.

3.3.3. Linear Deformations on the Boundary of the Microstructure. The simplest definition of a deformation boundary constraint in terms of the prescribed macroscopic deformation gradient $\bar{\boldsymbol{F}}(t)$ sets the fluctuations on the boundary equal to zero. It can be written as

$$\boldsymbol{\varphi}(\boldsymbol{X},t) = \bar{\boldsymbol{F}}(t)\boldsymbol{X} \quad \text{on} \quad \partial\mathcal{V} \tag{3.12}$$

where $\boldsymbol{\varphi}(t)$ represents the nonlinear time-dependent map of a referential point $\boldsymbol{X}$ onto its actual position $\boldsymbol{x}$ on the deformed configuration. This condition defines a linear deformation on the boundary $\partial\mathcal{V}$ of the representative elementary volume. The material points within the bulk of the microstructure are free to deform. Thus the deformation on the boundary is solely governed by the prescribed homogeneous macroscopic deformation gradient $\bar{\boldsymbol{F}}$.

3.3.4. Periodic Deformations on Opposite Boundaries. In a periodic material, the periodicity of the microstructure is assumed to extend to infinity in all spatial directions. In this case, the boundary conditions must be such that they lead to a periodic distribution of the field quantities. Hence, a representative unit cell is considered that encompasses the periodic geometry and material properties and allows to exactly describe the stiffness properties of the material. The periodicity of the material demands periodic deformations and antiperiodic tractions on the boundary of the representative cell. These requirements are considered to be constraints of the form

$$[\![\boldsymbol{\varphi}(\boldsymbol{X},t)]\!] = \bar{\boldsymbol{F}}(t)\,[\![\boldsymbol{X}]\!] \quad \text{and} \quad \boldsymbol{t}(\boldsymbol{X}^-,t) = -\boldsymbol{t}(\boldsymbol{X}^+,t) \quad \text{on} \quad \partial\mathcal{V}\ . \tag{3.13}$$

Here, the notion $[\![(\bullet)]\!] := (\bullet)^+ - (\bullet)^-$ denotes the jump of the field $(\bullet)$ on the surface of the representative volume with regard to corresponding points $\boldsymbol{X}^- \in \partial\mathcal{V}^-$ and $\boldsymbol{X}^+ \in \partial\mathcal{V}^+$ on opposite associated surfaces.

3.3.5. Uniform Tractions on the Boundary of the Microstructure. A statement dual to (3.12) assumes uniform tractions on the surface of the representative elementary volume

$$\boldsymbol{t}(\boldsymbol{X},t) = \bar{\boldsymbol{P}}(t)\boldsymbol{N}(\boldsymbol{X}) \quad \text{on} \quad \partial\mathcal{V} \tag{3.14}$$

in terms of the macroscopic first Piola-Kirchhoff stress tensor $\bar{\boldsymbol{P}}$. The vector $\boldsymbol{t}$ represents the traction vector on the deformed surface and $\boldsymbol{N}(\boldsymbol{X})$ a unit normal vector at a point $\boldsymbol{X}$ with respect to the undeformed surface of the microstructure. This condition defines constant tractions on parts of the surface with the same normal $\boldsymbol{N}$. However, (3.14) is not consistent with the deformation-driven approach employed here. The homogenized macroscopic stresses $\bar{\boldsymbol{P}}$ are not known *a priori* but intended to be computed for a prescribed homogeneous macroscopic deformation gradient $\bar{\boldsymbol{F}}$. In order to obtain an equivalent formulation to (3.14) in terms of a prescribed homogeneous macroscopic deformation $\bar{\boldsymbol{F}}$, the definition

$$\bar{\boldsymbol{F}} := \frac{1}{|\mathcal{V}|}\int_{\partial\mathcal{V}} \boldsymbol{\varphi} \otimes \boldsymbol{N} dA\ , \tag{3.15}$$

can be considered as a *weak* constraint on the boundary $\partial\mathcal{V}$ of the representative volume, where $\boldsymbol{\varphi} = \hat{\boldsymbol{\varphi}}(\boldsymbol{X},t)$ is the nonlinear point map between referential and actual configurations. Scalar contraction of this equation with a Lagrange parameter $\boldsymbol{s}(t)$ gives a global

constraint $\boldsymbol{c}(\boldsymbol{\varphi}, \boldsymbol{s}; \bar{\boldsymbol{F}}) = -\frac{1}{|\mathcal{V}|}\int_{\partial\mathcal{V}}(\boldsymbol{s}\boldsymbol{N})\cdot\boldsymbol{\varphi}\; dA + \boldsymbol{s} : \bar{\boldsymbol{F}} = \boldsymbol{0}$. Therein, the first term contains the standard external potential of tractions $\boldsymbol{t} = \bar{\boldsymbol{P}}\boldsymbol{N}$ on the boundary. Derivation of the constraint $\boldsymbol{c}$ with respect to the macro-deformation $\bar{\boldsymbol{F}}$ identifies $\bar{\boldsymbol{P}} = \partial_{\bar{\boldsymbol{F}}}\boldsymbol{c} = \boldsymbol{s}$, see also Miehe [77]. Thus, the weak constraint in equation (3.15) enforces the traction-type boundary condition (3.14) for given prescribed macro-deformations $\bar{\boldsymbol{F}}(t)$. This observation allows for a computation of uniform tractions on the boundary of the continuous microstructure in deformation-driven processes. In what follows, the discrete counterparts

Box 1: Continuous / Discrete Boundary Constraints

Continuous formulation:

(D) $\boldsymbol{\varphi}(\boldsymbol{X}, t) - \bar{\boldsymbol{F}}(t)\boldsymbol{X} = \boldsymbol{0}$

(P) $[\![\boldsymbol{\varphi}(\boldsymbol{X}, t)]\!] - \bar{\boldsymbol{F}}(t)\,[\![\boldsymbol{X}]\!] = \boldsymbol{0}$

(S) $\boldsymbol{t}(\boldsymbol{X}, t) - \bar{\boldsymbol{P}}(t)\boldsymbol{N}(\boldsymbol{X}) = \boldsymbol{0}$

Discrete formulation:

(D) $\boldsymbol{x}_q - \bar{\boldsymbol{F}}\boldsymbol{X}_q = \boldsymbol{0}$; $\quad \boldsymbol{Q}_q - \boldsymbol{1} = \boldsymbol{0}$

(P) $[\![\boldsymbol{x}_q]\!] - \bar{\boldsymbol{F}}\,[\![\boldsymbol{X}_q]\!] = \boldsymbol{0}$; $\quad [\![\boldsymbol{Q}_q]\!] = \boldsymbol{0}$

(S) $\sum_{q=1}^{M} \boldsymbol{x}_q \otimes \boldsymbol{A}_q - |\mathcal{V}|\bar{\boldsymbol{F}} = \boldsymbol{0}$

to the continuous formulations introduced here are developed. Finally, Box 1 summarizes both the continuous and the associated discrete formulations of the boundary constraints for continuous and granular microstructures.

3.4. Micro-Macro Transitions for Particle Microstructures

In the following section, consistent transfer of the above outlined micro-macro transitions of continuous representative volume elements to their associated representations for discontinuous granular microstructures is discussed. It will be shown that the expressions for the homogenized macroscopic stresses and the constraints for the three boundary conditions appear in quite similar forms. For the discrete particle microstructures under consideration, boundary constraints are introduced. For the first time in literature, these constraints include not only constraint definitions for the displacements, but also explicit formulations for the rotations of the particles on the boundary frame of the assembly.

3.4.1. Equilibrium Conditions for Particle Microstructures. For discrete granular microstructures where the particles split into those on the boundary frame and those in the bulk, equilibrium conditions are defined for (i) the particles in the interior domain, (ii) the ones that build the boundary frame and finally (iii) for the total aggregate.

Equilibrium Conditions for Particles in the Interior Domain. The particles $\mathcal{P}_p$ in the interior domain of the microstructure interact among each other through discrete contact forces $\boldsymbol{f}_p^c$ at discrete contact points $\boldsymbol{x}_p^c$ on the surfaces of the rigid particles, as shown in Figure 16b. In order to generate equilibrium conditions for the rigid particles in terms of the contact forces, the infinitesimal limit $\boldsymbol{t}da \to \boldsymbol{f}_p^c$ at contact point $\boldsymbol{x}_p^c$ is considered. Then the continuous equilibrium conditions (3.8) merge into their discrete

counterparts

$$\sum_{c\in\mathcal{A}_p^c} \boldsymbol{f}_p^c = \boldsymbol{0} \quad \text{and} \quad \sum_{c\in\mathcal{A}_p^c} (\boldsymbol{f}_p^c \otimes \boldsymbol{x}_p^c - \boldsymbol{x}_p^c \otimes \boldsymbol{f}_p^c) = \boldsymbol{0} \quad \text{for} \quad p = 1...N \ . \tag{3.16}$$

Note that the symbol $\mathcal{A}_p^c$ denotes the currently active set of contacts for the particular particle $\mathcal{P}_p$. Equation $(3.16)_2$ can be recast into $\sum_{c\in\mathcal{A}_p^c}(\boldsymbol{x}_p^c - \boldsymbol{x}_p) \times \boldsymbol{f}_p^c = \boldsymbol{0}$, where $\boldsymbol{x}_p$ denotes the displaced centroid of the particle $\mathcal{P}_p$. Therefore, the above equations (3.16)

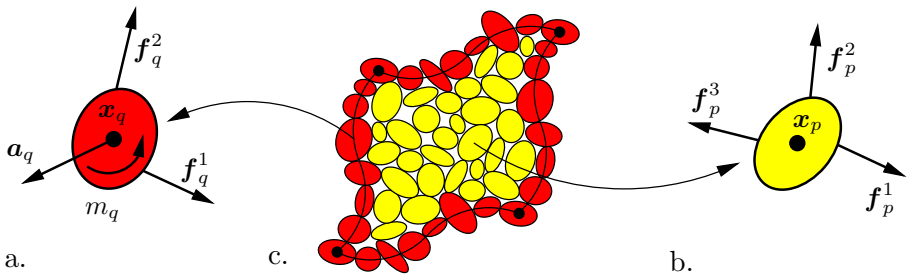

Figure 16: Equilibrium state of a particle aggregate, a. for particles on the boundary frame with support forces $\boldsymbol{a}_q$ and support couples m_q, b. for the granules in the interior domain and c. for the total granular microstructure.

represent the local equilibrium conditions for both forces and couples on each particle $\mathcal{P}_p$, $p = 1, \ldots, N$ with regard to their displaced centroids $\boldsymbol{x}_p$ in the interior domain of the granular microstructure.

Equilibrium Conditions for Particles on the Boundary Frame. The particles $\mathcal{P}_q$ on the defined boundary frame of the granular assembly interact with those in the interior domain through discrete contact forces $\boldsymbol{f}_q^c$ at contact points $\boldsymbol{x}_q^c$ on the deformed surfaces of the rigid particles. The driving of these particles is performed by *fictitious support forces* $\boldsymbol{a}_q$ and *fictitious support couples* m_q that act on the displaced and rotated centroids of the boundary frame particles $\mathcal{P}_q$, see Figure 16a. In analogy to equation (3.16), the discrete equilibrium conditions for the particles on the boundary read

$$\sum_{c\in\mathcal{A}_q^c} \boldsymbol{f}_p^c = -\boldsymbol{a}_q \quad \text{and} \quad \sum_{c\in\mathcal{A}_q^c} (\boldsymbol{x}_q^c - \boldsymbol{x}_q) \times \boldsymbol{f}_q^c = -m_q \boldsymbol{e}_3 \quad \text{for} \quad q = 1...M \ . \tag{3.17}$$

Here $\boldsymbol{e}_3$ is the Cartesian basis vector normal to the plane of the assembly when a two dimensional microstructure in the $\boldsymbol{e}_1$–$\boldsymbol{e}_2$ plane is considered. These equilibrium conditions are defined with regard to the displaced and rotated centroids $\boldsymbol{x}_q$ of the particles $\mathcal{P}_q, q = 1...M$ on the boundary frame. Again, the symbol $\mathcal{A}_q^c$ represents the set of currently active contact points for the particle $\mathcal{P}_q$.

Equilibrium Conditions for the Particle Aggregate. In the above equation (3.17), the contact forces $\boldsymbol{f}_q^c$ that act between the boundary- and the bulk particles are considered to be *real forces* while the externally applied support forces that enforce some particular state of deformation were introduced as artificial quantities. These forces are therefore considered to be *fictitious forces* that provide the fictitious supports of the finite-sized granular microstructure. These support forces replace the mechanical action of the adjacent periodic particle microstructures. Considering the relation $\boldsymbol{f}_q^c + \boldsymbol{f}_p^c = 0$ at a contact point $\boldsymbol{x}^c$ between two particles $\mathcal{P}_q$ and $\mathcal{P}_p$ of the boundary and the bulk domain,

respectively, the equilibrium conditions for the entire particle aggregate can be expressed solely in terms of the support forces $\boldsymbol{a}_q$ and couples m_q as

$$\sum_{q=1}^{M} \boldsymbol{a}_q = \boldsymbol{0} \quad \text{and} \quad \sum_{q=1}^{M} (\boldsymbol{x}_q \times \boldsymbol{a}_q + m_q \boldsymbol{e}_3) = \boldsymbol{0} \ . \tag{3.18}$$

Obviously, all interior contact forces drop out and the equilibrium conditions appear solely in terms of microscopic surface data.

3.4.2. Homogenized Macroscopic Stresses of Particle Microstructures. When considering the infinitesimal limit $\boldsymbol{t}da \to \boldsymbol{a}_q$ for the fictitious support forces on the boundary frame particles of the granular microstructure, the overall homogenized macroscopic Cauchy stress $\bar{\boldsymbol{\sigma}}$ follows from the continuous formulations (3.10) and (3.11) by a consistent transition to the discrete counterpart as

$$\boxed{\bar{\boldsymbol{\sigma}} = \frac{1}{|v|} \sum_{q=1}^{M} \boldsymbol{a}_q \otimes \boldsymbol{x}_q \ .} \tag{3.19}$$

Due to the balance of angular momentum $(3.7)_2$, this formulation is a priori symmetric if only forces, not couples, on the centers of the boundary particles are considered. Observe that this representation of the homogenized macroscopic stress does not include any quantities associated with the particles in the interior bulk. The definition includes only the particle forces and positions associated with the defined granular boundary frame of the assembly and is therefore easy and convenient in computational exploitations. This representation in terms of only the artificial support forces $\boldsymbol{a}_q$ acting on the boundary frame of the granular microstructure is considered to be the most compact statement of the overall macroscopic stress $\bar{\boldsymbol{\sigma}}$ of granular particle aggregates. The formulation is identical with the theory for continuous microstructures, see equation (3.11). In the cases of periodic and uniform traction boundary constraints, the support couples do not have an influence on the macroscopic stresses. This will be shown in the subsequent discussion of the boundary constraints. Due to the well-defined relationship between the driving deformation $\bar{\boldsymbol{F}}$ and the resulting overall stress, the first Piola-Kirchhoff stress $\bar{\boldsymbol{P}}$ differs from the Cauchy stress $\bar{\boldsymbol{\sigma}}$ only through the material and spatial position vectors $\boldsymbol{X}$ and $\boldsymbol{x}$ of the boundary particles as well as the initial and current volumes $|\mathcal{V}|$ and $|v|$, respectively.

An expression for the averaged stress similar to (3.19) in the context of small strains was derived by Bagi [6]. However, he does not take into account couples acting on the boundary particles of the aggregate. For the modeling of true periodicity, the couples play a crucial role. The obtained *symmetry* of the Cauchy stress definition (3.19) in the presence of fictitious couples on the boundary of precisely defined periodic aggregates is valued as an important result. It seems to clarify observations made in Bardet & Vardoulakis [9] who for certain non-periodic boundary conditions characterized the stress asymmetry in granular materials as a *boundary* effect. Again, it should be emphasized that in the treatment at hand the couples depicted in Figure 16a are *fictitious quantities that enforce the rotational periodicity* of the granules on the boundary of the unit cell. Hence, their presence does not motivate micropolar macroscopic theories where couple stresses appear as independent fields for which additional constitutive assumptions are needed. This is

considered for example in KANATANI [58], MÜHLHAUS & VARDOULAKIS [92], CHANG & LIAO [23], CHANG & MA [24] or EHLERS, RAMM ET AL. [38]. This is clearly underlined by the fact that these couples do not influence the obtained homogenized stress definition (3.19) in the case of periodic and uniform traction boundary constraints.

With the equilibrium conditions $(3.16)_1$ and $(3.17)_1$ for the forces acting on the particles on the boundary and the interior domain, the already obtained macroscopic stress representation (3.19) can be recast into

$$\bar{\boldsymbol{\sigma}} = -\frac{1}{|v|}\left[\sum_{q=1}^{M}\sum_{c\in\mathcal{A}_q^c}\boldsymbol{f}_q^c\otimes\boldsymbol{x}_q+\sum_{p=1}^{N}\sum_{c\in\mathcal{A}_p^c}\boldsymbol{f}_p^c\otimes\boldsymbol{x}_p\right] . \tag{3.20}$$

This formulation can be expressed in terms of a sum over *all present contacts* $\mathcal{A}^c$ in the granular aggregate

$$\bar{\boldsymbol{\sigma}} = -\frac{1}{|v|}\sum_{c\in\mathcal{A}^c}\left[\boldsymbol{f}_S^c\otimes\boldsymbol{x}_{S,c}+\boldsymbol{f}_M^c\otimes\boldsymbol{x}_{M,c}\right] , \tag{3.21}$$

where $\boldsymbol{x}_{S,c}$ and $\boldsymbol{x}_{M,c}$ are the centroids of the two contacting particles $\mathcal{P}_S$ and $\mathcal{P}_M$ as visualized in Figure 24. Note that the sum $\sum_{c\in\mathcal{A}^c}\boldsymbol{f}^c\otimes\boldsymbol{x}^c$ vanishes for all interparticle contacts within the granular microstructure, since every interparticle contact force has an equal but opposite reaction $\boldsymbol{f}_M^c=-\boldsymbol{f}_S^c$. Thus, only the support forces on the particles of the boundary frame remain in the formulation. Introducing the so-called *branch* or *fabric vector* $\boldsymbol{l}^c$ and the associated *branch contact force* $\boldsymbol{f}^c$ as

$$\boldsymbol{l}^c := \boldsymbol{x}_{S,c}-\boldsymbol{x}_{M,c} \quad\text{and}\quad \boldsymbol{f}^c := \boldsymbol{f}_M^c=-\boldsymbol{f}_S^c , \tag{3.22}$$

the macroscopic stress formulation (3.19) is recast into

$$\bar{\boldsymbol{\sigma}} = \frac{1}{2|v|}\sum_{c\in\mathcal{A}^c}\left(\boldsymbol{f}^c\otimes\boldsymbol{l}^c+\boldsymbol{l}^c\otimes\boldsymbol{f}^c\right) . \tag{3.23}$$

This classical definition of the macroscopic stress in terms of the branch contact forces $\boldsymbol{f}^c$ and branch vector $\boldsymbol{l}^c$ between the particles was used for example in CHRISTOFFERSEN, MEHRABADI & NEMAT-NASSER [25], KRUYT & ROTHENBURG [62], BORJA & WREN [16] and BARDET [7]. It can be motivated by a weighted sum of the average stresses in each particle of the aggregate

$$\bar{\boldsymbol{\sigma}} = \frac{1}{|v|}\sum_{p=1}^{N}\bar{\boldsymbol{\sigma}}_p|v_p| \quad\text{with}\quad \bar{\boldsymbol{\sigma}}_p := \frac{1}{|v_p|}\int_{v_p}\boldsymbol{\sigma}\,dV = \frac{1}{|v_p|}\sum_{c\in\mathcal{A}_p^c}(\boldsymbol{f}_p^c\otimes\boldsymbol{x}_p^c)_{sym} , \tag{3.24}$$

see for example the works BARDET [7] or LÄTZEL, LUDING & HERRMANN [69]. This shows that the above symmetric stress definition (3.19) for periodic aggregates is consistent with the classical definition in the context of quasistatic investigations. In the following three subsections, the three new representations of the classical boundary constraints for particle displacements and rotations are developed for the case of discrete granular microstructures. Therein, the influence of the couples on the boundary with regard to the macroscopic stresses (3.19) will be addressed.

3.4.3. Linear Deformations on the Boundary of the Microstructure. The initial positions and rotations of the particles are denoted by $\boldsymbol{X}_i, \Theta_i, i = 1...(M+N)$. The current positions and rotations then follow as

$$\boldsymbol{x}_i = \hat{\boldsymbol{x}}_i(\boldsymbol{X}_i, t) \quad \text{and} \quad \vartheta_i = \hat{\vartheta}_i(\Theta_i, t) \ . \tag{3.25}$$

The deformation map of a typical rigid particle $\mathcal{P}_i$ splits up into a part affine to the macroscopic deformation gradient $\bar{\boldsymbol{F}}(t)$, a superimposed fluctuation $\boldsymbol{w}(t)$ and the rotational part according to

$$\boldsymbol{x}_i = \bar{\boldsymbol{F}}(t)\boldsymbol{X}_i + \boldsymbol{w}_i(t) + \boldsymbol{Q}_i[\boldsymbol{X} - \boldsymbol{X}_i] \quad \text{for} \quad q = 1...(M+N) \ . \tag{3.26}$$

Here, $\bar{\boldsymbol{F}}(t)$ links the current macroscopic deformation $\bar{\boldsymbol{F}}$ to the microscopic deformation. Observe that in (3.26) the proper orthogonal rotation tensor $\boldsymbol{Q}_i(t) \in SO(3)$ was introduced, describing the rotation of a typical particle $\mathcal{P}_i$. In the two dimensional case, this tensor appears in the well-known form

$$\boldsymbol{Q}_i(t) = \begin{bmatrix} \cos\vartheta_i(t) & \sin\vartheta_i(t) \\ -\sin\vartheta_i(t) & \cos\vartheta_i(t) \end{bmatrix} \quad \text{for} \quad i = 1...(M+N). \tag{3.27}$$

The rotational part is, when viewed with regard to the continuous formulation, a new term that is due to the discrete finite-sized character of the granules. A consistent transfer of the constraint for linear deformations on the boundary, see equation (3.12), from the continuous formulation to the discrete part yields

$$\boxed{\boldsymbol{x}_q - \bar{\boldsymbol{F}}\boldsymbol{X}_q = \boldsymbol{0} \quad \text{for} \quad q = 1...M \ .} \tag{3.28}$$

Since the deformation of a particle is also governed by its centroidal rotation, a boundary constraint needs to be formulated for the rotation of the particles on the boundary. In order to yield the stiffest response for this type of constraint with respect to the aggregate stiffness, we require that the particles on the boundary frame do not rotate. This constraint is expressed as

$$\boxed{\boldsymbol{Q}_q - \boldsymbol{1} = \boldsymbol{0} \quad \text{for} \quad q = 1...M \ ,} \tag{3.29}$$

which just requires the rotation tensor to be equal to $\boldsymbol{Q}_q = \boldsymbol{1}$. This constraint yields an unequal distribution of support couples on the boundary of the microstructure.

3.4.4. Periodic Particle Deformations/Rotations on Opposite Boundaries. Periodic boundary constraints for granular materials have recently been investigated in Miehe & Dettmar [78]. Therein, an implicit discrete-element formulation is developed and periodic constraints are implemented by so-called link-forces between opposite boundary-frame particles. Taking into account the deformation map (3.26) of a typical particle $\mathcal{P}_i$, a non-trivial periodicity of the deformation of the granular aggregate may be described by *periodic fluctuations and rotations* of the form

$$\boldsymbol{w}_q^- = \boldsymbol{w}_q^+ \quad \text{and} \quad \boldsymbol{Q}_q^- = \boldsymbol{Q}_q^+ \tag{3.30}$$

of associated particles on opposite boundaries with Lagrangian positions $\boldsymbol{X}_q^-$ and $\boldsymbol{X}_q^+$, respectively. Consistent with this periodicity condition (3.30) is the *anti-periodicity of the particle support forces and support couples* on the boundary. Remember that these support forces act on the centroids of the particles. This anti-periodicity is stated by

$$\boldsymbol{a}_q^- = -\boldsymbol{a}_q^+ \quad \text{and} \quad m_q^- = -m_q^+ \tag{3.31}$$

on the centroids of opposite particles $\boldsymbol{x}_q^-$ and $\boldsymbol{x}_q^+$ on the boundary frame, see Figure 17. A deformation boundary constraint that accounts for the periodicity of the microstructure consistent with the continuous formulation (3.13) for the particle centroids reads

$$\boxed{[\![\boldsymbol{x}_q]\!] - \bar{\boldsymbol{F}}\,[\![\boldsymbol{X}_q]\!] = \boldsymbol{0} \quad \text{for} \quad q = 1...M^+ \ ,} \tag{3.32}$$

where M^+ denotes only one half of the boundary. Clearly, in order for the microstructure to be periodically extendable to infinity, *not only the displacements but also the rotations must fulfill the periodicity requirement*. Therefore, a constraint is introduced that enforces the rotations of associated particles on opposite boundaries to be equal,

$$\boxed{[\![\boldsymbol{Q}_q]\!] = \boldsymbol{0} \quad \text{for} \quad q = 1...M^+ \ .} \tag{3.33}$$

Note that the linear deformation boundary constraint introduced in Section 3.4.3 can be

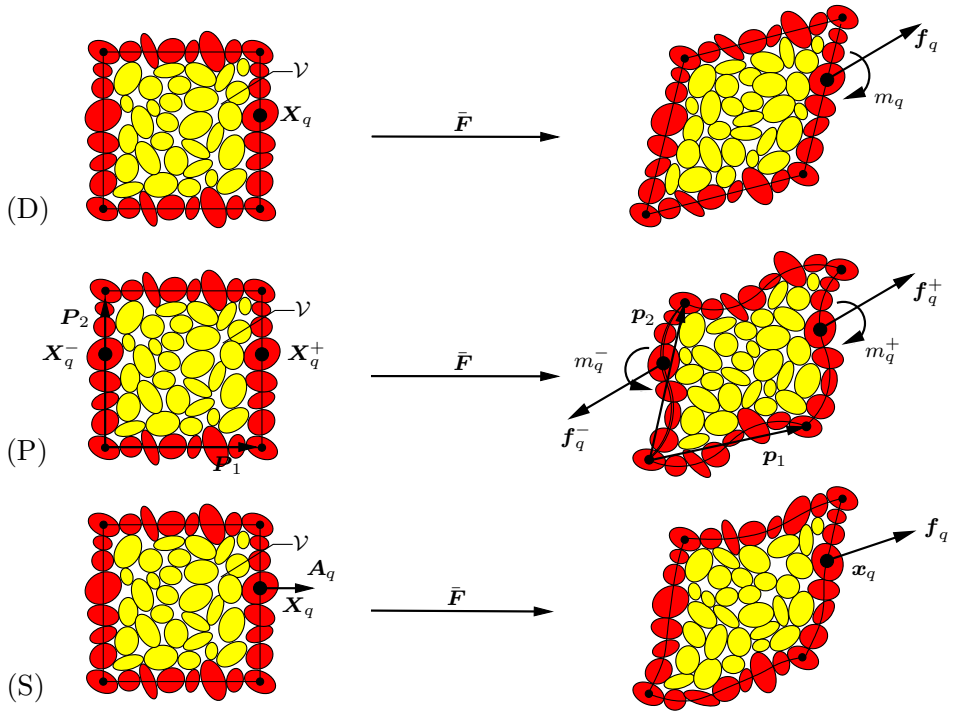

Figure 17: Deformation-driven boundary constraints for the discontinuous granular microstructures with fictitious support forces $\boldsymbol{f}_q$ and support couples m_q on particles $\mathcal{P}_q, q = 1...M$ associated with the boundary frame (D) linear displacements on the boundary, (P) periodic displacements and rotations on opposite boundary particles and (S) uniform tractions on the surface of the microstructure. $\boldsymbol{A}_q$ is the newly introduced area normal vector normal on the undeformed surface.

regarded as a special case of periodic deformation constraints where naturally the zero

deformations and rotations on all boundary-frame particles are equal and hence periodic. As a consequence of the anti-periodicity of the support couples in equation (3.31), the couples do not have an influence on the macroscopic stress in equation (3.19) because its sum vanishes. Thus, the symmetry of the stress tensor for the case of periodic boundary conditions is confirmed.

3.4.5. Uniform Tractions on the Boundary of the Microstructure. In order to derive a formulation for the uniform traction boundary constraints in the context of the deformation-driven approach employed here, the infinitesimal limit $\boldsymbol{N}dA \rightarrow \boldsymbol{A}_q$ is considered first. The continuous weak constraint (3.15) then becomes

$$\boxed{\sum_{q=1}^{M} \boldsymbol{x}_q \otimes \boldsymbol{A}_q - |\mathcal{V}|\bar{\boldsymbol{F}} = \boldsymbol{0} \quad \text{for} \quad q = 1...M \ .} \tag{3.34}$$

Here the so-called *area normal vector* $\boldsymbol{A}_q$ normal on the undeformed surface is introduced, see Figure 17 (S). Its length is associated with the surface of the boundary occupied by the respective finite-sized particle $\mathcal{P}_q$. It is the discrete form of the continuous infinitesimal vector $\boldsymbol{N}dA$. Then in the two dimensional case the referential volume of the microstructure can be calculated as

$$|\mathcal{V}| = \frac{1}{2}\sum_{q=1}^{M} \mathrm{tr}[\boldsymbol{X}_q \otimes \boldsymbol{A}_q] \ . \tag{3.35}$$

In contrast to the other two constraints introduced above, constraints are not imposed onto the particle rotations. This is due to the fact that constant tractions on the surface do not include 'couple stresses' or couple tractions. Therefore, the particles are free to rotate because of interparticle contacts with granules of the bulk. This will yield a softer response with respect to the stiffness of the particle aggregate. Consequently, no couples enter the expression for the macroscopic stress in (3.19) and for the case of uniform traction boundary constraints, symmetry is also confirmed. The case of linear deformations on the boundary is therefore the only constraints where the couples do not drop out of the stress formulations. However, for sufficiently large granular microstructures however, numerical tests imply that those couples are of minor influence to the symmetry of the Cauchy stresses (3.19).

3.5. Penalty-type Implementation of the Boundary Constraints

In this section the boundary constraints for discrete particle microstructures which were theoretically introduced above are algorithmically implemented by means of a penalty method with quadratic penalty terms. This allows for a unified implementation of all three constraints into explicit computer codes. The expressions are given for the planar case, the three dimensional formulation is omitted. The extension to three dimensions is a straightforward task since only the rotations and support couples appear in vectorial form, as opposed to scalar ones in the planar case.

3.5.1. Potential Functions for Particle Interaction Forces. In order to implement the boundary constraints into deformation-controlled simulation processes, potential functions Π_i for the particle-centroid interaction forces of all particles in the aggregate

are assumed to exist. This assumption is based on the fact that for dynamic problems the energy must be balanced in the system, that is, the field of forces due to contact interaction must be a potential field. These potential functions need to be minimized with respect to the particle positions $\boldsymbol{x}_i$,

$$\Pi(\boldsymbol{x}_i) \rightarrow \text{Min.} \quad \text{for} \quad i = 1...(M+N) \ . \tag{3.36}$$

The boundary constraints for the discontinuous granular microstructures discussed in the previous section are then introduced in the potential functions for the boundary frame particles by additional quadratic penalty terms $c_q = \hat{c}_q(\boldsymbol{x}_q, \boldsymbol{Q}_q)$ of the form

$$\Pi_p(\boldsymbol{x}_q, \boldsymbol{Q}_q) = \Pi(\boldsymbol{x}_q) + c_q(\boldsymbol{x}_q, \boldsymbol{Q}_q) \rightarrow \text{Min.} \quad \text{for} \quad q = 1...M \ . \tag{3.37}$$

Observe that these potentials only refer to the particles $\mathcal{P}_q, q = 1...M$ on the boundary frame $\partial\mathcal{V}$. Derivations of these particle interaction-force potentials with respect to the actual positions $\boldsymbol{x}_q$ and rotations ϑ_q then yield the support forces $\boldsymbol{f}_q$ and support couples m_q associated with the boundary constraint considered for the granular microstructures. Since the additional penalty forces basically follow exclusively by derivation of the penalty terms c_q, the above assumption of the existence of particle interaction force potentials is justified.

3.5.2. Penalty Forces for the New Class of Boundary Constraints. In what follows, the implementation and derivation of the above mentioned constraints in the context of the three boundary conditions is discussed.

Linear Deformations on the Boundary. The two constraints for linear deformations on the boundary (3.28) and (3.29) are added to the potential functions Π as quadratic penalty-terms of the form $\Pi_p^D(\boldsymbol{x}_q, \boldsymbol{Q}_q) = \Pi(\boldsymbol{x}_q) + c_q^D(\boldsymbol{x}_q, \boldsymbol{Q}_q)$. For the linear deformation boundary constraints with the fluctuations and rotations fixed, this penalty term is defined by

$$c_q^D(\boldsymbol{x}_q, \boldsymbol{Q}_q) = \frac{\epsilon_f}{2} \sum_{q=1}^{M} ||\boldsymbol{x}_q - \bar{\boldsymbol{F}}\boldsymbol{X}_q||^2 + \frac{\epsilon_c}{4} \sum_{q=1}^{M} ||\boldsymbol{Q}_q - \boldsymbol{1}||^2 \ . \tag{3.38}$$

The first term describes the constraint for the particle centroid displacements whereas the second one refers to the rotational constraint. The two penalty factors ϵ_f and ϵ_c are introduced for the displacement- and rotation constraints, respectively. Observe that in the two dimensional case the rotational constraint can algebraically be transformed as $||\boldsymbol{Q}_q - \boldsymbol{1}||^2 = 4(1 - \cos\vartheta_q)$. Thus the quadratic penalty term for the rotation gives a nonlinear trigonometric function in the rotation angle ϑ_q. The constraining center forces $\boldsymbol{f}_q$ and couples m_q acting on the boundary particles then follow as derivatives of (3.38) with respect to the positions $\boldsymbol{x}_q$ and rotations ϑ_q,

$$\boxed{\boldsymbol{f}_q = \partial_{\boldsymbol{x}_q} c_q^D = \epsilon_f \left[\boldsymbol{x} - \bar{\boldsymbol{F}}\boldsymbol{X}_q\right] \quad \text{and} \quad m_q = \partial_{\vartheta_q} c_q^D = \epsilon_c \left[\vartheta_q - \Theta_q\right] \ .} \tag{3.39}$$

Observe that in this expression the trigonometric function was linearized for small rotation angles.

Periodic Deformations on Opposite Boundaries. The constraints for periodic deformations are similarly implemented in the form $\Pi_p^P(\boldsymbol{x}_q, \boldsymbol{Q}_q) = \Pi(\boldsymbol{x}_q) + c_q^P(\boldsymbol{x}_q, \boldsymbol{Q}_q)$

Box 2: Penalty-type Boundary Constraints for Granular Microstructures

Assumed potentials for particle interaction forces:

$$\text{(D)}\quad \Pi_p^D(\boldsymbol{x}_q,\boldsymbol{Q}_q) = \Pi(\boldsymbol{x}_q) + \frac{\epsilon_f}{2}\sum_{q=1}^{M}||\boldsymbol{x}_q - \bar{\boldsymbol{F}}\boldsymbol{X}_q||^2 + \frac{\epsilon_c}{4}\sum_{q=1}^{M}||\boldsymbol{Q}_q - \boldsymbol{1}||^2$$

$$\text{(P)}\quad \Pi_p^P(\boldsymbol{x}_q,\boldsymbol{Q}_q) = \Pi(\boldsymbol{x}_q) + \frac{\epsilon_f}{2}\sum_{q=1}^{M^+}||\,[\![\boldsymbol{x}_q]\!] - \bar{\boldsymbol{F}}\,[\![\boldsymbol{X}_q]\!]\,||^2 + \frac{\epsilon_c}{4}\sum_{q=1}^{M^+}||\,[\![\boldsymbol{Q}_q]\!]\,||^2$$

$$\text{(S)}\quad \Pi_p^S(\boldsymbol{x}_q) = \Pi(\boldsymbol{x}_q) + \frac{\epsilon_f}{2}||\sum_{q=1}^{M}(\boldsymbol{x}_q\otimes\boldsymbol{A}_q) - |\mathcal{V}|\bar{\boldsymbol{F}}||^2$$

Constraining penalty forces and couples:

$$\text{(D)}\quad \boldsymbol{f}_q(\boldsymbol{x}_q) = \epsilon_f\left[\boldsymbol{x}_q - \bar{\boldsymbol{F}}\boldsymbol{X}_q\right]; \qquad m_q(\vartheta_q) = \epsilon_c\left[\vartheta_q - \Theta_q\right]$$

$$\text{(P)}\quad \boldsymbol{f}_q^{\pm}(\boldsymbol{x}_q^{\pm}) = \pm\epsilon_f\left[\boldsymbol{x}_q^{\pm} - \bar{\boldsymbol{F}}\boldsymbol{X}_q^{\pm}\right]; \qquad m_q^{\pm}(\vartheta_q^{\pm}) = \pm\epsilon_c\left[\vartheta_q^{\pm} - \Theta_q^{\pm}\right]$$

$$\text{(S)}\quad \boldsymbol{f}_q(\boldsymbol{x}_q) = \epsilon_f\left[\sum_{p=1}^{M}(\boldsymbol{A}_p\cdot\boldsymbol{A}_q)\boldsymbol{x}_p - |\mathcal{V}|\bar{\boldsymbol{F}}\boldsymbol{A}_q\right]; \quad m_q = 0$$

where the penalty term reads

$$c_q^P(\boldsymbol{x}_q,\boldsymbol{Q}_q) = \frac{\epsilon_f}{2}\sum_{q=1}^{M^+}||\,[\![\boldsymbol{x}_q]\!] - \bar{\boldsymbol{F}}\,[\![\boldsymbol{X}_q]\!]\,||^2 + \frac{\epsilon_c}{4}\sum_{q=1}^{M^+}||\,[\![\boldsymbol{Q}_q]\!]\,||^2\ . \tag{3.40}$$

Here, summation only needs to be performed over the one half $\partial\mathcal{V}^+$ of the surface particles, namely the M^+ particles. Again, observe that the first term enforces the displacement constraint and the second one the rotational part. Recall that in the two dimensional case the rotational expression can algebraically be transformed into $||\,[\![\boldsymbol{Q}_q]\!]\,||^2 = 4(1-\cos[\![\vartheta_q]\!])$. Derivation of (3.40) with respect to the particle centroid positions $\boldsymbol{x}_q^+$ and rotations ϑ_q^+ yields the support forces $\boldsymbol{f}_q^+$ and support couples m_q^+ (and due to the anti-periodicity, their negative counterparts $\boldsymbol{f}_q^-$ and m_q^-) on the boundary as

$$\boldsymbol{f}_q^{\pm} = \partial_{\boldsymbol{x}_q^{\pm}}c_q^D = \pm\epsilon_f\left[\boldsymbol{x}_q^{\pm} - \bar{\boldsymbol{F}}\boldsymbol{X}_q^{\pm}\right] \quad\text{and}\quad m_q^{\pm} = \partial_{\vartheta_q^{\pm}}c_q^D = \pm\epsilon_c\left[\vartheta_q^{\pm} - \Theta_q^{\pm}\right]\ . \tag{3.41}$$

Again, the trigonometric function was linearized for small rotation angles. The derivations with respect to $\boldsymbol{x}_q^-$ and ϑ_q^- also yield the negative counterparts to $\boldsymbol{f}_q^+$ and m_q^+ and confirm the anti-periodicity of the support forces and couples for this case of periodic boundary constraints.

Uniform Tractions on the Boundary. In the case of uniform tractions on the boundary, only displacements are considered since the particles are free to rotate. The displacement constraint is implemented into the potential function in the form $\Pi_p^S(\boldsymbol{x}_q) = \Pi(\boldsymbol{x}_q) + c_q^S(\boldsymbol{x}_q)$ where the penalty term appears as

$$c_q^S(\boldsymbol{x}_q) = \frac{\epsilon_f}{2}||\sum_{q=1}^{M}(\boldsymbol{x}_q\otimes\boldsymbol{A}_q) - |\mathcal{V}|\bar{\boldsymbol{F}}||^2\ . \tag{3.42}$$

Observe here that because a traction-type boundary condition is enforced, this constraint can be considered to be of Neumann-type while the other two previously discussed constraints clearly enforce displacement conditions of Dirichlet-type. Derivation of (3.42) with respect to the particle centroid position $\boldsymbol{x}_q$ yields the support forces that act on the centroids of the particles and enforce uniform tractions as

$$\boxed{\boldsymbol{f}_q = \partial_{\boldsymbol{x}_q} c_q^S = \epsilon_f \left[\sum_{p=1}^{M} (\boldsymbol{A}_p \cdot \boldsymbol{A}_q)\boldsymbol{x}_p - |\mathcal{V}| \bar{\boldsymbol{F}} \boldsymbol{A}_q \right] \quad \text{and} \quad m_q = \partial_{\vartheta_q} c_q^S = 0 \ .} \tag{3.43}$$

In Box 2 the potential functions with the penalty terms and the derived forces and couples enforcing the three classes of boundary constraints are summarized.

4. Micromechanical Modeling of Granular Materials

The micromechanical computational modeling of granular materials is usually traced back to the work of Cundall & Strack [29] who developed a discrete, explicitly integrated numerical model for the analysis of granular assemblies. In that approach, the interaction of the particles is viewed as a transient problem and energy is dissipated through particle friction, contact and global damping. The use of damping characteristics is necessary in order to reach a state of quasistatic equilibrium for all conditions. The first and foremost aspect that arises is the mechanical description of the contact laws that govern the interaction between particles. These contact forces basically determine the mechanical evolution of any system of granules and are of fundamental importance to the validity of any simulated granular assembly. Therefore, this section starts with a review of some classical constitutive contact interaction laws that can be found in literature on micromechanics of granular structures. Then the constitutive models for contact normal and tangential particle interactions in two and three dimensions used henceforth in this work are developed and discussed. This subchapter is divided into the theoretical formulation and its algorithmic implementation. A time-consuming operation in any granular code is the repeated detection of contacts between particles. There are several such sophisticated contact detection algorithms described in literature that speed up the process and thus reduce the computational effort considerably. Some of these algorithms are described in the next subchapter. Since we deal with granular microstructures, in the context of homogenization of Eulerian stress objects the actual volumes of such microstructures must be determined. This is fairly easy in two dimensions, but becomes quite complex in three. Thus, a method is described where the surface of the actual granular microstructure is at first traingulated and then meshed with triangular facets. Then, based on this triangulation, the actual volume can be computed. Subsequently, the explicit time integration algorithm for the evolution of the motion of the particles is briefly described. Therein, global and local damping mechanisms are introduced and the setup of the particle force and damping force vectors is described.

4.1. Classical Contact Force-Displacement Laws

The mechanical behavior between two particles in contact can be decomposed into mechanisms in directions *normal* and *tangential* to the contact normal. In what follows, three different constitutive contact normal laws are introduced, followed by a tangential law. These constitutive laws are taken from literature and are meant to provide an idea of how mechanical contact interaction can be handled.

4.1.1. Elastic Contact Normal Law of Hertz. As early as 1882 Hertz [48] considered the normal contact between two spheres $\mathcal{P}_M$ and $\mathcal{P}_S$ with radii R_M and R_S, respectively. Their Young moduli and Poisson ratios are denoted by E_M, ν_M and E_S, ν_S. The equivalent Young's modulus for the two spheres in contact is then given by $E^* = [(1-\nu_M^2)/E_M + (1-\nu_S^2)/(E_S)]^{-1}$. Similarly, the relative radius of the contact curvature is computed as $R^c = (1/R_M + 1/R_S)^{-1}$ which leads to the radius R^* of the circular contact area

$$R^* = \sqrt[3]{\frac{3P^cR^c}{4E^*}} \ , \tag{4.1}$$

where P^c is the contact normal force acting between the two spheres. Note that P^c could include inertial forces if dynamics were taken into account. The approach of the two

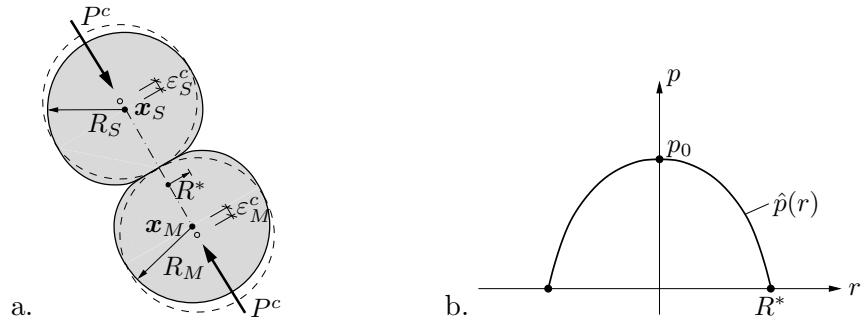

Figure 18: Two spheres in contact: a. Hertzian contact curvature due to normal pressure and b. distribution of normal pressure $\hat{p}(r)$ over the radius of the circular contact area.

spheres, i.e. the length ε^c that rigid particles would overlap, becomes

$$\varepsilon^c = R^{*2}/R^c = \sqrt[3]{\frac{9P^{c2}}{16R^cE^{c2}}} \ . \tag{4.2}$$

The distribution of the normal pressure p on the contact area as a function of the radius r from the center of the area and the maximum pressure p_0 at the center of the contact area are computed by

$$p = p_0\sqrt{1-\left(\frac{r}{R^*}\right)^2} \quad \text{and} \quad p_0 = \frac{3P^c}{2\pi R^{*2}} = \sqrt[3]{\frac{6P^cE^{*2}}{\pi^3R^{c2}}} \ . \tag{4.3}$$

With these relations at hand, the Hertzian contact normal law gives a *nonlinear elastic relation* between the force P^c and the displacement ε^c of the root-form

$$\boxed{P^c = c_p\sqrt{\varepsilon^c} \ .} \tag{4.4}$$

Note that due to the purely elastic relation, the restitution coefficient comes up to $e = 1$. This formulation of Hertz (4.4) is a widely-known elastic contact normal law which is frequently used in three dimensional micromechanics of granular materials since it gives a very good approximation of real-world behavior.

4.1.2. Elastoplastic Contact Normal Law of Walton & Brown**.** In many collision problems, plastic deformations occur that are not accounted for in the Hertzian model. Thus, Walton & Brown [121] suggested a bilinear force displacement law of the form

$$P^c = \begin{cases} c_{p1}\varepsilon^c & \text{for loading} \\ c_{p2}(\varepsilon^c - \varepsilon^c_0) & \text{for unloading} \end{cases} \tag{4.5}$$

that yields a residual displacement ε^c_0 after complete unloading, accounting for plastic deformation during the impact. The stiffness coefficients c_{p1} and c_{p2} characterize the slope of the two loading/unloading paths. Note that the restitution coefficient e and the stiffnesses c_{p1} and c_{p2} are related by

$$e = \sqrt{\frac{c_{p1}}{c_{p2}}} \ . \tag{4.6}$$

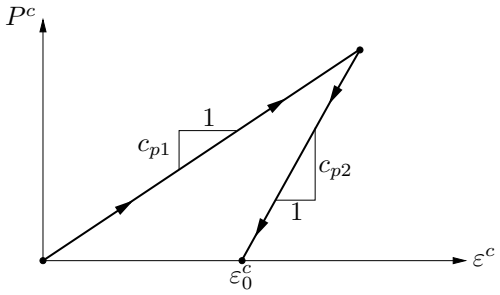

Figure 19: Elastoplastic force-displacement law as suggested in Walton & Brown [121]. The stiffness coefficients c_{p1} and c_{p2} determine the slopes of the linear interaction laws during loading and unloading, respectively. After unloading, a residual displacement ε_0^c due to plastic deformation remains.

Since the two stiffness coefficients are constants, the restitution coefficient is thus also a constant. Note that experimental measurements prove this relation to be an inconsistency, because the real restitution coefficient depends on the impact velocity. Nevertheless, the above relation is regarded as a reasonable approximation.

4.1.3. Elastic-Perfectly Plastic Contact Normal Law of Thornton. In the work Thornton [113], a quasistatic contact mechanism during the course of the impact between two elastic-perfectly plastic spheres is assumed. During elastic loading, the normal traction follows the Hertzian relationship. As soon as plastic deformation occurs, the normal traction is assumed to be less than or equal to a contact yield stress $(\sigma_y)_{Th}$ inside the contact area. After incipient plastic deformation, a linear relationship between the overlap ε^c and the contact normal force P^c is assumed, see Figure 20. Loading below the

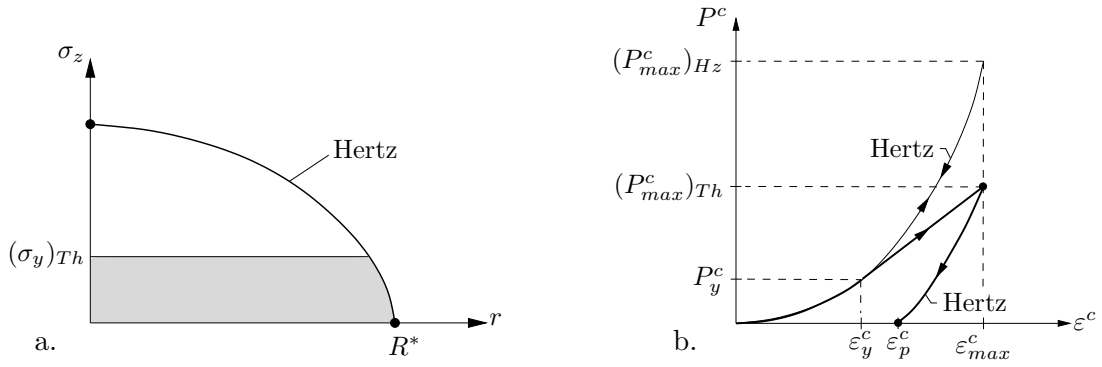

Figure 20: Elastic-perfectly plastic normal contact law as proposed in Thornton [113]: a. Distribution of normal traction in the Thornton- and the Hertz models; b. normal force-displacement law of Thornton, note the linear relationship between P^c and ε^c in the plastic loading regime. Below that, as well as during unloading, a Hertzian relation is assumed.

yield stress and unloading is assumed to be governed by a Hertzian root-type law, where in the case of unloading a larger radius R_p^c of the contact curvature due to irreversible plastic deformation is assumed. For a more detailed discussion, see Vu-Quoc & Zhang [120] and the references therein.

4.1.4. Tangential Contact Tangential Law of Cattaneo and Mindlin. Cattaneo [22] and Mindlin [87] independently considered the contact problem between two spherical particles under constant normal forces and varying tangential forces, see Figure 21a. They assumed a Hertzian normal pressure distribution on the contact surface,

an independent treatment of the effects of normal and tangential forces and furthermore that a complete stick on the contact surface causes the tangential stress go to infinity at the edge of contact. Again, the two spheres in question are subject to a normal load P^c.

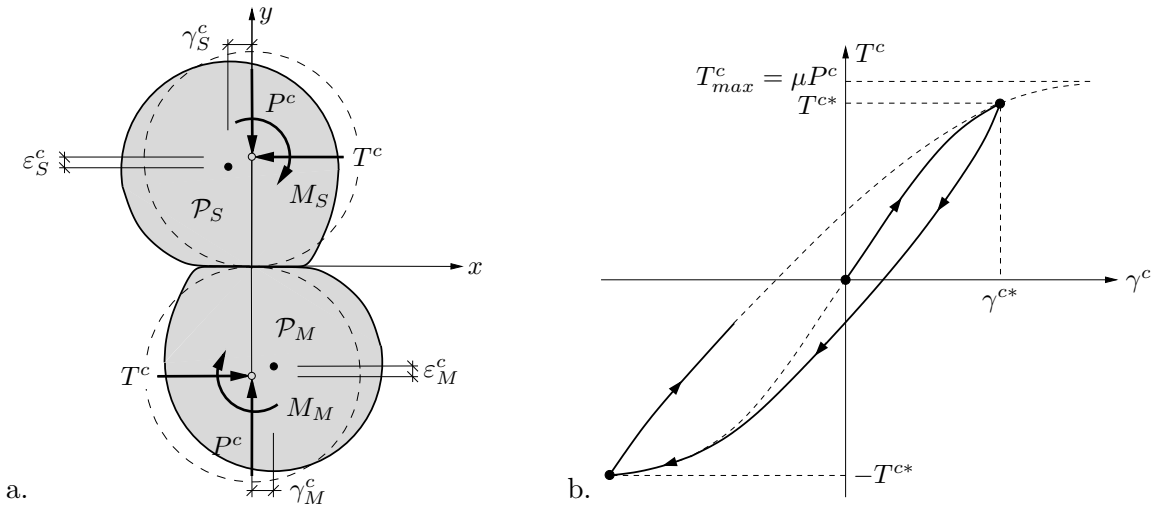

Figure 21: a. Two spheres in contact under normal P^c and tangential T^c loads. The couples M_S, M_M are required to ensure equilibrium; b. tangential force-displacement relation according to Mindlin & Deresiewicz [88] for the case of constant normal force P^c and varying tangential force T^c. Their suggestions yield the hysteresis loop shown which yields a residual displacement.

Also, the radius of the contact area R^* in equation (4.1), the normal overlap ε^c in (4.2) and the definitions used therein are considered. An incremental update scheme for the contact tangential force T^c in terms of the increment of the slip $\Delta\gamma$ can be written as

$$T^c = T_n^c + c_t \, \Delta\gamma^c \; . \tag{4.7}$$

The stiffness coefficient c_t is computed depending on the current states, the development of the contact normal force P^c and the tangential force T^c. According to Mindlin & Deresiewicz [88], for example, when increasing T^c and $|T^c| \leq |T^{c*}|$, the tangential contact stiffness becomes

$$c_t = c_{t0} \left(1 - \frac{T^c - T^{c*}}{2\mu P^c} \right) \; , \tag{4.8}$$

where T^{c*} is the tangential force at the last turning point in the loading history, see Figure 21b, and μ is the coefficient of friction between the two spheres in contact. The initial tangential stiffness coefficient c_{t0} can be determined by $c_{t0} = 8R^*[(2-\nu_M)/G_M + (2-\nu_S)/G_S]^{-1}$ in terms of the shear moduli and Poisson ratios G_M, ν_M and G_S, ν_S of the two spheres $\mathcal{P}_M$ and $\mathcal{P}_S$, respectively. The initial stiffness c_{t0} depends on the normal force P^c since the contact radius R^* depends on P^c. Thus, energy is dissipated due to friction even for elastic contacts. Mindlin & Deresiewicz [88] found that this dissipation is caused by micro-slips on the contact surface. For a more detailed discussion of this tangential force-displacement model, refer to the work Vu-Quc & Zhang [119] and the references therein.

4.2. Interparticle Contact between Arbitrary-Shaped Plane Granules

In this section the micromechanical model used in the subsequent simulations for the *quasistatic mechanical interaction* of two rigid particles in contact is presented. Since

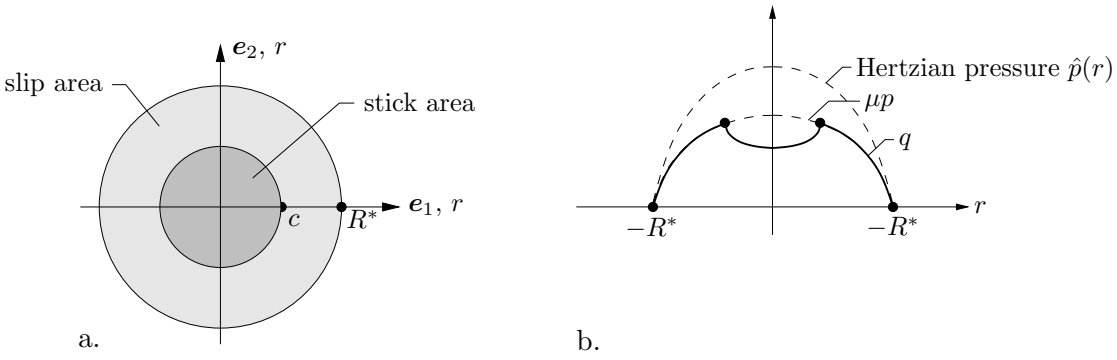

Figure 22: Slip and stick regions and associated tangential stress distribution: a. the slip area is the annulus $c \leq r \leq R^*$ where the tangential stress equals the frictional limit $q = \mu p$. Within the slip radius $r \leq c$, the tangential stress is below the frictional limit; b. tangential stress distribution within the diameter of $|r| \leq R^*$.

different types of particle structures are examined, the interaction laws for both spherical/ circular particles in three and two dimensions, respectively, as well as arbitrary-shaped plane granules are discussed. For the latter, the true elliptical shape is approximated by polygons. In this context, the contact-normal and frictional contact-tangential force mechanisms are independently developed.

4.2.1. Contact Properties. First of all, the focus is put on the mechanical interaction between two elliptically shaped particles in two spatial dimensions. In the context of a micromechanical model, at the current time two such granules are in contact. In the actual configuration, these two particles are located at $\boldsymbol{x}_M$ and $\boldsymbol{x}_S$ and in the subsequent discussion are referred to as *master* $\mathcal{P}_M$ and *slave* $\mathcal{P}_S$ *particles*, see Figure 23. Algorithmically, at first a coarse contact check is performed where the sum of the larger radii $R_{M,max}$ and $R_{S,max}$ of both particles in question are compared to the distance between the two centroids. Contact is possible if $(R_{M,max} + R_{S,max}) - |\boldsymbol{x}_M - \boldsymbol{x}_S| > 0$ holds. If contact is possible, then a fine check is performed where the surfaces of the elliptical particles are approximated by n polygonal segments. A typical node $\boldsymbol{x}_i$ is thereby computed as

$$\boldsymbol{x}_i = \boldsymbol{x}_M + \boldsymbol{Q}^{-1}\boldsymbol{\xi}_i \ , \quad i = 1...n \tag{4.9}$$

where the local position vector $\boldsymbol{\xi}_i$ is parameterized in a discrete parameter t_i and given as

$$\boldsymbol{\xi}_i = \begin{bmatrix} R_1 \cos(t_i) \\ R_2 \sin(t_i) \end{bmatrix} \quad \text{with} \quad t_i = 2(i-1)\pi/n \ , \quad i = 1...n \ . \tag{4.10}$$

Here, R_1 and R_2 are the two principal radii of the elliptical particle. The fine contact checks whether segments of the master particle intersect with segments of the slave particle. For small penetrations, i.e. those that exclude interpenetrations, only two such intersections can be found between two particles. If intersections are found, the area of overlap a^c is defined by the nodes of the two polygons approximating the elliptical shapes between the two intersection points in addition to the two intersection points. Let this set of nodes consist of N points. The area of overlap can then be calculated as

$$a^c = |\frac{1}{2}\sum_{I=1}^{N}(x_1^I - x_1^{I+1})(x_2^I + x_2^{I+1})| \quad \text{with } \boldsymbol{x}^{N+1} = \boldsymbol{x}^1 \ . \tag{4.11}$$

Following Matuttis & Luding [72] and references therein, for two polygonal particles in contact a *characteristic length scale* l^c is introduced of the form

$$l^c = 2(|\boldsymbol{r}_M^c| + |\boldsymbol{r}_S^c|) \tag{4.12}$$

that accounts for the shape of the particle contact in the penetration measure to be defined. Here, $\boldsymbol{r}_M^c$ and $\boldsymbol{r}_S^c$ are the vectors from the centroids of the master and slave particles, respectively, to the centroid of the contact area $\boldsymbol{x}^c$, see also Figure 23. The

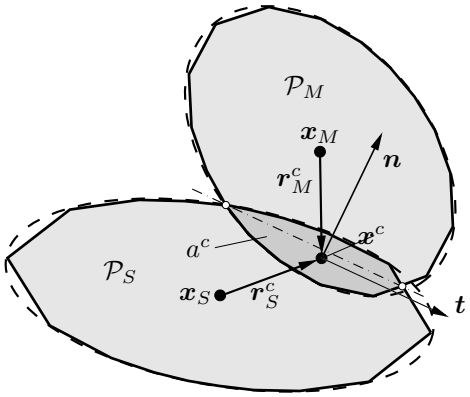

Figure 23: Configuration of two elliptically-shaped rigid particles in contact. The surfaces of the particles are approximated by polygons. The particles are in contact if two intersections between segments of the two polygons are found. The contact point $\boldsymbol{x}^c$ is the centroid of the contact area a^c, the contact tangential vector $\boldsymbol{t}$ is defined as the norm of the vector through the two intersections such that the normal vector $\boldsymbol{n}$ perpendicular to $\boldsymbol{t}$ points towards the master particle $\mathcal{P}_M$.

centroid of the contact area is defined as the contact point $\boldsymbol{x}^c$ and can be computed by summation over the weighted nodes that define the contact area,

$$\boldsymbol{x}^c = \frac{1}{N} \sum_{I=1}^{N} \boldsymbol{x}^I. \tag{4.13}$$

The contact tangential vector $\boldsymbol{t}$ is defined as the unit vector between the two intersection nodes of the two surfaces of the ellipses. The contact normal vector $\boldsymbol{n}$ appears from the cross product $\boldsymbol{n} = \boldsymbol{e}_3 \times \boldsymbol{t}$. Note that these vectors are chosen such that the contact normal vector $\boldsymbol{n}$ points towards the master particle $\mathcal{P}_M$. All quantities defined here are depicted in Figure 23. By checking possible contacts between all particles, a set $\mathcal{A}(t)$ of active particle contacts is established that can be stated as

$$\mathcal{A}(t) := \{c := (M, S) \,|\, \mathcal{P}_M \cap \mathcal{P}_S\}. \tag{4.14}$$

Having introduced and defined the contact properties, these can now be used to set up constitutive contact normal and tangential force-displacement laws.

4.2.2. Elastic Contact-Normal Force Mechanism. In order to establish an expression for the contact-normal force at the contact point, a *penetration measure* ε^c for the two particles in contact is introduced as the quotient of contact area and characteristic length,

$$\varepsilon^c = \frac{a^c}{l^c}. \tag{4.15}$$

Thus, the length scale parameter l^c accounts for a nonlinear relation between any contact force and contact area a^c. This new kinematic variable ε^c now enters a penalty-type constitutive equation for the contact-normal force at the contact point $\boldsymbol{x}^c$. Note that for circular and spherical particles, one would assume the measure of penetration ε^c to be the maximum overlap $\varepsilon^c = R_M + R_S - |\boldsymbol{x}_M - \boldsymbol{x}_S|$, where R_M and R_S are the radii of two overlapping particles. For the contact-normal force mechanism at the contact point $\boldsymbol{x}^c$ the constitutive relation

$$\boxed{P^c = \psi_p'(\varepsilon^c) \quad \text{for} \quad c \in \mathcal{A}} \tag{4.16}$$

is assumed. Here, $\psi_p = \hat{\psi}_p(\varepsilon^c)$ is a constitutive force-potential function for the contact pressure depending on the kinematic quantity ε^c that is presumed to be *a priori* convex. Its derivative ψ_p' is therefore monotonously increasing with initial value $\psi_p'(\varepsilon = 0) = 0$ and zero where the kinematic variable is negative (no contact), $\varepsilon^c < 0$. The potential function ψ_p can possibly be a nonlinear penalty function that approximately enforces the constraint $\varepsilon^c = 0$ in the case of an existing particle contact. Specific functions are discussed for example in Mindlin [87] and Mindlin & Deresiewicz [88]. The specific functions used in this work are defined in the numerical examples section.

4.2.3. Frictional-Cohesive Contact-Tangential Force Mechanism. Continuous Formulation. In an infinitesimally small time interval dt, the two contacting master and slave particles in question perform the independent infinitesimal rotations $d\vartheta_M$ and $d\vartheta_S$, respectively. Thus the relative displacement $d\boldsymbol{x}^c$ of the two particles at contact point $\boldsymbol{x}^c$ follows as $d\boldsymbol{x}^c = d\boldsymbol{x}_M - d\boldsymbol{x}_S + d\vartheta_M \boldsymbol{e}_3 \times \boldsymbol{r}_M^c - d\vartheta_S \boldsymbol{e}_3 \times \boldsymbol{r}_S^c$ and the incremental slip $d\gamma^c$ follows by projection of the incremental displacement onto the tangential direction at the contact point $d\gamma^c = d\boldsymbol{x}^c \cdot \boldsymbol{t}$. Based on this incremental observation, as a basic kinematic variable the *slip rate* $\dot{\gamma}^c$ is introduced as

$$\dot{\gamma}^c = \left[\dot{\boldsymbol{x}}_M - \dot{\boldsymbol{x}}_S + \dot{\vartheta}_M \boldsymbol{e}_3 \times \boldsymbol{r}_M^c - \dot{\vartheta}_S \boldsymbol{e}_3 \times \boldsymbol{r}_S^c\right] \cdot \boldsymbol{t} \tag{4.17}$$

under the assumption that any change of the tangential vector $\boldsymbol{t}$ in the time interval Δt can be neglected. The *current slip* may then be defined by time integration of the slip

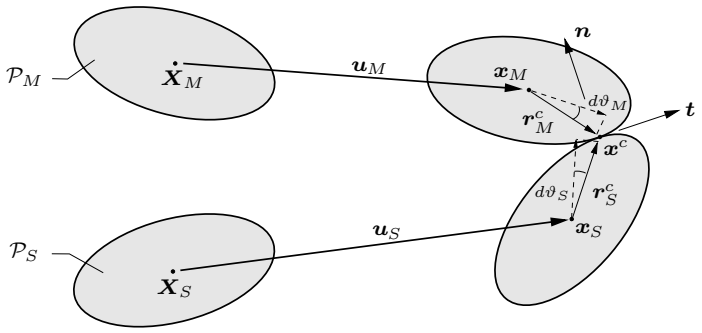

Figure 24: Displacements of two rigid elliptically-shaped plane particles that come into contact. The two particles are the master $\mathcal{P}_M$ and slave $\mathcal{P}_S$ particles with actual centroid positions and rotations $\boldsymbol{x}_M$, ϑ_M and $\boldsymbol{x}_S$, ϑ_S, respectively. The incremental slip at contact point $\boldsymbol{x}^c$ is computed from the incremental rotations $d\vartheta_M$ and $d\vartheta_S$.

rate

$$\gamma^c = \int_{t_0^c}^{t} \dot{\gamma}^c \, dt \quad \text{for} \quad c \in \mathcal{A} \tag{4.18}$$

within the time interval $[t_0^c, t]$ where the two particles are in contact. This total slip γ^c is then decomposed into *elastic* and *plastic contributions*

$$\gamma_e^c := \gamma^c - \gamma_p^c \quad \text{for} \quad c \in \mathcal{A} \, . \tag{4.19}$$

In analogy to the constitutive formulation for the contact normal force in equation (4.36), the *contact tangential force* is then assumed to be governed by the constitutive expression

$$\boxed{T^c = \psi_t'(\gamma_e^c) \quad \text{for} \quad c \in \mathcal{A}} \tag{4.20}$$

in terms of a convex constitutive potential $\psi_t = \hat{\psi}_t(\gamma_e^c)$ with initial value $\psi_t(0) = \psi_t'(0) = 0$. This tangential force is presumed to be bounded by a Coulomb-type *slip criterion function* of the form

$$\phi(T^c, P^c, \beta) = |T^c| - P^c \, \tan[\rho] - \beta \leq 0 \quad \text{with} \quad \beta = \psi_h'(\alpha) \, . \tag{4.21}$$

Here, the symbol ρ denotes the interparticle friction angle and β the cohesion parameter for the interparticle contact. The latter is assumed to be governed by a potential function $\psi_h = \hat{\psi}_h(\alpha)$ in terms of the hardening variable α. The *evolution of the tangential slip* in (4.19) and the cohesive hardening variable in (4.21) are assumed to be governed by

$$\dot{\gamma}_p^c = \lambda \, \frac{T^c}{|T^c|} \quad \text{and} \quad \dot{\alpha} = \lambda \, , \tag{4.22}$$

where the plastic parameter λ is determined by the well-known Kuhn-Tucker-type *loading-unloading conditions*

$$\lambda \geq 0, \quad \phi \leq 0, \quad \lambda\phi = 0 \, . \tag{4.23}$$

This rounds up the constitutive model for the description of the frictional-cohesive tangential contact mechanism used henceforth. Observe that the micromechanical model is described by the three fundamental micro-stress force-potential functions $\psi_p(\varepsilon_e^c)$, $\psi_t(\gamma_e^c)$, $\psi_h(\alpha)$ and by the slip criterion function $\phi(T^c, P^c, \beta)$. Specific forms of these functions are given and commented on in the numerical examples section below.

Algorithmic Formulation. In what follows, an implicit integration algorithm for the elastoplastic Coulomb-type model is developed which yields the total slip from the slip rate (4.18) in order to determine time-discrete values of the tangential force T^c in the case of active contact. At first, the time interval $[t_n, t_{n+1}]$ is considered where all values at the beginning t_n are known. Subsequently, all variables without a subscript refer to the actual time t_{n+1}. Implicit algorithmic integration of the slip rate (4.17) then yields the update of the total slip as

$$\gamma^c = \gamma_n^c + \{(\boldsymbol{x}_M - \boldsymbol{x}_{Mn}) - (\boldsymbol{x}_S - \boldsymbol{x}_{Bn}) + \boldsymbol{e}_3 \times [(\vartheta_M - \vartheta_{Mn})\boldsymbol{r}_M^c - (\vartheta_S - \vartheta_{Sn})\boldsymbol{r}_S^c]\} \cdot \boldsymbol{t} \tag{4.24}$$

for $c \in \mathcal{A}$. Note that $\boldsymbol{t}$ is the tangential unit vector characterized by the normed vector through the two points where the discretized polygonal particle surfaces intersect, see Figure 23. Then (4.24) represents the total relative tangential displacement of the two particles at the contact point $\boldsymbol{x}^c$. The incremental step remains elastic if the condition

$$\phi(T^{c*}, P^c, \beta^*) < 0 \quad \text{with} \quad T^{c*} := \psi_t'(\gamma^c - \gamma_{pn}^c) \quad \text{and} \quad \beta^* := \psi_h'(\alpha_n) \tag{4.25}$$

is met. Then the tangential force T^c simply follows as $T^c = T^{c*}$. The total slip and hardening variable are updated as $\gamma_p^c = \gamma_{pn}^c$ and $\alpha = \alpha_n$. If the postulation (4.25) is violated, a fully implicit integration of the evolution equations (4.22) yields the updates

$$\gamma_p^c = \gamma_{pn}^c + \gamma \, \frac{T^c}{|T^c|} \quad \text{and} \quad \alpha = \alpha_n + \gamma \tag{4.26}$$

for the plastic slip γ_p^c and hardening variable α with increment $\gamma \geq 0$. For this particular γ the Coulomb-type slip criterion function ϕ in equation (4.21) with tangential force from (4.20) is evaluated. Its linearization follows as

$$G := -\frac{\partial \phi}{\partial \gamma} = \psi_t''(\gamma^c - \gamma_p^c) + \psi_h''(\alpha) \tag{4.27}$$

and governs a Newton-type update of the incremental parameter γ of the form

$$\gamma \Leftarrow \gamma + G^{-1}\phi \; . \tag{4.28}$$

The iteration cycle (4.26) - (4.28) is repeated until convergence is obtained in the sense $|\phi| < tol$. Note that for a linear hardening function ψ_h' the solution can directly be obtained in one Newton iteration step. The algorithmic tangent modulus C_t^{ep} governs the sensitivity of the tangential force T^c with respect to a change of the total slip γ^c. Starting with the tangential force in (4.20) and substitution of the result $\partial_{\gamma^c}\gamma = G^{-1}\psi_t'' T^t/|T^c|$ obtained from the consistency condition $\phi = 0$ by the implicit function theorem, the closed-form expression of the algorithmic tangent can be derived as

$$C_t^{ep} := \frac{\partial T^c}{\partial \gamma^c} = \psi_t'' \; - \; G^{-1}\psi_t''^{\,2} \; . \tag{4.29}$$

The last term in (4.29) only occurs in the case of plastic loading together with a non-zero incremental parameter $\gamma > 0$. Note that in this formulation the plastic slip γ_p^c and the internal variable α appear as internal variables that describe the history-dependent material model of the interparticle contact. With regard to the updates (4.24) and (4.26) the data base

$$\mathcal{H}_n^c := \{\gamma_{pn}^c, \alpha_n; \; \gamma_n^c, \boldsymbol{x}_{Mn}, \vartheta_{Mn}, \boldsymbol{x}_{Sn}, \vartheta_{Sn}\} \tag{4.30}$$

is stored for each interparticle contact at time t_n. Clearly, the current tangential slip is set to zero when the two particles separate, that is

$$\gamma_p^c = \gamma^c = 0 \quad \text{for} \quad c \notin \mathcal{A} \; . \tag{4.31}$$

Having introduced the theoretical and algorithmical formulations of the interparticle contact between two arbitrary-shaped plane particles, subsequently a similar model for the contact between spherical granules in three dimensions is discussed.

4.3. Interparticle Contact between 3D Spherical Granules

In analogy to the formulations for two dimensional problems, the deformation map of a typical three dimensional rigid particle can be written in the form

$$\boldsymbol{x}(\boldsymbol{X},t) = \boldsymbol{x}_p(t) + \boldsymbol{Q}(t)[\boldsymbol{X} - \boldsymbol{X}_p] \tag{4.32}$$

where $\boldsymbol{x}_p(t)$ denotes the translation vector of the particle centroid (the actual position) and a superimposed rotation governed by the proper orthogonal tensor $\boldsymbol{Q}(t) \in SO(3)$. Thus the particle kinematics (4.32) are described by the *generalized position vector*

$$\boldsymbol{d}_p(t) := \left[\begin{array}{cccccc} x_{p1}(t) & x_{p2}(t) & x_{p3}(t) & \vartheta_{p1}(t) & \vartheta_{p2}(t) & \vartheta_{p3}(t) \end{array}\right]^T \in \mathcal{R}^6 \tag{4.33}$$

containing the particle's centroid position and rotation vectors $\boldsymbol{x}_p$ and $\boldsymbol{\vartheta}_p$, respectively.

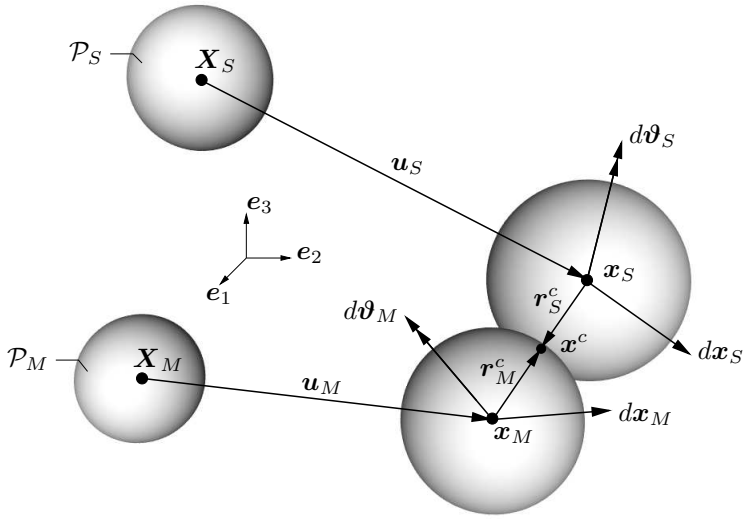

Figure 25: Displacements of two rigid spherical particles that come into contact. The two particles are the master $\mathcal{P}_M$ and slave $\mathcal{P}_S$ particles with actual position and rotation vectors $\boldsymbol{x}_M$, $\boldsymbol{\vartheta}_M$ and $\boldsymbol{x}_S$, $\boldsymbol{\vartheta}_S$, respectively. The incremental slip at contact point $\boldsymbol{x}^c$ is computed from both the incremental displacements $d\boldsymbol{x}_M$, $d\boldsymbol{x}_S$ and the incremental rotations $d\boldsymbol{\vartheta}_M$ and $d\boldsymbol{\vartheta}_S$.

In the context of a micromechanical model, two granules of spherical shapes are examined which at the current time are in contact. In the actual configuration, these master and slave particles $\mathcal{P}_M$ and $\mathcal{P}_S$ are located at $\boldsymbol{x}_M$ and $\boldsymbol{x}_S$, see Figure 25.

4.3.1. Elastic Contact-Normal Force Mechanism. In order to generate a micromechanical model for the three dimensional interparticle mechanism, a *penetration measure* is defined that is associated with the two particles $\mathcal{P}_M$ and $\mathcal{P}_S$,

$$\varepsilon^c := (R_S + R_M) - |\boldsymbol{l}^c| \quad \text{with} \quad c := (M,S)\ , \tag{4.34}$$

where R_M and R_S are again the radii of the master and slave particles, respectively. $\boldsymbol{l}^c = \boldsymbol{x}_s - \boldsymbol{x}_M$ is the branch vector that connects the two centroids of the particles. The penetration measure serves firstly as a local contact check, that is, the current *active set of particle contacts* is defined via

$$\mathcal{A}(t) := \{c := (M,S) \,|\, \varepsilon^c(t) > 0\} \tag{4.35}$$

Secondly, as a kinematic variable the penetration measure enters a penalty-type constitutive equation for the computation of the *contact normal force* P^c between contacting particles $\mathcal{P}_M$ and $\mathcal{P}_S$ of the form

$$\boxed{P^c = \psi_p'(\varepsilon^c) \quad \text{for} \quad c \in \mathcal{A}\ .} \tag{4.36}$$

Here, $\psi_p = \hat{\psi}_p(\varepsilon^c)$ is the constitutive potential function for the contact pressure. This potential function has the same properties as the one in equation (4.36). The functions employed here are given in the numerical examples section.

4.3.2. Frictional-Cohesive Contact-Tangential Force Mechanism. Continuous Formulation. In an infinitesimally small time interval dt, the two contacting master and slave particles in question perform the independent infinitesimal displacements $d\boldsymbol{x}_M = \boldsymbol{x}_M - \boldsymbol{x}_{Mn}$ and $d\boldsymbol{x}_S = \boldsymbol{x}_S - \boldsymbol{x}_{Sn}$ as well as the infinitesimal rotations $d\boldsymbol{\vartheta}_M = \boldsymbol{\vartheta}_M - \boldsymbol{\vartheta}_{Mn}$ and $d\boldsymbol{\vartheta}_S = \boldsymbol{\vartheta}_S - \boldsymbol{\vartheta}_{Sn}$, respectively. As before, variables with the subscript n are known values at time t_n, variables without that subscript refer to the current time t_{n+1}. The relative incremental translation of the slave particle with respect to the master one appears as $d\boldsymbol{x} = d\boldsymbol{x}_M - d\boldsymbol{x}_S$. This total relative displacement must be split up into parts normal and tangential to the contact normal. Thus, in three dimensions the projection of the relative displacement vector $d\boldsymbol{x}$ onto the tangential plane $\mathcal{T}$ at the contact point $\boldsymbol{x}^c$ becomes

$$d\boldsymbol{x}_t = d\boldsymbol{x} - (\Delta\boldsymbol{x} \cdot \boldsymbol{n})\boldsymbol{n}, \tag{4.37}$$

where $\boldsymbol{n} = (\boldsymbol{x}_S - \boldsymbol{x}_M)/|\boldsymbol{x}_S - \boldsymbol{x}_M|$ represents the contact unit normal vector that points from the centroid of the master towards the centroid of the slave particle. A visualization is given in Figure 26. Considering the position vectors $\boldsymbol{r}_M^c = \boldsymbol{x}^c - \boldsymbol{x}_M$ and $\boldsymbol{r}_S^c = \boldsymbol{x}^c - \boldsymbol{x}_S$

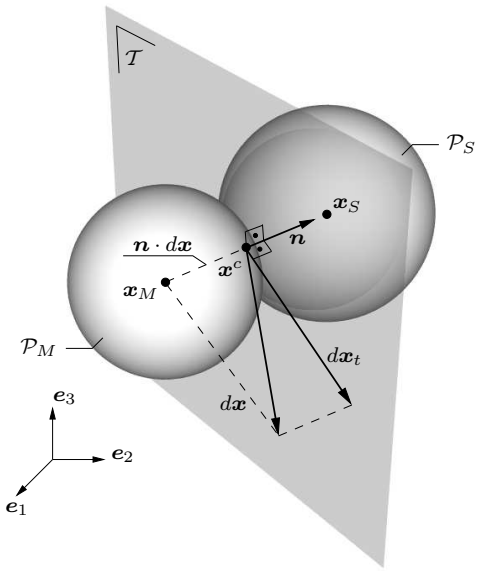

Figure 26: The plane $\mathcal{T}$ tangentially touches the two spheres $\mathcal{P}_M$, $\mathcal{P}_S$ in contact at the contact point $\boldsymbol{x}^c$. The relative incremental displacement $d\boldsymbol{x}$ of the two particles at the contact point is projected onto $\mathcal{T}$ to give $d\boldsymbol{x}_t$.

from the centroids of both particles to their collective contact point $\boldsymbol{x}^c$, the *incremental*

spatial slip vector can be computed as $d\boldsymbol{s}^c = d\boldsymbol{x}_t + d\boldsymbol{\vartheta}_M \times \boldsymbol{r}_M^c - d\boldsymbol{\vartheta}_S \times \boldsymbol{r}_S^c$. Based on this incremental observation, as a basic kinematic variable the *slip rate vector* $\dot{\boldsymbol{s}}^c$ is introduced where in the three dimensional setting here appears as

$$\dot{\boldsymbol{s}}^c = \dot{\boldsymbol{x}}_t + \dot{\boldsymbol{\vartheta}}_M \times \boldsymbol{r}_M^c - \dot{\boldsymbol{\vartheta}}_S \times \boldsymbol{r}_S^c \ . \tag{4.38}$$

The *current slip vector* then follows by integration of the slip rate over the contact time

$$\boldsymbol{s}^c = \int_{t_0^c}^{t} \dot{\boldsymbol{s}}^c \ dt \quad \text{for} \quad c \in \mathcal{A} \tag{4.39}$$

within the time interval $[t_0^c \ ; \ t]$ when the two particles are in contact. Note that at this point in the algorithm the contact unit tangential vector is computed simply by normalization of the slip vector $\boldsymbol{t} = \boldsymbol{s}^c/|\boldsymbol{s}^c|$. Now the total slip is given by $\gamma^c = |\boldsymbol{s}^c|$ and it can be decomposed into *elastic* and *plastic parts* according to

$$\gamma_e^c = \gamma^c - \gamma_p^c \quad \text{for} \quad c \in \mathcal{A} \ . \tag{4.40}$$

In analogy to the constitutive formulation for the contact normal force in equation (4.36), the *contact tangential force* is then assumed to be governed by the constitutive expression

$$\boxed{T^c = \psi_t'(\gamma_e^c) \quad \text{for} \quad c \in \mathcal{A}} \tag{4.41}$$

in terms of a convex constitutive potential $\psi_t = \hat{\psi}_t(\gamma_e^c)$ with initial value $\psi_t'(0) = 0$. This tangential force is again presumed to be bounded by a Coulomb-type *slip criterion function* of the form

$$\phi(T^c, P^c, \beta) = |T^c| - P^c \ \tan[\rho] - \beta \leq 0 \quad \text{with} \quad \beta = \psi_h'(\alpha) \ . \tag{4.42}$$

Here, ρ denotes the angle of interparticle friction and β a cohesion parameter for the interparticle contact. The latter is assumed to be governed by a potential function $\psi_h = \hat{\psi}_h(\alpha)$ in terms of the hardening variable α. The *evolution of the tangential slip* in (4.40) and the cohesive hardening variable in (4.42) are assumed to be governed by

$$\dot{\gamma}_p^c = \lambda \ \frac{T^c}{|T^c|} \quad \text{and} \quad \dot{\alpha} = \lambda \ , \tag{4.43}$$

where the plastic parameter λ is determined by the well-known Kuhn-Tucker-type *loading-unloading conditions*

$$\lambda \geq 0, \quad \phi \leq 0, \quad \lambda\phi = 0 \ . \tag{4.44}$$

This rounds up our constitutive model for the description of the frictional-cohesive tangential contact mechanism for spherical particles in three dimensions. In analogy to the above discussions, the micromechanical model is described by the three fundamental micro-stress force-potential functions ψ_p, ψ_t, ψ_h and the slip criterion function ϕ. These potential functions are particularly specified in the numerical examples section.

Algorithmic Formulation. In what follows, an implicit integration algorithm for the elastoplastic Coulomb-type model in three dimensions is developed similar to that in two

dimensions. The algorithm yields the total slip vector starting from the slip rate given in equation (4.38) in order to determine time-discrete values of the tangential force T^c in the case of active contact. Recall that the arbitrary time interval $[t_n, t_{n+1}]$ is considered where all values at the beginning t_n are known and all variables without a subscript are meant to describe values at the actual time time t_{n+1}. Implicit algorithmic integration of the slip rate vector (4.38) then yields the update of the total slip vector as

$$\boldsymbol{s}^c = \boldsymbol{s}_n + (\boldsymbol{x}_t - \boldsymbol{x}_{tn}) + (\boldsymbol{\vartheta}_M - \boldsymbol{\vartheta}_{Mn}) \times \boldsymbol{r}_M^c - (\boldsymbol{\vartheta}_S - \boldsymbol{\vartheta}_{Sn}) \times \boldsymbol{r}_S^c \tag{4.45}$$

for $c \in \mathcal{A}$. Then (4.45) represents the total relative tangential displacement vector of the two particles at the contact point $\boldsymbol{x}^c$. The norm of $\boldsymbol{s}^c$ gives the total slip, whereas its decomposition gives the elastic part of the slip $\gamma_e^c = \gamma^c - \gamma_p^c$. With respect tp the two dimensional formulation given above, the difference in three dimensions is that the slip is a vector quantity. However, the algorithmic treatment of the norm of the total slip is identical to that of the two dimensional formulation in equations (4.25) – (4.29). With regard to the updates (4.45) and (4.26), the data base

$$\mathcal{H}_n^c := \{\gamma_{pn}^c, \alpha_n;\ \gamma_n^c, \boldsymbol{x}_{Mn}, \boldsymbol{\vartheta}_{Mn}, \boldsymbol{x}_{Sn}, \boldsymbol{\vartheta}_{Sn}, \boldsymbol{s}_n^c\} \tag{4.46}$$

is stored for each interparticle contact at time t_n. The constitutive material models for two and three dimensional contact problems have now been introduced. In order to compute interparticle contact properties, the contact must be determined. Some popular such contact detection algorithms are described in the next section.

4.4. Contact Detection Algorithms

The set of all current possible particle contacts is obtained by so-called *contact detection algorithms* which determine the sets of interparticle contacts (4.14) in two and three (4.35) dimensions. For arbitrary-shaped two dimensional granules, such contact areas of the form (4.11) are determined. Analogously, for circular and spherical particle shapes the penetrations of the form (4.34) are found. Obviously, the determination of the actual sets of contacts, which needs to be performed at each time step in the process, is the major computational bottleneck in discrete element simulations. The contact detection process scales with both the number of objects in the simulation N and the complexity of each object's surface geometry, see also Williams & O'Connor [122]. The latter, i.e. the contact resolution that incorporates the geometry of elliptical and spherical objects, was already addressed in the previous sections. Here, focus will be put on the algorithm that checks for candidates that might be in contact with a particular particle. The easiest but most resource-consuming way of finding these sets of active contacts is to check for possible contacts between each and every particle. For a system of N objects, this detection process scales to an exhaustive number of almost N^2 checks, thus it is of quadratic order $\mathcal{O}(N^2)$. The quality of any detection algorithms must be measured with regard to the order of checks $\mathcal{O}$.

Literature contains several more advanced and sophisticated search algorithms for discrete element simulations which reduce the contact detection effort and hence computing time. For example, Munjiza, Owen & Bićanić [91] investigated the efficiency of several contact detection algorithms introduced next. In general, improvements to the above mentioned simple contact check methods can be gained by assuming a certain coherence between the granular systems at subsequent time steps. That is, the system will evolve

such that new contacts possibly form only with the particles in some confined neighborhood. Thus, computing time can be reduced by computing sets of neighboring particles for each granule. Then only checks between those particles in the neighborhood need to be performed and it might be sufficient to recompute the sets of neighboring particles not at each time step but every $\bar{n}_{step}$ time steps. A good assumption here is that all particles farther away than $d = \bar{n}_{step} \cdot \Delta t \cdot v_{max}$, where v_{max} is the maximum absolute particle velocity in the system, cannot form a contact within the next $\bar{n}_{step}$ time steps. In literature, this kind of structure is termed a *slowly varying topology*, see Williams & O'Connor [122], and is considered to be a reasonable assumption for granular solid materials. Several spatial sorting algorithms that try to reduce detection time exist in literature, for an overview see for example the comprehensive review paper by Williams & O'Connor [122]. The *grid-* and *adaptive grid subdivision methods* uniformly or adaptively divide the

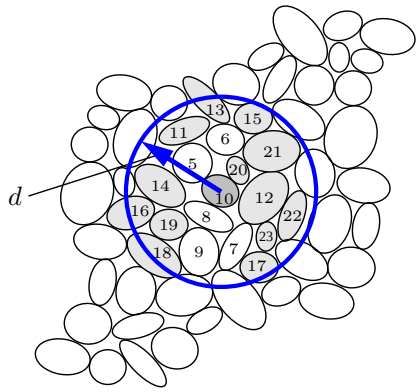

Figure 27: Exemplary Verlet neighbor list for the particle $\mathcal{P}_i$, $i = 10$. Only the granules with centroids within the circular area $d = \bar{n}_{step} \cdot \Delta t \cdot v_{max}$ are considered as possible contacts. For particle $\mathcal{P}_{10}$, only those other particles within the circular area d are *stored* in the Verlet neighbor list which have higher numbers (the grey shaded particles), $\mathcal{P}_j$, $j > 10$. For example, a possible contact between $\mathcal{P}_{10}$ and $\mathcal{P}_8$ would be stored in the neighbor list for particle $\mathcal{P}_8$. Thus, each possible contact in only stored once.

domain into rectilinear grid cells and the particles are attributed to one or (when close to the cell boundaries) more cells. Contact detection is then performed for objects according to their cell affiliations. These methods are sensitive to the homogeneity of the spatial particle distributions. The method was initially developed for monodisperse structures, but was recently extended to arbitrary object sizes and shapes for both two and three dimensions in the work of Williams, Perkins & Cook [123]. The algorithm developed achieves the partitioning with an order of $\mathcal{O}(N)$. These methods are also known as *linked cell methods*. Another efficient method that goes along with the idea of grid subdivision is the no-binary search (NBS) algorithm which stands in contrast to the other binary search methods. The NBS algorithm is described in the work Munjiza & Andrews [90], the advantage is that the contact detection time scales with only $\mathcal{O}(N)$. In the *tree methods* such as the *quadtree-* or the *binary tree* algorithms, the domain is again divided into grid cells but here only those that contain objects are kept. An improvement is given by Bonet & Peraire [14] who developed their so-called *alternating digital tree (ADT)* algorithm for three dimensional geometric searching and intersection problems, capable of finding intersections between several objects. In contrast to the grid subdivision methods mentioned above, in the *body-based cell method* the centroid of a cell (which do not necessarily need to be rectilinear, indeed for obvious reason is often taken to be circular)

is identical with a particle's centroid position. Any objects within this cell are possible contacts and stored in a neighbor list. These neighbor lists are frequently called *Verlet neighbor lists*, especially in conjunction with molecular dynamics simulations of atomistic structures, see the chapters on MD simulations later in this work. Finally, there are spatial sorting algorithms such as the *heapsort* and *quicksort* methods. These methods are mainly used in conjunction with the body-based cell method in order to improve the structure of the neighbor lists. The heapsort algorithm is a simple and relatively fast sorting algorithm that sorts the objects into a tree structure.

4.5. Surface Meshing and Current Volume of the Granular Microstructure

In the penalty-type formulation for the uniform traction boundary constraint, the *initial volume* $|\mathcal{V}|$ of the microstructure in the reference configuration is required. Moreover, if one is interested in not only homogenized macroscopic Lagrangian stresses but also Eulerian ones such as the true Cauchy stresses $\bar{\boldsymbol{\sigma}}$, also the *current volume* $|v|$ of the granular microstructure in the deformed configuration needs to be known. In contrast to continuous structures and due to the finiteness of the discrete elements, this treatment requires a careful consideration of the granular characteristics. In particular, first of all the definition of the volume occupied by the granular microstructure needs to be defined. Secondly, a computational algorithm for the determination of the current volume must be developed. These steps are described below.

4.5.1. Definitions of Surface and Volume of the Granular Microstructure. The volume of the microstructure is evidently bounded by some surface of the microstructure. We define that this surface be determined at discrete points by the actual centroidal positions of the boundary particles. Other approaches could be for example to define a convex hull around the finite particles that make up the microstructure, or the volume occupied by the specific volumes of all particles. But in order to preserve the periodicity of the structure, the surface is defined by only discrete points at the particle positions. This approach ensures that if the microstructure is periodically extended in space, no gaps or overlaps between the unit cells occur. The extension will in turn give another volume which is completely occupied by the solitary volumes of the associated granular microstructures. Hence, periodicity is truly retained. A meshing of these centroidal nodes with triangles (henceforth called facets) then gives the total surface of the microstructure. Thus the total surface is therefore made up of triangles or facets in space, see Figure 28. It is obvious that this surface is discontinuous in space and the computation of the volume is far from being trivial.

4.5.2. Computation of the Actual Volume. So far the actual *volume* $|v|$ is defined by its bounding *surface*. Therefore, it is convenient to transform the elementary definition of the current volume $|v| := \int_{|v|} dv$ of a volume $|v|$ into an integral over the surface of the volume. At first an equal representation of the Eulerian volume integral $|v| = \int_{|v|} \frac{1}{3} x_{i,j} \delta_{ij}\, dv$ is considered where δ_{ij} represents the Kronecker symbol. Transformation of the volume- into a surface integral using the theorem of Gauss gives

$$|v| = \frac{1}{3} \int_{\partial v} x_i n_j da \delta_{ij} = \frac{1}{3} \operatorname{tr}[\int_{\partial v} \boldsymbol{x} \otimes \boldsymbol{n}\; da] \; . \tag{4.47}$$

In this case where a discrete structure is investigated, considering the infinitesimal limit $\int \boldsymbol{n}\; da \to \boldsymbol{a}_q$ on the surface of the microstructure, the calculation of the actual volume v

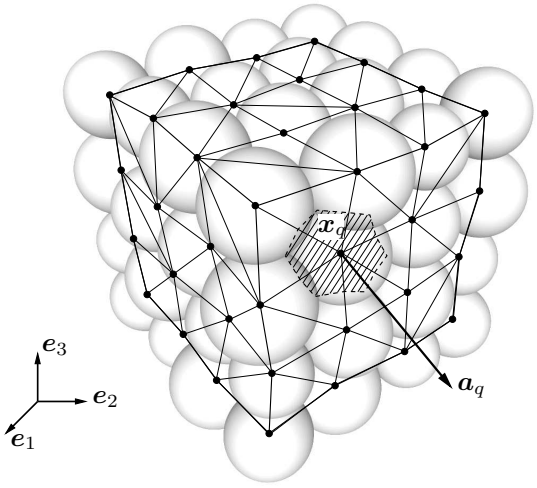

Figure 28: Surface mesh of the granular microstruture. The nodes of the mesh are given by the positions of the boundary particles. The meshing is generated using Delaunay triangulations and the code of Sloan [107], [108]. The area normal vector $\boldsymbol{a}_q$ at node $\boldsymbol{x}_q$ is the vectorial sum of the unit normal vectors of the triangular faces linked to node $\boldsymbol{x}_q$ multiplied by one third of each facet's area, the hatched part in the figure.

of the particle microstructure can be performed using the discrete sum

$$|v| = \frac{1}{3}\,\mathrm{tr}[\sum_{q=1}^{M} \boldsymbol{x}_q \otimes \boldsymbol{a}_q] \quad \text{for } q = 1, \ldots, M \ , \tag{4.48}$$

which, in analogy to the homogenized stress definitions introduced above, only includes quantities associated with the surface of the microstructure, that is, M particles. Here, $\boldsymbol{x}_q$ is the current position of the boundary particle $\mathcal{P}_q$ and $\boldsymbol{a}_q$ is the area vector. The latter is constructed by adding up the unit normal vectors to the associated triangular facets at points $\boldsymbol{x}_q$, multiplied by one third of each facet's area, see Figure 28.

4.5.3. Surface Meshing. Due to constant but slow changes in the arrangements of the boundary particles, the surface is remeshed every couple of load steps. This could be done at each step, but since the focus is put on granular solids with slowly varying topologies, it is sufficient to perform this triangulation after some serious deformations have been computed. The recurring new triangulations ensure the constant validity of the surface mesh. If it was not remeshed, one would eventually end up with corrupt meshes where triangular facets, which are only defined by the particle positions, interpenetrated each other. For the surface meshing, the `FORTRAN` routine `contri` for the computation of constrained Delaunay triangulations in two dimensions is used, based on the works of Sloan in [107] and [108]. The code was provided by the author himself and is hereby gratefully acknowledged.

The meshes are computed separately for each surface of the three dimensional particle assembly. A parallelepiped like the cubic microstructures investigated here possesses six principal surfaces, two in each of the three spatial directions. The particle positions on each such surface are projected onto a fictitious two dimensional plane since `contri` generates two dimensional meshes. This is even more convenient because the two dimensional

calculations are computationally much faster than equivalent three dimensional ones, and only two dimensional triangular meshes are needed. The set of particles which belong to the surface in question is split up into sets on the edges (e.g. that define the edges of the final mesh) and the remaining ones in the interior bulk. The fictitious in-plane coordinates are passed to the meshing routine. It returns the triangulation that is finally used for the computation of the area normals $\boldsymbol{a}_q, q = 1, \ldots, M$ used in equation (4.48). The Delaunay scheme adopted by the meshing routine automatically avoids the formation of long thin triangles and therefore gives good meshes. The time used to compute the meshes is approximately proportional to the number of nodal points and thus scales linearly.

4.6. Time Discretization and Explicit Integration

In this subsection an explicit integration algorithm for the equation of motion is discussed which includes all force vectors that occur in the granular mechanics formulation, that is, contact forces, contact damping forces, body forces as well as the penalty forces. They govern the dynamic relaxation of the transient system. In this section, the relations for global and local damping mechanism are introduced where after each load step relax the dynamic system in further time steps to quasistatic states.

4.6.1. Equation of Motion. Several explicit and implicit time integration algorithms for the semidiscrete differential equation of motion are given for example in Hughes [53]. For a typical particle $\mathcal{P}_p$, this equation reads

$$\boldsymbol{M}_p\ddot{\boldsymbol{x}}_p + \boldsymbol{C}_p\dot{\boldsymbol{x}}_p = (\boldsymbol{f}_c + \boldsymbol{f}_d + \boldsymbol{f}_q + \boldsymbol{f}_g)_p \tag{4.49}$$

with the mass matrix $\boldsymbol{M}_p$ and damping matrix $\boldsymbol{C}_p$ of the particle. $\ddot{\boldsymbol{x}}_p$ and $\dot{\boldsymbol{x}}_p$ are the vectors that contain the acceleration and velocity contributions of the particle. $(\bullet) := d(\bullet)/dt$ denotes the temporal derivative associated with the incremental driving step $[t_n, t_{n+1}]$ of the nonlinear static equilibrium response. The right side of (4.49) consists of the force contributions $\boldsymbol{f}_c$ as the interparticle contact forces, $\boldsymbol{f}_d$ the interparticle damping forces, $\boldsymbol{f}_q$ the penalty correction forces and $\boldsymbol{f}_q$ the body forces of the particle $\mathcal{P}_p$. Typically, the two matrices $\boldsymbol{M}_p$ and $\boldsymbol{C}_p$ are assumed to be lumped and furthermore the damping matrix proportional to the mass matrix, related by a *global damping factor* α_g,

$$\boldsymbol{M}_p := \mathrm{diag}[m_p,\ m_p,\ \theta_p] \quad \text{and} \quad \boldsymbol{C}_p = \alpha_g \boldsymbol{M}_p\ . \tag{4.50}$$

Here, m_p is simply the mass of the particle $\mathcal{P}_p$ computed with the fictitious density ϱ^*, and θ_p represents the mass moment of inertia of the particle with respect to its centroid. For elliptical particles, the mass moment of inertia is computed as $\theta_p = \frac{1}{4}m_p(r_1^2+r_2^2)_p$ where r_1 and r_2 are the two principal radii of the particle under consideration. An explicit, central difference scheme considers the approximations of velocity and acceleration at time t_n for constant time step lengths Δt as

$$\dot{\boldsymbol{x}}_{p,n} = \frac{1}{2}[\dot{\boldsymbol{x}}_{p,n-\frac{1}{2}} + \dot{\boldsymbol{x}}_{p,n+\frac{1}{2}}] \quad \text{and} \quad \ddot{\boldsymbol{x}}_{p,n} = \frac{1}{\Delta t}[\dot{\boldsymbol{x}}_{p,n+\frac{1}{2}} - \dot{\boldsymbol{x}}_{p,n-\frac{1}{2}}] \tag{4.51}$$

where $t_{n-\frac{1}{2}}$ and $t_{n+\frac{1}{2}}$ refer to times instances in the middle of the previous and actual time steps $[t_{n-1},\ t_n]$ and $[t_n,\ t_{n+1}]$, respectively. Insertion into the equation of motion (4.49) evaluated at time t_n gives the update equation of the actual velocity

$$\dot{\boldsymbol{x}}_{p,n+\frac{1}{2}} = \left[(1 - \frac{1}{2}\alpha_g\Delta t)\dot{\boldsymbol{x}}_{p,n-\frac{1}{2}} + \Delta t\boldsymbol{M}^{-1}\boldsymbol{f}\right] / (1 + \frac{1}{2}\alpha_g\Delta t) \tag{4.52}$$

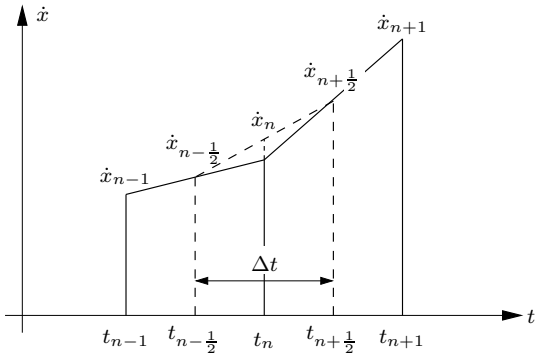

Figure 29: Approximations of velocity and acceleration in the context of the explicit central difference method.

for each particle $\mathcal{P}_p$. Standard integration then yields the actual positions of the particle at the new time t_{n+1} as

$$\boldsymbol{x}_{p,n+1} = \dot{\boldsymbol{x}}_{p,n} + \Delta t \dot{\boldsymbol{x}}_{p,n+\frac{1}{2}}. \tag{4.53}$$

A major advantage with regard to implicit methods is that the equations of motion for each degree of freedom can be integrated independently from the others. Systems of equations do not need to be solved, which gives a fast integration algorithm.

4.6.2. Global Damping Mechanism. Global damping is introduced in the equation of motion (4.52) by the global damping parameter α_g. In literature, many papers deal with the acceleration of relaxation processes in explicitly integrated codes, for example Underwood [116], Park [98] or Papadrakakis [96]. These authors focus mainly on an adjustment of the fictitious mass, the global damping coefficient or the time step length. In Bardet & Proubet [8], an adaptive dynamic relaxation method, especially for granular materials, is developed which eliminates the global artifical damping coefficient and automatically adjusts the other algorithm parameters. In the present work, for simplicity

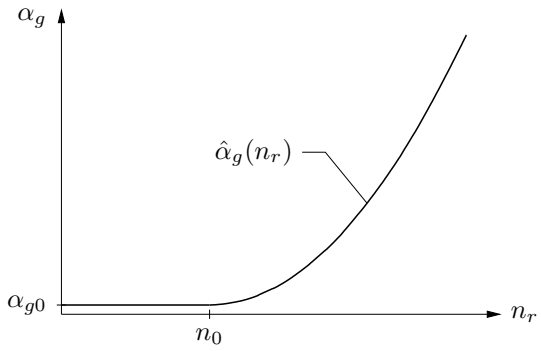

Figure 30: Qualitative illustration of an exemplary variation of the global damping coefficient, here taken as a function of the relaxation step. In the first part of the relaxation process, $n_r < n_0$, only slight damping α_{g0} is introduced. Global damping becomes more effective for $n_r > n_0$ until a static equilibrium state is reached.

the global damping parameter is considered to be a function $\alpha_g = \hat{\alpha}_g(n_r)$ of the relaxation

step $n_r \in \mathbb{N}_+$, which here is taken to be an empirical function of the form

$$\hat{\alpha}_g(n_r) = \begin{cases} \alpha_{g0} & \text{for } n_r \leq n_{r0} \\ \dfrac{1}{\bar{\alpha}}(n_r - n_{r0})^2 + \alpha_{g0} & \text{for } n_r > n_{r0} \ . \end{cases} \tag{4.54}$$

This relaxation model is motivated as follows. Immediately after the load step has been performed, that is when only the homogeneous deformation has been applied by adding the associated displacements onto the current particle positions, the assembly of particles is in a disordered state. Some particles overlap heavily whereas gaps occur between other ones. Slight or no damping at this stage then lets the particles move quicker than in a damped system such that a better ordered state can be reached as fast as possible. Once the relaxation has started, the assembly is in a highly dynamic state, further into the relaxation the particle movements oscillate about their final static positions. Obviously, it would be beneficial if global damping is introduced at this stage. Therefore, the new global damping characteristics of equation (4.54) are introduced. Before the relaxation step n_{r0} is reached, only slight global damping α_{g0} is used as described in order to let the particles move quickly towards new positions. Starting with the relaxation step n_{r0} higher damping is then increasingly introduced by a quadratic function. Here, the factor $\bar{\alpha}$ governs the intensity of the rise in α_g. Such specific coefficients are given in the numerical examples section.

4.6.3. Local Interparticle Damping Mechanism. A second kind of damping is referred to as contact damping. It essentially defines *additional viscous forces* P_v^c and T_v^c at the points where two particles are in contact. In analogy to the definition of the contact normal and tangential forces above, these additional viscous forces are also defined by constitutive potential functions as

$$P_v^c = \psi'_{pv}(\dot{\varepsilon}^c) \quad \text{and} \quad T_v^c = \psi'_{tv}(\dot{\gamma}^c) \quad \text{for} \quad c \in \mathcal{A} \tag{4.55}$$

in terms of the rate $\dot{\varepsilon}^c$ of penetration defined in equation (4.34) as well as the slip rate $\dot{\gamma}^c$ defined in (4.17). The algorithmic counterpart of the constitutive damping potentials (4.55) in a typical time step $\Delta t := t_{n+1} - t_n$ of the relaxation analysis are approximated as

$$\dot{\varepsilon}^c = \frac{1}{\Delta t}(\varepsilon^c_{n+1} - \varepsilon^c_n) \quad \text{and} \quad \dot{\gamma}^c = (\frac{1}{\Delta t}\gamma^c_{n+1} - \gamma^c_n). \tag{4.56}$$

The contact damping force couple is then determined in full analogy to the contact force couple, see above. The additional viscous damping forces enter the damping force vector $\boldsymbol{f}_d$ described below and thus the right hand side of the differential equation of motion.

4.6.4. Particle Force Vectors. The contact normal and tangential forces derived in the previous chapter are transferred to the centroids of the respective particles by means of equilibrium considerations. Also, the particle force vector for two dimensional analyses consists of two forces and one force couple, see 31. Analogously, in three dimensions it has six entries, three forces and three couples. Consequently the contact force vector $\boldsymbol{f}_c$ and

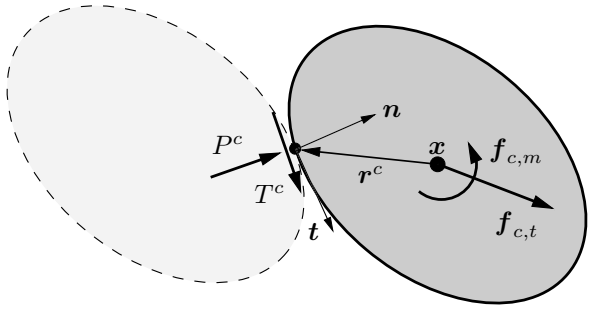

Figure 31: Contact normal and tangential forces P^c and T^c and associated particle contact force vector $\boldsymbol{f}_c$ that contains the translatoric forces $\boldsymbol{f}_{c,t}$ and the force couple $\boldsymbol{f}_{c,m}$ at the centroid of a typical particle.

the contact damping force vector $\boldsymbol{f}_d$ for each particle arise in terms of the contact unit normal $\boldsymbol{n}$, contact unit tangential $\boldsymbol{t}$ and the position vector $\boldsymbol{r}^c$ as

$$\boldsymbol{f}_c = \begin{bmatrix} (P^c\boldsymbol{n} + T^c\boldsymbol{t}) \\ \boldsymbol{r}^c \times (P^c\boldsymbol{n} + T^c\boldsymbol{t}) \end{bmatrix} \quad \text{and} \quad \boldsymbol{f}_d = \begin{bmatrix} (P_v^c\boldsymbol{n} + T_v^c\boldsymbol{t}) \\ \boldsymbol{r}^c \times (P_v^c\boldsymbol{n} + T_v^c\boldsymbol{t}) \end{bmatrix} \tag{4.57}$$

Now that the micromechanical model, the equation of motion and the homogenization technique for granular microstructures are known, in the next chapter several numerical examples that deal with granular microstructures with elliptical, circular and spherical particles in two and three dimensions will be discussed.

5. Numerical Simulations of Granular Microstructures

In this section, the homogenization technique for granular microstructures is applied in several numerical examples in two- and three dimensions. First of all, some key characteristics of plane elliptical particles are numerically analyzed before deformations of two- and three dimensional granular microstructures with spherical and arbitrary plane granules are investigated.

5.1. Computational Setup

At first a study of some representative two dimensional numerical examples of elliptically-shaped particles is performed. The elliptical shape is approximated by polygons of $n = 20$ segments. In what follows, different particle microstructures which undergo certain prescribed deformation modes in deformation-controlled frames are analyzed. The results are compared and the bound character of the three classical boundary conditions clearly verified.

5.1.1. Constitutive Force-Potential Functions. For a comprehensive presentation of the numerical results, the constitutive force-potential functions, which in section 4 where symbolically introduced, need to be specified. Generally, these potential functions are taken to be *quadratic* giving linear force-displacements relations. An exception is the potential function ψ_p that governs the constitutive normal force-displacement model. In the case of two dimensions it is also assumed to be quadratic, but in three dimensions a Hertzian root-relation is assumed, see HERTZ [48],

$$\psi_p^{2D} = \frac{1}{2} c_p (\varepsilon^c)^2 \ , \quad \psi_p^{3D} = \frac{3}{2} c_p (\varepsilon^c)^{\frac{3}{2}} \ , \quad \psi_t = \frac{1}{2} c_t (\gamma_e^c)^2 \ , \quad \psi_h = \frac{1}{2} h \alpha^2 \ . \tag{5.1}$$

The potentials are given in terms of the three physical parameters c_p, c_t and h for the quasistatic response outlined in section 4.2. In connection with the interparticle friction angle ϱ in the Coulomb-type slip criterion functions (4.21) and (4.42),

$$\phi(T^c, P^c, \beta) = |T^c| - P^c \ \tan[\rho] - \beta \leq 0 \ , \tag{5.2}$$

the potentials govern the micromechanical response of the interparticle contact. Furthermore, the potential functions governing the artificial local damping mechanism outlined in section 4.6.3 are also adopted to be a *quadratic* functions of the form

$$\psi_{pv} = \frac{1}{2} c_{pv} (\dot{\varepsilon}^c)^2 \ , \quad \psi_{tv} = \frac{1}{2} c_{tv} (\dot{\gamma}_e^c)^2 \tag{5.3}$$

for both the two and three dimensional numerical examples. These damping potentials are specified in terms of the two local parameters c_{pv} and c_{tv} where these two additional parameters are presumed to be proportional to the contact damping coefficients c_p and c_t, related by the parameter α_c in the sense

$$c_{pv} = \alpha_c c_p \quad \text{and} \quad c_{tv} = \alpha_c c_t. \tag{5.4}$$

These parameters govern, in connection with the global parameters ϱ^* and α_g in equation (4.52), the dynamic regularization of the quasistatic response of the granular microstructures.

5.1.2. Fabric Measures in Rigid Particle Structures. For all microstructures considered in the subsequent sections, so-called fabric measures are the *volume density* $\tilde{\varrho}$, *void ratio* e and *porosity* p, which can be calculated as

$$\tilde{\varrho} = \frac{|v_f|}{|\mathcal{V}|} \; ; \quad e = \frac{|v_v|}{|v_f|} \; ; \quad p = \frac{|v_v|}{|\mathcal{V}|} \; . \tag{5.5}$$

Here, $|\mathcal{V}|$ is the initial total volume of the microstructure, $|v_f|$ the portion of $|\mathcal{V}|$ that is occupied by the particles themselves and $|v_v|$ the void part. These fabric measures are commonly used to characterize granular microstructures. The *volume density* $\tilde{\varrho}$ relates the particle volume to the total one and thus gives the density of the microstructure. Consequently, the *void ratio* e describes a relation between the volume that is occupied by the particle masses and the volume of the microstructure which is unoccupied. Finally, the porosity p relates unoccupied and total volumes of the granular microstructure. As a further important micromechanical measure, the actual *average coordination number* $\bar{n}_c$ should be evaluated. This value is the mean average of the number of current contacts that the particles in the assembly at the current time possess,

$$\bar{n}_c := \frac{1}{N} \sum_{i=1}^{N} n_{c,i} = \frac{2}{N} \cdot n_{c,tot} \; , \tag{5.6}$$

where $n_{c,tot}$ denotes the *total* number of current contacts and $n_{c,i}$ is the number of actual contacts that the particular granule $\mathcal{P}_i$ is in contact with at the current time. N is the total number of particles in the microstructure. For the three dimensional granular microstructures, the initial void ratios $e_0 = |\mathcal{V}_v|/|\mathcal{V}_f| = \tilde{\varrho}^{-1} - 1$ will also be given. Here, $|\mathcal{V}_v|$ denotes the part of the total reference volume $|\mathcal{V}|$ not filled with particle matter, and $|\mathcal{V}_f|$ specifies that part of $|\mathcal{V}|$ filled with particle matter. Experimental results suggest unique relations between the average coordination number and the void ratio independent of the distribution of the particle sizes, though its general validity is still in question, see also the work Nemat-Nasser [93]. Literature contains further such fabric measures such as the *average branch length*, *density of contacts* and other vectorial measures. For an overview the reader is refered to the above mentioned work.

5.2. Numerical Examples in 2D: Key Characteristics

In order to prove the functionality of the micromechanical model introduced in the previous section, two numerical examples in two dimensions are presented. Apart from any homogenization computation these examples particularly confirm that the computational model for the interparticle contact of elliptical particles is suitable for the simulation of such granular shapes.

5.2.1. Elliptical Particle under Gravity onto an Inclined Plane. As an introductory example, a single elliptical particle is considered where under the influence of gravitation $g = 9.81 \; m/s^2$ falls onto an inclined plane as shown in Figure 32. The initial velocity of the particle is zero. The physical parameters used for this computation are given in Box 3 and the technical simulation parameters in Box 4. The use of such elliptical particles is based on the fact that the elliptical shape itself represents a generalization of the simple circular shape that is really a rigorous simplification of real-world granules. Experimental observations have shown that particle rolling is the major microscopic de-

Box 3: Physical Parameters

normal stiffness	c_p	=	10^8
tangential stiffness	c_t	=	10^8
linear hardening	h	=	10^4
interparticle friction angle	ϱ	=	30^o
fictitious density of discs	ϱ^*	=	100.0

Box 4: Technical Parameters

contact damping	α_c	=	0.001
global damping	α_g	=	1.0
time step length	Δt	=	0.01

formation mechanism, as opposed to the general assumption of particle sliding which is actually not the major deformation mechanism. Indeed, sliding occurs only at very few interparticle contacts, see NEMAT-NASSER [93]. In Figure 32, the initial configuration when the particle hits the inclined plane and the final static configuration of the one particle example are illustrated. Unlike circular particles, which would simply roll down the plane, the elliptical particle reaches a stationary state if enough friction is activated between the two bodies in contact. Evidently, this frictional force prohibits the particle from sliding down the plane.

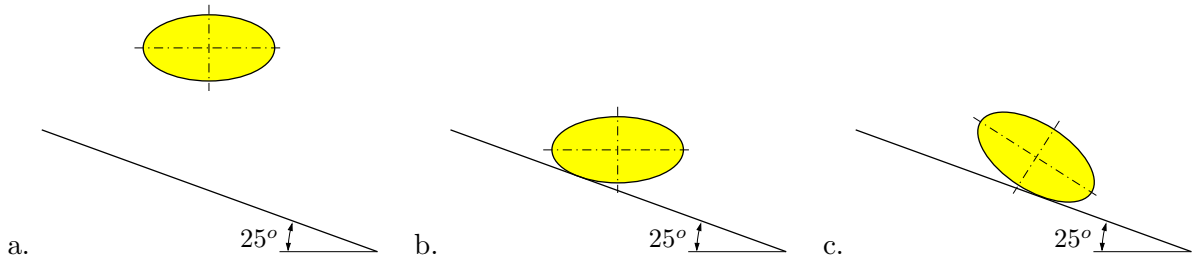

Figure 32: An elliptical particle falling onto a 25^o-degree inclined plane, a. initial configuration, b. particle first contacts plane, c. final static state. In contrast to circular particles, if enough friction is computed, the particle does not slide or roll down the plane. Observe that clearly in the final state the principal axis is not parallel to the plane.

5.2.2. Free Gravitational Motion of a Heap of Particles. Secondly, an assembly of elliptical particles as shown in Figure 33 under the influence of gravitational forces with $g = 9.81$ is considered. This could for example be a heap of granules bounded by lateral walls where these walls are then removed so that a free motion under gravitational load occurs. The two dimensional assemblies of elliptical granules were drawn up digitally with the aid of the CAD software package AutoCAD, and the data was then exported. At first the left and bottom surfaces were constructed and then copied such that equal and opposite surfaces were obtained, ensuring periodicity. Care needs to be taken when constructing the surface frame, because the particle centroids must not lie on a straight line so that artificial load paths cannot be *a priori* dictated. Secondly, this boundary frame was then filled with arbitrary elliptical particles. The CAD data was then read into the granular code and, with fixed boundary frame, some relaxation steps were performed

such that the bulk particles could reach a quasistatic configuration without any resulting forces on the particles in the bulk. The minimum principal radius of the elliptical particles is $r_{min} = 10$, the maximum principal radius $r_{max} = 31$ units. The aspect ratios r^r between the two principal radii range from almost circular particles with $r^r_{min} = 1.2$ up to very lengthy elliptical shapes with $r^r_{max} = 3.1$. The particles of the assembly fall onto a horizontal rigid plate, forming a complex evolution of particle interactions. It is characterized by many contacts which form and break during the deformation process. Initially, all particle velocities and accelerations are zero. Here, the same physical and technical parameters as in the previous example, see the Boxes 3 and 4, are employed.

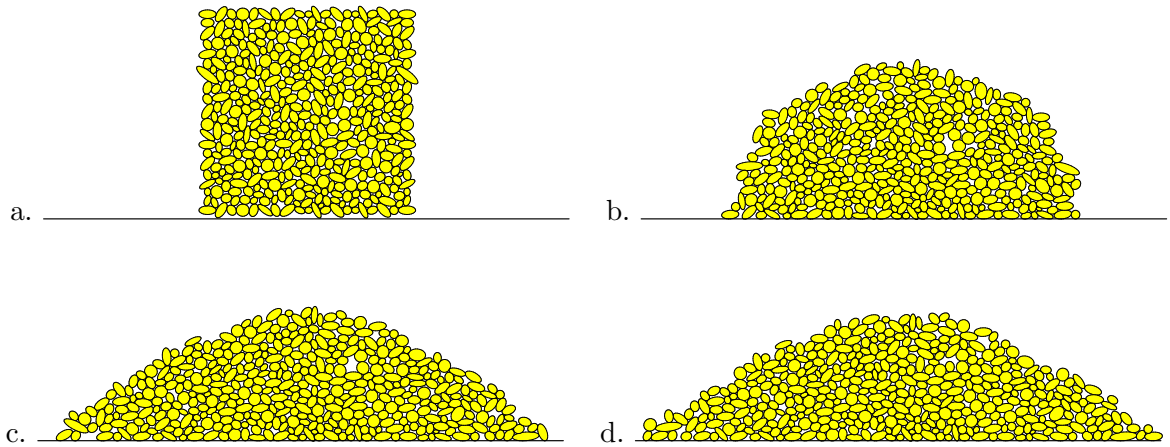

Figure 33: Heap of 433 elliptical particles under dead load: a. Initial configuration $t = 0$, b. deformed configuration at $t = 75$, c. deformed configuration at $t = 375$ and d. final static deformed configuration at $t = 750$ where a slope angle of 30^o was obtained.

In the end, the particles reach a final static state where the angle of the slope reflects the interparticle friction angle $\varrho = 30^o$. In Figure 33 the initial and three more deformation states are depicted, where the last picture shows the final state where all particles have reached a static equilibrium state. With these two introductory examples, the robustness and capability of the interparticle contact model for arbitrary-shaped particles has been proved. In the following section, the focus is put on the mechanical evolution of particle microstructures and the homogenization of associated microscopic quantities.

5.3. Numerical Examples in 2D: Microstructures with Elliptical Particles

In the interparticle contact model presented in section 4, a constitutive relation is developed that does not include cohesive or attractive forces between the granules since in practice almost all granular materials deform not in tension but compression. Hence, in order to study quasistatic properties of granular solids, several deformation modes are investigated which above all set the granular microstructure under (initial) compressive stresses. In contrast, if tensile stresses were imposed, the structure would disintegrate and no quasistatic states would be reachable.

5.3.1. Compression-Shear for a Rectangular, Periodic Microstructure. This example is concerned with an aggregate of 256 elliptical particles as shown in Figure 34. The initial total volume of the microstructure is $|\mathcal{V}| = 387576.34$ square units and the volume density of the assembly is characterized by $\tilde{\varrho} = 0.84$, adding up to a porosity of $p = 0.16$. The void ratio follows as $e = 0.19$. Each side of the rectangular, periodic boundary

Box 5: Physical Parameters

normal stiffness	c_p	=	10^8
tangential stiffness	c_t	=	10^8
linear hardening	h	=	10^4
interparticle friction angle	ϱ	=	20^o
fictitious density of discs	ϱ^*	=	1000.0

Box 6: Technical Parameters

contact damping	α_c	=	0.01
penalty force factor	ϵ_f	=	10^{10} / 10^6
penalty couple factor	ϵ_c	=	10^{10}
time step length	Δt	=	$7.5 \cdot 10^{-3}$
load increment	$\Delta\lambda$	=	0.01

frame consists of 15 particles totaling up to 56 particles forming the driving frame of the granular microstructure. The physical and technical parameters used in this simulation are denoted in Boxes 5 and 6, respectively. Note that the penalty force factor is chosen as $\epsilon_f = 10^{10}$ for the simulations with the boundary conditions of displacement- and periodic types and as $\epsilon_f = 10^6$ for the uniform traction boundary conditions. This difference follows from the nature of the applied boundary conditions. The contraints for linear displacements and periodic deformations represent boundary conditions of deformation-type constraints, i.e. Dirichlet conditions, whereas the uniform traction conditions represent von Neumann stress boundary conditions. The different nature of boundary constraints calls for different penalty factors ϵ_f which in the algorithm are multiplied with the constraints. The global damping function (4.54) is governed by the parameters $n_{r0} = 50$, $\alpha_{g0} = 0.01$ and $\bar{\alpha} = 200.0$. They ensure that global damping $\alpha_g = (n_r - n_0)^2/200$ is applied once 50 relaxation steps are performed. The deformation is applied in 210 load steps of $\Delta\lambda$. At first, a biaxial compression mode $\bar{\boldsymbol{F}}_{comp}$ is applied in 10 load steps of $\Delta\lambda$ until a state $\lambda_0 = 0.1$ is reached. Then the compression state is held and a simple shear mode $\bar{\boldsymbol{F}}_{shear}$ is applied in 200 load steps of $\Delta\lambda$. The deformation modes read

$$\bar{\boldsymbol{F}}_{comp} = \boldsymbol{1} + \lambda \begin{bmatrix} -0.05 & 0 \\ 0 & -0.05 \end{bmatrix}, \quad \bar{\boldsymbol{F}}_{shear} = \boldsymbol{1} + \begin{bmatrix} -0.005 & (\lambda - \lambda_0)0.5 \\ 0 & -0.005 \end{bmatrix} \tag{5.7}$$

Each load step is followed by n_{rel} relaxation time steps which relax the structure to stationary quasistatic states. Figure 37a depicts the varying numbers of relaxation steps executed after each load step required to reach this static state. Here, the global relaxation procedure, as outlined in section 4, is applied where the global relaxation factor is assumed to be a function of the relaxation step, $\hat{\alpha}_g(n_{rel})$. In Figure 37b the mean kinetic energy

$$E_{kin} = \frac{1}{2N} \sum_{p=1}^{N} \dot{\boldsymbol{x}}_p^T \boldsymbol{M}_p \dot{\boldsymbol{x}}_p \tag{5.8}$$

of the assembly for the $N = 256$ particles in some representative load steps in the time interval $[100,\ 120\ s]$ is plotted. This curve is obtained from the simulation with periodic

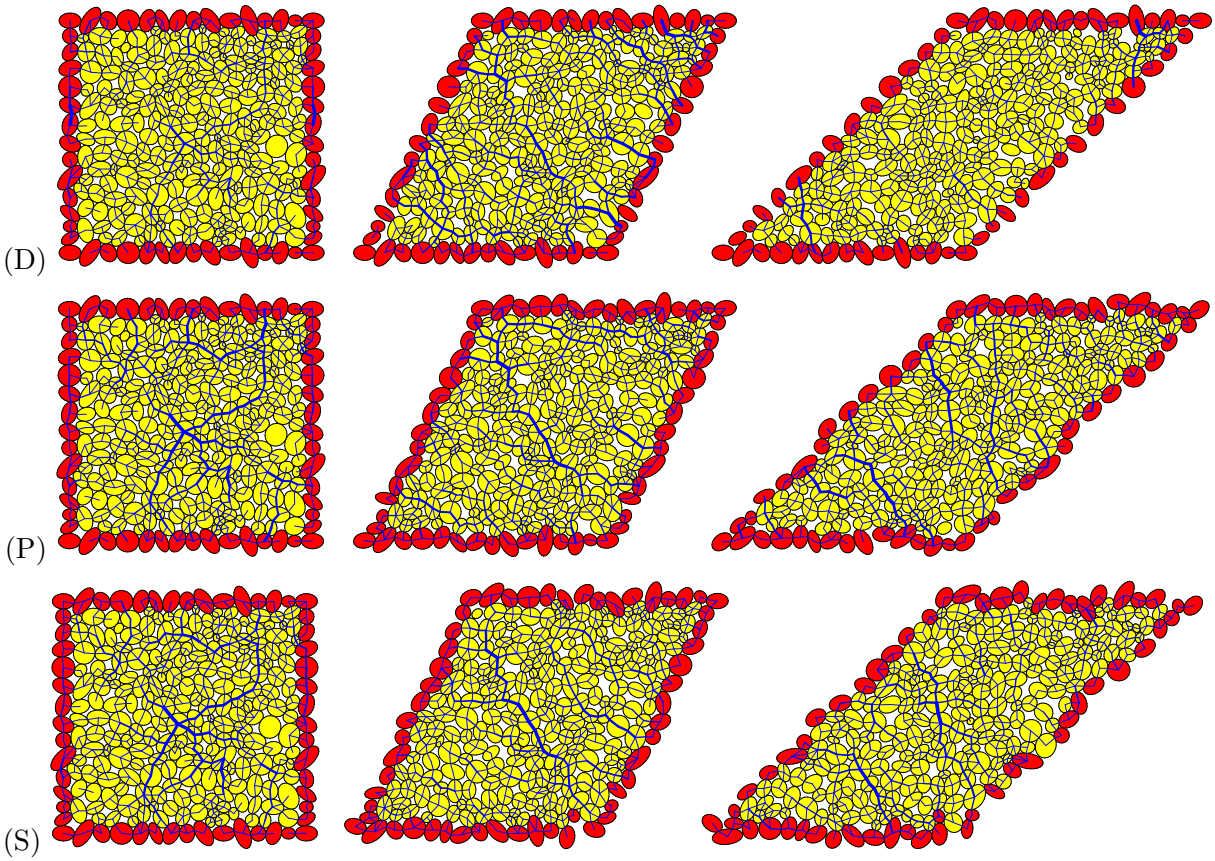

Figure 34: Irregular package of 256 discs under an initial biaxial compression mode followed by simple shearing. Displayed are the deformation states at the end of the compression mode/ beginning of shear deformation at $\bar{F}_{12} = 0.0$, $\bar{F}_{12} = 0.5$ and $\bar{F}_{12} = 1.0$ for the new class of three boundary conditions. Furthermore, the branch mesh of contact normal forces is qualitatively drawn in the deformed pictures.

boundary constraints. One can clearly see that at the end of each load step the mean kinetic energy always reaches a zero level and hence quasistatic states are gained. In Figure 34 three particular deformation states are displayed, namely at the end of the compression mode/ beginning of shear deformation characterized by $\bar{F}_{12} = 0.0$ and $\bar{F}_{11} = -0.005$, during deformation at $\bar{F}_{12} = 0.5$ and at the end of the deformation process $\bar{F}_{12} = 1.0$ for (D) linear displacements on the boundaries, (P) periodic deformations on opposite boundary particles and (S) uniform tractions on the boundaries. The contact normal forces displayed in the pictures give a qualitative illustration of the forces acting between the particles. This network of forces is frequently called a *branch mesh* of the granular microstructure. The width of the lines connecting the centroids of the particles correspond to the absolute value of the interparticle contact force. From these force visualizations the formation of so-called solid-paths can clearly be seen. The notion of these paths were introduced by Horne [50]. Some neighboring particles form a load line where the main forces are transmitted through the microstructure, that is, the main load is not transmitted uniformly through the heterogeneous structures but only by a few granules. Therein, gaps between particles do not occur which motivates the notion of *solid paths*. In Figure 35a. the homogenized macroscopic normal stress $\bar{\sigma}_{11}$ during the initial compression mode $\bar{\boldsymbol{F}}_{comp}$ is depicted. In this figure the bound character of the three boundary conditions already becomes obvious: the response of the periodic constraints lies in between the ones

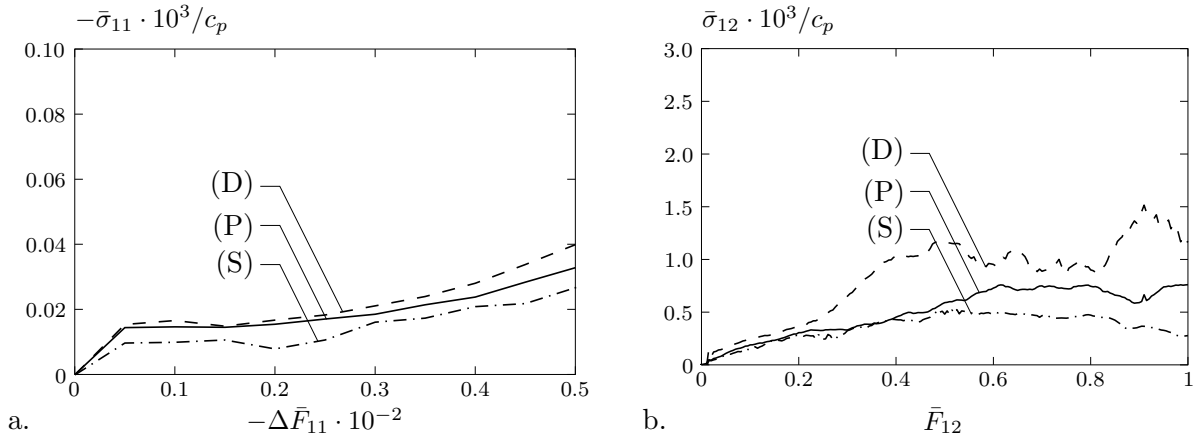

Figure 35: Homogenized macroscopic compressive stresses $-\bar{\sigma}_{11}$ versus initial compression $\Delta\bar{F}_{11}$ and macroscopic shear stresses $-\bar{\sigma}_{12}$ versus macroscopic shear deformation $\bar{F}_{12}$, respectively, for the three boundary conditions (D) linear displacements, (P) periodic deformations of opposite boundary particles and (S) uniform tractions on the surfaces.

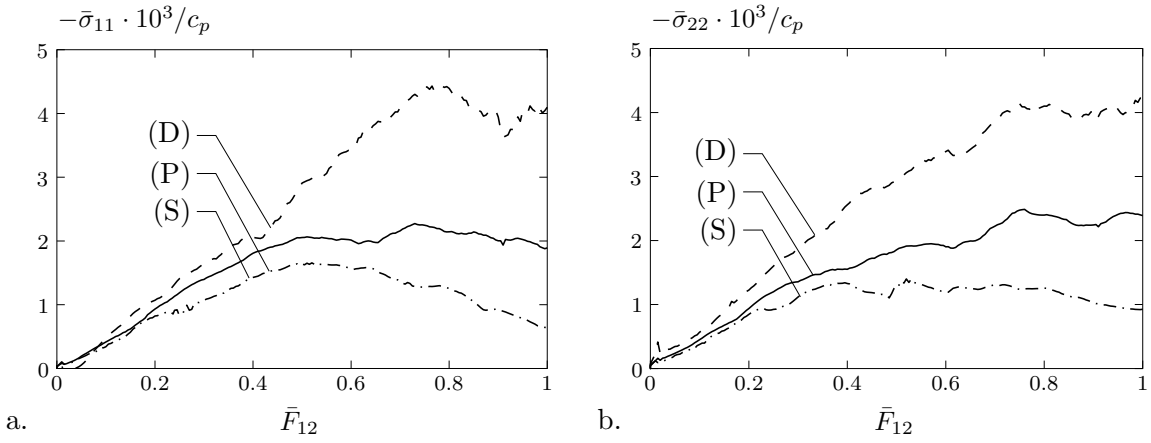

Figure 36: Homogenized macroscopic compressive stresses $-\bar{\sigma}_{11}$ and $\bar{\sigma}_{22}$ versus macroscopic shear deformation $\bar{F}_{12}$ for the three boundary conditions (D) linear displacements, (P) periodic deformations of opposite boundary particles and (S) uniform tractions on the surfaces.

from linear displacements (upper bound) and uniform tractions (lower bound). Figure 35b depicts the shear stress $\bar{\sigma}_{12}$ that develops during the simple shear deformation mode. Here the bound character can also be observed. In Figure 38 the rose diagrams that develop during deformation of the granular structure are shown. Rose diagrams are polar diagrams of the distributions of the contact unit contact normal vectors. In the figure, the rose diagrams correspond to deformation states at initial compression modes a $\bar{F}_{11} = \bar{F}_{22} = 0.0$, b $\bar{F}_{11} = \bar{F}_{22} = 0.5$ marking the beginning of simple shearing, and during simple shear mode c $\bar{F}_{12} = 0.25$, d $\bar{F}_{12} = 0.5$, e $\bar{F}_{12} = 0.75$ and f $\bar{F}_{12} = 1.0$ for the case of periodic deformations on opposite boundary-frame particles. Results for the other two boundary constraints are not plotted since they strongly resemble the results shown for periodic deformations. The diagrams plotted represent the number of unit contact normals for each load step. The orientations are summed over ranges of ten degree (10^o) and averaged with respect to the number of relaxation steps associated with the load step under consideration. Initially, the distribution of the contact normals is isotropic. This isotropy remains throughout the initial short compression mode, as one would expect. It

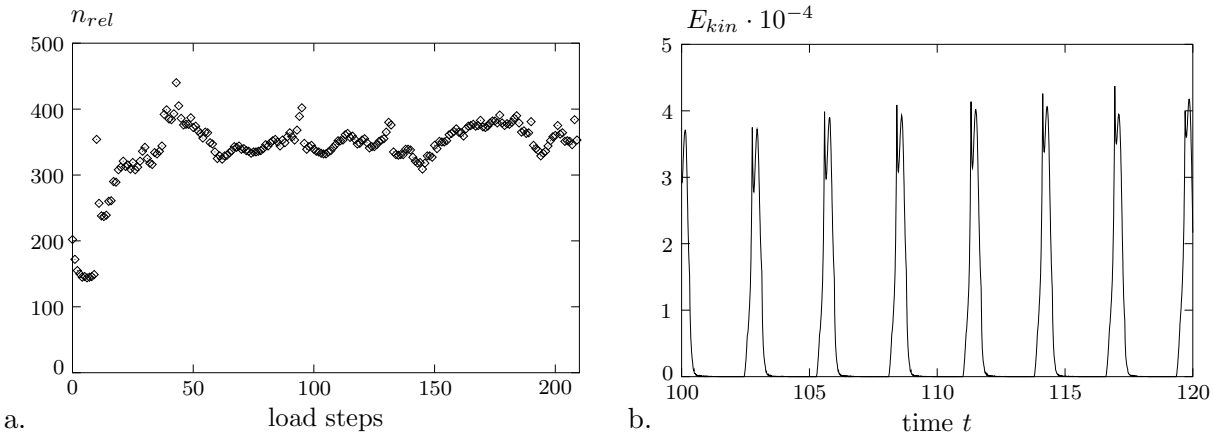

Figure 37: a. Number of relaxation steps n_{rel} versus load steps, b. mean kinetic energies E_{kin} in the time interval [100, 120 *sec*] for the case of periodic deformations for the simulation of the rectangular microstructure with 256 particles.

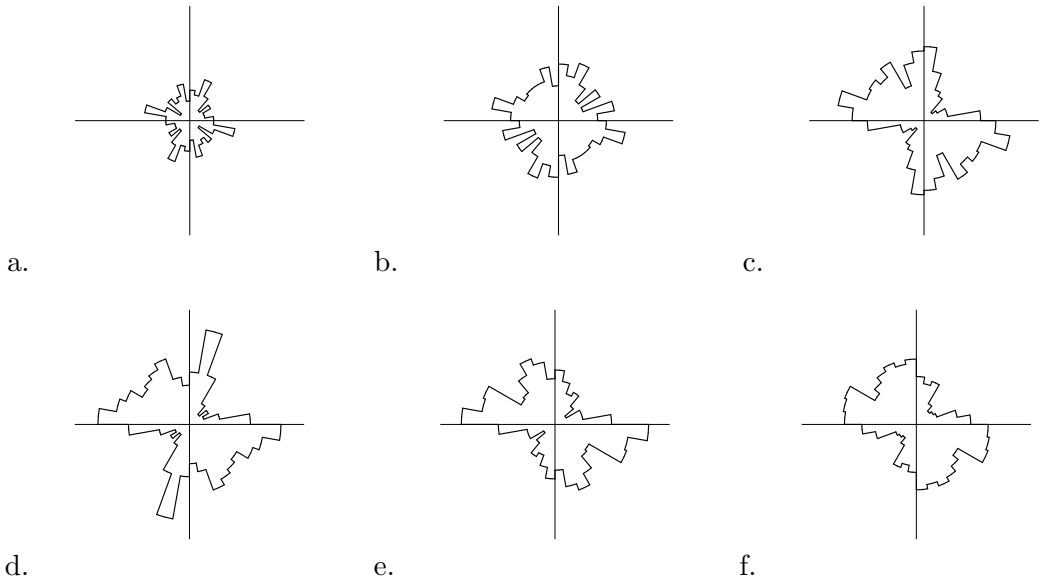

Figure 38: Rose diagrams of the distributions of the unit contact normals at initial compression modes a. $\bar{F}_{11} = \bar{F}_{22} = 0.0$, b. $\bar{F}_{11} = \bar{F}_{22} = 0.5$ marking the beginning of simple shearing and c. $\bar{F}_{12} = 0.25$, d. $\bar{F}_{12} = 0.5$, e. $\bar{F}_{12} = 0.75$ and f. $\bar{F}_{12} = 1.0$ for the case of periodic deformations. The results agree well with the changes of fabric experimentally measured on rod-like photoelastic granules by Konishi [61].

develops strong bias as the microstructure is sheared. As was experimentally shown in Oda, Konishi & Nemat-Nasser [94], the evolution of the fabric is closely related to the variation in the distribution of contact normals. Note that shearing produces a biased distribution as the particles slide and roll on each other. This fabric or induced anisotropy is at the basis of the micromechanics of the deformation of granular materials. Observe that this fabric strongly influences the dilatancy in frictional granules, see for example Nemat-Nasser [93] and the references therein. By further shearing the assembly, the distribution of contact normals changes such that a greater concentration of the unit normals along the direction of maximum principal compression is attained. Note that the average direction of these contact normals tends to concentrate in the direction of the

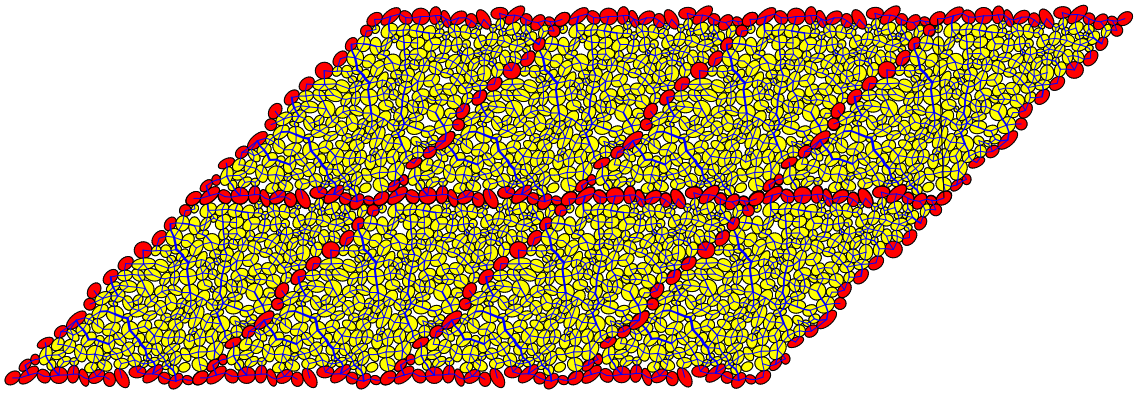

Figure 39: Assembly of eight deformed periodic unit cells of the irregular elliptical particle aggregate at a shear deformation $\bar{\boldsymbol{F}}_{12} = 1.0$. Obviously, the periodicity constraints for the particle fluctuations $\boldsymbol{w}^- = \boldsymbol{w}^+$ and rotations $\vartheta^- = \vartheta^+$ on the surfaces of the unit cells are satisfied and thus compatibility is ensured.

principal compressive force trajectories (solid paths as discussed above), see Figure 34, which results in the observed strong fabric anisotropy. Figure 39 illustrates a composition of eight deformed periodic plane microstructures that proves the compatibility of the periodicity constraints.

5.3.2. Compression followed by Cyclic Shear Loading. Now the same microstructure is again deformed using the same initial compression mode, followed by a simple shear mode applied cyclically, where the shear increases up to maximum values $\lambda - \lambda_0 = 0.5$ and then linearly decreases until $\lambda - \lambda_0 = 0.0$. Then this cycle is started all over again, giving the so-called *sawtooth* load function. In Figure 40 the homogenized macroscopic shear stresses $\bar{\sigma}_{12}$ and the normal stresses $-\bar{\sigma}_{22}$ that develop during the shearing process are depicted versus the homogeneous shear deformation mode applied. The picture illustrates the curves of the three boundary conditions discussed. Here, only the first shear load cycle is depicted. The shear stresses of the traction- and the periodic boundary conditions yield similar results, whereas the linear displacement conditions give a stiffer response. At the beginning of the unloading process (after the peak of the shear stress) a strong decay in stresses occurs where this unloading part can be considered to be elastic. Also, when the shear is completely unloaded, negative stresses remain. Another cycle would then immediately yield a stiff elastic behavior such that the response of the next cycle falls together with that from the first cycle. For the sake of clarity, the next cycles are left out in the picture. Interestingly, a negative normal stress $\bar{\sigma}_{22}$ also remains at the end of the first shear cycle. These remaining stresses are due to the fact that during the loading phase the particles are finitely displaced and a rearrangement of the configuration of the particle microstructure occurs. Then during unloading the aggregate is again rearranged where the initial state is not obtained. A different state is reached, which obviously yields the different stress states.

5.3.3. Compression-Shear for Circular, Nonperiodic Microstructures. The third subsection deals with microstructures of circular shape. It is mainly chosen because in the homogenization approach, it is assumed that granular microstructures of some shape are attached at macroscopic points $\bar{\boldsymbol{X}}$, see section 3. Hence, circular microstructural shapes would be the first and self-evident choice. On the other hand, circular microstructures can obviously not be extended periodically, therefore only deformations under linear

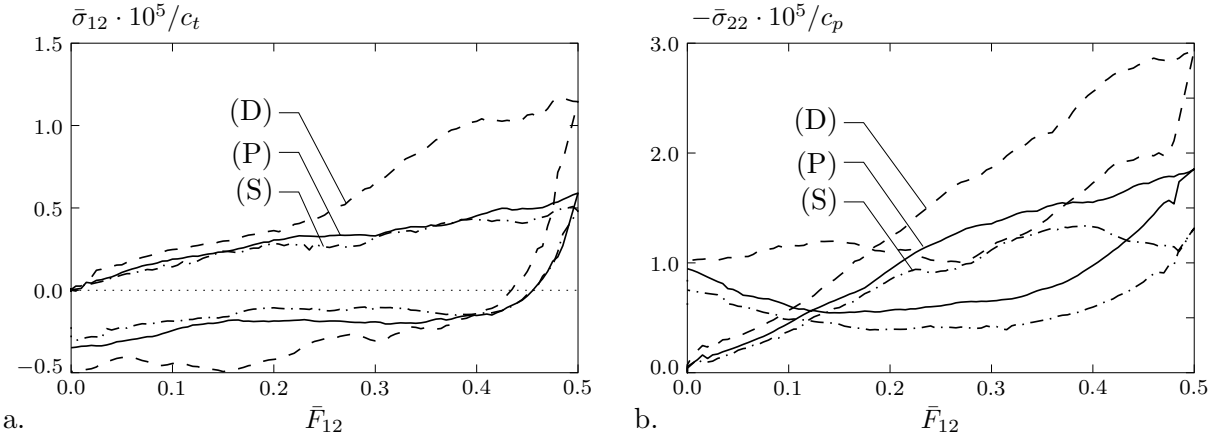

Figure 40: Rectangular microstructure of 256 particles under cyclic shear loading: a. shear stresses $\bar{\sigma}_{12}$ versus shear deformation $\bar{F}_{12}$, b. normal stresses $\bar{\sigma}_{22}$ versus shear deformation $\bar{F}_{12}$ for the three types of boundary conditions (D) linear displacements on the boundaries, (P) periodic deformations on opposite particles and (S) uniform stresses on the boundaries. Displayed are the normalized stresses for one load cycle.

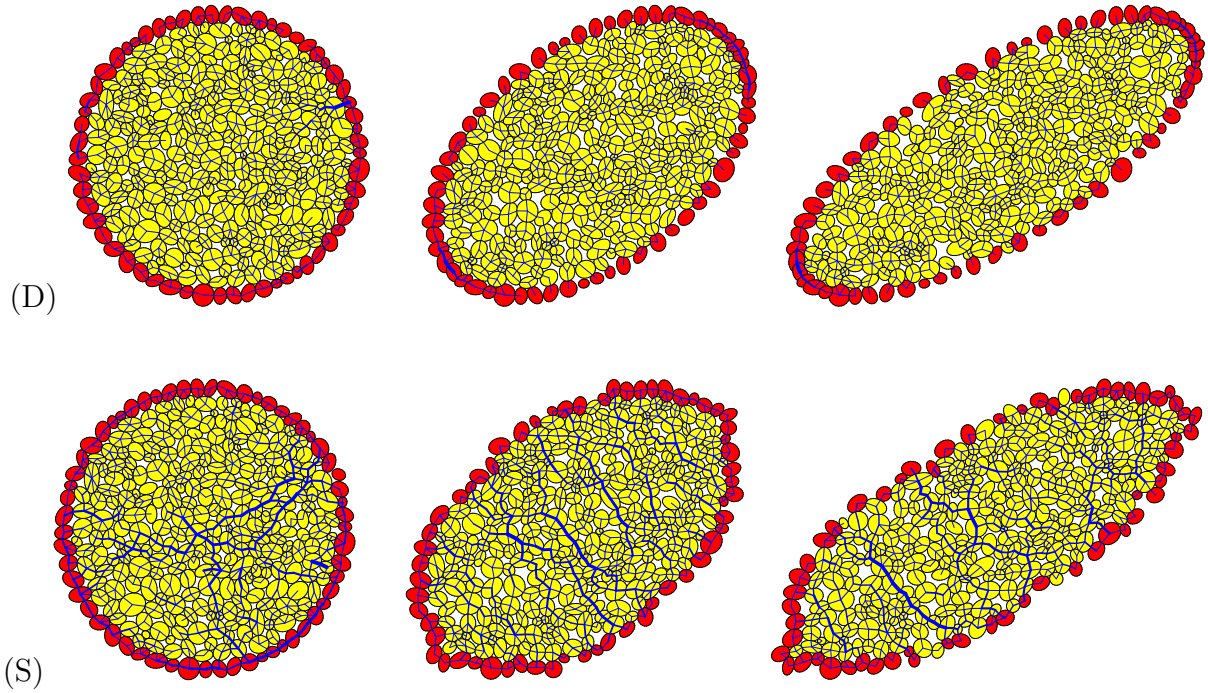

Figure 41: Irregular circular package of 305 elliptical particles under an initial biaxial compression mode followed by simple shearing. Here, three deformation states are shown, at the end of the compression mode/ beginning of shear deformation $\bar{F}_{12} = 0.0$, at $\bar{F}_{12} = 0.5$ and at $\bar{F}_{12} = 1.0$ for (D) linear displacements on the boundary and (S) uniform tractions on the boundaries. A circular microstructure cannot be continued periodically, therefore this boundary condition is not investigated. In the pictures of the deformed configurations the branch meshes of the contact normal forces are qualitatively drawn.

displacement- and uniform traction boundary conditions are calculated and investigated. In what follows, two circular assemblies are simulated with different numbers of particles. The assembly depicted in Figure 41 consists of a particle microstructure of 305 elliptical particles. In the stress diagrams to be discussed, the curves for a similar assembly of only 161 particles are also considered (the small assembly is not depicted in figures).

The initial total volume of the assembly with 305 particles is $|\mathcal{V}| = 442704$ units, for the smaller assembly with 161 particles it adds up to $|\mathcal{V}| = 220999.26$ square units. The volume density of both assemblies is equally $\tilde{\varrho} = 0.85$ adding up to a porosity of $p = 0.15$, and the void ratio follows as $e = 0.18$. The boundary frame is composed of 59 particles for the large example and 42 granules for the second one. Thus the interior domains are built by 246 and 119 particles, respectively. Here, in order to obtain comparable results, the physical and technical simulation parameters from the previous example are used, see Boxes 5 and 6. Also, the same deformation process and relaxation function are used, see equation (5.7). In Figure 41 three deformation states are displayed. The first one depicts the structure at the end of the compression mode/ beginning of shear deformation characterized by $\bar{F}_{12} = 0.0$ and $\bar{F}_{11} = \bar{F}_{22} = -0.005$, during deformation at $\bar{F}_{12} = 0.5$ and at the end of deformation $\bar{F}_{12} = 1.0$ for (D) linear displacements on the boundaries and (S) uniform tractions on the boundaries. Furthermore, the branch meshes of contact normal forces are qualitatively drawn in the pictures. Figure 42 depicts the homogenized macro-

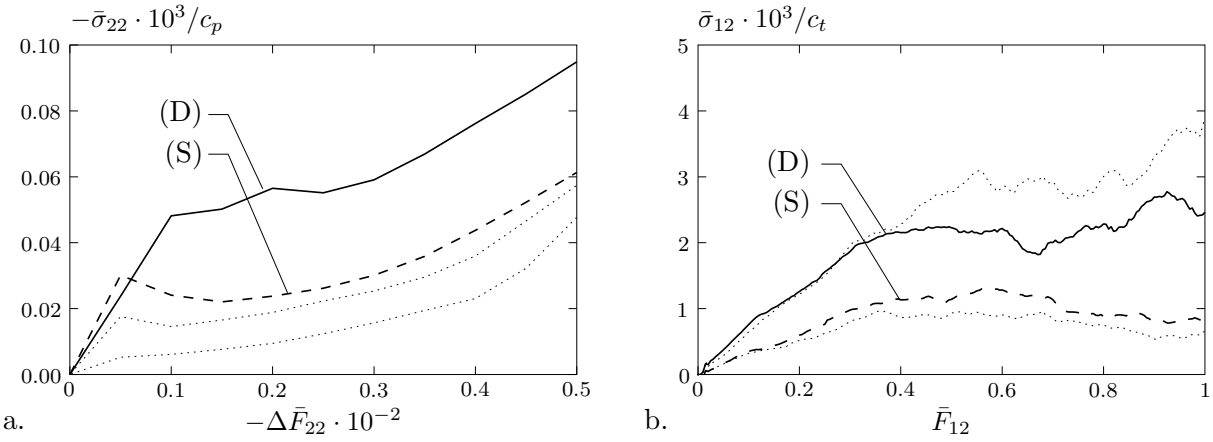

Figure 42: Stress diagrams of the circular microstructures with 305 and 161 elliptical particles: a. Homogenized normal stresses $-\bar{\sigma}_{22}$ versus deformation $-\Delta\bar{F}_{22}$ during compression, b. visualizes the shear stresses $\bar{\sigma}_{12}$ versus shear deformation $\bar{F}_{12}$ for (D) linear displacements on the boundaries and (S) uniform stresses on the surfaces. The thick lines represent the stresses obtained with the large example with 305 particles, the thin, dotted ones the stresses of the one with 161 particles.

scopic normal stresses $-\bar{\sigma}_{22}$ during the initial compression mode and the homogenized shear stresses $\bar{\sigma}_{12}$ during shear deformation. The dotted lines refer to the response from the small granular microstructure with 161 particles, the bold solid and dashed curves refer to the response of the one with 305 granules. Interestingly, the larger microstructure yields a stiffer result in compression. In shear, in the first part of the deformation the responses are almost identical and only deviate for large shear deformations. In total, the response in compression of these circular microstructures is much stiffer than the response in compression of the previous rectangular microstructures. Finally, Figure 43 depicts the homogenized normal stresses $-\bar{\sigma}_{11}$ and $-\bar{\sigma}_{22}$ versus the applied homogeneous shear deformation mode $\bar{F}_{12}$. Here, the curves from the small and the large examples with 161 and 305 particles, respectively, yield similar results in the first part of the deformation and deviate only slightly in the advanced range of the responses.

5.3.4. Compression-Shear for Non-Standard, Periodic Microstructure. This example is concerned with an aggregate of 187 elliptical particles as shown in Figure 44.

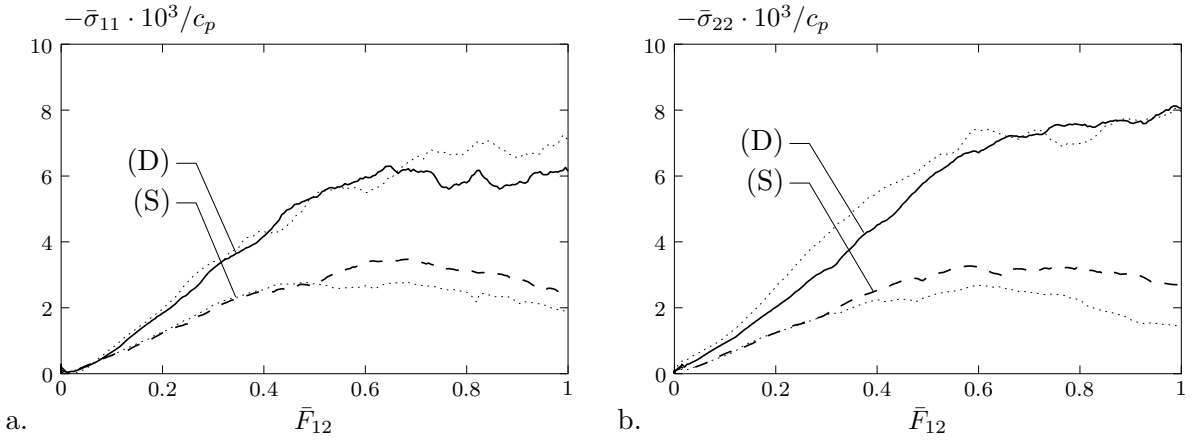

Figure 43: Stress response of the circular microstructures with 305 and 161 elliptical particles: a. Homogenized normal stresses $-\bar{\sigma}_{11}$ versus shear $\bar{F}_{12}$, b. normal stresses $-\bar{\sigma}_{22}$ versus shear deformation for (D) linear displacements on the boundaries and (S) uniform stresses on the surfaces. The thick lines represent the stresses obtained with the large example with 305 particles, the thin dotted lines represent the stresses of the example with 161 particles.

The microstructure is periodic, but in contrast to the previous examples the four sides are not straight lines. Nevertheless, the microstructure is truly periodic and its initial total volume is $|\mathcal{V}| = 262440$ square units. The volume density of the assembly is $\tilde{\varrho} = 0.83$ which gives a porosity of $p = 0.17$, and the void ratio sums up to $e = 0.20$. Each side of the boundary frame consists of 14 particles making up a total of 54 particles that form the boundary frame of the granular microstructure. The physical and technical parameters used in these simulations are the same from the previous examples, denoted in Boxes 5 and 6. Also, the same deformation process and similar relaxation functions are used, see equation (5.7). Figure 44 depicts three deformation states for each of the three boundary conditions developed at homogeneous deformation states $\bar{F}_{12} = 0.0$, $\bar{F}_{12} = 0.5$ and $\bar{F}_{12} = 1.0$. In the case of periodic and traction boundary conditions the qualitative force trajectories are clearly visible and they appear as expected. Recall that Horne [50] introduced these as *solid paths*. In the case of linear displacements on the boundary with zero particle rotations, the largest shear forces develop at the left and right boundaries where the initially inclined sides are heavily compressed together. In contrast to the other two boundary conditions, in this case of linear boundary conditions the particles cannot rotate under the influence of the contacting particles since the rotations are assumed to be fixed. In Figure 45a the homogenized macroscopic normal stresses $-\bar{\sigma}_{11}$ during the initial compression part are shown for the three types of boundary conditions. Figure 45b depicts the shear stresses $\bar{\sigma}_{12}$ versus shear deformation $\bar{F}_{12}$. Due to the previously discussed heavy compression of the boundary particles in certain parts for the case of linear displacements on the boundaries with fixed rotations, this type of boundary conditions yields a much stiffer response than the other two conditions. This becomes particularly obvious in the advanced deformation states. The two curves obtained with the periodic- and the uniform stress conditions resemble those obtained from the rectangular microstructures from previous examples, see Figure 35. Figure 46 depicts the homogenized normal stress responses $-\bar{\sigma}_{11}$ and $-\bar{\sigma}_{22}$ during shear deformation. Here, the same characteristics are observed where the linear displacement boundary conditions yield much stiffer curves than the other two. Nevertheless, the bound character is clearly visible in that the linear displacement boundary conditions give an upper and the uniform traction conditions a lower

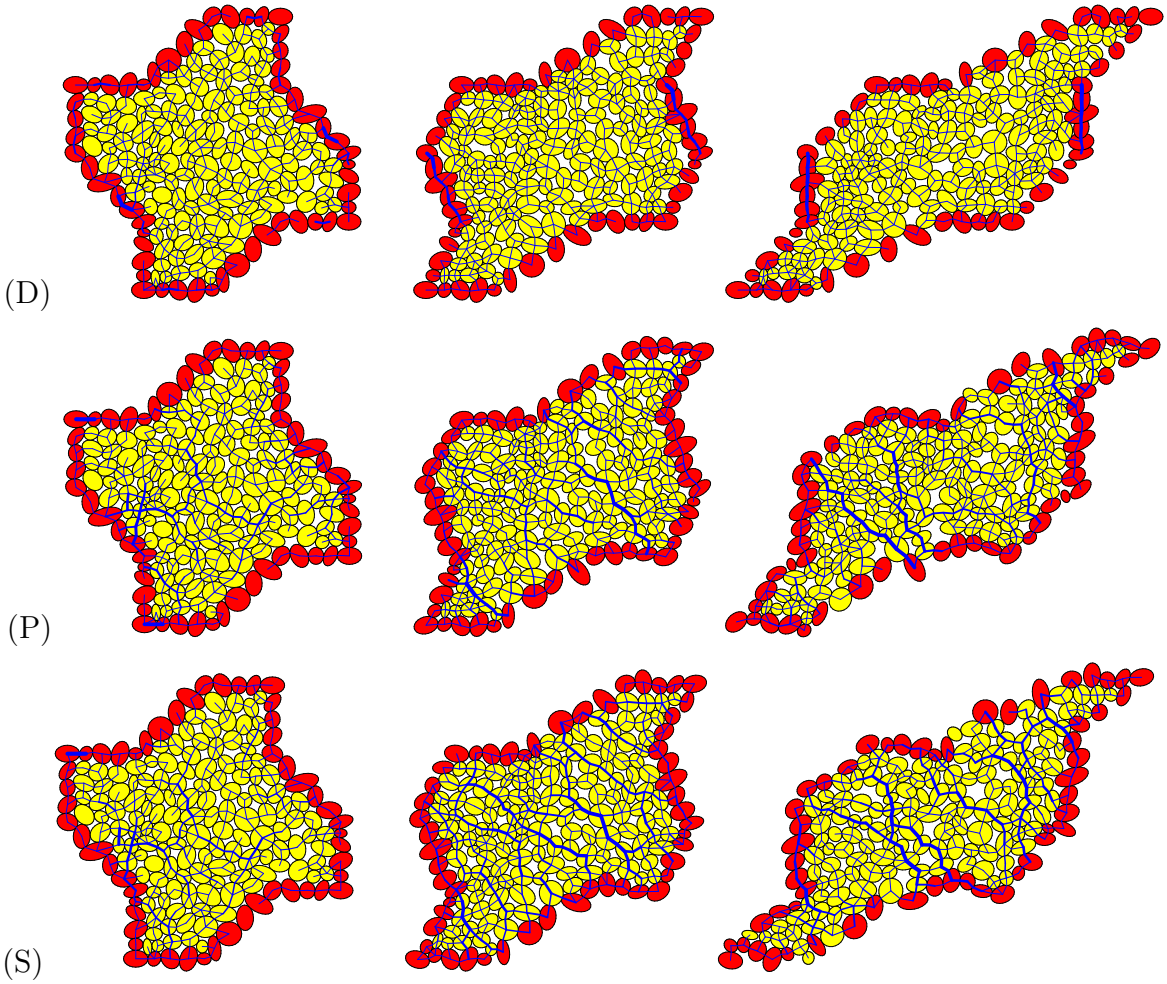

Figure 44: Irregular non-rectangular periodic package of 187 circular granules under initial compression followed by a simple shear mode. The boundary frame consists of 54 particles in total, where 14 granules belong to each side of the surface. Displayed are the three shear deformation states $\bar{F}_{12} = 0.0$, $\bar{F}_{12} = 0.50$ and $\bar{F}_{12} = 1.0$ for the new class of three boundary conditions.

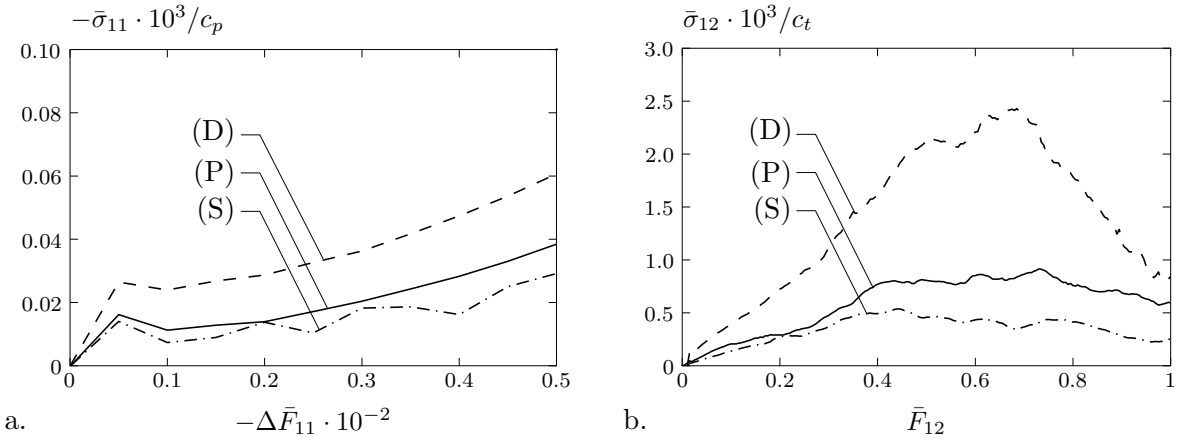

Figure 45: Homogenized normalized macroscopic compressive stresses $-\bar{\sigma}_{11}$ versus initial compression mode $-\Delta\bar{F}_{11}$, and shear stresses $\bar{\sigma}_{12}$ versus simple shearing $\bar{F}_{12}$ for the three classical boundary conditions (D) linear displacements, (P) periodic deformations of opposite boundary particles and (S) uniform tractions on the surfaces.

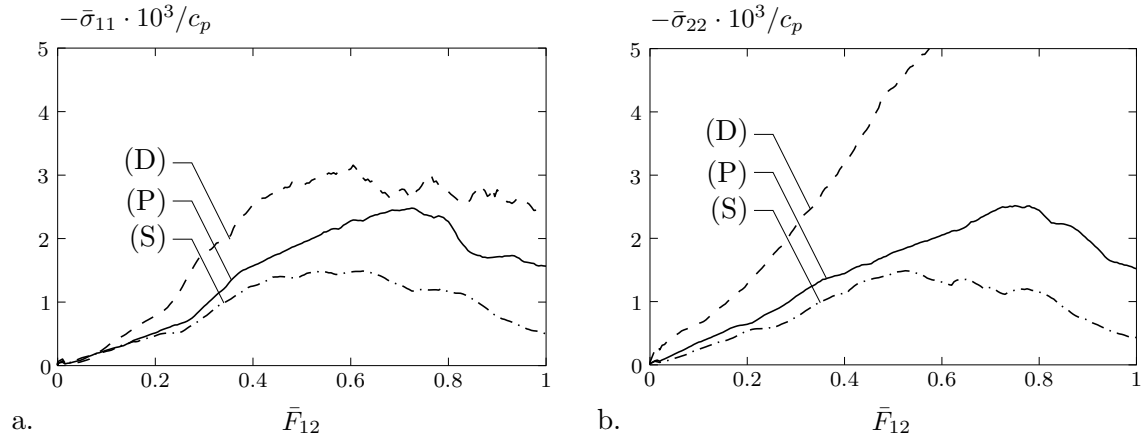

Figure 46: Homogenized macroscopic normal stresses $-\bar{\sigma}_{11}$ and $-\bar{\sigma}_{22}$ versus macroscopic shear deformation $\bar{F}_{12}$ for the three classical boundary conditions (D) linear displacements, (P) periodic deformations of opposite boundary particles and (S) uniform tractions on the surfaces.

bound for the periodic deformation conditions. The plastic ranges in the stress curves follow from interparticle sliding. If more compression was applied, the curves would initially all form straight lines from the deformation process. This is caused by heavy compression, therefore sliding and dissipation would not occur. This behavior could then be considered to be elastic. Figure 47a gives an image of the number of relaxation steps performed after

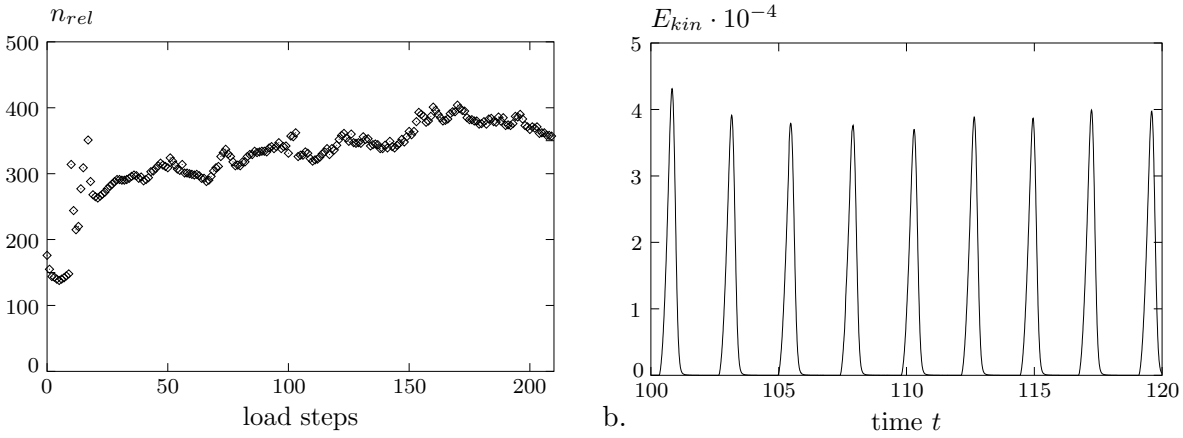

Figure 47: Irregular non-rectangular periodic microstructure of 187 particles: a. Number of relaxation steps n_{rel} versus load steps, b. mean kinetic energies E_{kin} in the time interval [100, 120 *sec*] for the case of periodic deformations.

each load step. These steps are necessary to reach static equilibrium states. In Figure 47b the mean kinetic energies of equation (5.10) in some representative load steps during the time interval [100, 120 s] are visualized. This curve is obtained with the simulation of periodic boundary constraints. Again, one can clearly see that at the end of each load step the mean kinetic energy reaches a zero level.

5.4. Numerical Examples in 3D: Microstructures with Spherical Particles

Despite simulations of granular media in two spatial dimensions having academic value, real material behavior can only be resembled if three dimensional structures are investigated. Therefore, in what follows a study of some representative three dimensional nu-

merical examples of spherical particles is presented. Therein, two cubic microstructures are deformed, the results are compared and the bound character of the three classical boundary conditions clearly verified. Initially, generation of *periodic* cubic microstructures proved to be a formidable task. This was accomplished by constructing three dimensional CAD data using the software package AutoCAD. As was shown above, in periodic structures opposite faces must be identical. Thus at first in each spatial direction one such face was contructed using three dimensional spherical objects. It must be noted hereby that the centroids of the spheres must not lie in one plane. If that was done, these faces would represent artifical load paths during compressive deformations and loads would not be transmitted into the bulk of these structures. Having constructed three such faces, they

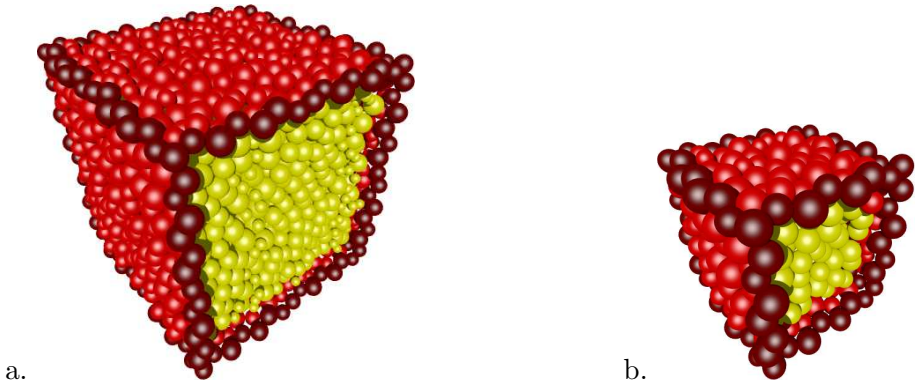

Figure 48: The two assemblies of a. 4076 and b. 513 spherical particles. For the first assembly, 1242 particles make up the boundary frame, for the second one there are 312 spheres that form the boundary. Note that in these pictures for clarity the boundary particles on the one face are removed.

were copied to their associated opposite faces and some particles in the middle of the upper $\boldsymbol{x}_3$ face were temporarily removed. Then a huge assembly of particles was placed above the structure. The CAD data of all particles was obtained and read into the granular mechanics code. Artifical walls were placed around the particle assembly above the cubic structure, and a chute was formed with wall elements that formed a funnel from the walls around the particle assembly to the opening in the middle of the top face of the cubic microstructure. A standard granular mechanics computation was then performed where gravitational forces were applied onto all particles. The particles of the suface of the microstructure were constrained to their initial positions. The computation let the particles in the assembly move down the chute and fall into the microstructure box. This was done until the structure was filled up with particles. At the end, the temporarily removed particles were re-inserted into the top face, some relaxation steps were executed and a periodic cubic microstructure with a high volume density was generated.

5.4.1. Compression-Shear Mode for Two Cubic Microstructures. In what follows, two such cubic microstructures of different sizes made of spherical particles are investigated. The first one is made up of 4076 particles, where 1242 spheres form the periodic boundary frame, i.e. opposite faces of the microstructure are equal as described above. The radii of the particles lie between 30.0 and 60.5 units. The second assembly is made up of 513 spheres, where their radii lie between 37.0 and 60.5 units. Here, 312 particle form the periodic boundary frame. In Figure 48 the two microstructures to be investigated are shown. In 48a the large assembly that consists of 4076 spheres is illustrated, in 48b the one with 513 particles. The red (or shaded) particles denote the boundary particles

Box 7: Properties of Granular Microstructures

Assembly		4076 spheres	513 spheres
number of particles		4076	513
particles on boundary		1242	312
number of linked particles		707	200
range of particle radii		$30.0 \leq R \leq 60.5$	$37.0 \leq R \leq 60.5$
reference volume	V_0	$2531.5 \cdot 10^6$	$316.4 \cdot 10^6$
initial volume density	$\tilde{\varrho}$	0.52	0.50
initial void ratio	e	0.93	1.02

where for clarity the edge particles are depicted in dark red (or dark-shaded). The yellow (or light-shaded) particles resemble the granules in the interior domain. In this picture the particles on one face are left out so that the particles in the interior domain are visible. The initial volume densities $\tilde{\varrho}_0$ are calculated as 0.52 and 0.50, respectively, and thus differ only slightly. Table 7 summarizes the properties of the two three dimensional microstructures to be investigated. The physical parameters which directly govern the

Box 8: Physical Parameters

normal stiffness	c_p	=	$1.4 \cdot 10^7$
tangential stiffness	c_t	=	$1.4 \cdot 10^7$
linear hardening	h	=	0
interparticle friction angle	ϱ	=	25^o
fictitious density of discs	ϱ^*	=	1.0

behavior of the microstructures during deformation are denoted in Box 7. Note that zero hardening is assumed in the calculations here. Also, the fictitious density of the spheres is much less than that usually assumed for planar particles because in the three dimensional case the mass is calculated using the volume of a particle, not its plane area. Finally, Box 9

Box 9: Technical Parameters

contact damping	α_c	=	0.01
initial global damping	α_{g0}	=	20.0
low–damping relaxation steps	n_{r0}	=	50
intensity of relaxation function	$\bar{\alpha}$	=	1.0
penalty force factor	ϵ_f	=	10^8 / 10^1
penalty couple factor	ϵ_c	=	10^8
time step length	Δt	=	$2.0 \cdot 10^{-3}$
load increment	$\Delta\lambda$	=	0.1

summarizes the technical parameters used for the simulation of the initial boundary-value problems. Note that the penalty force parameter is chosen as $\epsilon_f = 10^8$ for the simulation with Dirichlet-type linear displacement- and periodic boundary conditions and as $\epsilon_f = 10^1$ for the von Neumann-type uniform traction constraints. Initially, all particles are at rest

with zero initial velocities and zero initial accelerations. Despite the generation process, in the simulation of the boundary-value problem gravitational forces are not employed. The homogeneous macroscopic deformation that drives the structure is applied in 1100

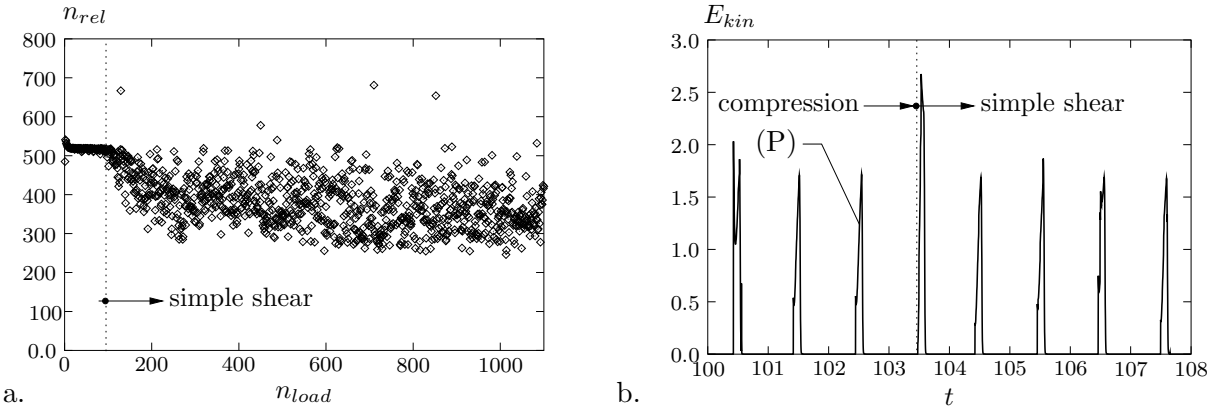

Figure 49: a. Number of relaxation steps n_{rel} versus load steps n_{load} for the case of periodic boundary conditions of 513 spheres and b. mean kinetic energy E_{kin} versus simulation time in the increment $t = [100,\ 108]$ where the transition from the compression to the simple shear mode occurs.

load steps of $\Delta\lambda$. Initially, a triaxial compression mode $\bar{\boldsymbol{F}}_{co}$ is applied in 100 load steps of $\Delta\lambda$ until a deformation $\lambda_0 = 10.0$ is reached. Then the compressive state is held and a simple shear mode $\bar{\boldsymbol{F}}_{sh}$ is applied in 1000 further load steps. The two deformation modes are governed by

$$\bar{\boldsymbol{F}}_{co} = \mathbf{1} - \lambda \begin{bmatrix} 0.002 & 0 & \\ 0 & 0.002 & 0 \\ 0 & 0 & 0.002 \end{bmatrix}, \quad \bar{\boldsymbol{F}}_{sh} = \mathbf{1} + \begin{bmatrix} -0.2 & 0 & (\lambda - \lambda_0)0.01 \\ 0 & -0.2 & 0 \\ 0 & 0 & -0.2 \end{bmatrix}. \tag{5.9}$$

Each load step is followed by n_{rel} relaxation time steps which relax the assembly until a quasistatic configuration is reached. Figure 49a depicts this number n_{rel} required to reach this static state for the simulation with 513 particles. Due to the relaxation technique employed in this work, n_{rel} is not constant but differs between load steps such that a good reduction in total computing time is achieved. In Figure 49b the mean kinetic energy

$$E_{kin} = \frac{1}{2N} \sum_{p=1}^{N} \dot{\boldsymbol{x}}_p^T \boldsymbol{M}_p \dot{\boldsymbol{x}}_p \tag{5.10}$$

for the $N = 513$ particles in some representative load steps at the transition from the compression- to the simple shear mode in the time interval $[100,\ 108\ s]$ is plotted. This curve is obtained with the simulation of periodic boundary constraints. One can clearly see that after the onset $n_{r0} = 50$ relaxation time steps with low global damping the mean kinetic energy rapidly decreases. The relaxation is terminated as soon as the ratio $E_{kin}/E_{kin,max}$, where $E_{kin,max}$ is the maximum mean kinetic energy during the actual load step, falls below a certain tolerance tol, that is $E_{kin}/E_{kin,max} \leq tol = 10^{-8}$. In Figure 50 three deformation states for the large assembly at $\bar{F}_{13} = 0.0$, at $\bar{F}_{13} = 0.5$ and the final one at $\bar{F}_{13} = 1.0$ for the three boundary conditions are depicted. Figure 51 summarizes the stress development during the deformation of the large assembly. Figure 51a visualizes the macroscopic normal stresses $-\bar{\sigma}_{11}$ during the initial triaxial compression mode. This

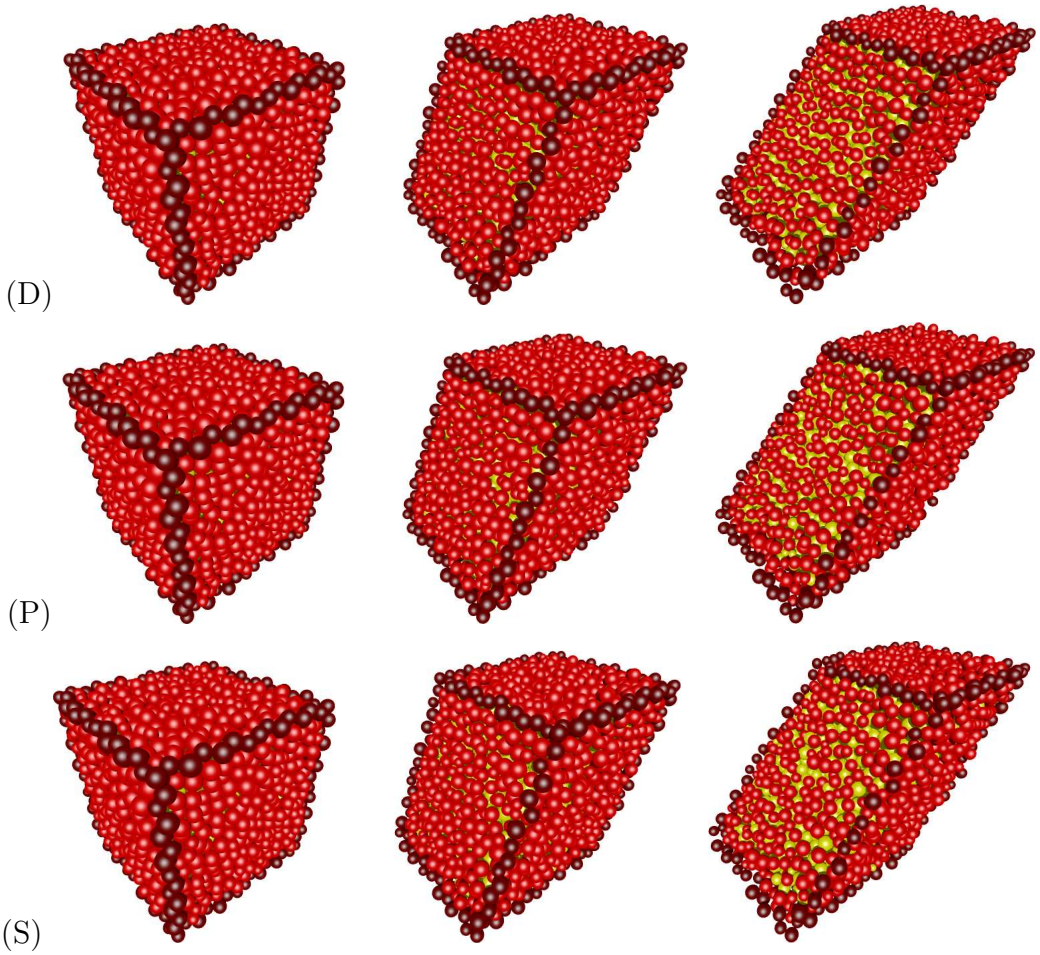

Figure 50: Microstructure of 4076 spherical particles under an initial biaxial compression mode followed by simple shearing F_{13}. The figure shows the deformation states of the assembly at the end of the compression mode/ beginning of shear deformation $\bar{F}_{11} = 0.98/$ $\bar{F}_{13} = 0.0$, at $\bar{F}_{13} = 0.5$ and at $\bar{F}_{13} = 1.0$ for the class of three boundary conditions.

deformation is governed by an almost purely elastic deformation due to the nonlinear elastic contact normal interaction law. Observe that this deformation and thus its stress development is not governed by sliding or friction between the particles. In Figures 51b and d the normal stresses $-\bar{\sigma}_{11}$ and $-\bar{\sigma}_{33}$, respectively, during the simple shear mode are shown. Clearly, the linear displacement (D) and the uniform traction (S) constraints provide upper and lower bounds, respectively, with respect to the periodic boundary constraints. In Figure 51c the shear stresses $\bar{\sigma}_{13}$ during the simple shear deformation are depicted. In contrast to the compression mode, this behavior is governed by tangential sliding and sticking between the particles, thus resulting in the elastoplastic-like stress-deformation behavior as shown in the Figure. Figure 52 depicts three deformation states of the smaller assembly with 513 spherical particles. These states are the associated ones to the larger assembly, see Figure 50. In Figure 52, the differences in deformation between the three boundary conditions are much clearer. This is because for the larger assembly the effect of different boundary conditions becomes less influential. This effect will be discussed subsequently. In contrast to the stress-deformation curves of the large assembly, in Figure 54 the associated curves for the smaller assembly with 513 spherical particles are shown. Figure 54a depicts the macroscopic homogenized normal stresses $-\bar{\sigma}_{11}$ during the initial homogeneous compression mode. Again it is governed by elastic behavior.

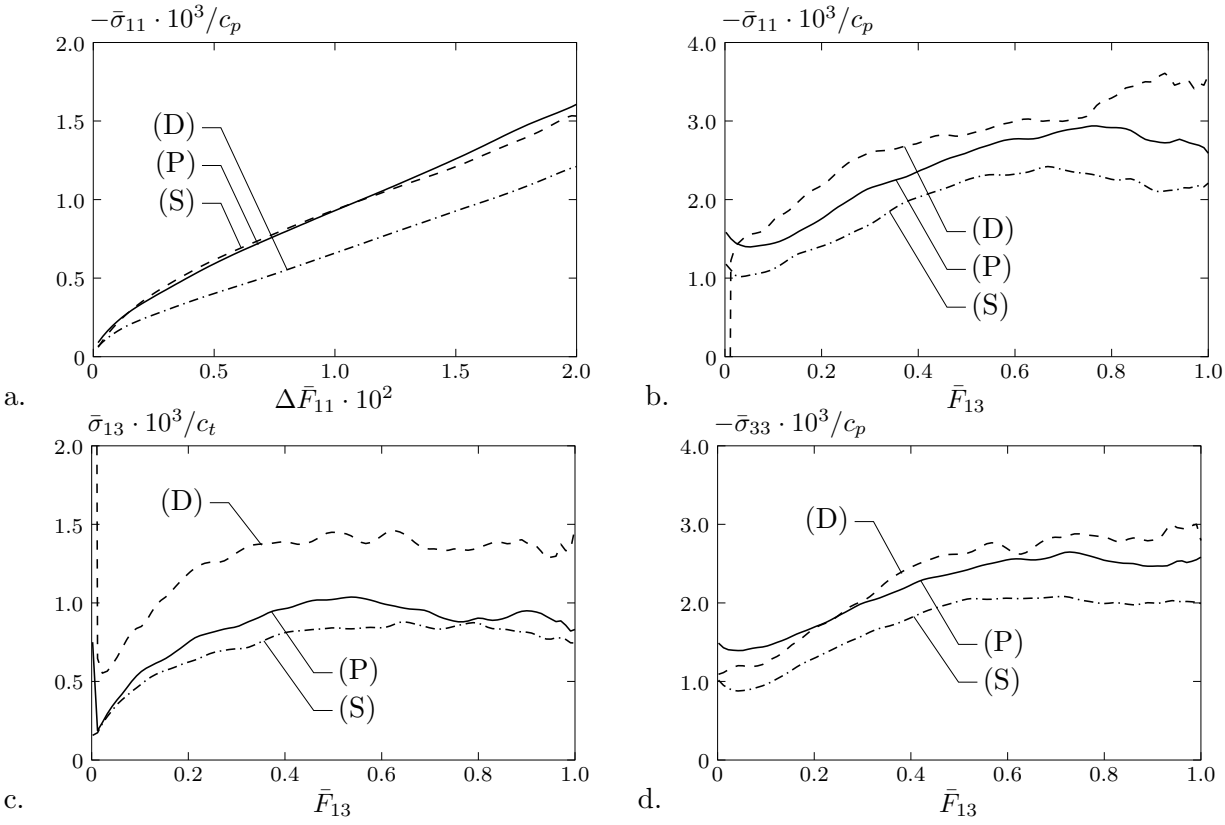

Figure 51: Development of homogenized macroscopic Cauchy stresses for the assembly with 4076 spheres: a. Normal stresses $-\bar{\sigma}_{11}$ versus compression increment $\Delta\bar{F}_{11}$, b. normal stresses $-\bar{\sigma}_{11}$ versus simple shearing $\bar{F}_{13}$, c. shear stresses $\bar{\sigma}_{13}$ versus simple shearing $\bar{F}_{13}$ and d. normal stresses $-\bar{\sigma}_{33}$ during shear deformation $\bar{F}_{13}$ for the three boundary conditions (D) linear displacements on the boundaries, (P) periodic deformations on opposite boundary particles and (S) uniform tractions on the surfaces. The bound character of (D) (upper) and (S) (lower) with respect to the periodic conditions (P) is clearly verified.

Figures 54b and d depict the normal stresses $-\bar{\sigma}_{11}$ and $-\bar{\sigma}_{33}$ during the macroscopic simple shear deformation mode. Finally, Figure 54c shows the macroscopic shear stress $\bar{\sigma}_{13}$ during the simple shear deformation. On the qualitative side, the two simulations, with 4076 and 513 particles, yield similar results. In Figure 53 the results in graph for a, the homogenized macroscopic normal stresses $-\bar{\sigma}_{11}$ during the initial compression mode, and graph b, the homogenized shear stresses $\bar{\sigma}_{13}$ during shearing for both simulations, are visualized in separate diagrams. It is obvious that in the initial compression mode the smaller assembly exhibits a stiffer behavior than the larger one. This difference is due to the fact that in the smaller example the forces are transmitted through fewer particles than in the larger one. Therefore, only fewer particles can evade the forces, which finally results in this stiffer normal-stress behavior. Observe also that the three curves associated with the (D) linear displacements, (P) periodic deformations and (S) uniform traction boundary constraints in the large assembly lie closer together than in the small one. Clearly, for even bigger examples the effect of the three boundary constraints becomes less influential and tending to the infinity limit would eventually vanish. In Figure 55a the average coordination number $\bar{n}_c$ and in Figure 55b the volume density $\tilde{\varrho}$ versus load steps n_{load} as further scalar quantities are depicted. In Figure 55a the development of the coordination number for the class of three boundary conditions and the two assemblies are shown. During the first part of the deformation, the particles of the smaller assembly have

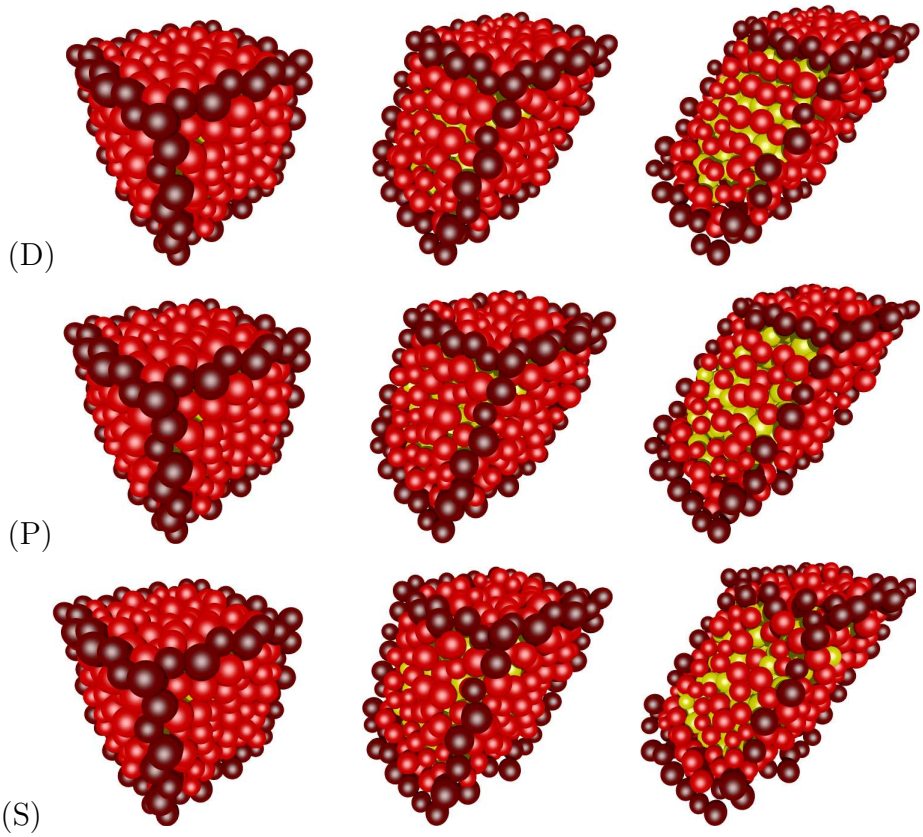

Figure 52: Microstructure of 513 spherical particles under an initial biaxial compression mode followed by simple shearing F_{13}. The figure shows the deformation states of the assembly at the end of the compression mode/ beginning of shear deformation $\bar{F}_{11} = 0.98/$ $\bar{F}_{13} = 0.0$, at $\bar{F}_{13} = 0.5$ and at $\bar{F}_{13} = 1.0$ for the class of three boundary conditions.

more contacts than the larger one. Both curves converge toward each other as shearing of the assembly proceeds. Figure 55b depicts the development of the void ratio $\tilde{\varrho}$ for the (S) uniform traction boundary constraint during deformation for both assemblies. The

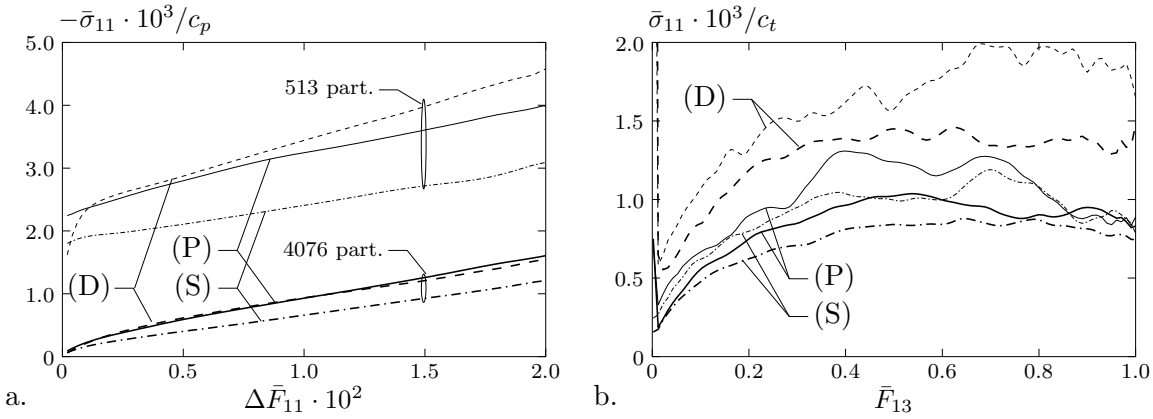

Figure 53: Development of the macroscopic Cauchy stresses for the assemblies with 4076 (thick lines) and 513 (thin lines) spheres: a. normal stresses $-\bar{\sigma}_{11}$ versus compression increments $\Delta\bar{F}_{11}$ and b. shear stresses $\bar{\sigma}_{13}$ versus simple shearing $\bar{F}_{13}$ for the three boundary conditions (D) linear displacements on the boundaries, (P) periodic deformations on opposite boundary particles and (S) uniform tractions on the surfaces. The bound character of (D) (upper) and (S) (lower) with respect to the periodic conditions (P) is clearly verified.

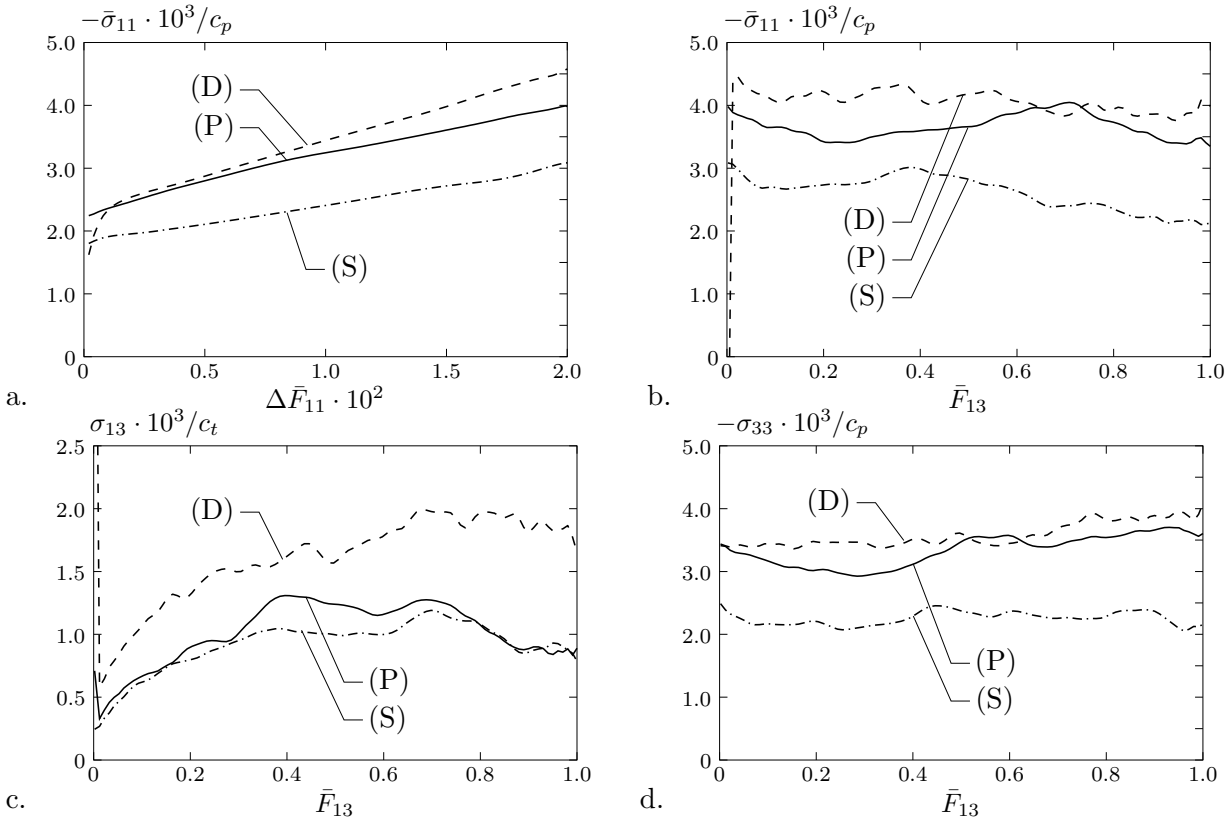

Figure 54: Development of the macroscopic homogenized Cauchy stresses for the assembly with 513 spheres: a. normal stresses $-\bar{\sigma}_{11}$ versus compression increment $\Delta\bar{F}_{11}$, b. normal stresses $-\bar{\sigma}_{11}$ versus simple shearing $\bar{F}_{13}$, c. shear stresses $\bar{\sigma}_{13}$ versus simple shearing $\bar{F}_{13}$ and d. normal stresses $-\bar{\sigma}_{33}$ during shear deformation $\bar{F}_{13}$ for the three boundary conditions (D) linear displacements on the boundaries, (P) periodic deformations on opposite boundary particles and (S) uniform tractions on the surfaces. The bound character of (D) (upper) and (S) (lower) with respect to the periodic conditions (P) is clearly verified.

uniform traction constraint is the only one of the three constraints where the volume of

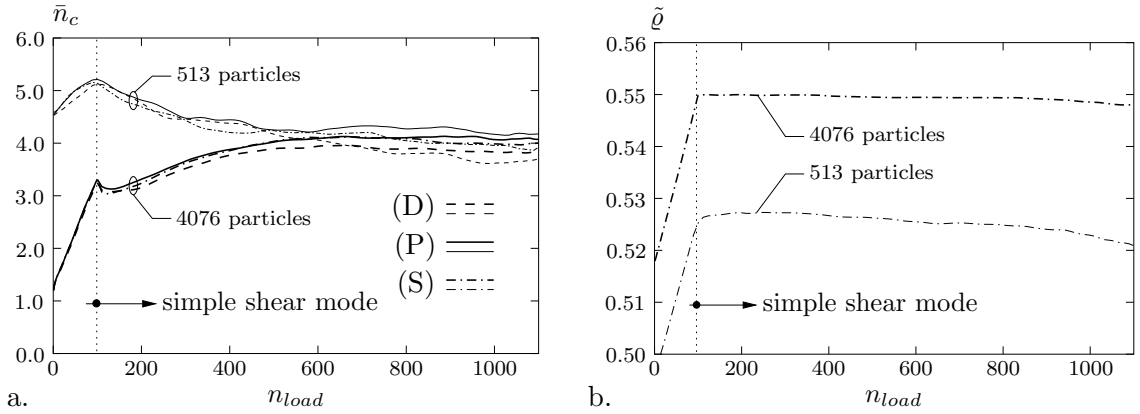

Figure 55: a. Average coordination numbers $\bar{n}_c$ versus load steps n_{load} for the three boundary conditions (D) linear displacements on the boundaries, (P) periodic deformations on opposite boundary particles and (S) uniform tractions on the surfaces during the course of deformation. b. Development of the volume density during deformation for the uniform traction boundary condition (S). The dilatancy developing after the incipient simple shear is clearly visible.

the microstructure changes during the simple shear mode. Clearly, due to the volume-preserving macroscopic simple shear deformation, periodicity of the deformed structures in the case of (D) linear displacements and (P) periodic deformations is preserved and their microstructural volumes do not change from the homogeneous one. During the initial compression, the density and the void ratio of the granular microstructure increase. As known from experimental tests, during the subsequent shearing mode the *dilatancy* effect can clearly be observed by noting that the void ratio decreases. The difference in the two curves stems from the slightly different initial void ratios of the two assemblies.

6. Multiscale Analyses of Granular Materials at Finite Strains

In this section the theoretical and computational setup of true two scale analyses of granular microstructures are described. So far the modeling of such discrete materials on the micro scale has been shown in connection with a consistent averaging of the macroscopic observables of interest such as the stresses. For computational convenience, focus will be put onto two dimensional irregular microstructures with circular particles. In this context, the determination of the overlapping areas between arbitrary-shaped particles does not need to be accounted for. Instead, for circular particles simply the overlapping distance is computed as the difference between the distance between the centroids of the particles and the sum of their radii. A first step towards such an approach is shown in the paper Kaneko, Terada et al. [59] with a different and in the author's opinion non-periodic definition of the microscopic unit cell. Therein, the particles are merely placed into a rectangular box, where only the box itself can periodically be repeated. Also, the driving of the granular microstructure is performed by application of the macroscopic strain as an external driving force. In contrast, in the algorithm presented here, the microscopic deformation is computed using the macroscopic deformation gradient as the homogeneous part and, with this part at hand, it then solves for the microscopic fluctuation with regard to this homogeneous part.

Material modeling can generally be described as the solution of boundary value problems. Therein, for a given physical system, a set of governing equations is derived which is based on fundamental principles (i.e. equilibrium, conservation of mass, Newton's law, etc.). In this context, constitutive laws are formulated that determine the response of the material to its environment. For the granular structures introduced in the previous chapters, the constitutive laws describe the interparticle behavior, thus they are basically relations between interparticle forces and interparticle overlaps. Finally, initial and boundary values of the variables are prescribed in order to match the physical system of interest, and then the governing equations are solved. For the solution of the boundary value problem on the macroscopic scale, the finite element method in connection with an explicit time integration scheme is employed. This choice circumvents the need of a tangent matrix, only the homogenized stresses, as the constitutive law, find input into the macroscopic solution procedure. On the microscopic scale, the before mentioned discrete element method is used in connection with the already outlined homogenization technique that influences the solution on the macroscopic scale. Subsequently, the global overall solution procedure for the two coupled boundary-value problems is described. Finally, some numerical examples of true two scale analyses are given. The first ones serve as an introductory example explaining general technical properties. However, the second example is a geotechnical application of the method. Specifically, a biaxial test for granular materials as done in Desrues & Viggiani [35] is computationally modeled as a coupled initial boundary-value problem and simulated.

6.1. Finite Element Formulations at Finite Deformations

In the framework of the finite element method, the integro-differential equations of the continuous domain are discretized such that they are reduced to matrix equations that can be solved on a computer. The FEM is naturally suited for interfacing with smaller scales like discrete elements and atomistics. In the FEM approach, the continuous physical system is represented by a grid of discrete nodes and leads to a computational scheme

that in its structure is very close to that found in the discrete formulations at lower scales. In this work, focus will be put on quasistatic problems at large strains.

The point of departure for the finite element method is the strong form of quasistatic equilibrium given by $\mathrm{Div}[\bar{\boldsymbol{P}}] + \bar{\boldsymbol{\gamma}} = \boldsymbol{0}$, where $\bar{\boldsymbol{P}}$ represents the first Piola-Kirchhoff stress tensor and $\bar{\boldsymbol{\gamma}}$ an externally applied body force, see Figure 13. A Galerkin procedure and some algebraic manipulations yield the well-known principle of virtual work

$$G(\bar{\boldsymbol{\varphi}}, \delta\bar{\boldsymbol{\varphi}}) = \int_{\bar{\mathcal{B}}} \bar{\boldsymbol{P}} : \delta\bar{\boldsymbol{F}} \; dV - \int_{\bar{\mathcal{B}}} \bar{\boldsymbol{\gamma}} \cdot \delta\bar{\boldsymbol{\varphi}} \; dV - \int_{\partial\bar{\mathcal{B}}_t} \boldsymbol{t} \cdot \delta\bar{\boldsymbol{\varphi}} \; dA = 0 \tag{6.1}$$

where the first integral represents the internal and the latter two the external virtual work contributions. $\delta\bar{\boldsymbol{\varphi}}$ is a test function and $\bar{\boldsymbol{t}}$ an externally applied force on the undeformed boundary $\partial\bar{\mathcal{B}}_t \subset \partial\bar{\mathcal{B}}$. Note that the virtual deformation gradient $\delta\bar{\boldsymbol{F}}$ is a function of the test function in the form $\delta\bar{\boldsymbol{F}} = \delta(\nabla_{\bar{\boldsymbol{X}}}\bar{\boldsymbol{\varphi}}) = \nabla_{\bar{\boldsymbol{X}}}(\delta\bar{\boldsymbol{\varphi}})$. In literature, the variation $\delta\bar{\boldsymbol{u}}$ is frequently used instead of $\delta\bar{\boldsymbol{\varphi}}$ due to classical formulations at small strains. In large strain analyses, the nonlinear deformation $\bar{\boldsymbol{\varphi}}$ is considered to be the primary variable and hence its variation the correct formulation. However, the variations of $\bar{\boldsymbol{\varphi}}$ and $\bar{\boldsymbol{u}}$ are identical in that $\delta\bar{\boldsymbol{\varphi}} = \delta(\bar{\boldsymbol{X}} + \bar{\boldsymbol{u}}) = \delta\bar{\boldsymbol{u}}$. Observe also that $\bar{\boldsymbol{u}}$ cannot be interpreted as a component of either the Lagrangian or Eulerian configurations. Initially, the body $\bar{\mathcal{B}}$ is assumed to be stress and strain free, but subject to fixed displacements on some portion of its boundary as well as prescribed loading in the form of tractions on the remainder of the boundary, thus

$$\bar{\boldsymbol{\varphi}} = \bar{\boldsymbol{\varphi}}_0 \quad \text{on } \partial\bar{\mathcal{B}}_{\bar{\boldsymbol{\varphi}}} \quad \text{and} \quad \bar{\boldsymbol{t}} = \bar{\boldsymbol{t}}_0 \quad \text{on } \partial\bar{\mathcal{B}}_{\boldsymbol{t}} \quad \text{with} \quad \partial\bar{\mathcal{B}} = \partial\bar{\mathcal{B}}_{\boldsymbol{t}} \cup \partial\bar{\mathcal{B}}_{\bar{\boldsymbol{\varphi}}} \; . \tag{6.2}$$

Free surfaces are therefore parts of $\partial\bar{\mathcal{B}}_{\boldsymbol{t}}$ with $\bar{\boldsymbol{t}}_0 = 0$. With equations (6.2), the initial boundary value problem with (6.1) is completely described.

6.1.1. Spatial Discretization. Displacement fields that satisfy (6.1) in the continuous domain are difficult or even impossible to obtain for complex geometries or material behavior. Therefore, the continuous field $\bar{\boldsymbol{\varphi}}$ is replaced by a discrete representation by selecting a set of nodes throughout the body and solving explicitly for only the nodal displacements $\boldsymbol{d}$. The displacement fields between the nodes are obtained by adequate interpolations of the nodal values $\boldsymbol{d}$. These interpolation (shape) functions for each degree of freedom i are henceforth denoted by N_i, its assembly gives the row vector $\boldsymbol{N}$. The selection of nodes is completely arbitrary and can be a non-uniform distribution of points. However, the positions and densities of the nodes strongly affect the accuracy of the approximate solution. Within a displacement-type finite element procedure the nonlinear macroscopic deformation map $\bar{\boldsymbol{\varphi}}$ and its associated variation $\delta\bar{\boldsymbol{\varphi}}$ are approximated in terms of the shape functions $\boldsymbol{N}$ as

$$\bar{\boldsymbol{\varphi}}^h = \sum_{I=1}^{n_{nodes}} N^I \cdot \boldsymbol{d}_I = \boldsymbol{N}\boldsymbol{d} \quad \text{and} \quad \delta\bar{\boldsymbol{\varphi}}^h = \sum_{I=1}^{n_{nodes}} N^I \cdot \delta\boldsymbol{d}_I = \boldsymbol{N}\delta\boldsymbol{d} \tag{6.3}$$

in terms of the nodal displacements and variations $\boldsymbol{d}$ and $\delta\boldsymbol{d}$, respectively. The particular choice of shape functions depends on the element used and will be introduced in a later subchapter. Subsequently, with $\bar{\boldsymbol{\varphi}} = \bar{\boldsymbol{X}} + \bar{\boldsymbol{u}}$, where $\bar{\boldsymbol{u}}$ is the displacement field, the approximations for the deformation gradient and its variation follow as

$$\bar{\boldsymbol{F}} = \boldsymbol{1} + \sum_{I=1}^{n_{nodes}} N^I_{,\bar{\boldsymbol{X}}} \cdot \boldsymbol{d}_I =: \boldsymbol{1} + \bar{\boldsymbol{B}}\boldsymbol{d} \quad \text{and} \quad \delta\bar{\boldsymbol{F}} = \bar{\boldsymbol{B}}\delta\boldsymbol{d} \; , \tag{6.4}$$

where $\bar{\boldsymbol{B}}$ is the so-called strain-displacement matrix acting as a linear operator on the nodal displacement field. Insertion into the weak form of equilibrium (6.1) gives the discretized form

$$G^h = \delta \boldsymbol{d}^T \cdot [\boldsymbol{f}_{int}(\boldsymbol{d}) - \boldsymbol{f}_{ext}] = 0 \tag{6.5}$$

with the internal and external forces

$$\boldsymbol{f}_{int}(\boldsymbol{d}) = \int_{\bar{\mathcal{B}}} \bar{\boldsymbol{B}}^T \bar{\boldsymbol{P}}(\boldsymbol{d})\, dV \quad \text{and} \quad \boldsymbol{f}_{ext} = \int_{\bar{\mathcal{B}}} \boldsymbol{N}^T \bar{\boldsymbol{\gamma}}\, dV + \int_{\partial \bar{\mathcal{B}}_t} \boldsymbol{N}^T \bar{\boldsymbol{t}}\, dA\ . \tag{6.6}$$

Here, the projection of body forces to the nodes $\int_{\bar{\mathcal{B}}} \boldsymbol{N}^T \bar{\boldsymbol{\gamma}}\, dV$ will be discussed in a following subchapter such that an equal body force distribution throughout the finite element mesh is achieved. Clearly, for arbitrary variations $\delta \boldsymbol{d}$ in equation (6.5), the term in brackets must vanish. This gives the system of nonlinear equations in $\boldsymbol{d}$ that needs to be solved for equilibrium as

$$\boxed{\boldsymbol{f}_{int}(\boldsymbol{d}) - \boldsymbol{f}_{ext} = \boldsymbol{0}\ .} \tag{6.7}$$

In what follows, an explicit solution scheme to this equation is discussed.

6.1.2. Time Discretization. Recall that the homogenized stresses $\bar{\boldsymbol{P}}$ cannot analytically be determined in the case of granular microstructures. Thus, the equation system in (6.7) cannot be linearized with respect to the macroscopic nodal displacements $\boldsymbol{d}$ as done in standard implicit finite element codes. This is because the stresses $\bar{\boldsymbol{P}}$ do not depend on the nodal displacements $\boldsymbol{d}$ through some energy functional, but depend discontinuously on the current configuration of the deformed granular microstructure and the forces acting between the granules. Subsequently, the stresses can algorithmically not be differentiated to yield the tangent matrix as needed in implicit codes. Therefore, in order to solve the system of equations without the demand for a second derivative, a dynamic solution technique for the balance of momentum is used, similar to that employed for the solution of the equation of motion on the discrete microscopic scale, of the form

$$\bar{\boldsymbol{M}} \ddot{\boldsymbol{d}} + \bar{\boldsymbol{C}} \dot{\boldsymbol{d}} + \boldsymbol{f}_{int}(\boldsymbol{d}) = \boldsymbol{f}_{ext}\ , \tag{6.8}$$

where the first two terms represent the dynamical parts of the balance equation. Here, $\ddot{\boldsymbol{d}}$ and $\dot{\boldsymbol{d}}$ represent the nodal acceleration and velocity vectors, respectively. A standard central difference scheme uses the approximations for the nodal accelerations $\ddot{\boldsymbol{d}}_n$ and velocities $\dot{\boldsymbol{d}}_n$ at time t_n based on two time steps Δt in the time intervals $[t_{n-1}, t_n, t_{n+1}]$

$$\ddot{\boldsymbol{d}}_n := \frac{1}{\Delta t}(\dot{\boldsymbol{d}}_{n+\frac{1}{2}} - \dot{\boldsymbol{d}}_{n-\frac{1}{2}}) \quad \text{and} \quad \dot{\boldsymbol{d}}_n := \frac{1}{2}(\dot{\boldsymbol{d}}_{n+\frac{1}{2}} + \dot{\boldsymbol{d}}_{n-\frac{1}{2}})\ . \tag{6.9}$$

The velocities employed here are taken to be the mean average in one time step and thus evaluated halfway through the time steps. Insertion of the approximations into the equation of motion evaluated at time t_n yields the update formula for the nodal velocities in the new time step $t_{n+\frac{1}{2}}$ as

$$\dot{\boldsymbol{d}}_{n+1} = \frac{1}{2 + \bar{\alpha_g} \Delta t} \left[(2 - \bar{\alpha_g} \Delta t) \dot{\boldsymbol{d}}_{n-\frac{1}{2}} + 2 \Delta t \boldsymbol{M}^{-1} (\boldsymbol{f}_{ext} - \boldsymbol{f}_{int}(\boldsymbol{d}_n)) \right] \tag{6.10}$$

where for the macroscopic damping matrix a relation with the mass matrix of the form $\bar{\boldsymbol{C}} := \bar{\alpha_g}\bar{\boldsymbol{M}}$ is introduced. Here, $\bar{\alpha_g}$ serves as the global damping parameter. Finally, the actual nodal displacements at time t_{n+1} simply follow as the update

$$\boldsymbol{d}_{n+1} = \boldsymbol{d}_n + \Delta t \cdot \dot{\boldsymbol{d}}_{n+\frac{1}{2}} \ . \tag{6.11}$$

In what follows, the calculation of the mass matrix $\bar{\boldsymbol{M}}$ needed in the above equation is described as well as the solution procedures for the two boundary value problems on both scales.

6.1.3. Mass Lumping. In the macroscopic equation of motion (6.8), a mass matrix $\boldsymbol{M}$ is needed that represents a continuous distribution of the mass in a discrete setting. A consistent element mass matrix follows directly from the integral

$$\bar{\boldsymbol{M}} = \int_{\bar{\mathcal{B}}} \varrho \boldsymbol{N}^T \boldsymbol{N} \ dV \ , \tag{6.12}$$

giving a non-diagonal matrix, where $\boldsymbol{N}$ is the row vector representing the shape functions. In order for the equation of motion to be solved directly and independently, a *mass lumping process* is required to yield a diagonal form of $\bar{\boldsymbol{M}}$. In literature, basically two such lumping schemes are reported. The first one, referred to as *optimal lumping*, is concerned with the application of a quadrature rule with degree of precision $2(p-m)$ where p is the highest degree of the complete polynomial in $\boldsymbol{N}$ and m the highest-order derivative in the strain energy. Diagonal mass matrices integrated in this way are known as *optimally lumped*. However, for some types of elements, e.g. quadratic triangles (which will also be employed here) and other higher order elements, optimally lumped diagonal mass matrices prevalently yield zero or negative nodal masses. The second lumping scheme is referred to as *HRZ lumping scheme* which circumvents the generation of negative nodal values and is thus used to generate diagonal mass matrices. Here, the key idea is to use the diagonal terms of the consistent mass matrix only, but scale them such that summation of all mass contributions gives the total mass of the element. Therein, only the diagonal entries of the consistent mass matrix in (6.12) need to be computed. A more in-depth discussion can for example be found in Cook, Malkus, Plesha [27] and the references cited therein. Note also that lumped mass matrices provide for possibly larger time steps Δt than consistent ones in solving the equation of motion.

6.1.4. Adaptive Global Damping. In order to converge to a static solution, i.e. $\ddot{\boldsymbol{d}} \leq tol \geq \dot{\boldsymbol{d}}$, as fast as possible within the context of dynamic relaxation the time step length, the mass matrix and/ or the global damping parameter $\bar{\alpha}_g$ can adaptively be adjusted for each time step such that the transient response is attenuated leaving the steady state or static solution for the externally applied loads, see Underwood [116]. Here, at first the approximation of the adjustment global damping parameter $\bar{\alpha}_g$ will be discussed. Of course, its value should be such that a static solution is obtained in the fastest possible way. Subsequently, the approximation of the time step Δt giving the best rate of convergence is presented. First of all, the damping matrix $\bar{\boldsymbol{C}}$ is taken to be proportional to the diagonal lumped mass matrix $\bar{\boldsymbol{M}}$, related by the global damping parameter $\bar{\alpha}_g$,

$$\bar{\boldsymbol{C}} := \bar{\alpha}_g \bar{\boldsymbol{M}} \ . \tag{6.13}$$

For a one-mass system with linear spring and viscous damping device ($m\ddot{d}+c\dot{d}+kd=0$), Lehr's damping coefficient is calculated as $D = d/(2m\omega)$, where ω is the eigen angular frequency of the system. For fastest convergence to the static solution, the damping coefficient should approach unity. With the above introduced relation $d = \bar{\alpha}_g c$, it follows that

$$\frac{\bar{\alpha}_g}{2\omega} = 1 \quad \Rightarrow \quad \bar{\alpha}_g = 2\omega \ . \tag{6.14}$$

For the nonlinear finite element system with many nodal degrees of freedoms, it is assumed that the overall global damping coefficient $\bar{\alpha}_g$ is governed by the lowest eigen angular frequency $\omega = \omega_0$, which can be approximated by means of the Rayleigh quotient as

$$\omega^2 = \frac{\boldsymbol{d}_0^T \cdot \bar{\boldsymbol{K}} \boldsymbol{d}_0}{\boldsymbol{d}_0^T \cdot \bar{\boldsymbol{M}} \boldsymbol{d}_0} \ , \tag{6.15}$$

where the $\boldsymbol{d}_0$ are the eigenvectors associated with the system under consideration. As a further assumption, the eigenvector $\boldsymbol{d}_0$ is approximated by the actual nodal displacement $\boldsymbol{d}_{n+1}$ in each time step. Note also that since the displacements change nonlinearly, the eigen angular frequency in (6.15) also changes nonlinearly. With the static equation $\bar{\boldsymbol{K}} \boldsymbol{d}_{n+1} = \boldsymbol{f}_{ext} - \boldsymbol{f}_{int}(\boldsymbol{d}_n)$, from the above equation (6.15) the new expression in terms of only known nodal displacements, internal and external forces as well as the diagonal mass matrix for the new time step follows approximately as

$$\omega_{n+1}^2 \approx \frac{\boldsymbol{d}_{n+1}^T \cdot [\boldsymbol{f}_{ext} - \boldsymbol{f}_{int}(\boldsymbol{d}_n)]}{\boldsymbol{d}_{n+1}^T \cdot \bar{\boldsymbol{M}} \boldsymbol{d}_{n+1}} \ , \tag{6.16}$$

and the update for the global damping parameter to be used in the next time step is computed accordingly as

$$\bar{\alpha}_{g,n+1} = 2\omega_{n+1} = 2 \left(\frac{\boldsymbol{d}_{n+1}^T \cdot [\boldsymbol{f}_{ext} - \boldsymbol{f}_{int}(\boldsymbol{d}_n)]}{\boldsymbol{d}_{n+1}^T \cdot \boldsymbol{M} \boldsymbol{d}_{n+1}} \right)^{1/2} \ . \tag{6.17}$$

Observe that the lowest eigen angular frequency ω_0 is only approximated and not exactly determined, but it is considered to be a suitable assumption for the dynamic relaxation procedure. With ω_{n+1} at hand, Underwood [116] showed that the best time step that ensures optimum convergence can be approximated by

$$\Delta t_{n+1} = \frac{1}{\omega_{n+1}} \ . \tag{6.18}$$

For stability, in the solution process a maximum time step is also dictated. The two scale solution process in the context of the update equation (6.11) is performed as long as the kinetic energy in the macroscopic system, given by the equation

$$\bar{E}_{kin} = \frac{1}{2} \boldsymbol{d}_{n+1}^T \cdot \bar{\boldsymbol{M}} \boldsymbol{d}_{n+1} \ , \tag{6.19}$$

is larger than a prescribed tolerance. The adaptive update of the global damping parameter $\bar{\alpha}_{g,n+1}$ yields a faster convergence to static solutions than a constant parameter would. Also, it must be mentioned that only the forces need to represent the physical system, whereas the global damping parameter $\bar{\alpha}_g$ and the lumped mass matrix $\bar{\boldsymbol{M}}$ do not. Other methods as well as more in-depth discussions for the automatic evaluation of such dynamic parameters are described in the works Papadrakakis [96], Skeie, Astrup & Bergan [106] and Park [98], to name just a few.

6.1.5. Linear and Quadratic Triangular Elements. For the simulation on the macroscopic scale, a six-noded triangular isoparametric element, as shown in Figure 56, or a linear triangle with only three nodes can possibly be selected. Here, the quadratic element is described, however, in the numerical implementation linear triangles will also be used. The quadratic triangle is an excellent element for stress analyses, due to the quadratic form of the shape functions the effect of shear-locking is *a priori* excluded. In two dimensions, each node has two translational degrees of freedom, the sides of the element can deform into quadratic curves. The shape functions used are of the form

$$N_I = \xi_I(2\xi_I - 1) \text{ for } I = 1,2,3 \quad \text{and} \quad N_4 = 4\xi_1\xi_2 \ , \ N_5 = 4\xi_2\xi_3 \ , \ N_6 = 4\xi_3\xi_1 \tag{6.20}$$

in terms of the area coordinates $\boldsymbol{\xi} = \xi_i, i = 1,2,3$. The area coordinates are not independent, due to the constraint $\sum_{i=1}^{3} \xi_i = 1$, one can write $\xi_3 = 1 - \xi_1 - \xi_2$. For a function

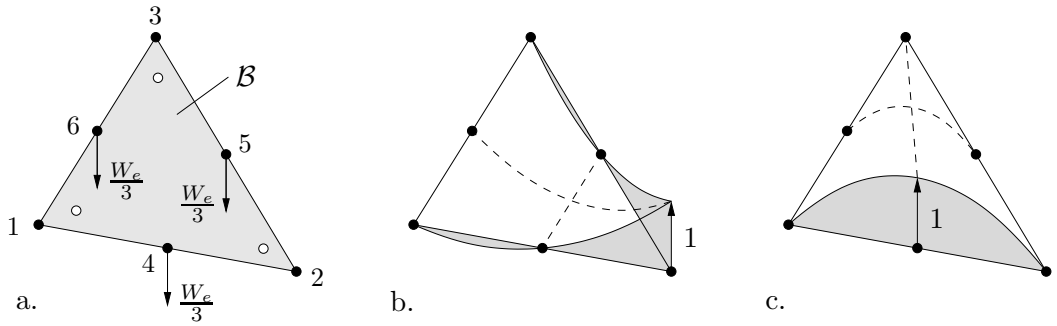

Figure 56: Quadratic triangular element with six nodes, a. node numbering, location of sampling points (empty circles) and 'consistent' body force mapping to the middle nodes, b. corner-node shape function and c. side-node shape function.

$\phi = \hat{\phi}(\xi_1, \xi_2, \xi_3)$ as for example in the integration of the mass matrix or the externally applied surface tractions, the Gauss quadrature rule for integration over a triangular domains $\bar{\mathcal{B}}$ reads

$$\int_{\bar{\mathcal{B}}} \hat{\phi}(\xi_1, \xi_2, \xi_3) \ dV = \frac{1}{2} \sum_{i=1}^{n} W_i J_i \phi_i \tag{6.21}$$

with weight W_i, Jacobian J_i and the function ϕ evaluated at the sampling point i. A three-point integration formula with a degree of precision of 2 is used where the the coordinates of one sampling point are given by $\boldsymbol{\xi} = [2/3, 1/6, 1/6]^T$, the other two coordinates follow by cyclic permutations. Due to symmetry with respect to the area coordinates, the weights are given by $W_i = 1/3$ for $i = 1,2,3$.

6.1.6. Element nodal loads. Element nodal loads are caused by body forces and externally applied surface tractions. Taking $\bar{\boldsymbol{\gamma}}$ as some arbitrary uniform body force throughout the triangular quadratic element, a standard evaluation of $\int_{\bar{\mathcal{B}}} \boldsymbol{N}^T \bar{\boldsymbol{\gamma}} \ dA$ maps the entire force $W_e = \varrho A_e \bar{\boldsymbol{\gamma}}$ in the element equally to the midside nodes, provided that the element sides are straight and side nodes are at the midpoints, see Figure 56a. Clearly, for the multiscale analyses here this form of the attribution is not satisfactory, because a continuous distribution of body forces is supposed to somehow lead to equally distributed nodal loads representing the body forces. Furthermore, a projection of the body forces to the nodes as described would in the assembling lead to disproportionally larger loads on nodes

which belong to two elements compared to those on the edges. Thus, since the body forces only need to be apportioned once to the nodes on the reference configuration, a different method is adopted, see Figure 57. Based on the assumption of a constant density ϱ across

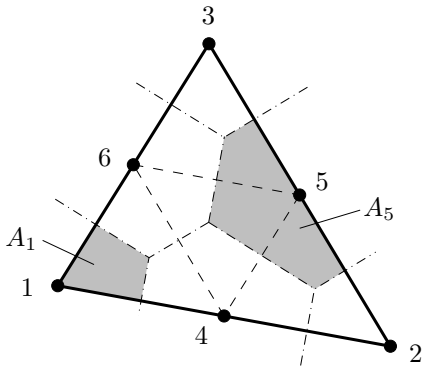

Figure 57: Apportioning of the continuously distributed body forces $\bar{\gamma}$ to all six nodes of a triangular element by means of a Delaunay triangulation. The exemplary grey shaded areas around nodes 1 and 5 describe the portions of the total area of the element that are apportioned to the respective node, that is, A_1 and A_5.

the whole domain, a Delaunay triangulation is used that divides the domain into equal areas around the nodes, see Figure 57. Then the body force vector $\bar{\boldsymbol{\gamma}}$ is multiplied by the density and the areas associated with the node under consideration and assigned as the nodal force,

$$\bar{\boldsymbol{f}}_{b,I} := \varrho A_i \bar{\boldsymbol{\gamma}} \quad \text{at node } I. \tag{6.22}$$

Thus, taking into account the global mesh assembly, each node obtaines an equal part of the body forces directly related to the magnitude of the surrounding area, in contrast to a consistent mapping as shown in Figure 56.

6.2. Solution Procedure of the Coupled Boundary-Value Problems

So far, the macroscopic finite element method in context with an explicit time integration process has been described. The solution process of the microscopic problem was outlined in detail in the previous chapters. In this subchapter, the simultaneous integrated solution process of the coupled boundary value problems on both scales are outlined. The procedure starts on the macroscopic scale where, once and for all, the lumped nodal mass matrix $\bar{\boldsymbol{M}}$ and the nodal body forces $\bar{\boldsymbol{f}}_b$ are computed, see Box 10 (A1). Therein, all variables and technical parameters are initialized and, where appropriate, reset to zero. Prescribed forces and displacements on nodes are imposed incrementally, that is, they are increased in each load step until the maximum prescribed value is reached. In step (A2) the time, prescribed loads and displacements are incrementally increased. Step (A3) comprehends a loop over all elements in the macroscopic mesh. At each sampling point of every finite element, the macroscopic deformation gradient $\bar{\boldsymbol{F}}$ is evaluated, see (A3.1), using the approximation in equation (6.4). This quantity then serves as the primary homogeneous deformation that in the next step is imposed onto the granular microstructure attached at the specific sampling point (A3.2) and therefore drives the structure.

On this microscopic level, this homogeneous deformation and certain history variables comprised in $state_n$ are given, see Box 11 (B1). The deformation is imposed onto the

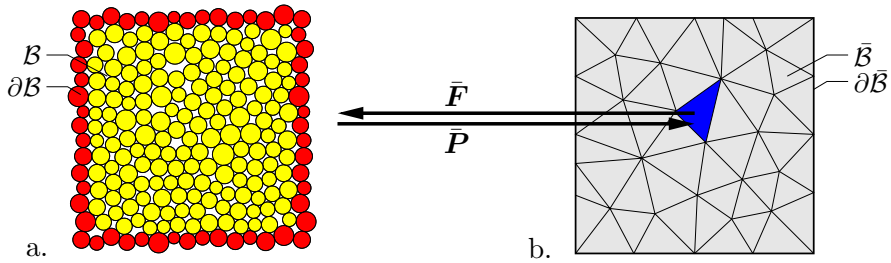

Figure 58: Schematic picture of the coupling of a. micro- and b. macroscopic boundary value problems. From the macroscopic scale, the actual deformation gradient $\bar{\boldsymbol{F}}$ is passed onto the microscopic scale where it serves as the homogeneous part of the deformation. Having computed the total microscopic deformation, the homogenized stress $\bar{\boldsymbol{P}}$ is evaluated and supplied back onto the FE model.

granular structure as described in the previous chapters. For all particle degrees of freedom, the equation of motion is solved (B2). To retain the periodicity constraints of the granular structure, in the next step the penalty correction forces $\boldsymbol{f}_t$ are computed (B3). Furthermore, the new contact branch mesh is determined and the interparticle contact and damping forces are evaluated (B4). If the average microscopic kinetic energy in the system falls below a certain tolerance level, the computation is terminated (B5). If the kinetic energy is higher, the microscopic global damping coefficient α_g is computed (B6) and the loop continues with (B2). If the kinetic energy falls below the tolerance level, the granular structure is considered to be in quasistatic equilibrium. The averaged homogenized first Piola-Kirchhoff stresses $\bar{\boldsymbol{P}}$ are computed (B7) by direct evaluation of micro-macro transitions on the microscale. See equation (3.19) where the stress transformation $\bar{\boldsymbol{P}} = J\bar{\boldsymbol{\sigma}}\bar{\boldsymbol{F}}^{-T}$ is applied. Finally, the actual state of deformation and interparticle plastic parameters

Box 10: Macro Scale: Solution procedure of the coupled IBVPs

(A1) Initialization: Compute nodal masses $\bar{\boldsymbol{M}}$ and body forces $\bar{\boldsymbol{f}}_b$
(A2) Increment time, external loads, prescribed displacements
(A3) In all elements at all Gauss points:
  (A3.1) Determine macroscopic deformation gradient $\bar{\boldsymbol{F}}$
  (A3.2) Exploit microstructure with algorithm in Box 11
  (A3.3) Get homogenized stresses $\bar{\boldsymbol{P}}$ from micro scale
(A4) Compute external forces for prescribed nodal displacements
(A5) Solve macroscopic equation of motion for all nodal d.o.f.'s
(A6) Check relative kinetic energy, if $\bar{E}_{kin}/\bar{E}_{max} < tol$ goto (A8)
(A7) Adjust global damping $\bar{\alpha}_g$, time step Δt and goto (A3)
(A8) Save history data, goto next load step (A2)

are all saved in the current history state $state_{n+1}$ (B8). The homogenized stresses $\bar{\boldsymbol{P}}$ are then passed back to the macroscopic level (A3.3) and the macroscopic solution procedure resumes. Basically, this procedure on the microscopic level serves as the *material model*

for the macroscopic boundary value problem. Note that such granular microstructures are independently attached at each macroscopic sampling point. The transfer of the macroscopic deformation gradient $\bar{\boldsymbol{F}}$ from the macro- to the microscopic scale and the transfer of the micromechanically determined first Piola-Kirchhoff stresses from the micro level back onto the macroscopic ones mark the links between the two boundary value problems, hence the verbalism *two scale boundary value problem*. In Figure 58 the transfer between the two scales is illustrated.

Box 11: Micro Scale: Discrete element solution procedure

(B1) Macroscopic deformation gradient $\bar{\boldsymbol{F}}$ and history $state_n$ given
(B2) Solve equation of motion for all particle d.o.f.s
(B3) Compute penalty correction forces $\boldsymbol{f}_t$ to preserve periodicity
(B4) Compute contact forces $\boldsymbol{f}_c$, $\boldsymbol{f}_d$ from interparticle contacts
(B5) Check kinetic energy, if $E_{kin} < tol$ goto (B7)
(B6) Adjust microscopic global damping α_g and goto (B2)
(B7) In quasistatic equilibrium compute homogenized stresses $\bar{\boldsymbol{P}}$
(B8) Save history $state_{n+1}$ and return to macro level

Back on the macroscopic level (A3.3), with the stresses $\bar{\boldsymbol{P}}$ at hand, it is now an easy and straightforward task to compute the nodal forces for the prescribed boundary values (A4). Subsequently, with the nodal masses and forces at hand, the macroscopic equations of motion are solved for all macroscopic degrees of freedom (A5). Also, the relative average kinetic energy with respect to its maximum value during the load step $\bar{E}_{lin}/\bar{E}_{max}$ is computed (A6). If it falls below a certain tolerance tol, the macroscopic relaxation procedure for this load step terminates, the history data are stored and the next load step is initiated by switching from (A8) to (A2). If the kinetic energy is greater than the tolerance, the global damping parameter $\bar{\alpha}_g$ and the macroscopic time step Δt for the next time step are adaptively adjusted (A7) with the formulas in equations (6.17) and (6.18). The fictitious time within the relaxation procedure is then incremented and the relaxation procedure continues with (A3).

6.3. Applications of Multiscale Analyses

Before the two scale technique is applied to the simulation of granular materials, first and foremost a general question must be answered: How do granular structures fail? Basically, every failure of granular structures can be traced back to a failure in shear, thus the shear strength of a soil material is the primary variable in the modeling. Under the strength of soil materials, usually its resistance to applied shear deformations is understood. The shear strength defines the soil's capacity to absorb shear stresses, it completely governes the compressive strength of a granular material. The shear strength is the principal quantity governing the stability of retaining walls, dams and other slopes. Also, the load capacity of foundations is governed by the shear strength of the embedding soil. In practice, experiments on granular soils can be divided into consolidated drained and unconsolidated, undrained tests. In the numerical simulations at hand, the focus

is restrained to dry soil samples, fluid considerations are not incorporated. It must be mentioned that the micromechanical interaction model used herein is not sophisticated enough to grasp the complete physics. For example, it does not incorporate pore water pressure. As the focus of this work lies on the more fundamental level of homogenization techniques for microscopic and macroscopic scales, *qualitatively* reasonable results are aimed at instead of *quantitative* ones. In fact, the introduction of physically-motivated equations rather than phenomenological ones for pore water pressure and other physical phenomena on the microscopic level is still an intensive research issue.

6.3.1. Example: Compression Test of a Quadratic Specimen. The first example is concerned with a compression test of a quadratic specimen as depicted in Figure 58. Attached at each sampling point is a granular microstructure of 219 circular particles of which 56 build the periodic boundary frame. Thus, 30 links are generated between opposite boundary particles. The radii of the granules in the microstructure lie between $r_{min} = 39$ and $r_{max} = 71$ units. The initial volume density is calculated as $\tilde{\varrho} = 0.82$, the void ratio $e = 0.22$, the porosity $p = 0.18$ and the reference volume of the microstructure follows as $|\mathcal{V}| = 2078160.21$. The macroscopic quadratic FE mesh has a side length $l = 25.0$ units and is made of 50 triangular elements. The top and bottom nodes are fixed, where on the top nodes a vertical displacement is imposed as $d_{max} = 4.0$. The penalty parameters are taken to be $c_p = c_t = 10^8$, the local and the initial global damping parameters are $\alpha_c = 0.01$ and $\alpha_g = 1.0$, respectively. Hardening is not assumed here. The density of the particles is $\varrho = 100.0$ and the interparticle friction angle is 30^o. Laterally, a confining uniform pressure boundary condition is employed as $\bar{\sigma}_0 = 10^5$. The Dirichlet boundary conditions are imposed incrementally over 20 load steps, the von Neumann conditions reach their maximum after the first 10 load steps. The maximum time step length allowed is prescribed as $\Delta t_{max} = 5 \times 10^{-3}$ (although a higher one such as 1×10^{-2} would also work). The initial global damping parameter is given by $\bar{\alpha}_g = 2.0$. Gravity forces are not employed here. The purpose of this example is to investigate some fundamental issues which arise in the coupled simulations of such granular structures. Specifically, the ramifications of the global adaptive damping procedure on the macroscopic scale will be addressed. In Figure 59, the current configurations of the macro mesh and four selected granular microstructure at two macroscopic deformation states a. $d_a = 2.0$ and b. at $d_b = 4.0$ are shown. The macroscopic figures are contour plots where, as a measure of localization, the Frobenius (or Euclidean) norm of the macroscopic rotation $||\bar{\boldsymbol{R}}|| = ||\bar{\boldsymbol{F}}\bar{\boldsymbol{U}}^{-1}|| = (\bar{\boldsymbol{R}} : \bar{\boldsymbol{R}})^{1/2}$ are plotted. For details on the polar decomposition of the deformation gradient and the computation of the macroscopic rotational part $\bar{\boldsymbol{R}}$, see the introductory chapter on large strain continuum mechanics at the beginning of this thesis. Periodic boundary conditions are availed on the microscopic level, the periodicity constraints can clearly be observed in the microstructures plotted in the figures. The test specimen is put under compressive loads. In Figure 60a the load-displacement curve corresponding to the top plate of the macroscopic specimen is plotted. The force F_v plotted is the equivalent load that needs to be imposed vertically in order to reach the prescribed displacement d. The load-displacement curve reaches a maximum at about $d = 1.4$. Until then, almost no sliding between particles occurs on the micro level, the resistance of the structures to deformations are high. Figure 61 shows three microscopic configurations of the upper left microstructure in Figures 59a and b, together with the contact normal force branch meshes. Figure 61a depicts the deformation at a macroscopic deformation state of $d = 1.4$ corresponding to the load peak in Figure 60a. It can clearly be seen that the

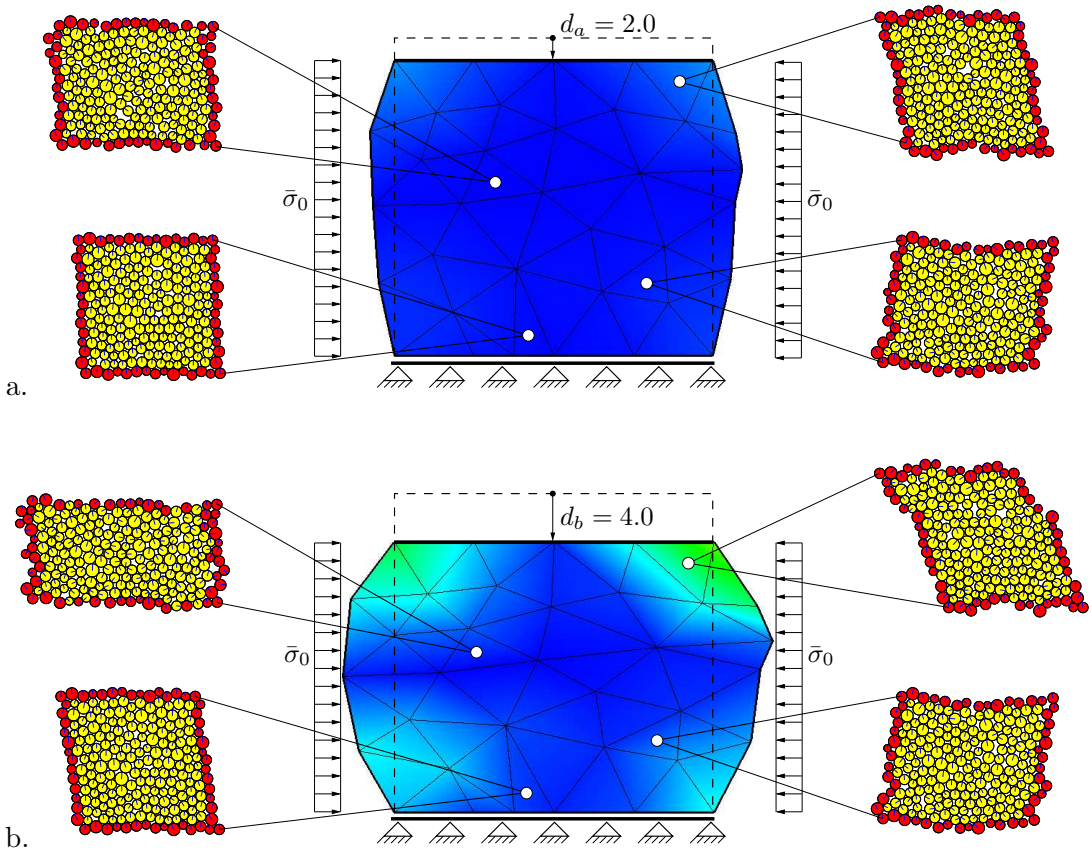

Figure 59: Two-scale simulation of a macroscopically quadratic plane specimen with side length $l = 25.0$ and granular periodic microstructures attached at each sampling point. Top and bottom plates are fixed and the uniform lateral stress is prescribed as $\bar{\sigma}_0 = 10^4$. The figure shows the macroscopic deformation and the microscopic configurations of four selected granular structures at a. macroscopic top displacement of $d_a = 2.0$ and b. at $d_b = 4.0$.

contact normal forces are very high, but the kinematic configuration is quite similar to the initial one. After the load peak, the granules begin to slide against one another and the material fails. The macroscopic load drops considerably as the microstructures rearrange, see Figures 61b,c. Consequently, the interparticle normal forces decrease substantially.

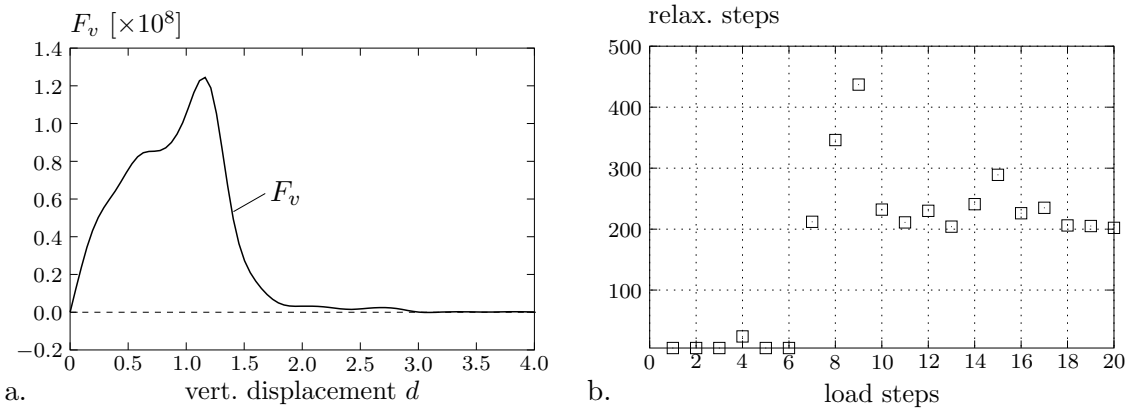

Figure 60: a. Load displacement curve of the biaxial compression test and b. number of relaxation steps that were performed in each load step. The adaptive adjustments of the global damping parameter and the time step lead to a substantial reduction of computing time.

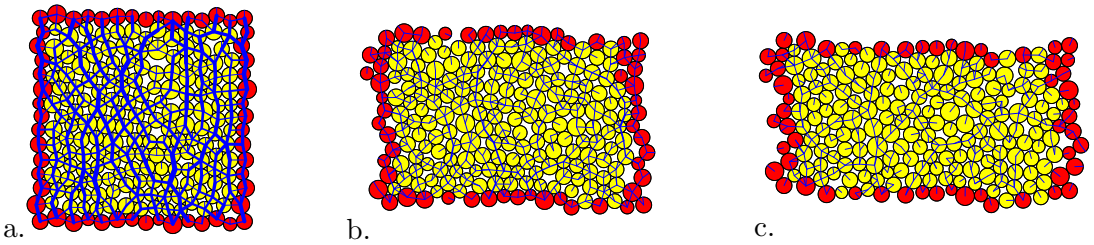

Figure 61: Deformations states of the upper left microstructure in Figure 59 with contact normal force branch mesh at load steps a. $d = 1.4$ (the load peak in Figure 60), b. $d = 2.8$ and c. $d = 4.0$. Clearly, at the load peak in a., the intergranular contact forces are highest.

Consequences of the macroscopic adaptive relaxation procedure as outlined above are depicted in Figure 60b, where the number of relaxation steps that are needed after each load increase to reach static equilibrium are plotted. The number of such steps varies considerably. If adaptive damping was not applied, a maximum number of such relaxation steps would have been needed greater than the maximum number of steps expected (in this case greater than ≈ 430 steps) and the total computing time would have seriously increased. From experience, it is interesting to note that the average number of steps needed depends on the number of finite elements and hence on the number of nodes. That is because deformations need the relaxation steps to 'travel' through the structure. For larger structures, deformations at one end need more time steps to reach the other end, and vice versa. This issue will be discussed in the next example as well where the numerical behavior of a larger finite element mesh is investigated. In Figures 62a and

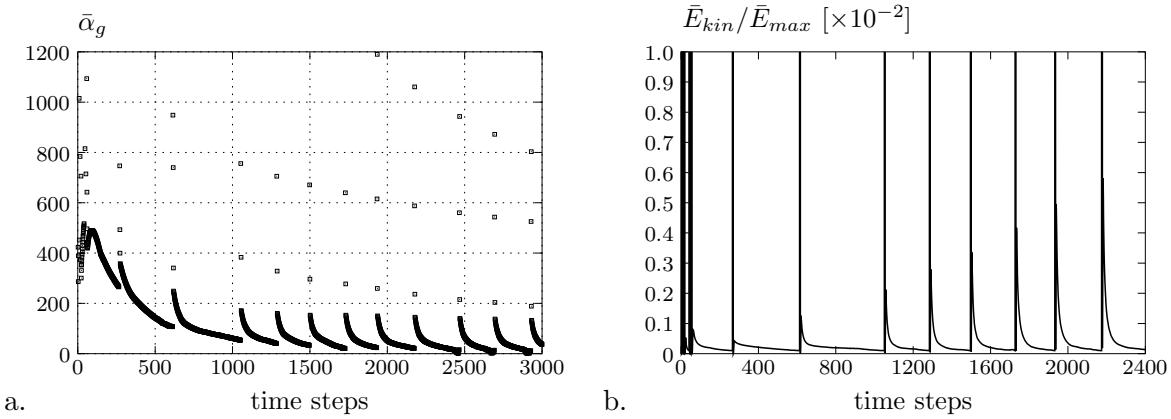

a. b.

Figure 62: a. Adjusted values of the macroscopic relaxation parameter $\bar{\alpha}_g$ during the first 3000 time steps, b. relative macroscopic kinetic energy $\bar{E}_{kin}/\bar{E}_{max}$ during the first 2400 time steps. In both pictures, the shifts to the next load steps can easily be observed.

b, further sequiturs of the adaptive global damping procedure are outlined. In 62a, the adaptively computed macroscopic global damping factors $\bar{\alpha}_g$ versus the first 3000 time steps in the computation are shown. The particular ends of each relaxation procedure and the shift to the following load step can clearly be observed. It is interesting to note that at the end of each relaxation period, the value of the macroscopic damping value decreases. In Figure 62b, the quotient of macroscopic kinetic energy and maximum kinetic energy (within the relaxation period of each load step) are plotted. This value serves as the stop criterion of the relaxation process. That is, once this value falls below a certain tolerance, in this case $tol = 10^{-5}$, the relaxation is terminated, current variables are saved as history data and the new load step is initiated. Observe that at the beginning of such a relaxation

process, the factor $\bar{E}_{kin}/\bar{E}_{max}$ is high but drops quickly, however, the static equilibrium state is attained slowly. Thus, the majority of relaxation time steps brings about only a slight change in this factor.

6.3.2. Application: Simulation of a Biaxial Compression Test. So far, a first introductory example has been shown where its numerical implications have been outlined. As a second example, a biaxial laboratory experiment is chosen for two scale modeling where the actual compression test is numerically simulated.

Experimental setup. The biaxial apparatus selected for the computational simulation is the device that was built and extensively applied in a Grenoble laboratory. It is basically used for testing the strength and dilatancy of particular solids. The apparatus is described in the work Vardoulakis & Goldscheider [117], a comprehensive review of many test results is given in the review paper Desrues & Viggiani [35]. The biaxial

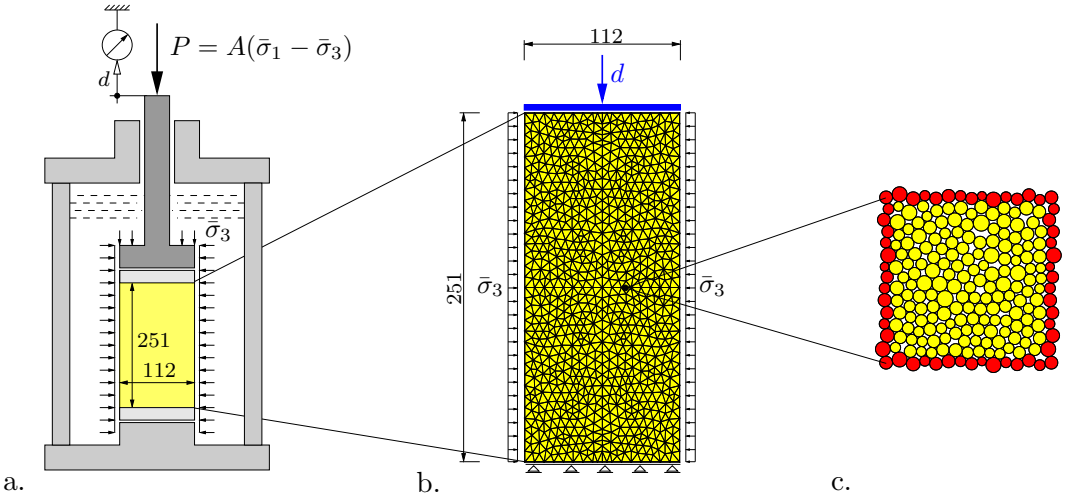

Figure 63: Biaxial test apparatus: a. Cross section through test apparatus (drainage lines omitted), b. macroscopic finite element model with 1604 triangular finite elements and prescribed displacements d and c. microscopic granular structure with 219 circular plane particles. A denotes the cross-sectional horizontal area of the specimen and $\bar{\sigma}_3$ the hydrostatic pressure in which the specimen is placed.

test apparatus allows to experimentally determine the cohesion parameter and mobilized friction angle of a specific soil sample. A prismatic test specimen of granular material is placed into a pressure cell, see Figure 63a. At first the specimen is subjected to a uniform hydrostatic pressure $\bar{\sigma}_3$. The soil specimen is encased by a latex membrane, the hydrostatic pressure imposed through a fluid, e.g. silicone oil, into which the specimen is placed. Finally, a vertical strain-controlled axial compressive loading is applied onto the test specimen by pressing down a rigid die as shown in the figure. The contact surface of the die is lubricated with silicone grease to minimize friction. The hydrostatic lateral pressure $\bar{\sigma}_3$ is kept constant during axial loading. Such sophisticated test apparatuses allow the soil to drain during consolidation and/or shearing through filter layers either on one or on both ends of the soil sample. The test apparatus and the associated two dimensional finite element model with which the laboratory experiment is computationally modeled are depicted in Figure 63. Due to many possible variations in $\bar{\sigma}_1$ and $\bar{\sigma}_3$, various environmental boundary conditions can be simulated.

Numerical Models. The numerical models consist of boundary value problems on

both the discrete microscopic scale and the continuous macroscopic one. The aim here is to simulate the test named `shf03` of the reference DESRUES & VIGGIANI [35]. This test is a biaxial plane strain compression test of a specimen of dry Hostun sand with specimen dimensions $112 \times 251mm$ that yields doubly symmetric localized zones and shear bands that develop cross-diagonally through the test specimen. On the macroscopic side, bearing that result in mind allowed only one fourth of the test specimen to be modeled. Therefore, only the upper left quarter is modeled by a finite element mesh of 401 triangular elements with 227 nodes giving about 500 macroscopic degrees of freedom. On the right side the horizontal degrees of freedom are fixed, whereas on the bottom side the vertical ones are. On the left side, a hydrostatic uniform pressure is applied onto the solid, the uniformly distributed load is transformed into equivalent nodal loads. The top degrees of freedom are fixed where vertical downward displacements are incrementally prescribed onto the top nodes during the course of deformation. On the microscopic side, the same granular microstructure as used in the previous example with 219 circular plane particles is employed, giving a total of about one million microscopic degrees of freedom for the complete structure. Of course, periodic boundary constraints are enforced on the microscopic system. The maximum macroscopic time step is prescribed as $\Delta t_{max} =$

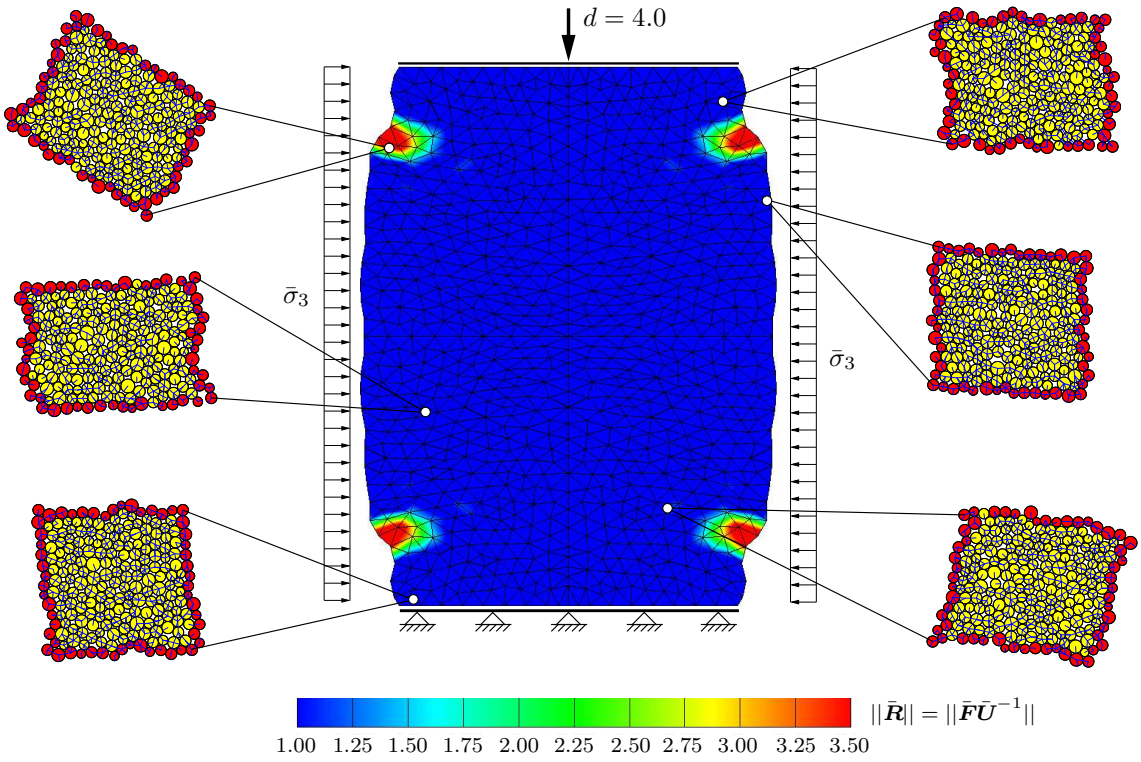

Figure 64: Coupled two-scale simulation of a biaxial compression test with macroscopic finite element mesh and six selected granular microstructures of 256 circular particles in the deformed configuration $d = 4.0$. Due to symmetry, only one quarter of the specimen is simulated. The macroscopic vertical deformation was applied in a strain-controlled process. The constant hydrostatic pressure in which the test specimen was placed was simulated by a lateral constant stress on the nodes.

1×10^{-2}, the prescribed forces (lateral stresses) and displacements are imposed in 8 and 40 load steps, respectively. The fictitious macroscopic density is taken to be $\bar{\varrho} = 100.0$ and the initial global damping parameter is $\bar{\alpha}_g = 50.0$. On the microscopic side, the local and

initial global damping parameters are $\alpha_c = 0.01$ and $\alpha_g = 1.0$, respectively. Hardening is not considered. The density of the particles is taken to be $\varrho = 100.0$ and the interparticle friction angle is 30^o. In the above mentioned papers, several identical tests were performed where each test yielded different localized shear zones. In order to match the pattern of test `shf03`, the microscopic interparticle friction angle is slightly reduced in the finite elements where the shear band is expected to develop. Through this reduction, the onset of the localization is basically triggered. The lateral stress is equally increased during the first 8 load steps up to a final value of $\bar{\sigma}_3 = 8/3 \cdot 10^4$. The total downward displacements $d = -2.0$ of the top nodes is applied during 40 macroscopic load steps.

Results and Discussion. In Figure 64 the assembled deformed macroscopic structure with a top displacement of $d = -4.0$ and four representative granular microstructures at selected elements and sampling points are plotted. The localized zone has successfully been triggered and the shear bands have already started to develop inwardly. The contour plot shows the Frobenius norm $||\bar{\boldsymbol{R}}|| = ||\bar{\boldsymbol{F}}\bar{\boldsymbol{U}}^{-1}||$ of the rotational part of the deformation, for a discussion of this norm see the first example. In Figure 65 the relation of the

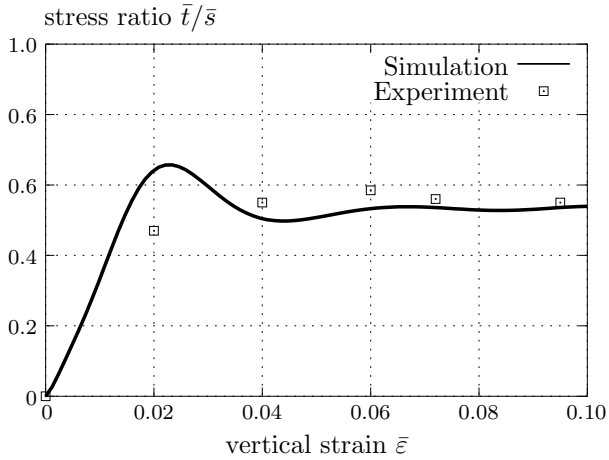

Figure 65: Roscoe stress measure $\bar{t}/\bar{s}$ versus axial strain $\bar{\varepsilon}$ obtained from the biaxial compression simulation and comparison with experimental results of the paper Desrues & Viggiani [35].

Roscoe planar stress measures $\bar{s}/\bar{t}$ against the logarithmic axial strain $\bar{\varepsilon}$ is plotted and compared with the experimental results of Desrues & Viggiani [35]. The stress and strain measures are computed as

$$\bar{s} = \frac{1}{2}(\bar{\sigma}_1 - \bar{\sigma}_3) > 0 \,, \quad \bar{t} = \frac{1}{2}(\bar{\sigma}_1 + \bar{\sigma}_3) \geq 0 \quad \text{and} \quad \bar{\varepsilon} = -\ln \frac{H}{H_0} \,,$$

where H and H_0 are the actual and initial heights of the macroscopic specimen and $\bar{\sigma}_1$ and $\bar{\sigma}_3$ denote the major principal stress and hydrostatic macroscopic stress in the specimen, respectively. $\bar{t}$ denotes the deviatoric and $\bar{s}$ the mean Roscoe planar stresses. Observe that the effective mobilized friction angle ϕ_m can be computed as $\sin(\phi_m) = \bar{t}/\bar{s}$, see the above mentioned paper and the references therein. Here, a distinction between effective and total stresses is not made since in the computational simulation, pore water pressure is not considered and hence the total stresses conform with the effective ones. The first part of the load-displacement curve in Figure 65 shows a stiffer behavior than the experimentally determined values. The softer behavior of the experiment is thought to be attributed to the lubrication of the top die that minimizes friction between the die and the

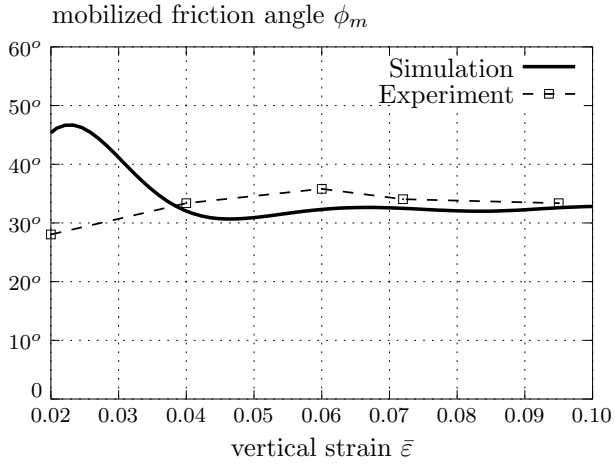

Figure 66: Effective mobilized friction angle ϕ_m versus axial strain $\bar{\varepsilon}$; comparison of numerical simulation and experimental results of Desrues & Viggiani [35].

specimen. That lubrication lets the top particles move not only vertically but also dodge horizontally under the applied load. In the macroscopic boundary value problem, the top nodes are fixed in both directions and only a vertical displacement is prescribed that results in the initially stiffer behavior. The influence of this effect vanishes with increasing load. In Figure 66 the macroscopic mobilized friction angles ϕ_m of the simulation and the experiment are plotted versus the axial strain $\bar{\varepsilon}$ where the lateral stress $\bar{\sigma}_3$ has reached its maximum. Initially, the simulated ϕ_m is higher due to the lack of lubrication present in the boundary value problem. As the vertical strain advances, the simulation and experiment reach almost similar values of about $\phi_m \approx 33^o$. Note that on the microscopic level, in each and every relaxation step about an average of 230 000 interparticle contacts are evaluated.

In Figure 67, the development of the relative macroscopic kinetic energy $\bar{E}_{kin}/\bar{E}_{max}$ is

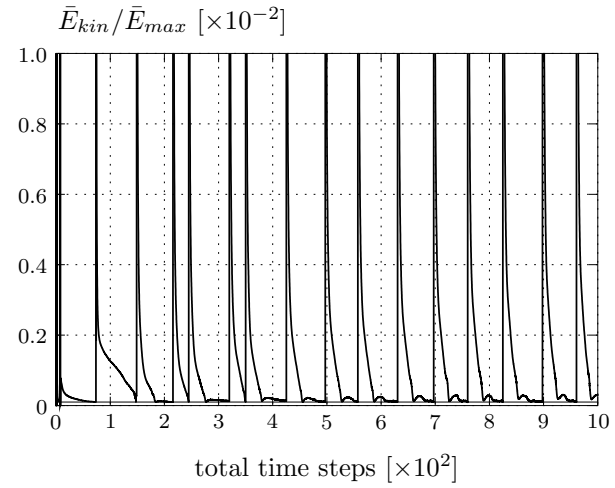

Figure 67: Relative macroscopic kinetic energy $\bar{E}_{kin}/\bar{E}_{max}$ during the first 10000 time steps, which cover about 16 macroscopic load steps, of the macroscopic simulation. The particular load steps and relaxation cycles can easily be observed.

plotted against the overall macroscopic time steps. The relaxation to the quasistatic states can easily be grasped. Observe that the relaxation process in the first few steps differs from the other. At this stage the structure is not under enough compression. The quasistatic states are still attained but the development of the kinetic energies differs since more

dynamics and oscillations are allowed within the granular microstructures. Nevertheless, the macro- and microscopic models and their simulations still represent a reduction of the true natural systems or structures: focus is put onto circular particles and pore water pressure is not considered, just to name a few issues. The goal here was the development and justification of a two-scale simulation method, not its ability to yet grasp all physically relevant phenomena of the material modeled. The computational modeling of granular materials is currently still an important research topic. Better and more advanced results in the context of discrete modeling techniques inevitably come along with the availability of more powerful computers. However, today's ever increasing computational resources will certainly provide for better, faster and physically more exact results in the future.

7. Atomistic Simulations on the Nano Scale

In classical continuum mechanics, the constitutive laws that describe the material behavior are based on an idealized macroscopic phenomenology and an assumed quasi-continuous distribution of the field variables such as strain and temperature. This purely phenomenological description excludes the ultimate particulate structure of the materials on the nanoscale; the atomistic degrees of freedom are *smeared out*, see Figures 68 and 78.

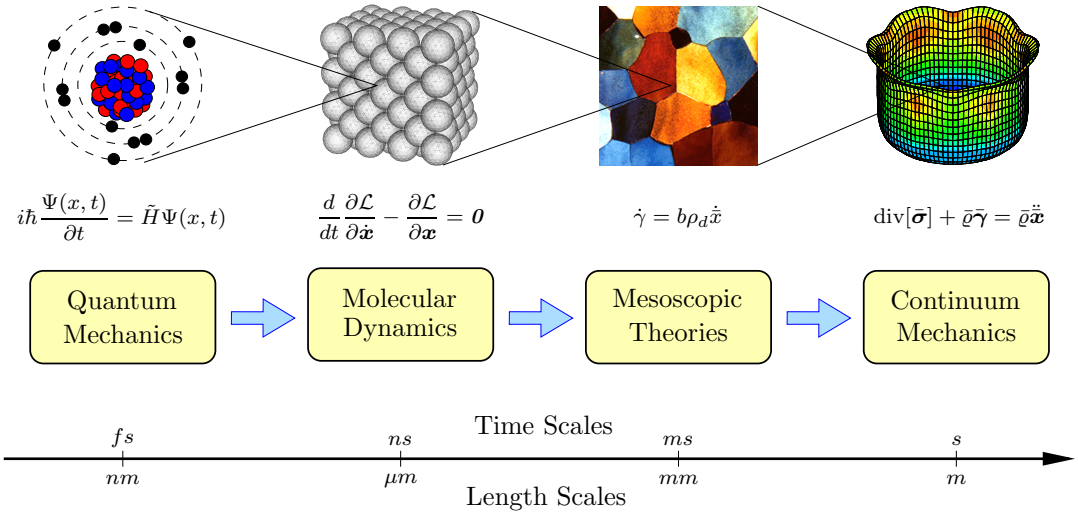

Figure 68: Several simulation tools are used on the different time and length scales. Quantum mechanics focuses on the subatomic scale, molecular dynamics on the interactions between atoms. Mesoscale theories span the bridge to the purely phenomenologic models used in continuum mechanics.

On the other hand, if one focuses on the nanostructure of materials, processes observed here should form the basis for the observed or measured macroscopic behavior. Computations on the atomistic level are meant to inform higher-level mesoscopic continuum descriptions of the materials. The understanding of the coupling between structure and deformation mechanisms at the nanoscale affects the funtionality and reliability of newly developed engineering materials; it is still one of the greatest challenges in modeling and simulation. On the nanoscale, the microscopic degrees of freedom and their evolutions are explicitly treated which is computationally absolutely ineffective. To resolve this difficulty in large-scale simulations, continuum methods such as the finite element method can be employed to model the large-scale specimen without accurate modeling of the nano scale physics. Nanoscopically, atomistic methods are used where the nano scale physics need to be modeled accurately. The coupling of the two methods can finally be achieved through the concept of dynamic homogenization where atomistic quantities are averaged in some sense and inform the coarse scale finite element method.

7.1. Current State of Research

Atomistic methods and the molecular dynamics technique were initially developed for the computational simulation of gases and thus for fluids. These first methods were solely focused on single scales. A first concept of homogenization was introduced by developing expressions for the pressure in such a gas (aggregate of particles) starting from the

so-called virial theorem of Clausius, see for example Allen & Tildesley [2], Frenkel & Smit [42] or Haile [46]. The virial pressure equation can be seen as a first step towards scale bridging in atomistics. The virial equation has served as a starting point for various efforts to derive formulations for the so-called virial stress tensor that is meant to describe the current state of stress in an atomistic solid. Ever since, the development of scale bridging techniques for atomistic structures has been a key research focus and still represents a challenging topic in nanomechanics. It requires a combination of theoretical notions from physics, mechanics, chemistry and materials science. Current important research areas of atomistic scale bridging methods are multiple scale techniques that bridge different time and length scales, homogenization approaches and coupling with statistical mechanics. A very popular method coupling atomistics and higher scales, though without the concept of homogenization, is the quasicontinuum (QC) method, initially developed by Tadmor [110] and Tadmor, Ortiz & Phillips [111]. A recent review paper on the current state of the method is provided in Miller & Tadmor [85]. Therein, atomistic (molecular dynamics) and continuum (finite element technique) methods for the simulation of the mechanical response of polycrystalline materials are linked. The number of degrees of freedom that a full molecular dynamics computation of the same domain would possess is substantially reduced. Specifically, full atomistic resolution is only maintained in regions where defects develop, for example dislocations. Adaptivity techniques are employed to adapt the finite element mesh in the region with full atomistic resolution to the propagation of the deformation. The remaining regions usually represent the majority of the specimen simulated and are assumed to be governed by homogeneous elastic deformations and particulary the Cauchy-Born rule. This Cauchy-Born rule assumes that a uniform higher scale deformation $\bar{\boldsymbol{F}}$ can directly be mapped to the same deformation on the nanoscopic scale. Essentially, the Cauchy-Born rule here represents the link between the atomistic and higher scales in elastically deforming regions. The deformations in these regions are approximately computed using finite elements. Each of them covers a domain with a possibly large number of atoms. Thus, the degrees of freedom of all these atoms are reduced to only the nodal degrees of freedom of the nodes of the specific finite element. With the classical version of the quasicontinuum methods, crystals could only be simulated at zero temperature, and the problems reduced to lattice statics. Recently however, extensions of the method to finite temperatures have been developed and the method is still in constant development by a great community of researchers.

An analytical approach to couple continuum, molecular dynamics and semi-empirical tight binding methods is given in the papers Abraham, Broughton, Bernstein & Kaxiras [40, 17]. These authors introduce so-called 'handshake' potentials in regions where finite element, molecular dynamics and the tight-binding domains overlap and integrate the equations of motions of all three methods forward using the same time step. A numerical drawback of all methods that employ the finite element method and grade the meshes down to the atomistic spacing is that the time step in the simulation is consequently governed by the smallest element in the mesh. If full atomistic resolution is used, it would be the nearest-neighbor interatomic distance in the lattice. Thus, many time steps would be wasted in such simulations. Moreover, it seems unphysical that variables at the higher level evolve at time scales of the underlying atomistic level, see Park & Liu [97]. Other problems in such simulations are wave reflections at the atomistic/ FE interfaces or, in the quasicontinuum method, so-called ghost forces. These issues, altthough they have been partially solved by employing artifical or computational tricks, can be circum-

vented by using the concept of dynamic homogenization of atomistic aggregates. In these approaches, overlapping regions with different simulation tools are not needed, instead, the boundary constraints used are crucial for the accurate simulation of the structure. Also, the issue of the driving of the nanosystem is important with regard to a coupling to the simulation tool on the higher scale. Some works that deal with simulations of atomistic nanosystems in the context of stress-driven mesoscopic approaches are for example Parrinello & Rahman [100], Ashurst & Hoover [5], deCelis, Argon & Yip [32] and the recent work Cleri [26] with a new stress-controlled multiple scale approach. These formulations will be discussed in more detail in section 9.4 on atomistic boundary constraints. In the present work however, a new *deformation-controlled* uniform traction boundary constraint in the fully dynamic context is presented suitable for implementation into large-scale engineering computations. It represents a dynamic extension of the formulation outlined in the context of static homogenization of granular media, see the first part of this work. However, it is shown that only the uniform traction constraints are appropriate for use with atomistic nanosystems since only these constraints allow defects and cracks to propagate through such structures. In the author's opinion, the uniform traction constraint combined with the deformation-controlled implementation is a novel formulation in literature on homogenization techniques for atomistic systems.

7.2. Molecular Dynamics Technique

In this section, the basic structure of classical molecular dynamic algorithms is discussed. It is partly based on the introductory textbooks of Allen & Tildesley [2], Frenkel & Smit [42] and finally Haile [46]. An ensemble of spherical particles which represent the atoms and their associated electron shells is considered. These particles are henceforth denoted as atoms. Such an ensemble can for example be an fcc (*f*ace-*c*entered-*c*ubic) crystal. In the examples section, metallic structures with such fcc properties are investigated. The term *molecular dynamics* (MD) denotes a computer simulation method where the temporal evolution of some set of atoms (particles) is followed through integration of the governing equation of motion. In molecular dynamics, this equation is Newton's first law

$$\boldsymbol{f}_i = m_i \ddot{\boldsymbol{x}}_i \quad \text{for all } i = 1, \dots N \tag{7.1}$$

for each atom $\mathcal{A}_i$ in the ensemble of N atoms. m_i is the atomic mass, $\ddot{\boldsymbol{x}}_i = \partial^2 \boldsymbol{x}_i / \partial t^2$ its acceleration and $\boldsymbol{f}_i$ the force acting on the particular atom. This force is due to the interaction with other atoms. Therefore, molecular dynamics is also termed a *deterministic* technique where, based on a given set of positions and atom properties, the subsequent time evolution is completely determined. Based on Newton's first law, the simulations compute $6N$-dimensional trajectories of the atoms in the so-called *phase space* made of $3N$ atom coordinates and $3N$ momenta. Therefore, the molecular dynamics technique is a form of statistical mechanics. A trajectory obtained from molecular dynamics provides a set of configurations which in turn yields certain homogenized physical quantities on the next higher scale. These homogenized quantities are computed as arithmetic averages of the various instantaneous values assumed by the yielded quantities during the molecular dynamics simulation. Statistical mechanics is the link between the behavior on the nanoscale and thermodynamics. In the limit of very long simulation times, the phase space can be expected to be fully sampled. In that limit the averaging process for some thermodynamic quantities would yield the exact properties. Practically, the simulation runs are

only of finite lengths and the results may therefore deviate from the exact ones. Hence, caution should be exerted in the assessment of the properties obtained from statistical sampling.

7.3. Restrictions of Atomistic Simulations

With today's powerful computers, molecular dynamics simulations can be performed with systems of tens of thousands or even millions of atoms and for simulations times of femtoseconds up to hundreds of nanoseconds. Nevertheless, overcoming time and size limitations are the most tackled aspects in today's research in nanoscale mechanics. Results of a simulation are reliable when the simulation time is much longer than the relaxation time of the macroscopic quantities that are sampled. It is notable that different properties need different time periods to relax. For example, systems tend to slow down in the proximity of phase transitions and the relaxation time is many orders of magnitudes larger than the times that are simulated by the computer. Also, the size of the ensemble can also pose a problem in that some correlation lengths might be larger than the size of the system under consideration, for example long-range forces or long-range waves.

In summary, molecular dynamics is a powerful tool but has its restrictions. For example, it is known that atoms at the quantum level obey quantum laws (i.e. the Schrödinger equation) rather than Newton's classical law. For the purposes of solid bodies considered here this classical approximation is still very good. Bad approximations arise for example for fluids at the triple point and very light atomic systems such as hydrogen, helium and neon. Moreover, the quantum effects one scale below the atomistic level become important at very low temperatures. They are measurable for example in the anomalous behavior of the thermal expansion coefficient or the specific heat of crystals below the Debye temperature. The Debye temperature is the temperature of a crystal's highest normal mode of vibration in which all atoms move with the same frequency and phase.

7.4. Lagrangian of Second Kind and Energy Contributions

Another formulation of Newton's first law is the *Lagrangian of second kind* equation of motion that governs the system's time evolution and mechanical properties. For all atoms in the system, it reads

$$\frac{d}{dt}\frac{\partial \mathcal{L}(\dot{\boldsymbol{x}}, \boldsymbol{x})}{\partial \dot{\boldsymbol{x}}} - \frac{\partial \mathcal{L}(\dot{\boldsymbol{x}}, \boldsymbol{x})}{\partial \boldsymbol{x}} = \boldsymbol{0} \tag{7.2}$$

with the Lagrange function $\mathcal{L}(\dot{\boldsymbol{x}}, \boldsymbol{x}) = \mathcal{K}(\dot{\boldsymbol{x}}) - \mathcal{U}(\boldsymbol{x})$ in terms of the generalized coordinates $\boldsymbol{x}$ and temporal derivatives $\dot{\boldsymbol{x}}$ of the *molecular centers of masses* of the particles. Note that the kinetic energy is assumed to only depend on the *atom velocities* $\mathcal{K} = \hat{\mathcal{K}}(\dot{\boldsymbol{x}})$ and the potential energy term only on the actual *atom positions*, $\mathcal{U} = \hat{\mathcal{U}}(\boldsymbol{x})$. The kinetic energy term with the conjugate momenta $\boldsymbol{p}_i = m_i \dot{\boldsymbol{x}}_i$ of a typical particle $\mathcal{A}_i$ is given by

$$\mathcal{K}(\boldsymbol{x}) = \frac{1}{2}\sum_{i=1}^{N} \frac{1}{m_i}\boldsymbol{p}_i^2 = \frac{1}{2}\sum_{i=1}^{N} m_i \dot{\boldsymbol{x}}_i^2 \ . \tag{7.3}$$

Here, m_i denotes the mass of particle $\mathcal{A}_i$. The potential energy contribution to the total energy of the system reads

$$\mathcal{U}(\boldsymbol{x}) = \sum_{i=1}^{N} \phi_i(\boldsymbol{x}_i) + \sum_{i=1}^{N}\sum_{j>i}^{N} \phi_{ij}(\boldsymbol{x}_i, \boldsymbol{x}_j) + \sum_{i=1}^{N}\sum_{j>i}^{N}\sum_{k>j>i}^{N} \phi_{ijk}(\boldsymbol{x}_i, \boldsymbol{x}_j, \boldsymbol{x}_k) + \dots \tag{7.4}$$

Therein, $\phi_i(\boldsymbol{x}_i)$ describes the potential of externally applied boundary values. $\phi_{ij}(\boldsymbol{x}_i, \boldsymbol{x}_j)$ denotes the so-called two-body atom interaction potential of forces acting between two atoms. The three-body potential $\phi_{ijk}(\boldsymbol{x}_i, \boldsymbol{x}_j, \boldsymbol{x}_k)$ describes potential energy contributions based on not only the positions of the three interacting atoms $\mathcal{A}_i$, $\mathcal{A}_j$ and $\mathcal{A}_k$, but also accounts for their angular dependencies. Higher-order potential contributions are small compared to the ones described above and thus usually neglected in computer simulations. Three-body contributions of the form ϕ_{ijk} are computationally costly and often implicitly subsumed into *effective pair potentials* ϕ_{ij}^{eff}, such that the potential energy term contracts to a form

$$\mathcal{U}(\boldsymbol{x}) \approx \sum_{i=1}^{N} \phi_i(\boldsymbol{x}_i) + \sum_{i=1}^{N} \sum_{j>i}^{N} \phi_{ij}^{eff}(r_{ij} = |\boldsymbol{x}_j - \boldsymbol{x}_i|) \ . \tag{7.5}$$

As a consequence, such effective pair potentials ϕ_{ij}^{eff} may depend on the density, ensemble temperature and other quantities of the system, while the true potentials do not. There exists a wide spectrum of potential formulations in literature and the choice of the particular (effective) potential ϕ_{ij} depends on the material and the desired degree of accuracy. In the next chapter several popular two- and three-body interaction potentials are presented.

7.5. Molecular Dynamics at Finite Temperatures

In the context of molecular dynamics simulations, temperature is really a thermodynamic quantity and therefore also termed *thermodynamic temperature*. This temperature is nothing more than a measure of the average kinetic energy of all N atoms in the system, related by the *Boltzmann* constant k_B in the expressions for the kinetic energy

$$\mathcal{K} = \frac{1}{2} \sum_{i=1}^{N} m_i v_i^2 =: \frac{3k_B}{2} \sum_{i=1}^{N} T_i \ . \tag{7.6}$$

The Boltzmann constant goes back to the Austrian physicist Ludwig Boltzmann [1844–1906] and relates temperature and kinetic energy, so it is really a factor of unit conversion, specified by $k_B = 1.380\,662 \cdot 10^{-23} J/K = 8.617\,380 \cdot 10^5 eV/K$. In computer implementations, the *equipartition theorem of kinetic energy* is used in order to compute and distribute the atom velocities due to thermodynamic temperature. Therein, the degrees of freedom of an atom are associated with the kinetic energy of translations and possibly rotations and vibrations. The equipartition theorem of kinetic energy states that in a three dimensional system in equilibrium, each component of the average kinetic energy makes the same contribution to the temperature,

$$T = \frac{m}{3k_B N} \sum_{i=1}^{N} \boldsymbol{v}_i \cdot \boldsymbol{v}_i \ . \tag{7.7}$$

Thus for computer simulations, in a very first step the initial temperature must be imposed onto the system as kinetic energy. For this purpose, random initial velocities are generated using four independent normally distributed random numbers for each atom. These initial atom velocities $\boldsymbol{v}_i = \dot{\boldsymbol{x}}_i$ are then corrected in order to conserve a zero overall momentum $\boldsymbol{P} = \sum_{i=1}^{N} m_i \boldsymbol{v}_i^2 = 0$, i.e.

$$\boldsymbol{v}_i \Leftarrow \boldsymbol{v}_i - \frac{1}{N} \sum_{I=1}^{N} \boldsymbol{v}_I \quad \text{for all atoms } i = 1, \ldots, N \ . \tag{7.8}$$

These initial velocities then represent a particular macroscopic temperature T_0. In a second step, they are then scaled to represent the required temperature by

$$\boldsymbol{v}_i \Leftarrow \boldsymbol{v}_i \cdot \sqrt{\frac{T_0}{T}} \tag{7.9}$$

where the actual temperature T follows from the *equipartition theorem*, see the above equation (7.7).

7.6. Time Discretization: Verlet Integration

The explicit *Verlet* integration algorithm is one of the most popular schemes to integrate Newton's first law in the context of molecular dynamics simulations. It is attributed to Verlet (1967). It is a direct solution of Newton's first law $m_i\ddot{\boldsymbol{x}}_i = \boldsymbol{f}_i$ where $\ddot{\boldsymbol{x}}$ denotes the acceleration of the atom $\mathcal{A}_i$, m_i its mass and $\boldsymbol{f}_i$ the total force. A Taylor expansions of the position variable $\boldsymbol{x}$ at the previous $[t_n - \Delta t]$ and actual $[t_n + \Delta t]$ time steps gives

$$\begin{aligned} \boldsymbol{x}(t_n + \Delta t) &= \boldsymbol{x}(t_n) + \Delta t\dot{\boldsymbol{x}}(t_n) + \tfrac{1}{2}\Delta t^2\ddot{\boldsymbol{x}}(t_n) + \dots \\ \boldsymbol{x}(t_n - \Delta t) &= \boldsymbol{x}(t_n) - \Delta t\dot{\boldsymbol{x}}(t_n) + \tfrac{1}{2}\Delta t^2\ddot{\boldsymbol{x}}(t_n) - \dots \end{aligned} \tag{7.10}$$

Addition of these two equations yields the update formula for the positions as

$$\boldsymbol{x}(t_n + \Delta t) = 2\boldsymbol{x}(t_n) - \boldsymbol{x}(t_n - \Delta t) + \Delta t^2\ddot{\boldsymbol{x}}(t_n) \tag{7.11}$$

that is exact except for errors of order Δt^4. This is a very compact algorithm and easy to program. It possesses excellent energy conservation properties due to its time-reversibility. On the other hand, the downside is the bad handling of velocities, since the solution at $(t_n + \Delta t)$ is needed before the velocity $\dot{\boldsymbol{x}}_n$ can be obtained. Moreover, the algorithm might be sensitive to truncation errors since in equations (7.10), small numbers $\frac{1}{2}\Delta t^2\ddot{\boldsymbol{x}}(t_n)$ are added to the differences of two large numbers. The velocities $\dot{\boldsymbol{x}}$ of the atoms do not explicitly appear in (7.11), but for an estimate of the kinetic energies they can be computed as

$$\dot{\boldsymbol{x}}(t_n) = \frac{\boldsymbol{x}(t_n + \Delta t) - \boldsymbol{x}(t - \Delta t)}{2\Delta t} \tag{7.12}$$

subject to errors of order Δt^2. An improvement to the Verlet algorithm is for example given by the *Beeman* algorithm, see Beeman [13], where the positions $\boldsymbol{x}$ are identical with the ones obtained with the classical Verlet algorithm, but the velocities are more accurate. Further improvements in the accuracy can be achieved by employing the *Predictor-Corrector* scheme, see for example Rahman [103], where positions, velocites and accelerations at the actual time $(t_n + \Delta t)$ are at first predicted and in a second step corrected.

8. Empirical Interatomic Potentials

In molecular dynamics, the forces that act between the atoms are derived from interatomic potential energy functions, therefore modeling of materials basically boils down to finding an adequate potential function. The physical properties predicted by an atomistic simulation are only as good as the quality of the underlying interatomic potential. Knowing that the quantum mechanical behavior is essentially governed by the Schrödinger equation rather than Newton's first law, the question is whether such a potential function really exists. It is well-known that an ensemble of interacting atoms is really made of nuclei and associated electrons that interact among each other. The Hamiltonian that characterizes motions and interactions of all nuclei and electrons in such a system of interest is given by

$$\mathcal{H} = \sum_i \frac{\boldsymbol{P}_i^2}{2M} + \sum_j \frac{\boldsymbol{p}_j^2}{2m} + \frac{1}{2}\sum_{ij} \frac{e^2}{|\boldsymbol{r}_i - \boldsymbol{r}_j|} - \sum_{ij} \frac{Ze^2}{|\boldsymbol{r}_i - \boldsymbol{R}_j|} + \sum_{ij} \frac{Z^2e^2}{|\boldsymbol{R}_i - \boldsymbol{R}_j|} \,, \quad (8.1)$$

with the electron and nuclei masses m and M, momenta $\boldsymbol{p}$ and $\boldsymbol{P}$ and position vectors $\boldsymbol{r}$ and $\boldsymbol{R}$. Z denotes the atomic number. Note that the five terms refer to the kinetic energy of the nuclei, kinetic energy of the electrons, Coulomb interaction between electrons, Coulomb interaction between electrons and nucleus, and the Coulomb interaction among the nuclei, respectively.

In that respect, the question arises of how realistic a molecular dynamics simulation can be. As mentioned above, in molecular dynamics atoms interact with each other through interatomic forces and the atom positions and momenta evolve under the action of those instantaneous forces. As the atoms move, the relative positions change and therefore the interaction forces change accordingly. Thus, the physics of the systems are essentially constituted by the forces. As a consequence, the computer simulation is realistic only to the extent that the interatomic forces are similar to those that the real atoms would experience when arranged in exactly the same configuration. The interatomic forces are usually obtained as the gradients of potential energy functions. Several such empirical functions are described below. These potential functions depend on the relative positions of the atoms. Hence, the quality of the simulation strongly depends on the ability of the potential to reproduce the behavior of the material under the conditions (boundary, temperature, pressure and so on) at which the simulation is performed.

8.1. Interatomic Bonding

Interatomic potentials can become quite complex. One reason for the complexity that arises in the quest for capturing all effects is founded in the nature of different interatomic bonds. Bonding is basically the attraction between positive and negative charges, specifically the positive charge of the nucleus and the negative charge of the electrons. The different tendencies of atoms to gain or lose electrons allow them to attract one another in various ways and form different kinds of bonds. Ignoring inert gases here since they are not good at forming bonds, there are two types of atoms, namely metallic and nonmetallic atoms. These atoms can be bonded together in three primary ways of chemical bonding: (i) metal atoms can bond to other metal atoms by the so-called *metallic bonding*, (ii) nonmetal atoms can bond to other nonmetal atoms by non-metallic bonding, called *covalent bonding*, and (iii) metal atoms can bond to nonmetal atoms in *ionic bonding*. In addition, van der Waals-type bonding should also be mentioned. It is of minor effect at

short ranges, but governs the long-range interactions that become important in certain atomistic simulations such as when two slabs of materials are brought into contact. Ionic and covalent bonding are most important in chemistry because they can result in the formation of compounds. On the other hand, metallic bonding results in the formation of alloys rather than compounds. In this section, the three strong bonding types and the weak van der Waals forces are briefly outlined.

Ionic Bonding. Ionic bonding is the easiest of the bond types to comprehend because it goes with the idea that opposites attract. Specifically, opposite electric charges attract one another. Normally, atoms are neutral with no charge, but metallic atoms tend to lose electrons. When they do, they become positively charged ions called cations. On the other hand, non-metallic atoms tend to gain electrons to become negatively charged ions, the so-called anions. These oppositely charged cations and anions then attract each other because of their opposite charges. This attraction is called an *ionic bond*. The charge of an ion is often refered to as the oxidation state of that element. Ionic bonding is non-directional, that is, the magnitude of the bonds is equal in all directions around the ion. Furthermore, high bonding energies result in high melting temperatures. Ionic bonding generally occurs in hard and brittle materials, it is the most common type of bonding for ceramic materials and they have electrical and thermal insulative properties.

Covalent Bonding. Covalent bonding is the strong attraction that holds together the atoms of non-metallic elements. This type of bonding is associated with a great variety of materials. Covalent bonding is found in elements and in compounds, in networks and molecules and also within polyatomic ions. Essentially it is found in any material in which non-metallic atoms are bonded together. In covalent bonding, both atoms are trying to attract electrons, that is, the same electrons are attracted by a number of atoms and the electrons are tightly shared between the atoms. The force of attraction that each atom exerts on the shared electrons holds the atoms together. Electrons are usually shared between two atoms, but they can also be shared by several atoms. Covalent bonding usually results in a limited number of atoms being bonded together, these clusters of atoms are called molecules. An important distinction between ionic and covalent bonding is that ionic bonding results in network materials and covalent bonding usually results in molecular materials. Molecules are the clusters of atoms that are covalently bonded together. It may be a few dozen as in many of the organic compounds, but also hundreds or thousands of atoms as in many biochemical compounds.

Metallic Bonding. Metals are the most numerous of the elements, about 80 percent of all elements are considered metals. Metals possess a substance and are naturally not easily torn apart. They are ductile and malleable and can thus be drawn and their shape can be changed. They conduct heat and electricity and can be mixed to form alloys. The nature of metallic atoms is that they have loosely held valence electrons (electrons in the outer shell) that can be removed quite easily, therefore they are fairly free to move from one atom to another. Chemists often describe metals as consisting of metal ions floating in a sea of electrons. The mutual attraction between all these positive and negative charges bonds them all together. An atom is bonded to a neighboring electron, which is bonded to a neighboring atom and so forth. Such an array of atoms bonded to one another is called a network. The network of metallic bonding holds an entire piece of metal together. Each metallic bond contributes strength and the network extends this strength over the entire piece. This model of metallic bonding is used to explain the properties of metals such as

Figure 69: Common metals and metallic materials are for example steel, aluminium, iron, brass, bronze, copper (Source: www.ndt-ed.org).

electrical and thermal conductivity and malleability. The key is that the above mentioned loosely held electrons spread around between all the metal atoms and metal ions. These electrons can move easily about, allowing for good electrical conductivity. To a limited extent, the atoms can also move from one place to another and still remain in contact with and bonded to the other atoms and electrons around them. Although the external shape of the metal is changing, the internal pattern is pretty much the same which is what allows metals to change shapes. The atomic vibration that is observed as heat can easily be passed from one atom to the next making metals good conductors of heat and electricity. Structural patterns within metals are called hexagonal close packings. In two

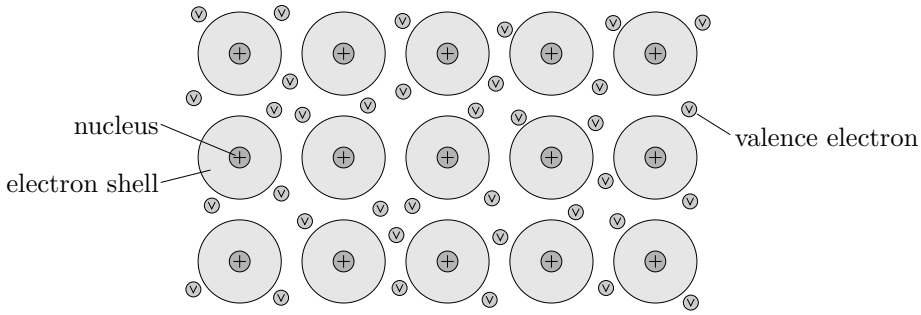

Figure 70: Metallic elements contain maximal three electrons in the outer shell. Their bonding to the nucleus is weak, and if these valence electrons (V) become grouped in a chunk of metal, the electrons in the outer shell easily leave their positively charged hosts to become part of the 'sea of electrons', making for ductility and good electrical and thermal conductivity of the material.

dimensions, one atom is directly surrounded by six other atoms, in three dimensions there are twelve neighboring atoms, making up the *metallic crystal structure*. If a piece of metal is made up of all the same atoms, it is called a *pure* or *monoatomic metal*. If different elements and atoms are mixed, the structure becomes an *alloy*. Those alloys can be divided into substitution alloys and interstitial alloys. Substitution alloys are structures where the different kinds of atoms are about the same size and the crystal pattern remains about the same as in a pure metal. Interstitial alloys consist of ensembles of atoms with different

sizes, where the added atoms in the alloy are much smaller than the original ones. An example is steel where small carbon atoms are added to iron. The carbon atoms fit into the holes between the layers of iron atoms in the network. The presence of different kinds of atoms changes the bonding and the properties of the metal, such as in carbon-steel which is stronger than iron.

Van der Waals Bonding. In addition to chemical bonding between atoms, another type of attractive force exists between atoms, ions, or molecules known as van der Waals forces. Van der Waals bonds are very weak compared to other types of bonds. These forces are caused by an unequal charge distribution as electrons constantly move about within an atom, ion, or molecule. This unequal charge distribution (or temporary dipole) induces a unequal charge distribution on a nearby atom, ion, or molecule. Every instant, billions of these temporary dipoles form, break apart, and reform to act as weak electrostatic forces of bonding known as van der Waals forces. It is important to note that van der Waals forces exist between all kinds of molecules.

8.2. Empirical Interatomic Potentials and Forces

In what follows, the particular derivation of the interatomic forces acting between the atoms is described. From the last chapter, recall that for one particular atom $\mathcal{A}_i$, the internal potential energy $\mathcal{U}_i^{int}$ is summed up over the neighboring atoms according to

$$\mathcal{U}_i^{int} = \frac{1}{2}\sum_{j\neq i}\phi(r_{ij}) = \frac{1}{2}\sum_{j\neq i}\phi_{ij} \tag{8.2}$$

where the pair potential function $\phi(r_{ij})$ governs the interactomic mechanical behavior. Examples for typical pair potentials and their derivatives are given below. The total internal potential energy of the crystal lattice follows as the sum over the particular potential energy contributions of all atoms in the ensemble,

$$\mathcal{U}^{int} = \sum_{i=1}^{N}\mathcal{U}_i^{int} \ . \tag{8.3}$$

Per definitionem, the total force $\boldsymbol{f}_i$ acting on an atom $\mathcal{A}_i$ due to atomic interactions is the negative derivative of the total internal potential energy $\mathcal{U}_i^{int}$ of the atom with respect to its position $\boldsymbol{x}_i$,

$$\boldsymbol{f}_i = -\frac{\partial}{\partial \boldsymbol{x}_i}\mathcal{U}_i^{int} = -\frac{1}{2}\sum_{j\neq i}\frac{\partial}{\partial \boldsymbol{x}_i}\phi_{ij}(r_{ij}) = -\frac{1}{2}\sum_{j\neq i}\frac{\partial\phi_{ij}(r_{ij})}{\partial r_{ij}}\frac{r_{ij}}{\boldsymbol{r}_{ij}}\frac{\partial \boldsymbol{r}_{ij}}{\partial \boldsymbol{x}_i} \ . \tag{8.4}$$

Therein, derivation of the interatomic potential function ϕ_{ij} with respect to the atom position $\boldsymbol{x}_i$ gives the negative interatomic force acting between these atoms $\mathcal{A}_i$ and $\mathcal{A}_j$ in terms of the actual interatomic distance $r_{ij} = |\boldsymbol{r}_{ij}| = |\boldsymbol{x}_i - \boldsymbol{x}_j|$ and thus

$$\boxed{\boldsymbol{f}_{ij} = \frac{1}{r_{ij}}\phi'_{ij}\boldsymbol{r}_{ij} = \phi'_{ij}\boldsymbol{n}_{ij} \ .} \tag{8.5}$$

Therein, $\boldsymbol{n}_{ij} := \boldsymbol{r}_{ij}/r_{ij}$ denotes the unit normal vector that points from atom $\mathcal{A}_j$ towards atom $\mathcal{A}_i$. In order to compute the total force on each atom, a summation of the separate interatomic forces $\boldsymbol{f}_i$ in equation (8.4) over all other atoms must be performed. This

in turn must be executed for all atoms in the system and is therefore computationally expensive. Usually, a *cutoff radius* r_c is introduced for the potential functions under the assumption that the atoms only interact with their neighbors in some vicinity. This approach is reasonable since with increasing interatomic distances the associated interatomic potentials quickly decay towards stationary values, usually zero. The truncated pair-wise interaction potential is then written as

$$\phi_{ij}^{tr}(r) = \begin{cases} \phi_{ij}(r) & \text{for } r \leq r_c, \\ 0 & \text{for } r > r_c \ , \end{cases} \tag{8.6}$$

where r describes the distance to atom $\mathcal{A}_i$. The choice of the cutoff radius depends on the material to be simulated, a typical value might be $r_c = 2\mathring{A}$ where an Ångstroem is $1\mathring{A} = 10^{-10}m$. A disadvantage arises in the use of the cutoff radius because due to

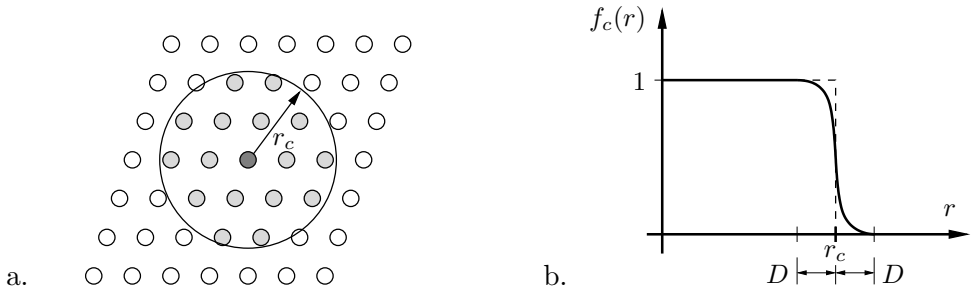

Figure 71: a. Cutoff radius r_c and b. skin factor $f_c = \hat{f}_c(r)$ to limit summation range of interatomic forces to a domain around the atom considered.

the discontinuity, it does not conserve the energy in the system. Therefore, to assure continuity and thus differentiability of the interatomic pair potential ϕ_{ij}, a *skin factor* f_c can be used of the form

$$\phi_{ij}^{tr}(r) = f_c(r) \cdot \phi_{ij}^{eff}(r) \quad \text{for } |r - r_c| \leq D \ , \tag{8.7}$$

where D denotes the range around the cutoff radius r_c where the skin factor f_c is applied, see Figure 71. For $0 < r < (r_c - D)$, the skin factor is $f_c = 1$. The skin factor f_c assures a smooth and quick transition from one to zero as r approaches the cutoff limit r_c. In what follows, several typically used interatomic potentials are discussed.

8.3. Two-Body (Pair) Potentials

At the subatomic level the positively charged atomic nucleus is neutralized by the negatively charged electron clouds that surround the nucleus. The quantum mechanical description of electron motion contains a probabilistic approach to evaluate the probability densities of electrons occupying a certain location in space. The negatively charged electron clouds experience cross-atomic attractions that grow as the nuclei approach one another. At a certain distance, the so-called *equilibrium bond length*, this attraction is equilibrated by the repulsive caused by the positively charged nuclei. A further decrease in the distance yields to a quick growth of the resultant repulsive force. The two exemplary pair potentials discussed below describe this simple physical observation.

8.3.1. Lennard-Jones 12-6 Potential. The Lennard-Jones 12-6 potential function for the interaction between a pair of atoms was introduced in Jones [56], [57]. It is defined

by the expression

$$\phi_{ij}(r = r_{ij}) = 4\varepsilon \left[\left(\frac{\sigma}{r}\right)^{12} - \left(\frac{\sigma}{r}\right)^{6} \right] \tag{8.8}$$

in terms of the collision diameter σ and a bonding-/ dislocation energy parameter ε. σ is directly related to the equilibrium bond length $r_0 = \sqrt[6]{2}\sigma$ where the potential becomes stationary. The Lennard-Jones potential has an attractive tail at large interatomic distances r, passes through zero at $r = \sigma$ and is strongly repulsive at shorter distances $r < r_0$. The first term $(\frac{\sigma}{r})^{12}$ dominates at shorter distances and thus governs the repulsion between atoms that are close to each other. This stems from the fact that when the electronic clouds that surround the atoms start to overlap, the energy of the system abruptly increases. On the other hand, the latter term $(\frac{\sigma}{r})^{6}$ dominates at large distances. It governs

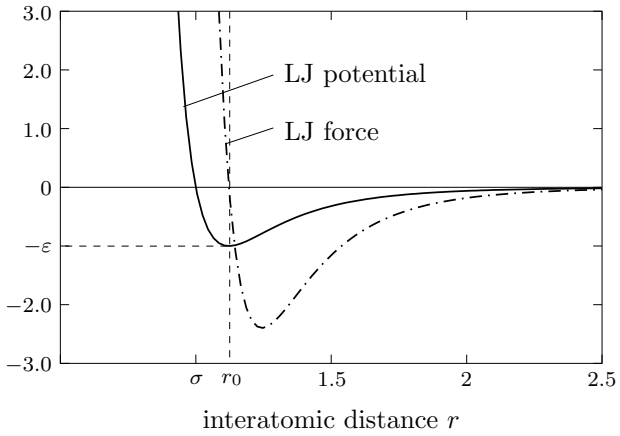

Figure 72: Lennard-Jones 12-6 potential function and its negative derivative with unit parameters $\sigma = \varepsilon = 1$. The minimum of the potential at $r_0 = \sqrt[6]{2}\sigma$ is termed the *equilibrium bond length*.

the attractive part of the potential and adds cohesion to the system. This attraction is founded on the weak van der Waals interactions which also govern the bonding character of closed-shell systems like rare gases such as argon. Therefore, the Lennard-Jones potential can capture the effects of those materials quite well. In contrast, the Lennard-Jones potential is not adequate for open-shell systems where strong localized bonds as in covalent systems may form or where seas of electrons surround the ions as for example in metallic materials. Derivation of the Lennard-Jones potential ϕ_{ij} with respect to the interatomic distance r gives the negative force acting between the two atoms of the form

$$f(r) = -\frac{\partial}{\partial r}\phi_{ij}(r) = 24\frac{\varepsilon}{\sigma}\left[2\left(\frac{\sigma}{r}\right)^{13} - \left(\frac{\sigma}{r}\right)^{7} \right] . \tag{8.9}$$

Despite all the above mentioned shortcomings, the Lennard-Jones potential is considered to be a very important model. It has been used in a vast variety of applications for the modeling of solids, fluids, surfaces, clusters and so on. It is the standard potential for research where the focus is more on fundamental issues rather than the properties of the specific material. In the end, due to their simplicity, two-body potentials of the Lennard-Jones form provide for the shortest computing times. Such atomistic systems are commonly refered to as *Lennard-Jones systems*.

For the interaction between different atoms i and j, the so-called Lorentz-Berthelot combining rules, see the work DELHOMMELLE & MILLIE [33], can be used to parametrize effective pair potential models or to calculate thermodynamic properties of mixtures. Therein, it is quite common to use a geometric mean average for the energy parameter ε (the Berthelot rule) and an arithmetic mean average for the collision diameter σ (the Lorentz rule). These effective parameters then appear as

$$\varepsilon_{ij} := \sqrt{\varepsilon_i \cdot \varepsilon_j} \quad \text{and} \quad \sigma_{ij} := \frac{1}{2}(\sigma_i + \sigma_j) \; . \tag{8.10}$$

These are the simplest combining rules available in literature. However, they do not provide the best approximations and thus several advanced combining rules have been developed, see DELHOMMELLE & MILLIE [33] and the references therein.

8.3.2. Morse Potential. As a second pair potential, the Morse potential function is introduced. It is discussed in the works GIRIFALCO & WEIZER [43], LINCOLN, KOLIWAD & GHATE [67] and MACDONALD & MACDONALD [70] and given by the expression

$$\phi_{ij}(r) = \varepsilon \left[e^{2\beta(\rho - r)} - 2e^{\beta(\rho - r)} \right] \tag{8.11}$$

in terms of the lattice parameter ρ and two further fitting parameters β with unit $\mathring{A}^{-1}$ and ε. The latter one describes the dislocation energy similar to ε in the Lennard-Jones potential, see equation (8.8). Again, the first term governs the atomic repulsion at small separation distances and the last term atomic attraction (bonding) at larger distances. Due to the three fitting parameters, the Morse potential can be better fitted to materials than the two parameter Lennard-Jones potential. On that account, the Morse potential

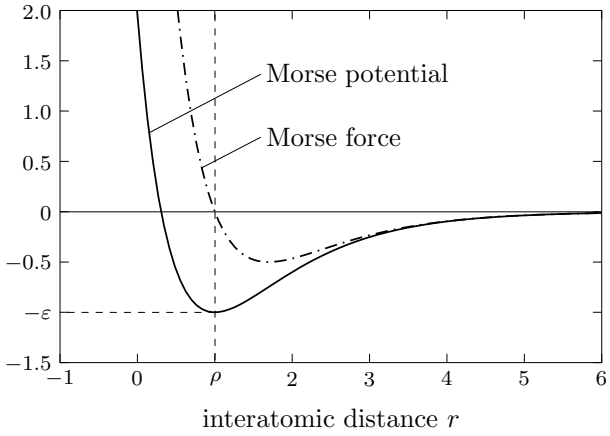

Figure 73: Exponential Morse potential function and its negative derivative with unit parameters $\rho = \varepsilon = \beta = 1$. The equilibrium bond length is directly given by the parameter ρ.

has been used for a wide variety of materials, especially for cubic metals. A list is given in the reference GIRIFALCO & WEIZER [43]. Moreover, it was applied to study second-order elastic constants, the equation of state and point and line defects, among others. Figure 73 depicts the Morse function and its negative derivative

$$f(r) = -\frac{\partial}{\partial r}\phi_{ij}(r) = 2\varepsilon\beta \left[e^{2\beta(\rho - r)} - e^{\beta(\rho - r)} \right] \tag{8.12}$$

as a function of the interatomic distance r for unit parameters $\varepsilon = \rho = \beta = 1$. Observe that ρ is directly specified by the lattice constant at temperature zero, $0K$. For the monoatomic material aluminium (Al) for example, several such parameters are given in literature, Table 1 summarizes the parameters of three key references.

Table 1: Morse Potential Parameters for Aluminium (Al)

Reference	$\varepsilon\ [eV]$	$\rho\ [\mathring{A}]$	$\beta\ [\mathring{A}^{-1}]$
[43] Girifalco & Weizer (1959)	0.270300	3.2530	1.1646
[67] Lincoln, Koliwad & Ghate (1967)	0.270033	3.4068	1.0341
[70] MacDonald & MacDonald (1981)	0.397522	2.8485	1.1611

8.4. Multi-Body Atom Interactions for Metals

Major progress was made during the 1980s by the development of many-body potential formulations such as the N-body Finnis-Sinclair potentials, see for example Finnis & Sinclair [41], and the Embedded Atom Method (EAM), see Daw & Baskes [30], Daw, Foiles & Baskes [31] and others, for metallic structures. These potentials are now the current state of the art empirical descriptions of cohesion in metals. They were developed on the physical observation of coordination (or density). A crucial observation is that bonds become weaker when the local environment densifies. Thus, with increasing density or coordination the cohesive energy should not be decreasing linearly as in two-body systems, it should decrease faster for low densities and slower for increasing coordination. In the above mentioned approaches, the total internal potential energy is represented by a pair potential that governs atomic repulsion and a cohesive functional of pair-wise interactions governing the atomic attraction (bonding) of the form

$$\mathcal{U}^{int} = \frac{1}{2}\sum_{i\neq j}^{N} \phi_{ij}(r_{ij}) + \sum_{i=1}^{N} G(n_i)\ , \tag{8.13}$$

where $G(n_i)$ is a function that provides the energy of an atom depending on the coordination n_i. This coordination number is in turn constructed as the sum of the particular contributions from neighboring atoms,

$$n_i = \sum_{j=1}^{N} \varrho(r_{ij})\ . \tag{8.14}$$

Therein, $\varrho(r)$ is a short-ranged decreasing function of the interatomic distance r_{ij}. The functional $G(n_i)$ gives rise to N-body interactions in the sense that the force exerted by one atom onto another depends on the disposition of all neighbors to both atoms concerned. Observe that in contrast, a pair potential alone gives rise to a force that depends only on the separation of the two atoms concerned, not their neighborhoods. A fundamental result of the tight binding formalism, see reference Carlsson [21], is that the energy is proportional to the square root of the coordination, rather than to the coordination itself as in two-body potentials. The best illustration of the predictive power of the EAM and Finnis-Sinclair models gives an investigation of relaxations that occur on free surfaces. On such a metal surface, it generally leads to an inward contraction of the first layer towards

the second, which is totally in agreement with experimental observations of metal surfaces. Using the concepts in this section, this is easy to understand. The atoms at the surface have fewer bonds than those within the bulk, and consequently move toward the bulk to saturate their bonding. The atoms in the next layer now see more coordination than the average bulk value and therefore the spacing between the following layer increases. This effect can persist for many layers into the bulk. The potentials discussed here offer relatively accurate predictions of these interlayer spacings. In this section, the empirical Sutton & Chen potential as a particular form of the Finnis-Sinclair type potentials, and the Embedded Atom Method are discussed.

8.4.1. Embedded Atom Method (EAM). The Embedded Atom Method has led to a considerable improvement in the quality of predictions for metallic structures. It has been and still is applied in many simulations of metallic and intermetallic structures, for examples for impurities, surface formations, defects, grain boundaries and others. The EAM requires about 2-5 times the computational work of a classical pair potential, yet it includes some multi-body effects important in the description of metallic systems. In the Embedded Atom Method proposed in Daw & Baskes [30], the internal energy $\mathcal{U}_i$ at an atom site i is given by

$$\mathcal{U}_i = \sum_{j \neq i}^{N} \phi_{ij}(r_{ij}) + F_i(\varrho_i) \quad \text{with} \quad \varrho_i = \sum_{j \neq i}^{N} f(r_{ij}) \ , \tag{8.15}$$

in terms of an *embedding function* F_i at atom site i which in turn is a function of the electron density ϱ_i. Furthermore, ϕ_{ij} is a standard pair potential that governs mainly the repulsive part of the energy functional. The computational procedure is that for each atom i, both the pair potential ϕ_{ij} and $f(r_{ij})$ are summed over neighbors j, and then a single evaluation of $F(\varrho_i)$ is performed. A radial cutoff for ϕ_{ij} and $f(r_{ij})$ scales the total

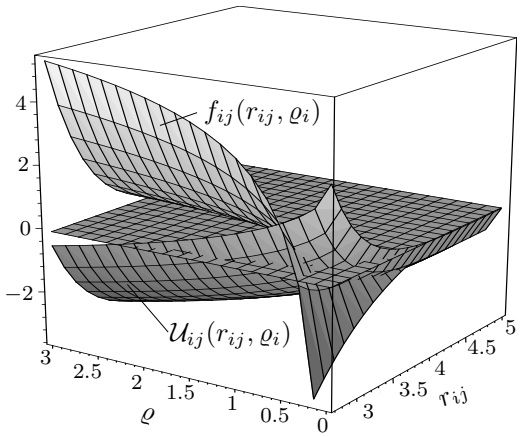

Figure 74: Interatomic potential $\mathcal{U}_{ij}$ and force f_{ij} of the Embedded Atom Method as functions of the interatomic distance r_{ij} and electron density ϱ_i with parameters for aluminium ($A = 0.763905\,eV$, $B = 0.075016\,eV$, $C = 0.159472\,eV$, $\alpha = 1.767488\,\mathring{A}$, $\beta = 2.017519\,\mathring{A}$, $\xi = 0.147690$, $r^* = 4.05\,\mathring{A}$). Note the critical nonlinear behavior for small electron densities ϱ_i which results in a change of sign of the interatomic force.

computational work to N. ϱ_i is a measure of atomic coordination or density of atom i, thus $f(r_{ij})$ must be a monotonocally decreasing function of r_{ij}. The key to the EAM is the nonlinearity of the embedding function $F(\varrho_i)$, this nonlinearity provides a multi-body

contribution to the potential energy, see Figure 74. In many EAM models, the embedding function and its derivatives are not given in analytical forms but instead in so-called look-up tables with experimentally determined values. For simplicity, in this work the analytical form HUANG, ZHANG, SUE & WANG [52] is employed where the embedding energy function and the electron density function are given by

$$F_i(\varrho_i) = -A\sqrt{\frac{\varrho_i}{\xi}} \quad \text{and} \quad \varrho_i(r_{ij}) = \sum_{j\neq i}^{N} \xi e^{-\beta(r_{ij}-r^*)} \ , \tag{8.16}$$

and the pair potential is specified by

$$\phi_{ij}(r_{ij}) = 2Be^{-\frac{1}{2}\beta(r_{ij}-r^*)} - C\left[1+\alpha(r_{ij}-r^*)\right]e^{-\alpha(r_{ij}-r^*)} \ , \tag{8.17}$$

all in terms of the seven material parameters A, B, C, α, β, ξ and the equilibrium bond length parameter r^*. From a physical point of view, F_i can be interpreted as the quantum-mechanical energy needed to embed an atom i into a homogeneous electron gas with density ϱ_i. For an equilibrated solid, the force to expand due to the embedding function is exactly balanced by the force to contract due to the pair-wise interactions and vice versa. A good detailed discussion of the EAM is found in VOTER [118]. A straightforward derivation of the energy expression in (8.15) with respect to the interatomic distance r_{ij} between the atoms i and j yields the magnitude of the interatomic force acting between those atoms as

$$f_{ij} = \frac{\partial\phi_{ij}}{\partial r_{ij}} + \frac{\partial F_i}{\partial\varrho_i}\frac{\partial\varrho_i}{\partial r_{ij}} \ . \tag{8.18}$$

For the analytic form of the EAM in the work HUANG, ZHANG, SUE & WANG [52], the particular derivations of the embedding function follow as

$$\frac{\partial F_i}{\partial\varrho_i} = -\frac{A}{2\sqrt{\varrho_i\cdot\xi}} \quad \text{and} \quad \frac{\partial\varrho_i}{\partial r_{ij}} = -\xi\beta e^{-\beta(r_{ij}-r^*)} \ , \tag{8.19}$$

and the one of the pair potential as

$$\frac{\partial\phi_{ij}}{\partial r_{ij}} = -B\beta e^{-\frac{1}{2}\beta(r_{ij}-r^*)} + C\alpha^2 e^{-\alpha(r_{ij}-r^*)}(r_{ij}-r^*) \ . \tag{8.20}$$

The optimal material parameters for aluminium in HUANG, ZHANG, SUE & WANG [52] were found to be $A = 0.763905\,eV$, $B = 0.075016\,eV$, $C = 0.159472\,eV$, $\alpha = 1.767488\,\mathring{A}$, $\beta = 2.017519\,\mathring{A}$, $\xi = 0.147690$ and the lattice parameter $r^* = 4.05\,\mathring{A}$. Observe that due to the extra summation of the electron density, this coordination is found to be smaller at surfaces in comparison to the bulk. This issue needs to be circumvented in the simulation and computation of nanosystems which are considered as cut-outs from larger systems and thus do not possess any free surfaces. Therefore, the true electron densities of the boundary atoms are approximated as follows. For all bulk and surface atoms the average coordination numbers are computed,

$$\bar{n}_{c,bulk} := \frac{1}{N}\sum_{i=1}^{N} n_{c,i} \quad \text{and} \quad \bar{n}_{c,surf} := \frac{1}{M}\sum_{i=1}^{M} n_{c,i} \ . \tag{8.21}$$

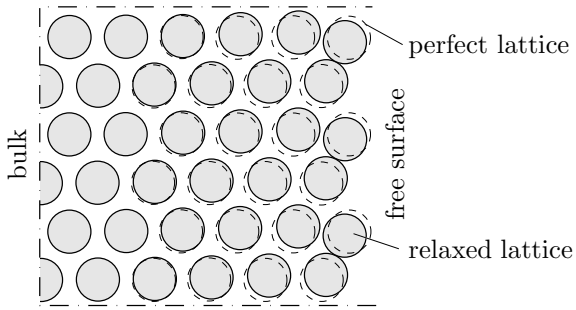

Figure 75: Molecular dynamics (MD) equilibration of the relaxation on a free surface of a two-dimensional triangular lattice with the Embedded Atom Method EAM (displacements five times magnified) and parameters for aluminium. The outermost layer contracts to the second due to smaller electron densities on the free surface. This relaxation can persist for several layers into the bulk.

Then each electron density of the surface atoms is multiplied with the ratio of the above two values,

$$\varrho_i := \frac{\bar{n}_{c,bulk}}{\bar{n}_{c,surf}} \varrho_i \quad \text{for } i = 1, \ldots, M \ . \tag{8.22}$$

This way each surface atom receives an electron density that goes along with the average electron density of those in the bulk, but still accounts for the current environment around the atom. Another method could be to just assign the average bulk electron density $\bar{n}_{c,bulk}$ to each surface atom, but the information of the local environment would be lost. For the EAM and related methods, direct analytic mixing rules for the interaction of different materials by the EAM are not used. Instead, for the interaction between different materials the particular parameters need to be determined. For the EAM and Sutton & Chen potentials (see next section), several such parameters for mixed materials are listed in the reference Huang, Zhang, Sui and Wang [52].

8.4.2. A Finnis-Sinclair Potential: The Sutton & Chen Model. This Finnis-Sinclair type N-body potential was delevoped for computer simulations where van der Waals type interactions at long ranges are as important as metallic bonding at short ranges, see the reference texts Sutton & Chen [109] and Rafii-Tabar & Sutton [102]. From the discussion of the Lennard-Jones potential it is known that van der Waals interactions are usually given by an attractive $1/r^6$ tail. The Finnis-Sinclair-type potential energy at an atomic site is defined in the form

$$\mathcal{U}_i = \varepsilon \left[\frac{1}{2} \sum_{j=1}^{N} \phi_{ij}(r_{ij}) - c\sqrt{\bar{\varrho}_i} \right] \ , \tag{8.23}$$

with the pair potential ϕ_{ij} and embedding energy $\bar{\varrho}_i$ as a function of the electron density ϱ_{ij} specified by

$$\phi_{ij} := \left(\frac{a}{r_{ij}} \right)^n \quad \text{and} \quad \bar{\varrho}_i = \sum_{j \neq i} \varrho_{ij} = \sum_{j \neq i} \left(\frac{a}{r_{ij}} \right)^m \tag{8.24}$$

in terms of the material parameters ε, c, m and n. The magnitude of the force between two atoms i and j follows by derivation with respect to the interatomic distance r_{ij},

$$f_{ij} := -\frac{\partial \mathcal{U}_i}{\partial r_{ij}} = -\varepsilon \left[\frac{1}{2} \frac{\partial \phi_{ij}}{\partial r_{ij}} - c \frac{1}{2\sqrt{\bar{\varrho}_i}} \frac{\partial \bar{\varrho}_i}{\partial r_{ij}} \right] \tag{8.25}$$

with the particular contributions

$$\frac{\partial \phi_{ij}}{\partial r_{ij}} = -\frac{n}{r_{ij}} \left(\frac{a}{r_{ij}} \right)^n \quad \text{and} \quad \frac{\partial \bar{\varrho}_i}{\partial r_{ij}} = -\frac{m}{r_{ij}} \left(\frac{a}{r_{ij}} \right)^m . \tag{8.26}$$

For aluminium (Al), the material parameters were found to be $\varepsilon = 9.1435 \times 10^{-3}\, eV$, $c = 52.2066$, $m = 5$ and $n = 9$, taken from the reference Jin, Sheng & Lu [55]. For alloys comprised of different types of atoms, for examples atoms A and B, the interatomic potential ϕ_{ij}^{A-B} and electron density function ϱ_{ij}^{A-B} governing the mechanical behavior between the two atoms can empirically be determined by assuming

$$\phi_{ij}^{A-B} = \sqrt{\phi_{ij}^{A}\, \phi_{ij}^{B}} \quad \text{and} \quad \varrho_{ij}^{A-B} = \sqrt{\varrho_{ij}^{A}\, \varrho_{ij}^{B}} \, , \tag{8.27}$$

which leads to the parameters that govern the mixed functions $m^{A-B} = \frac{1}{2}\,(m^A + m^B)$, $n^{A-B} = \frac{1}{2}\,(n^A + n^B)$, $a^{A-B} = \sqrt{a^A\, a^B}$ and $\varepsilon^{A-B} = \sqrt{\varepsilon^A\, \varepsilon^B}$, see Rafii-Tabar & Sutton [102]. Note that in computer code, a separate loop to determine the particular atom coordinations ϱ_i, $i = 1, \ldots, N$ must be performed before the main loop; only then the computation of the interatomic forces can be commenced. Thus these potentials are computationally more costly than the simple Lennard-Jones pair models.

8.5. A Note on Unit Conversions

In applications with ensembles of just one type of material, for example pure aluminium, the mass of the atom can be used as the fundamental unit $m = 1$. Thus the atom momenta and velocities become identical as do the forces and accelerations. Further fundamental units of energy, temperature etc. can be defined based on these considerations. In real units, several quantities such as times and masses become very small in SI units, for example one atomic mass unit (not a SI unit) is equivalent to $1.660\ 540\ 2 \times 10^{-27} kg$ (with kilogram being an SI unit). Such small variables might pose accuracy problems when they are stored as computer variables. The use of reduced units might exclude possible truncation errors. Table 2 gives an overview of some common non-SI units used in atomistic simulations. The conversions to the SI units (length in meter, mass in kilogram, time in second and thermodynamic temperature in Kelvin) are also given. The use of

Table 2: Derived Non-SI Units and Conversions

Quantity	*Unit Name*	*Symbol*	*Conversion*
force	Newton	N	$1N = 1kg\ m/s^2$
length	Ångstrom	$\mathring{A}$	$1\mathring{A} = 1 \times 10^{-10} m$
time	femtosecond	fs	$1fs = 10^{-15} s$
work, energy, heat	joule	J	$1\,J = 1Nm = 1kg\ m^2/s^2$
energy, work	energy	erg	$1erg = 10^{-7} J$
energy	electron volt	eV	$1\,eV = 1.602\ 177\ 33 \times 10^{-19} J$
mass	atomic mass unit	amu	$1amu = 1.660\ 540\ 2 \times 10^{-27} kg$

reduced units is relatively easy with simple interatomic potentials such as Lennard-Jones. For more advanced potentials the advantage gained by reduced units decreases. For example, in simulations where the atomic masses are specified in atomic mass units amu, the lengths in Ångstrom $\mathring{A}$ and the time in seconds, the equivalence to electron volt eV is

given by $1eV = 9.648\,526 \times 10^{27}\ amu\,\mathring{A}^2/s^2$. For mixtures and compounds, the advantage gained by the use of reduced units vanishes since for example the atomic mass can only be reduced to unity of one atom type. In further work, real units are employed and the possibility of truncation errors is accepted.

9. Dynamic Homogenization of Atomistic Nanostructures

In this section, the homogenization of atomistic nanostructures in a *fully dynamic context* is developed. The dynamics are necessary to capture the effects of the atomic vibrations that add temperature to the system. Essentially, they also represent temperature in the system. Damping is not applied in order to conserve the temperature imposed on the system. In contrast to the quasistatic homogenization of granular structures, the atomistic ones are not relaxed towards quasistatic states but towards fully dynamic stationary ones. At first a statistical mechanics approach to the theoretical basis is outlined that describes the connection between nano- and mesoscopic quantities. Then several types of classical boundary constraints from literature are described, followed by a detailed discussion of a uniform traction boundary constraint for atomistic nanostructures. This type of constraint is algorithmically implemented in a deformation-controlled process which occurs for example in multiscale applications. This deformation-controlled scenario combined with the uniform traction constraint is new, to the author's knowledge present literature does not contain deformation-controlled dynamic homogenization techniques for atomistic structures.

9.1. A Statistical Mechanics Approach to Homogenization

Molecular dynamics simulations generate information at the nano level, including atomic positions and momenta. The conversion of this nanoscopic information to meso- or macroscopic observable quantities such as pressure, energy, temperature and so on requires statistical mechanics. Statistical mechanics studies mesoscopic systems from a molecular point of view such that it provides the theoretical link between the nano- and mesoscales by means of *ensemble averages*. This conversion of the atomistic quantities by means of appropriate averaging techniques is termed homogenization. Statistical mechanics provides the rigorous mathematical expressions that relate mesoscopic properties to the distribution and motion of the atoms of the N-body system, and molecular dynamics simulations provides the means to solve Newton's equations for the atoms and evaluate their mathematical formulas.

9.1.1. Statistical Ensembles. In statistical mechanics, ensembles are classified according to the mechanisms of contact with their surroundings. An ensemble is a collection of all possible systems that have different nanoscopic states but possess identical mesoscopic or thermodynamic states. Therein, a thermodynamic state of a system is defined by a small set of parameters, for example temperature T, volume V and number of particles N. Further thermodynamic properties can be derived from these quantities. Also, the nanoscopic state of a system is defined by its atomic positions $\boldsymbol{x}$ and momenta $\boldsymbol{q} = m\dot{\boldsymbol{x}}$ which can also be considered as coordinates in the multidimensional *phase space*. In a system with N particles, the phase space has $6N$ dimensions. A single six-dimensional point in this phase space is denoted by $\boldsymbol{\Gamma} = [\boldsymbol{x},\ \boldsymbol{q}]^T$. In this context, different ensemble types with different characteristics are frequently encountered, namely the microcanonical, the canonical and the grand canonical ensemble. In the *microcanonical NVE ensemble*, the number of atoms N, the volume V and the total energy E are conserved, such that the system is basically treated in isolation and exchanges nothing with its environment. If the *canonical NVT ensemble* is chosen, the system sits within a heat reservoir with much more energy than the ensemble itself. Thus the thermodynamic state of the ensemble is characterized by a fixed number of atoms N, a fixed volume V as well as a constant

temperature T. Because of its interaction with the heat reservoir, the *total* energy is a variable. The surrounding heat reservoir is assumed to be sufficiently large such that any transfer of energy does not change its temperature. Thus at (dynamic) equilibrium (that is, a stationary state), the thermodynamic temperature of the ensemble is determined by the temperature of the heat reservoir. A closely related ensemble has a fixed pressure P rather than a fixed volume V and is hence termed *isobaric-isothermal NPT ensemble*. Finally, the *grand canonical μVT ensemble* is sometimes used and is the least restrictive of the ensembles. Therein, the ensemble is entitled to exchange both energy and atoms with the surrounding reservoir. μ describes the fixed chemical potential. Apart from the number of particles, the energy variable is also not fixed. In this work, the simulations are performed at constant temperature and thus the *canonical NVT ensemble* is the ensemble type of choice, see for example Andersen [3] and Parrinello & Rahman [99]. The choice of the proper type of ensemble is crucial because in the context of the ergodic hypothesis, see below, it is assumed that time averages of certain mesoscopic observables are equal to the particular (microcanonical, canonical, etc.) ensemble average of the same mesoscopic property. Specifically, the functions of the ensemble averages depend heavily on the type of ensemble chosen.

9.1.2. Ensemble Averages versus Time Averages. Focusing firstly on statistical mechanics, an ensemble is characterized by a collection of a large number M of identical systems that evolve in time under identical mesoscopic conditions but different nanoscopic initial conditions. Therein, averages that correspond to experimental observables are defined in terms of ensemble averages. If $\rho(\mathbf{\Gamma}_i)M$ denotes the number of such systems in a particular state $\mathbf{\Gamma}_i$, then $\rho(\mathbf{\Gamma}_i)$ can be interpreted as the probability of finding an ensemble number in a state i. Then a certain mesoscopic property $\mathcal{A}$ (the observable of interest) can be calculated as the weighted average

$$< \mathcal{A} >_{ensemble} = \int_{\mathbf{\Gamma}} \rho(\mathbf{\Gamma}) \mathcal{A}(\mathbf{\Gamma}) \; d\mathbf{\Gamma} \approx \sum_{i=1}^{M} \rho(\mathbf{\Gamma}_i) \mathcal{A}(\mathbf{\Gamma}_i) \; . \tag{9.1}$$

The probability density function $\rho(\mathbf{\Gamma})$ and the associated partition function Q_{NVT} for the canonical NVT ensemble employed here are given by

$$\rho(\mathbf{\Gamma}) = \frac{1}{Q_{NVT}} \exp\left[-\frac{\mathcal{H}(\mathbf{\Gamma})}{k_B T}\right] \quad \text{and} \quad Q_{NVT} = \int_{\mathbf{\Gamma}} \exp\left[-\frac{\mathcal{H}(\mathbf{\Gamma})}{k_B T}\right] d\mathbf{\Gamma} \; , \tag{9.2}$$

where $\mathcal{H}(\mathbf{\Gamma})$ denotes the Hamiltonian, see also Allen & Tildesley [2]. In general, the latter integral is extremely difficult to compute because all possible states of the system must be generated. In molecular dynamics simulations, which can be regarded as computer experiments where $< \mathcal{A} >$ can directly be determined rather then the probability $\rho(\mathbf{\Gamma})$ be generated, the points in the ensemble are computed sequentially in time. Thus, in order to compute an ensemble average, the molecular dynamics simulation must pass through all possible states that correspond to the particular thermodynamic constraints. Equation (9.1) implies that for a given ensemble of systems, any mesoscopic property $< \mathcal{A} >_{ensemble}$ can be measured by averaging the value $\mathcal{A}(\mathbf{\Gamma}_i)$ over all systems i. However, even in real laboratory experiments the measurements are not performed over a large number of systems, usually one system with an extremely large number of atoms is examined over some period in time (at frozen mesoscopic conditions) and the time average

of $\mathcal{A}(\mathbf{\Gamma})$ is determined, expressed as

$$< \mathcal{A} >_{time} = \lim_{\tau \to \infty} \frac{1}{\tau} \int_{t=0}^{\tau} \mathcal{A}(\mathbf{\Gamma}(t))\ dt \approx \frac{1}{M} \sum_{t=1}^{M} \mathcal{A}(\mathbf{\Gamma}(t))\ , \tag{9.3}$$

where t is the time simulated, M the number of time steps in the molecular dynamics simulation and $\mathcal{A}(t)$ the instantaneous value of $\mathcal{A}$. Obviously, the value calculated by means of the molecular dynamics technique is the *time average*, but the experimental observables are assumed to be *ensemble averages*. Resolving this leads to one of the most fundamental axioms in statistical mechanics, the *ergodic hypothesis*. It states that time averages of the form (9.3) are idential to ensemble averages of the form (9.1).

9.1.3. The Ergodic Hypothesis. "The ergodic hypothesis is an attempt to provide a dynamical basis for statistical mechanics", Patrascioiu [101]. In statistical mechanics, thermodynamic quantities are defined in terms of *ensemble averages*. For example, the temperature is proportional to the value of the kinetic energy averaged over every state in the ensemble. On the other hand, a molecular dynamics simulation produces a time sequence of events and physical properties are averaged over some time period. The

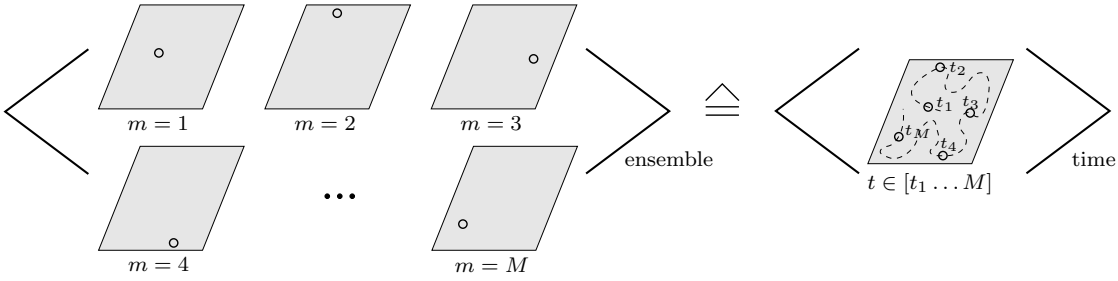

Figure 76: The *ergodic hypothesis* assumes that under identical (frozen) mesoscopic conditions, an ensemble average (average of *many* systems with different nanoscopic structures) is equal to a time average of *one* system at frozen mesoscopic deformation. The picture shows one atom systems under identical mesoscopic deformations but different nanoscopic structures. It is assumed that if the time average is sampled long enough, then the one atom will eventually have passed through every possible position that the atom occupies in any of the ensemble average systems.

ergodic hypothesis, usually attributed to Ludwig Boltzmann, states that in the long run, that is when the system becomes stationary, a system of atoms will eventually become arbitrarily close to all conceivable nano states. If this hypothesis is assumed, then there is a unique time average for any mesoscopic state and its value can be computed within the framework of Newtonian mechanics. Since there is a one-to-one relationship between the initial conditions of a system and the state at some other time, averaging over a large number of initial conditions is equivalent to averaging over time-evolved states of the system. Thus the ergodic hypothesis assumes that ensemble averages are equal to time averages of the same mesoscopic property $\mathcal{A}$,

$$\boxed{< \mathcal{A}(\mathbf{\Gamma}_i) >_{ensemble} = < \mathcal{A}(\mathbf{\Gamma}(t)) >_{time}\ .} \tag{9.4}$$

The ergodic hypothesis allows to convert the averaging from ensemble members to time instances of the same system. As an example, the above discussed relation between ther-

modynamic temperature T and the average of kinetic energy $< \mathcal{K} >$ for N particles

$$\mathcal{K} =< \mathcal{K} >= \frac{1}{2} < \sum_{i=1}^{N} m_i \boldsymbol{v}_i^2 >_{time} = \frac{3}{2} N k_B T \tag{9.5}$$

is used where the brackets $< \bullet >=< \bullet >_{time}$ denotes the time average and T the mesoscopically observed thermodynamic temperature. The sum over the velocities $\boldsymbol{v}_i$ and mass m_i of the N particles is the quantity that is computed in the molecular dynamics simulation. Other mesoscopic quantities that can be computed as appropriate averages of nanoscopic quantities are for example the density ϱ and average potential energy $\mathcal{U}$ defined by

$$\varrho =< \varrho >= \frac{1}{V} \sum_{i=1}^{N} m_i \quad \text{and} \quad \mathcal{U} =< \mathcal{U} >= \frac{1}{M} \sum_{i=1}^{M} \mathcal{U}_i \ , \tag{9.6}$$

where M is the number of configurations in the simulation and m_i the mass of particle i. Because the simulation will be performed over a finite time period, it is required that the molecular dynamics simulation is sufficiently long such that the phase space is adequately sampled. It remains to be noted that the ergodic hypothesis is an assumption and it is not generally true. However, it is widely agreed that it works well in most cases. Examples for which the theorem is known to be invalid are meta stable systems such as supercooled liquids and amorphous materials, but certainly not metallic systems at temperatures relevant in engineering applications.

9.2. Dynamic Equilibrium of Atomistic Systems

For a comprehensive discussion of the mechanical behavior of nanoscopic structures, it is at first necessary to define the dynamic equilibrium conditions for such atomistic nanosystems. Based on these expressions, the formulations for homogenized stresses and other mesoscopic observables can be derived. The local forms of the balances of linear and angular momenta with full dynamics but with the neglection of volume forces in the Eulerian setting of continuous systems are given by

$$\operatorname{div}[\boldsymbol{\sigma}] - \varrho \ddot{\boldsymbol{x}} = \boldsymbol{0} \quad \text{and} \quad \boldsymbol{\sigma}^T - \boldsymbol{\sigma} = \boldsymbol{0} \quad \text{in } v = \boldsymbol{\varphi}_t(\mathcal{V}) \ , \tag{9.7}$$

where ρ denotes the current density of the material and $\boldsymbol{\sigma}$ the Eulerian nanoscopic Cauchy stress tensor. These formulations are called local because they must be fulfilled at every point in the nanostructure. Integration of (9.7) over the current domain $\boldsymbol{\varphi}_t(\mathcal{V})$ and application of the theorem of Gauss yields the global forms (that hold for the total nanosystems) of the balance of linear momentum

$$\int\limits_{\boldsymbol{\varphi}_t(\partial\mathcal{V})} \boldsymbol{t} \ da - \int\limits_{m} \ddot{\boldsymbol{x}} \ dm = \boldsymbol{0} \tag{9.8}$$

and balance of angular momentum as

$$\int\limits_{\boldsymbol{\varphi}_t(\partial\mathcal{V})} \boldsymbol{t} \otimes \boldsymbol{x} \ da - \int\limits_{m} \ddot{\boldsymbol{x}} \otimes \boldsymbol{x} \ dm = \int\limits_{\boldsymbol{\varphi}_t(\partial\mathcal{V})} \boldsymbol{x} \otimes \boldsymbol{t} \ da - \int\limits_{m} \boldsymbol{x} \otimes \ddot{\boldsymbol{x}} \ dm \ , \tag{9.9}$$

and thus also yield the dynamic equilibrium conditions for continuous systems in terms of the Cauchy traction vector $\boldsymbol{t}$ on the Eulerian surface $\boldsymbol{\varphi}_t(\partial\mathcal{V})$ of the body. m denotes

the actual mass of the solid. For discrete systems, for example atomistic structures, the continuous limits transform into the following discrete quantities at particular atomistic sites

$$\boldsymbol{t}\, da \rightarrow \boldsymbol{a}_q \quad \text{and} \quad \ddot{\boldsymbol{x}}\, dm \rightarrow m_i \ddot{\boldsymbol{x}}_i \ . \tag{9.10}$$

Therein, $\boldsymbol{a}_q, q = 1, \ldots, M$ are discrete artificial support forces that act on the M surface atoms of the nanosystem. m_i and $\ddot{\boldsymbol{x}}_i, i = 1, \ldots, (M+N)$ are the mass and acceleration of all the $(M+N)$ atoms in the total nanostructure. Considering these limits with the continuous equations (9.8) and (9.9) yields the discrete global equilibrium conditions of atomistic nanosystems as

$$\boxed{\sum_{q=1}^{M} \boldsymbol{a}_q - \sum_{i=1}^{M+N} m_i \ddot{\boldsymbol{x}}_i = \boldsymbol{0}} \tag{9.11}$$

and

$$\boxed{\sum_{q=1}^{M} \boldsymbol{a}_q \otimes \boldsymbol{x}_q - \sum_{i=1}^{M+N} m_i \ddot{\boldsymbol{x}}_i \otimes \boldsymbol{x}_i = \sum_{q=1}^{M} \boldsymbol{x}_q \otimes \boldsymbol{a}_q - \sum_{i=1}^{M+N} m_i \boldsymbol{x}_i \otimes \ddot{\boldsymbol{x}}_i \ .} \tag{9.12}$$

With this discrete formulation at hand, the expressions for homogenized mechanical mesoscopic observables such as the homogenized Cauchy stress tensor $\bar{\boldsymbol{\sigma}}$ can be developed. Observe that the actual positions $\boldsymbol{x}_i$ of all $(M+N)$ particles in an atomistic unit cell are given by the deformation map

$$\boldsymbol{x}_i(\bar{\boldsymbol{F}}, \boldsymbol{X}_i, t) = \bar{\boldsymbol{F}} \boldsymbol{X}_i + \tilde{\boldsymbol{w}}_i(t) \quad \text{for } i = 1, \ldots, (M+N) \ , \tag{9.13}$$

where $\bar{\boldsymbol{F}}$ is the prescribed homogeneous mesoscopic deformation map at the current mesoscopic time, and $\boldsymbol{X}_i$ denotes the initial position of the atom i. The object $\tilde{\boldsymbol{w}}_i(t)$ represents the fluctuation of the particle i with respect to the homogeneous deformation $\bar{\boldsymbol{F}} \boldsymbol{X}_i$, the variable that is basically solved for on the microscopic scale.

9.3. Dynamic Homogenization of Nanostructural Quantities

The correct coupling of stresses between the subatomic-, nano-, intermediate- (meso-) and macroscopic continuum scales has long been and still is an important issue in research. From liquids, the virial theorem is known to define the pressure and thus the hydrostatic stress in the atomistic system under consideration. Based on this virial theorem of Clausius (1870), many attempts have been made to define exact definitions for the stress tensor which is then termed the *virial stress tensor*. Unfortunately, all these attempts are based on one or more assumptions or approximations, therefore the physical relevance is still in question. In the first part of this work on granular discrete microstructures undergoing large-strain deformations in deformation-controlled processes, it is shown that the macroscopic stress in *quasistatic* processes can be formulated in terms of a summation over only the *fictitious support forces* solely on the boundary of the granular unit cell. In the present case here where the dynamics must be accounted for, a related formulation is developed. The dyadic of the external forces remains the same, but an additional dyadic over all atoms in the assembly accounting for the dynamics is added.

9.3.1. Mesoscopic Mechanical Cauchy Stress. Recall that the local balance of angular momentum $(9.7)_2$, in the absence of couples, confirmes the *symmetry* of the nanoscopic Cauchy stress tensor $\boldsymbol{\sigma}$. Thus, focusing on the equivalence of mesoscopic and nanoscopic stresses, the homogenized mesoscopic Cauchy stress tensor $\bar{\boldsymbol{\sigma}}$ is defined as the volume average of the nanoscopic Cauchy stress tensor $\boldsymbol{\sigma}$

$$\bar{\boldsymbol{\sigma}} := \frac{1}{|v|} \int_v \boldsymbol{\sigma} \; dv \; , \tag{9.14}$$

where $|v|$ denotes the actual volume of the body. Note that such averages of stress measures can only be generated for the Cauchy $\bar{\boldsymbol{\sigma}}$, Kirchhoff $\bar{\boldsymbol{\tau}}$ and first Piola-Kirchhoff $\bar{\boldsymbol{P}}$ stress tensors, not for the second Piola-Kirchhoff tensor $\bar{\boldsymbol{S}}$. Using the identity $\mathrm{div}[\boldsymbol{\sigma} \otimes \boldsymbol{x}] = \boldsymbol{\sigma} - \mathrm{div}[\boldsymbol{\sigma}] \otimes \boldsymbol{x}$ and application of the theorems of Gauss ($\int_v \mathrm{div}[\boldsymbol{\phi}] \; dv = \int_{\partial v} \boldsymbol{\phi} \cdot \boldsymbol{n} \; da$) and Cauchy ($\boldsymbol{\sigma} \cdot \boldsymbol{n} = \boldsymbol{t}$) yields the symmetric continuous instantaneous mesoscopic Cauchy stress tensor $\bar{\boldsymbol{\sigma}}$ solely in terms of fine scale quantities as

$$\bar{\boldsymbol{\sigma}} = \frac{1}{|v|} \left[\int_{\partial v} \boldsymbol{t} \otimes \boldsymbol{x} \; da - \int_m \ddot{\boldsymbol{x}} \otimes \boldsymbol{x} \; dm \right] \; , \tag{9.15}$$

where ∂v denotes the actual surface of the body and m its mass. Using the nanoscopic symmetry condition $(9.7)_2$ for the derivation of this formulation yields the transpose of (9.15) and thus also confirms the symmetry of the mesoscopic homogenized Cauchy stress tensor,

$$\bar{\boldsymbol{\sigma}}^T - \bar{\boldsymbol{\sigma}} = \boldsymbol{0} \; . \tag{9.16}$$

Note that in general, the mechanical and the kinetic terms in the definition (9.15) alone are unsymmetric. A consistent transfer of the continuous formulation (9.15) to its associated discrete form is done by using the discrete limits of (9.10) and yields the exact symmetric discrete form of the instantaneous mesoscopic Cauchy stress tensor $\bar{\boldsymbol{\sigma}}(t)$ as

$$\boxed{\bar{\boldsymbol{\sigma}}(t) = \frac{1}{|v(t)|} \left[\sum_{q=1}^{M} \boldsymbol{a}_q(t) \otimes \boldsymbol{x}_q(t) - \sum_{i=1}^{M+N} m_i \ddot{\boldsymbol{x}}_i(t) \otimes \boldsymbol{x}_i(t) \right] \; .} \tag{9.17}$$

The first term is the standard quasistatic Cauchy stress definition already developed for quasistatic granular assemblies, see equation (3.19). Observe that this formulation (9.17) defines the homogenized Cauchy stress tensor $\bar{\boldsymbol{\sigma}} = \hat{\bar{\boldsymbol{\sigma}}}(t)$ at the current time t, although it is neither an ensemble nor a time average yet. Equation (9.17) defines the *instantaneous* homogenized mesoscopic Cauchy stress tensor that also holds true for nanostructures at zero temperature (in this case, the last (kinetic) term also equals zero). At finite thermodynamic temperatures $T > 0$, the mesoscopic Cauchy stress tensor must be generated by a statistical *ensemble* average $\bar{\boldsymbol{\sigma}} =< \bar{\boldsymbol{\sigma}}_i >_{ensemble}$. Application of the ergodic hypothesis (9.4) suggests a use of a *time* average $\bar{\boldsymbol{\sigma}} =< \bar{\boldsymbol{\sigma}}_i >_{ensemble} =< \bar{\boldsymbol{\sigma}}(t) >_{time}$ instead. Sampling of the instantaneous stresses $\bar{\boldsymbol{\sigma}}(t)$ over a sufficiently long time period, during which the nanostructure is held in a particular mesoscopic deformation state ($\bar{\boldsymbol{F}}$ fixed), then yields

the unique homogenized Cauchy stress tensor for that mesoscopic state as

$$\begin{aligned} \bar{\boldsymbol{\sigma}} &:= \lim_{t\to\infty} \frac{1}{t} \int_{t=0}^{t} \frac{1}{|v(t)|} \left[\sum_{q=1}^{M} \boldsymbol{a}_q(t) \otimes \boldsymbol{x}_q(t) - \sum_{i=1}^{M+N} m_i \ddot{\boldsymbol{x}}_i(t) \otimes \boldsymbol{x}_i(t) \right] dt \\ &\approx \frac{1}{\tau} \sum_{k=1}^{\tau} \frac{1}{|v(t_k)|} \left[\sum_{q=1}^{M} \boldsymbol{a}_q(t_k) \otimes \boldsymbol{x}_q(t_k) - \sum_{i=1}^{M+N} m_i \ddot{\boldsymbol{x}}_i(t_k) \otimes \boldsymbol{x}_i(t_k) \right] . \end{aligned} \tag{9.18}$$

The time period must be sampled carefully. Specifically, in order to compute a *unique* homogenized quantity, the dynamic nanostructure must be in a stationary state throughout the total sampling period. In a dynamically stationary state, the temporal change of the total kinetic energy, averaged over some period of time, equals zero,

$$< \dot{\mathcal{K}}(\dot{\boldsymbol{x}}(t)) >_{time} = 0 \ . \tag{9.19}$$

This criterion may serve to determine whether a dynamically stationary state has been reached before the sampling of homogenized quantities is started. In Figure 77 a unidi-

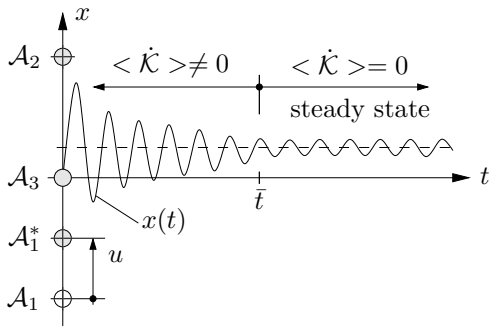

Figure 77: Schematic picture of a unidimensional example of one atom between two other fixed ones. Only after a time $\bar{t}$ does atom $\mathcal{A}_3$ reach a steady state and thus a dynamically equilibrated configuration.

mensional atomistic example with three atoms is considered. Atoms $\mathcal{A}_1$ and $\mathcal{A}_2$ are held fixed while atom $\mathcal{A}_3$ is free to move between the former two atoms. At $t = 0$ the system is in equilibrium and atom $\mathcal{A}_3$ lies at $x = 0$. Then atom $\mathcal{A}_1$ is displaced a distance u towards $\mathcal{A}_3$ to the new position labeled $\mathcal{A}_1^*$. Equilibrium is lost and therefore atom $\mathcal{A}_3$ begins to oscillate between the other two fixed atoms. This transient effect decays until at a time $\bar{t}$ a steady state is reached where $< \dot{\mathcal{K}} >_{time} = 0$. Only then, that is at time $\bar{t}$, should the sampling of any homogenized quantities be commenced.

9.3.2. A Note on the Classical Virial Stress. The classical virial stress tensor describing some form of stress within an atomistic structure is based on a generalization of the virial theorem of Clausius (1870), see Allen & Tildesley [2]. Therein, the average virial stress in an effective volume can be written as a discrete sum of contributions from all the atoms in the domain of volume $\mathcal{V}$. The atomic virial stress $\boldsymbol{\pi}_i$ over a volume ω_i around a particle i at position $\boldsymbol{x}_i$ is approximated from pressure and a spatial balance of momentum as

$$\boldsymbol{\pi}_i := \frac{1}{\omega_i} \left[\frac{1}{2} \sum_{j \neq i} \boldsymbol{r}_{ij} \otimes \boldsymbol{f}_{ij} - m_i \dot{\boldsymbol{x}}_i \otimes \dot{\boldsymbol{x}}_i \right] \tag{9.20}$$

with the interatomic branch vector $\boldsymbol{r}_{ij} := \boldsymbol{x}_j - \boldsymbol{x}_i$ and, due to Newton's third law, the interatomic force vector $\boldsymbol{f}_{ij} = -\boldsymbol{f}_{ji} = \frac{\partial \phi_{ij}}{\partial r_{ij}} \frac{\boldsymbol{r}_{ij}}{r_{ij}}$. For a system of N atoms, the total averaged virial stress then follows as the volume average

$$\boldsymbol{\Sigma} := \frac{1}{\mathcal{V}} \sum_{i=1}^{N} \omega_i \boldsymbol{\pi}_i \quad \text{with} \quad \mathcal{V} := \sum_{i=1}^{N} \omega_i \ . \tag{9.21}$$

Here, the symbol N denotes the total number of atoms in the system. Equations (9.20) and (9.21) are known to produce unphysical results, in particular for inhomogeneous atomistic solids. For example, the virial stresses are inexact at cracks, dislocations and surfaces since the volumes assigned to the atoms differ from those in the homogeneously deformed areas. An improved solution was found by Basinski, Duesbery & Taylor [10] where the Voronoi cell volumes were computed instead of the equal atomic volumes ω. A good discussion of the topic can be found for example in Cleri [26]. The last term in the virial expression (9.20) describes the mass transfer of the system, the first the mechanical approach. Recently, Zhou [125] found that the virial stress including the kinetic (mass transfer) part is not equivalent to the Cauchy stress. His paper is presently an issue of controversial discussions. Note that for atomistic simulations of solids (in contrast to fluids), the kinetic part of the stress formulation, that is the mass transfer in (9.20) and the last term in (9.18), are small compared to the mechanical contributions and may be neglected in such computations. In summary, the Cauchy stress formulation is considered to be the mechanical approach, whereas the virial stress represents the thermodynamic approach in that it starts from the rate of momentum flux. In the engineering studies of this work, clearly the Cauchy stress formulation as given in equation (9.18) is desired and applied since it is considered as a physically-based stress measure, whereas the physical relevance of the virial stresses is in question. Therefore, the Cauchy stress formulation (9.18) allows for an adequate exact coupling of the atomistics scale with mesoscopic continuum theories. This formulation excludes the calculation or artificial approximation of any atomic volumes or atomic stresses since it only includes support forces and atom positions on the boundary of the nanostructure and positions and accelerations of the atoms in the bulk. Furthermore, the use of uniform traction boundary constraints is also supported by the Cauchy principle of continuum mechanics stating that if a body is cut out from a larger medium, the mechanical action of the outer part is replaced by stresses acting on the surface of the remaining body, i.e. the tractions. Nevertheless, one should be aware that any averaging of nanoscopic variables to mesoscopic observables represents some kind of post-processing. In atomistics, the true physics is represented only by the interatomic forces, and any homogenization of mechanical variables is essentially a certain kind of overall representation of the interatomic forces in the system. In what follows, a particular type of von Neumann-type boundary conditions for dynamically computed nanostructures is discussed.

9.4. Boundary Conditions for Atomistic Nanostructures

First of all, a homogenized mesoscopic continuum $\bar{\mathcal{B}} \subset \mathbb{R}^3$ is considered, see Figure 78. Associated with a typical point $\bar{\boldsymbol{X}} \in \bar{\mathcal{B}}$ is a discrete substructure $\mathcal{V} \subset \mathbb{R}^3$ that in this exemplary case is characterized by a two dimensional triangular atomistic crystal and considered to be representative for the surrounding structure. This substructure is henceforth called *nanostructure* or *nanosystem*. In literature on atomistics, the notion of

microstructure is frequently adopted, but in order to focus on homogenization techniques that link simulations on the nano- and mesoscopic scales the term *nanostructure* is consequently adopted here. In contrast, in this work the terminology *microstructure* is reserved for the multiscale modeling of granular microstructures which takes place on much higher time and length scales. The length scale difference between the two scales is considered to be large, that is ($l_{nano} \ll l_{meso}$). Typically, molecular dynamics simulations are per-

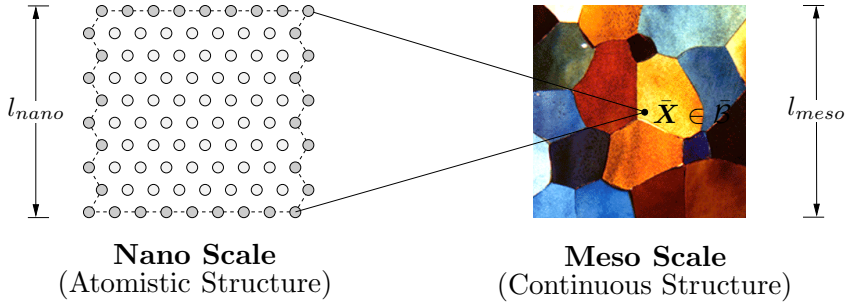

Figure 78: Nano scale mechanics informs higher-level continuum theories on the meso scale.

formed on nanostructures with a few thousand atoms, this is extremely small compared to real-world structures. For example, in a cubic nanostructure with a perfect fcc crystal structure of 4631 atoms, 1202 of them lie on the surface of the structure. These atoms experience different forces than those within the bulk. Thus, such small atomistic systems are dominated by surface effects, that is, they are governed by the boundary or surface conditions applied. Note that large systems reduce the contaminating influences of surface effects, but they do not eliminate them. Several forms of boundary conditions have been proposed in literature which can generally be classified into Dirichlet and Neumann boundary conditions. The Dirichlet boundary conditions describe displacements on the surface of the atomistic nanostructure. They can further be subdivided into periodic and linear displacement constraints. In what follows, several of these boundary constraints are briefly introduced and their consequences discussed.

9.4.1. Periodic Boundary Constraints. To overcome surface-induced effects, especially for atomistic studies of liquids, it is common to impose periodic boundary conditions where the system is assumed to be surrounded by an infinite number of identical structures. During the simulation, the atoms in each of the structures move in the same way and, for liquids, if an atom leaves a structure at one surface, an identical atom enters on the opposite surface, see also the textbook Allen & Tildesley [2]. For solids, associated atoms on opposite surfaces move in the same way. However, the use of periodic boundary conditions may give spurious effects in that a possible defect may fictitiously interact with itself, known as the problem of image forces. Furthermore, the use of periodic boundary constraints is inconsistent with the existence of a net Burgers vector $\boldsymbol{b}$ in the simulation cell, see Figure 79. As shown in Figure 79a, a dislocation that runs through such a nanostructure can not be modeled correctly with periodic boundary constraints. In order to use a periodic frame, two dislocations must run through the cell, see Figure 79b, which is clearly not an appropriate frame.

9.4.2. Linear or Constant Displacement Boundary Constraints. Linear or constant displacement boundary constraints keep the atoms on the surfaces of the nanostructure fixed to some prescribed state of deformation. These constraints can be regarded as special forms of periodic constraints since periodicity is implicitly preserved throughout

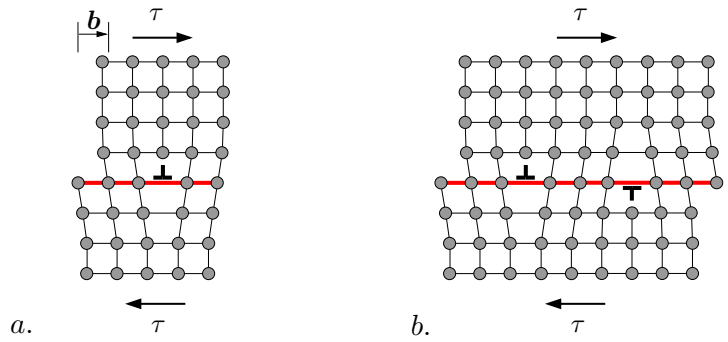

Figure 79: A dislocation moves through the lattice along the slip plane under the shear stress τ. Obviously, with periodic boundary constraints the situation shown in a) can not be modelled since a net Burgers vector $\boldsymbol{b}$ can not exist. Only in configurations as in b) with two similar dislocations moving through the nanostructure, periodicity throughout the cell is preserved.

the course of deformation. A prescribed displacement distribution is for example described in the works deCelis, Argon & Yip [32] and Ashurst & Hoover [5]. Although linear displacement boundary constraints are easy to implement, they are known to give far too stiff unphysical results since interaction with the surrounding medium is not incorporated.

9.4.3. Uniform Stress Boundary Constraints. All the above introduced Dirichlet-type constraints inevitably possess certain implications with regard to the physical response under applied loading conditions. Thus, in the context of dynamic homogenization methods between discrete nano- and continuous mesoscopic scales, the focus should be put onto a framework that is more generally applicable where consistency with mesoscopic continuum theories is ensured. Recall that the Cauchy principle of continuum mechanics states that if a body is cut out from a larger medium, the mechanical action of the outer (cut-away) part is replaced by stresses acting on the surface of the remaining body, that is, tractions. Therefore, the use of some Neumann-type boundary constraints that impose external stresses is self-evident. Several such uniform stress conditions have been used in a variety of formulations. In the work Parrinello & Rahman [100] a Lagrangian formulation is presented that gives a homogeneous distribution of stress throughout the nanostructure. Therein, the total overall stress tensor governs the change of shape and size of the structure and acts as the primary constraint on the atomistic cell. But for the nucleation of cracks or the onset of dislocations, a stress concentration usually occurs in the vicinity of the crack tip. Thus the real stress field becomes inhomogeneous and this inhomogeneity cannot be modeled with this approach. It is noteworthy to mention that this remark has already been discussed in the original paper [100]. Other formulations use constant external forces on the whole or a part of the surface of such nanostructures to impose loading, see Ashurst & Hoover [5] and deCelis, Argon & Yip [32]. These stress-controlled approaches seem to have been used mainly for simulations of problems in nanofracture. Quite recently, Cleri [26] developed a stress-driven constant-traction molecular dynamics method in order to guarantee consistency between atomistic and continuum-mechanical descriptions. Therein, some homogeneous stress tensor is imposed onto the atomistic structure under consideration that reproduces the loading conditions of an infinite continuum. In the work at hand, a similar focus is adopted but rather in a deformation-controlled scenario which is suitable for implementations as material models in strain-driven multiscale finite element simulations of problems on some mesoscopic

scale, as implemented in the previous chapter on granular materials.

9.5. Deformation-Controlled Uniform Stress Boundary Constraints

This section deals with a uniform traction boundary constraint formulation for discrete atomistic nanostructures. In other structures, such as heterogeneous continuous or granular discontinuous materials, theoretical and computational investigations have shown that linear deformation and uniform traction constraints on the boundary of a representative volume element yield upper and lower bound characteristics for periodic boundary conditions with respect to the stiffness and stress response of the elementary volume. In large-strain formulations, uniform tractions on the surface of some nanosystem are enforced by the Cauchy-like theorem

$$\boldsymbol{t}(\boldsymbol{X},t) = \bar{\boldsymbol{P}}(t)\boldsymbol{N}(\boldsymbol{X}) \quad \text{on} \quad \partial\mathcal{V} \ , \tag{9.22}$$

where the mesoscopic first Piola-Kirchhoff stress tensor $\bar{\boldsymbol{P}}$ describes the current stress state of the structure. The vector $\boldsymbol{t}$ represents the traction vector on the deformed surface and $\boldsymbol{N} = \hat{\boldsymbol{N}}(\boldsymbol{X})$ a unit normal vector at a point $\boldsymbol{X}$ on the undeformed surface of the nanostructure. This condition defines constant tractions on parts of the surface with the same unit normal $\boldsymbol{N}$. The tensor $\bar{\boldsymbol{P}}$ would a priori be known in force-driven approaches, but not in deformation-controlled processes favored here where the aim is to compute $\bar{\boldsymbol{P}}$ from some deformation state. Thus the definition of the mesoscopic homogeneous deformation gradient $\bar{\boldsymbol{F}}$ may serve as a weak constraint enforcing the uniform traction surface condition. For continuous systems, the definition is given in equation (3.15). For the discrete atomistic systems investigated here, using the discrete limit $(9.10)_1$ with (3.15) gives the discrete counterpart as

$$\sum_{q=1}^{M} \boldsymbol{x}_q(t) \otimes \boldsymbol{A}_q - |\mathcal{V}|\bar{\boldsymbol{F}} = \boldsymbol{0} \quad \text{for } q = 1, \dots, M \ , \tag{9.23}$$

where the index q runs over all boundary/ surface atoms M of the atomistic structure. In an approach similar to the one in the granular structures, potential functions for the resultant atomic forces are assumed that need to be minimized, that is

$$\Pi(\boldsymbol{x}_i) \rightarrow \text{Min.} \quad \text{for } i = 1, \dots, (M+N) \tag{9.24}$$

for all $(M+N)$ atoms in the system. Then the constraint (9.23) can be treated as the basis for a quadratic penalty term

$$c(\boldsymbol{x}_q(t)) := \frac{1}{2}\epsilon||\sum_{q=1}^{M} \boldsymbol{x}_q(t) \otimes \boldsymbol{A}_q - |\mathcal{V}|\ \bar{\boldsymbol{F}}||^2 \ , \tag{9.25}$$

with the penalty factor ϵ. Furthermore, implementation into (9.24) yields the full potential $\Pi_p(\boldsymbol{x}_q)$ with the penalty term $c(\boldsymbol{x}_q)$ to be minimized in the form

$$\Pi_p(\boldsymbol{x}_q(t)) = \Pi(\boldsymbol{x}_q(t)) + \frac{1}{2}\epsilon||\sum_{q=1}^{M} \boldsymbol{x}_q(t) \otimes \boldsymbol{A}_q - |\mathcal{V}|\ \bar{\boldsymbol{F}}||^2 \ . \tag{9.26}$$

Derivation with respect to the actual atomic positions $\boldsymbol{x}_q$ of the surface atoms then yields the support forces $\boldsymbol{f}_q$ acting at the positions that are necessary to preserve the uniform traction constraint (3.15) of the form

$$\boldsymbol{f}_q(\boldsymbol{x}_q(t)) := \frac{\partial}{\partial \boldsymbol{x}_q}\Pi_p(\boldsymbol{x}_q(t)) = \epsilon \left[\sum_{p=1}^{M}(\boldsymbol{A}_p \cdot \boldsymbol{A}_q)\boldsymbol{x}_p(t) - |\mathcal{V}|\ \bar{\boldsymbol{F}}\boldsymbol{A}_q\right] . \tag{9.27}$$

This formulation allows for a computation of uniform tractions on the surface of atomistic nanostructures in *deformation-driven* processes. Observe that the object $\boldsymbol{f}_q$ derived here complies with the object $\boldsymbol{a}_q$, the artifical support forces, in the formulations of the homogenized mesoscopic Cauchy stresses in equations (9.10) – (9.18). The time dependence of the actual positions $\boldsymbol{x}_q(t)$ has explicitly been written down to stress the time dependence of the solution in the context of the dynamic homogenization procedure shown above. In this formulation, the homogeneous deformation gradient $\bar{\boldsymbol{F}}$ serves as the primary object that drives the nanostructure. Subsequently, after each load increment $\Delta\bar{\boldsymbol{F}}$ has been imposed and dynamically stationary states have been reached, homogenized quantities such as stresses $\bar{\boldsymbol{\sigma}}$, $\bar{\boldsymbol{P}}$ and others can be computed. Note that the support forces change in each time step, thus they must be recomputed every time.

10. Molecular Dynamics Applications

In this chapter some representative molecular dynamics computations in context with the deformation-driven approach discussed before for atomistic nanosystems are presented. The focus is put on nanostructures cut out from large-scale structures, such that free surfaces do not occur. First of all, simple elastic deformations of fcc metals are studied. The focus will then be put on metallic failure. In general, metallic failure can be classified into two generic types: ductile deformation and brittle fracture. In ductile behavior, plastic deformations occur due to dislocations between rows or lines of atoms where the interatomic bonds break, see for example ABRAHAM, WALKUP, ET. AL. [1]. Brittle failure on the other hand is observed when many interatomic bonds break consecutively within a crystal. It is characterized by the sudden breaking of interatomic bonds along some crack front. In brittle failure, thousands of cracks break the material, a good example is glass that shatters, see for example BUEHLER [18]. The aim of this section is to demonstrate the ability of the newly developed boundary constraint for deformation-controlled processes to model and simulate elastic as well as ductile and brittle plastic behavior in metallic materials. The examples deal with both two and three dimensional nanosystems.

10.1. Elastic Deformations in Metallic Structures

Materials deform under the action of applied stresses. Temporary deformations, which are self-reversing when the applied stress is removed, are called elastic. The elastic regime is usually limited to small deformations at low stresses. On the atomistic side, elastic deformations are characterized by the *stretching* of the interatomic bonds where the original arrangement of the atoms is preserved.

10.1.1. 3D Elastic Shear Deformation of an fcc Crystal. As an introductory example to the examples section, the stiffness of a three dimensional ideal monoatomic fcc crystal is studied under an applied homogeneous shear deformation. The nanostructure used in the simulation is an fcc cube of $10a \times 10a \times 10a\,\mathring{A}^2$ unit cells where the lattice parameter a depends on the material, see Table 3. The cutoff radius is chosen as $r_c = 2.1a$. The total number of atoms in the example is 4631, where 1202 atoms lie on the surface of the nanosystem. The penalty parameter that enforces the uniform traction constraint is $\epsilon = 10^{27}$. The empirical potential of choice is the Sutton & Chen potential discussed in

Table 3: Sutton & Chen Potential Parameters for fcc Metals

Material	*Symbol*	m	n	$\varepsilon\,[eV]$	c	$a\,[\mathring{A}]$
Aluminium	Al	6	7	$3.3147 \cdot 10^{-2}$	16.399	4.05
Gold	Au	8	10	$1.2793 \cdot 10^{-1}$	34.408	4.08
Lead	Pb	7	10	$5.5765 \cdot 10^{-3}$	45.778	4.95
Silver	Ag	6	12	$2.5415 \cdot 10^{-3}$	144.41	4.09
Copper	Cu	6	9	$1.2382 \cdot 10^{-2}$	39.432	3.61

section 8.4.2. The behavior of the pure fcc metals aluminium (Al), gold (Au), lead (Pb), silver (Ag) and copper (Cu) will be compared. The Sutton & Chen potential parameters for these five materials are shown in Table 3. Initially, the NVT nanosystems are equilibrated at a temperature of $300\,K$ in 1000 time steps of $\Delta t = 2 \times 10^{-16}\,s$. The mesoscopic homogeneous shear deformation that drives the nanostructure is presribed by $\bar{F}_{13} = 0.25$

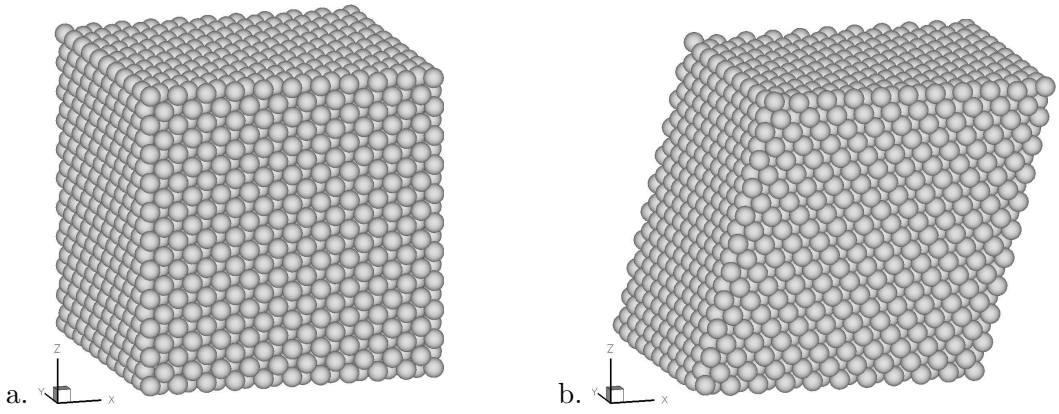

Figure 80: Elastic shearing of an fcc cube with 4631 atoms, a. initial configuration and b. final deformation at $\bar{F}_{13} = 0.25$. The computation was performed using the Sutton & Chen potential [109] with several material parameters.

where also a slight compression is imposed as $\bar{F}_{ii} = -0.10, i = 1, 2, 3$. The deformation is imposed in 50 incremental load steps, each step followed by 1000 relaxation time steps at frozen mesoscopic deformation. The mesoscopic homogenized observables such as the stresses, see Figure 81, are averaged over the last 500 time steps within each load step.

In Figure 80 the initial and final configurations of the nanostructure are shown. The deformation is reversible and elastic, interatomic bonds are only stretched and not broken.

In Figures 81a and b, the homogenized shear $\bar{\sigma}_{13}$ and normal $\bar{\sigma}_{22}$ stresses during the

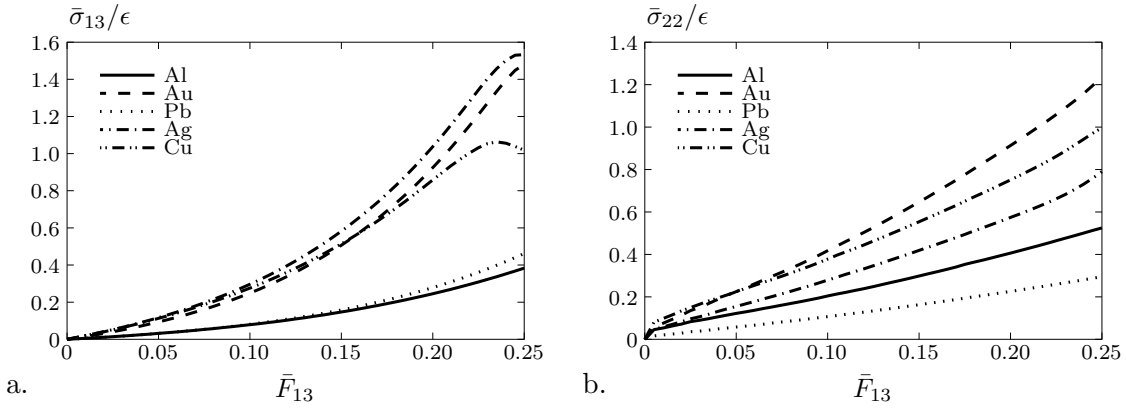

Figure 81: Elastic stresses a. $\bar{\sigma}_{13}$ and a. $\bar{\sigma}_{22}$ versus mesoscopic homogeneous shear deformation $\bar{F}_{13}$ for various metallic materials. Copper (Cu) already reached the end of the elastic domain in a.

applied shear deformation $\bar{F}_{13}$ are plotted. It is obvious that aluminium and lead exhibit the softest, whereas silver, gold and copper the stiffer elastic behavior of the five materials studied. For copper, at a mesoscopic deformation of $\bar{F}_{13} \approx 0.23$, the end of the elastic deformation is already reached since the stress-strain curve flattens. Plastic behavior of such nanosystems will be studied in the subsequent examples.

10.2. Plastic Deformations in Metallic Structures

If the stress is sufficiently large to irreversibly deform the structure, the deformation is called plastic. This deformation involves the breaking of a limited number of interatomic bonds by the movement of dislocations where the atoms slip past each other. The force

needed to break the bonds between all atoms in a crystal plane is very large, however, dislocations in such crystal planes occur at much lower stress levels. The slip generally

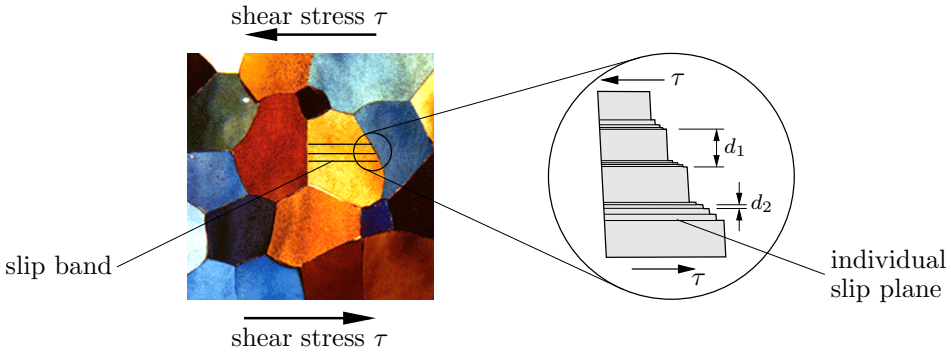

Figure 82: Plastic deformation in crystals is characterized by the movement of dislocations. The distance between the individual *slip planes* lies in the range of about $d_2 \approx 100$ atomic diameters, whereas the distance between the *slip bands* can typically be $d_2 \approx 10000$ atomic diameters.

occurs along parallel planes within a crystal, see Figure 82, because the energy required for the dislocation to move is lowest along the densest planes. Therefore, dislocations have preferred directions within crystal grains. The individual *slip planes*, see Figure 82, group together to form the *slip bands* which can even be seen under a microscope.

10.2.1. 2D Point Defect in Triangular Single Crystal Lattice. As an introductory example, the ductile deformation in the form of a movement of a point defect during shear deformation in a two dimensional triangular single crystal lattice is investigated, see Figure 83a. The nanosystem consists of 263 Al-like atoms where 60 are on the surfaces of the structure. For the simulation, the embedded atom method (EAM), see chapter 8.4.1, is used as the only constitutive input with the following Al parameters for simulations in two dimensions: $A = 0.320307\,eV$, $B = 0.075016\,eV$, $C = 0.159472\,eV$, $\alpha = 1.767488\,\mathring{A}$, $\beta = 2.017519\,\mathring{A}$, $\xi = 0.147690$ and $r^* = 3.365875\mathring{A}$. The cutoff radius is prescribed as $r_c = 2.5r^*$. The NVT system is equilibrated at a thermodynamic temperature of 300 K. This equilibrated structure with the defect is shown in Figure 83a. For the simulation a time step of $\Delta t = 2 \times 10^{-16}$ is used. The total shear deformation of $\bar{F}_{12} = 0.25$ is

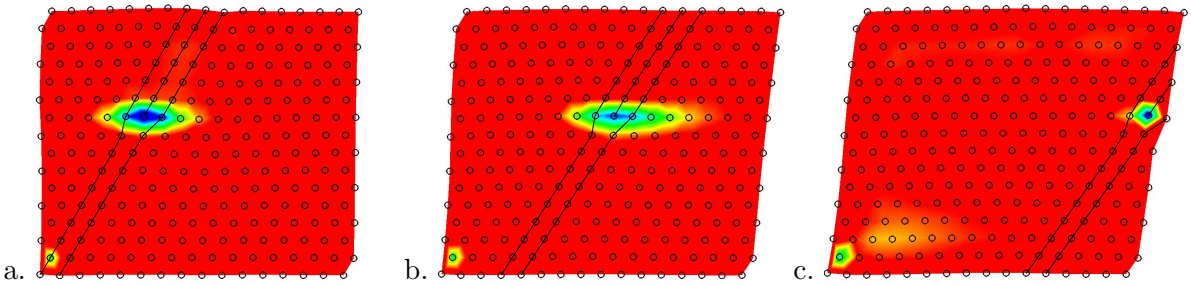

Figure 83: Dislocation movement of a point defect through a two dimensional single crystal *Al* lattice, a. $\bar{F}_{12} = 0.015$, b. $\bar{F}_{12} = 0.085$, and c. $\bar{F}_{12} = 0.150$. The bright spots indicate areas where the potential site energies are lower than the bulk average, i.e. where the defects currently reside.

applied in 50 incremental load steps $\Delta\bar{F}_{12} = 0.005$, after each load steps 1000 relaxation time steps are computed. The mesoscopic Cauchy stress is averaged over the last 500

relaxation time steps. Under the applied prescribed homogeneous deformation, the defect begins to move through the crystal until it reaches the right surface. The contour plots in Figures 83a-c show the distribution of potential atomic site energies $\mathcal{U}_i$. The bright spots indicate regions of lower potential energies, that is, the defect sites. Dislocations occur only where the potential energies are lower than in the surrounding bulk. In Fig-

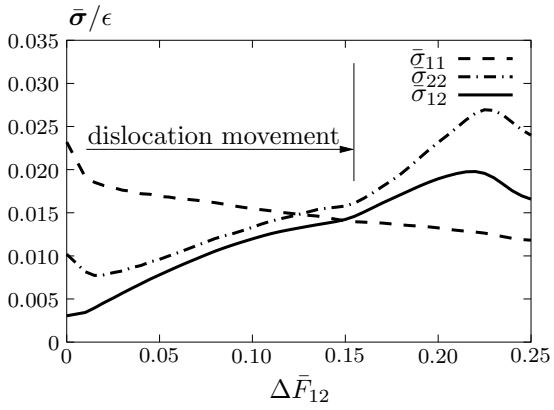

Figure 84: Stresses $\bar{\sigma}_{11}$, $\bar{\sigma}_{22}$, $\bar{\sigma}_{12}$ versus homogeneous shear deformation $\Delta\bar{F}_{12}$ during movement of the point defect through the monoatomic two dimensional *Al* lattice. The shear stress in particular increases once the dislocation has reached the surface of the structure at a deformation state of about $\Delta\bar{F}_{12} \approx 0.15$.

ure 84 the mesoscopic Cauchy stress development is plotted against the prescribed shear deformation. The homogeneous components $\bar{\sigma}_{22}$ and $\bar{\sigma}_{12}$ of the uniform stresses on the surface only slightly increase as long as the defects moves through the nanosystem. It reaches the surface at about $\bar{F}_{12} = 0.15$, see the Figures 83c and 84. Once the defect has left the structure, the system is an ideal crystal with a stiffer behavior than before. Consequently, the stress curves $\bar{\sigma}_{22}$ and $\bar{\sigma}_{12}$ become steeper. Note that throughout the total simulation, the uniform $\bar{\sigma}_{11}$ stress component decreases as the defect runs into the x_1 direction. Finally, in Figure 85 the development of the total kinetic and potential

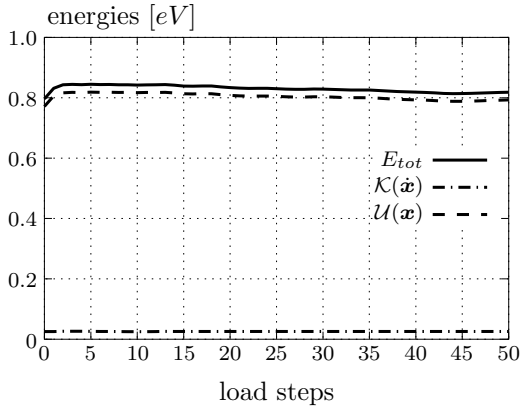

Figure 85: Development of potential $\mathcal{U}(\boldsymbol{x})$, kinetic $\mathcal{K}(\dot{\boldsymbol{x}})$ and total E_{tot} energies during the deformation of the two dimensional lattice with point defect.

energies in the nanostructure during the deformation and the propagation of the point defect is shown versus all 50 000 time steps (50 load steps $\times$1000 relaxation steps). Since an NVT ensemble type is used, the total energy E_{tot} is not constant during deformation.

10.2.2. 2D Annihilation of Two Point Defects in a Triangular Lattice. As a second example, a nanoystem with two opposite point defects in the two dimensional triangular single crystal lattice structure is observed. Here, the nanostructure is bigger than before, made up of a total of 1440 Al-like atoms with 147 on the surfaces. Again, the structure is initially equilibrated at 300 K and the embedded atom method EAM is employed as the constitutive input. Time step and parameters are the same as in the previous example. The system is driven by a mesoscopic homogeneous shear deformation mode $\bar{F}_{12} = 0.25$ applied in 50 incremental load steps $\Delta\bar{F}_{12} = 0.005$, and 1000 relaxation steps are computed after each load increase. In Figure 86a-c the initial, intermediate and final configuration at deformation states a $\bar{F}_{12} = 0.01$, b $\bar{F}_{12} = 0.13$ and c $\bar{F}_{12} = 0.25$ are shown. The contour plots show the distribution of the potential atomic site energies.

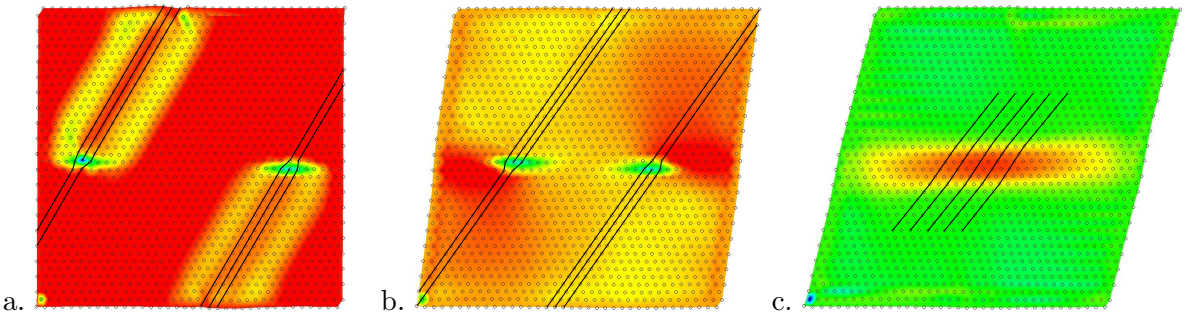

Figure 86: Two point defects annihilate themselves during deformation in a two-dimensional *Al* lattice, a. $\bar{F}_{12} = 0.01$, b. $\bar{F}_{12} = 0.13$ and c. $\bar{F}_{12} = 0.25$. The highlighted spots indicate areas where the potential site energies are lower than the bulk average, i.e. where defects develop.

Again, the defect lies where the site energy drops significantly. Under deformation, the two point defects move toward one another until at a deformation of about $\bar{F}_{12} = 0.25$ they annihilate one another, leaving an ideal crystal lattice structure.

10.2.3. 3D Nanovoid Deformation in Copper under Shear. This example deals with a three dimensional fcc metal with material properties of Copper in the Sutton & Chen multi-body potential. The nanostructure consists of $20a \times 20a \times 20a\,\mathring{A}^2$ unit cells with a nanovoid at the center. This nanovoid is such that the atoms in a spherical domain with radius $r_0 = 2.0a$ in the center $x_0 = y_0 = z_0 = 10a$ have been removed from the nanostructure. The lattice parameter of Copper (Cu) is given as $a = 3.61\mathring{A}$. Thus the atomistic structure is made of a total number of 34 320 atoms of which 4802 lie on the surface. The initial structure occupies a reference volume of $V_0 = 376\ 367.048\,\mathring{A}^2$. For example, Marian, Knap & Ortiz [71] use the quasicontinuum method (QC) at zero temperature to minimize boundary and cell-size effects in simulations of nanovoid deformation in Al structures. In Figure 87 the initial nanostructure is depicted in two pictures. In 87a the total structure is shown, whereas in 87b only the atoms on the upper and lower surfaces and those around the nanovoid are plotted. Here, the contour shading is associated with the centrosymmetry parameter introduced below. In Figure 88 the dislocations and defects that start at the inner surface of the nanovoid are located and imaged by the so-called centrosymmetry parameter, see Kelchner, Plimpton & Hamilton [60], defined as

$$p = \sum_{i=1}^{6} |\boldsymbol{r}_i + \boldsymbol{r}_{i+6}|^2 \ ,$$

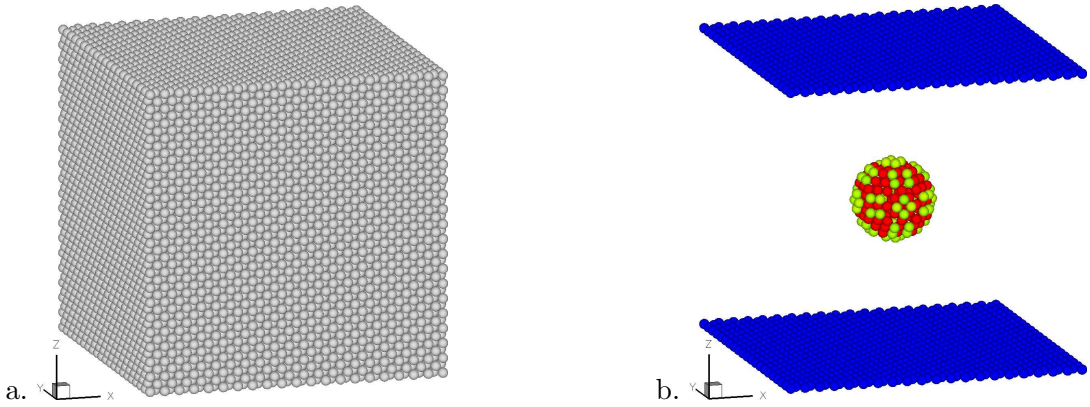

Figure 87: Initial three dimensional nanostructure with nanovoid at the center, a. total structure with all atoms and b. only atoms on the top and bottom surface and those around the equiaxed nanovoid are shown.

where $\boldsymbol{r}_i$ and $\boldsymbol{r}_{i+6}$ are the interatomic vectors that correspond to the six pairs of opposite nearest neighbors in the three dimensional fcc lattice. The advantage of using the centrosymmetry parameter is that it does not identify elastically deformed lattice atoms, whereas techniques relying on the electron density, potential energy and other parameters do. In Figures 88a-d the initial lattice structure and incipient partial dislocation struc-

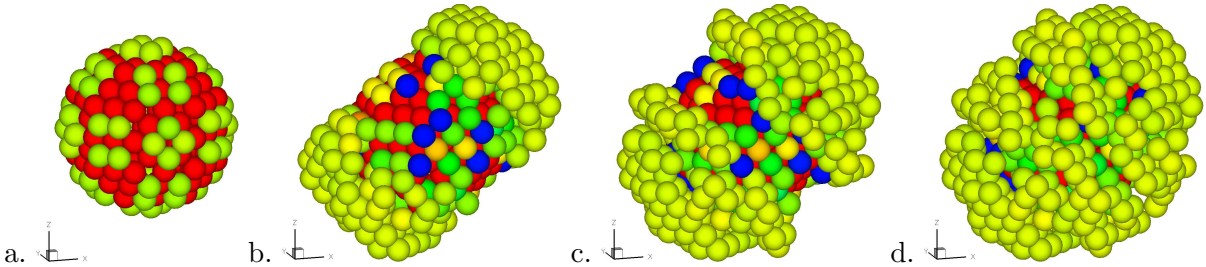

Figure 88: Initial nanovoid and incipient partial dislocation structures in the vicinity of the nanovoid due to the applied mesoscopic homogeneous shear deformations a. $\bar{F}_{13} = 0.00$, b. $\bar{F}_{13} = 0.15$, c. $\bar{F}_{13} = 0.16$ and d. $\bar{F}_{13} = 0.17$.

tures around the nanovoid due to the applied mesoscopic homogeneous shear deformations are depicted at meso-deformations a $\bar{F}_{13} = 0.0$, b $\bar{F}_{13} = 0.15$, c $\bar{F}_{13} = 0.16$ and finally

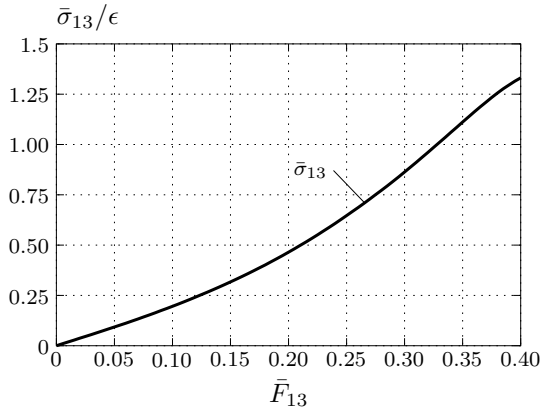

Figure 89: Shear stress $\bar{\sigma}_{13}$ during deformation $\bar{F}_{13}$ of the three dimensional atomistic nanostructure with nanovoid.

$\bar{F}_{13} = 0.17$. The dislocations develop point-symmetrically at an angle of approximately 45^o to the shear direction. Also, in Figure 90a the distribution of the potential atomic

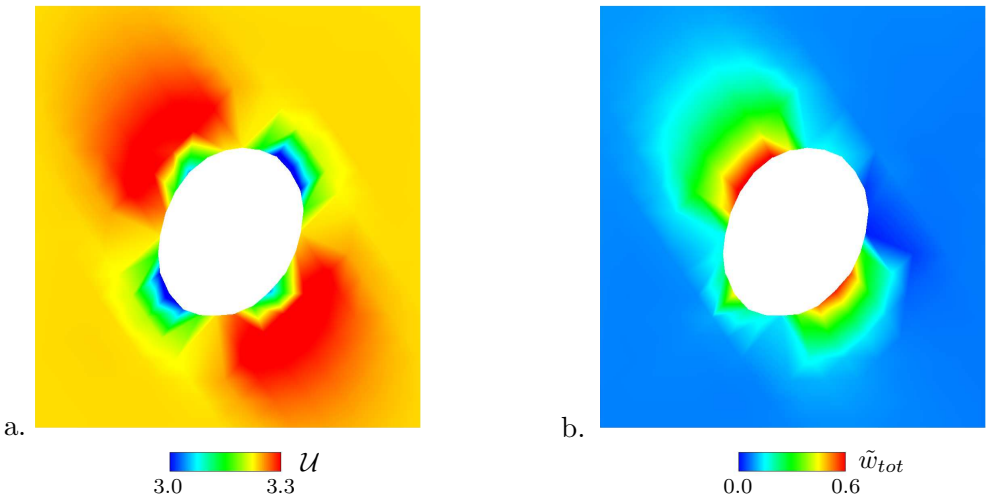

Figure 90: Distribution of a. potential atomic site energies $\mathcal{U}$ and b. absolute total atomic fluctutation $w_{tot} = |w_x| + |w_y|$ in a two dimensional cross section of the three dimensional atomistic system in the vicinity of the nanovoid.

site energies $\mathcal{U} = \hat{\mathcal{U}}(\boldsymbol{x})$ and in Figure 90b the associated distribution of the total fluctutation $\tilde{w}_{tot} = |\tilde{w}_x| + |\tilde{w}_y|$ are plotted. Recall that the the fluctuation vector $\tilde{\boldsymbol{w}} = [\tilde{w}_x\ \tilde{w}_y]^T$ describes the displacement of the atoms with respect to the homogeneously applied deformation $\bar{\boldsymbol{F}}$, such that the total displacement appears as $\boldsymbol{x} = \bar{\boldsymbol{F}}\boldsymbol{X} + \boldsymbol{w}$. Thus, every point in Figure 90b with deviations from zero indicates a non-homogeneously displaced atom. In both Figures 90a andb, the deviations in both potential site energies and total fluctuations develop at an angle of approximately 45^o degrees. These fluctuations indicate the developing partial dislocation structures as already seen in the three dimensional pictures 88a-d. Finally, in Figure 89 the overall mesoscopic homogenized Cauchy shear stress $\bar{\sigma}_{13}$ versus the applied homogeneous shear deformation $\bar{F}_{13}$ that drives the structure is shown.

10.2.4. 2D Fracture Study of a Triangular Al Lattice with Nanovoid. In this example the uniform traction constraint in connection with molecular dynamics simulations is applied to the second generic class of materials failure, namely *brittle* failure. In the example, a two dimensional triangular monoatomic lattice with Al properties, see the examples above, is studied. The nanosystem consists of 2910 atoms where 213 particles are surface atoms. The unit cell has dimensions of $l = 50.0 \times h = 49.36\,\mathring{A}$, the interatomic equilibrium distance is $r_0 = 3.4068\mathring{A}$. The simulation is carried out using the empirical Lennard-Jones 12-6 potential, see section 8.3.1, with parameters $\varepsilon = 0.25\,eV$, $\sigma = 3.03511\,\mathring{A}$ and atom mass $m = 27.0\,amu$. The cutoff radius was chosen to be $r_c = 2.5 \cdot \sigma$. Initially, 19 atoms were removed from an elliptical region with principal diameters $d_x = l/8$ and $d_y = l/16$. The centroid of the nanovoid lies at $x_0 = 0.6\,l$ and $y_0 = 0.55\,l$. This configuration was deliberately chosen in order to avoid a symmetric nanostructure. The mesoscopic homogeneous deformation applied is characterized by a tensile stretching in x_1 direction and slight compression in the lateral one. The final deformation coordinates are $\bar{F}_{11} = 0.25$ and $\bar{F}_{22} = -0.025$, and the off-diagonal shear entries of $\bar{\boldsymbol{F}}$ are zero. The deformation is incrementally applied in 50 load steps where after each load step 1000 relaxation steps with constant mesoscopic homogeneous deformation are

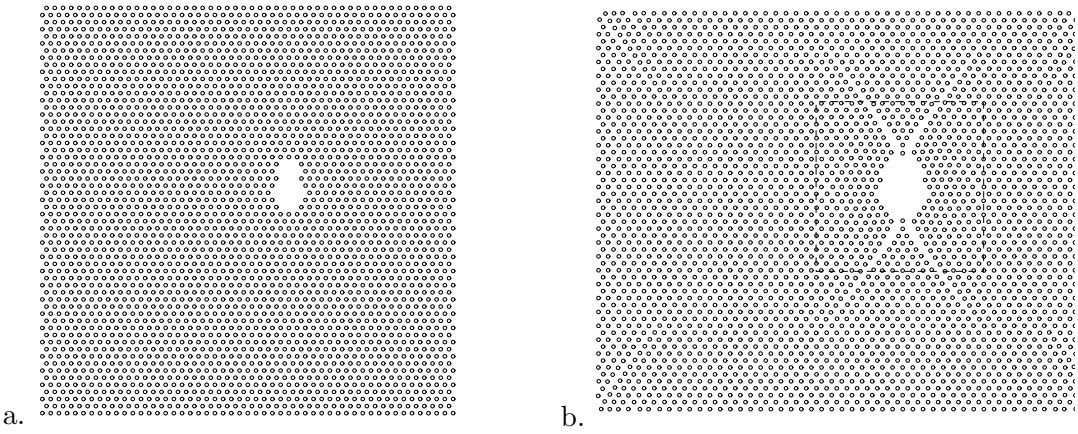

Figure 91: Atomistic nanosystem with a void: a. Initial configuration with 2910 atoms and b. final configuration with $\Delta\bar{F}_{11} = 0.25$ and $\Delta\bar{F}_{22} = -0.025$ with propagated cracks starting at the void.

executed. The support forces which enforce the uniformity of the stress on the surface are updated in each relaxation step. The averaging of the overall Cauchy stress is performed during the last 500 relaxation steps, assuming that after the first 500 relaxation steps a dynamically steady state is reached. The simulation is done at a constant temperature of $300\,K$, thus an NVT ensemble type is employed. The initial equilibration period comprised of 1000 steps, where a time step of $\Delta t = 2 \cdot 10^{-16}\,s$ is employed. In

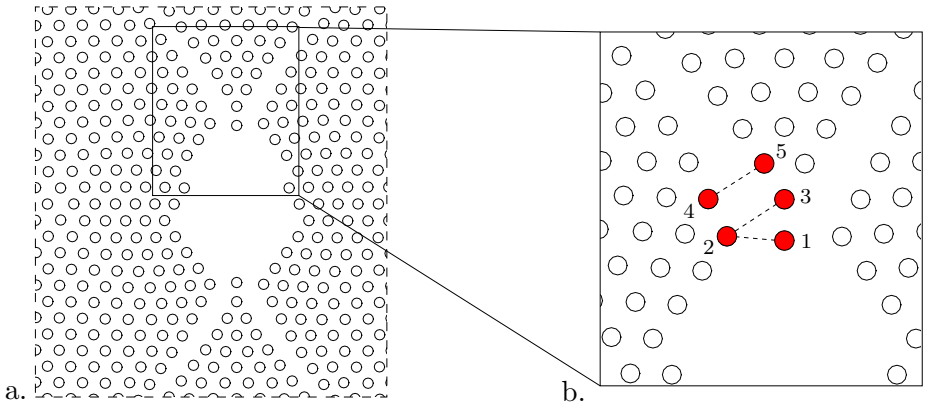

Figure 92: Magnifications of the fracturing area of the nanosystem in Figure 91. In b. the five atoms are highlighted whose interatomic forces are evaluated in Figure 93b.

Figure 91 the initial and final configurations of the nanosystem are shown. In the final system, cracks have developed cross diagonally from both the upper and lower ends of the elliptical nanovoid, as expected. The crack started to grow in a cleavage mode leaving a smooth cracked surface. This is also found in the research paper Hua, Rafii-Tabar & Cross [51]. In Figure 92 the area around the nanovoid is magnified in two pictures. Additionally, in Figure 92b five particular atoms at the initiation of one crack are highlighted whose interatomic forces are explicitly evaluated. In Figure 93b the interatomic Lennard-Jones forces between the atoms 1 – 5 of Figure 92b during the course of mesoscopic deformation are shown. All three forces shown here increase monotonically during the deformation where the lattice is uncracked. The fracture process is then characterized by *sharp* and sudden consecutive declines of the interatomic forces. Finally, Figure 93a shows the mesoscopic homogeneous and time averaged Cauchy stresses $\bar{\sigma}_{11}$ and $\bar{\sigma}_{22}$ during

the course of mesoscopic deformation. A softening behavior can clearly be observed once

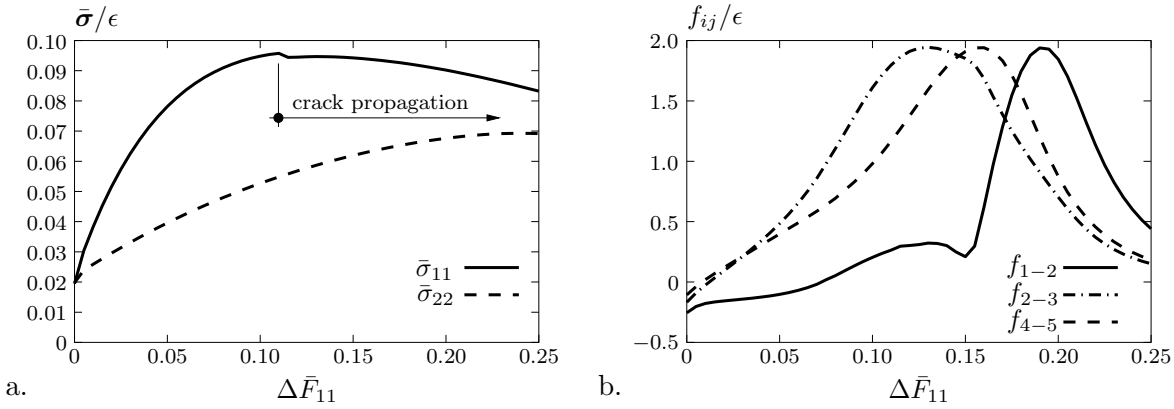

Figure 93: a. Mesoscopic homogeneous stress development of the cracking nanosystem. b. Development of the interatomic forces between the five atoms highlighted in Figure 92b. During incipient crack a sudden drop of the interatomic forces can clearly be observed.

the crack has started to develop. Especially in the $\bar{\sigma}_{11}$ curve, the sudden development of the crack can be observed by a kink and drop of the stress at a mesoscopic deformation of about $\Delta\bar{F}_{11} \approx 0.11$. With the cracks propagating through the lattice, the mesoscopic behavior then softens significantly. In Figure 94, the development of the total kinetic and potential energies in the nanostructure during the fracture process is shown versus all 50 000 time steps. Due to the fracturing lattice, the mechanical behavior softens because

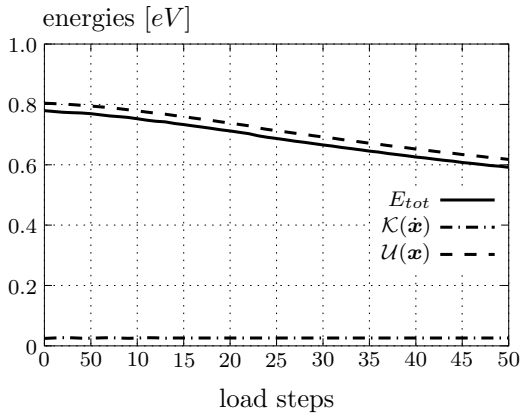

Figure 94: Development of potential $\mathcal{U}(\boldsymbol{x})$, kinetic $\mathcal{K}(\dot{\boldsymbol{x}})$ and total E_{tot} energies during the fracturing two dimensional triangular Al lattice.

fewer interatomic bonds and potentials contribute to the total potential energy in the nanostructure. Thus, not only the total potential energy $\mathcal{U}$, but also the total energy E_{tot} in the nanosystem decreases during the course of deformation.

11. Conclusion and Outlook

This work deals with scale bridging methods for discrete microscopic granular and nanoscopic atomistic aggregates of particles between different length and time scales. The scale bridging is performed in the context of direct homogenization of micro- and nanoscopic physical quantities. Several types of boundary constraints are discussed, the strain-driven implementation is performed such that they are suitable for use in higher or coarse scale continuum methods like the finite element method.

The first part of the work deals with *static* homogenization techniques and multiple scale simulations for aggregates of granular solids at large strains. First of all, the definition of a granular microstructure is introduced with particles on the boundary that represent the driving frame of the structure. Therein, particles on opposite surfaces are assumed to be equal in size and rotation such that a periodic extension to infinity can be achieved. This well defined boundary frame allows for arbitrary shapes of microstructures and a consistent transfer of homogenization definitions from continuous to discrete RVEs. The three classical boundary constraints for continuous structures already available in literature, see for example Miehe [76, 77], are consistently transferred to discrete formulations that for the first time incorporate the discrete character of the granules. Specifically, particle displacements and rotations are accounted for in the constraint formulation. The implementation is performed by means of a penalty method with quadratic penalty terms that proves to be convenient in explicit time integration techniques. The results underline the fact that the constraints for linear deformations and uniform tractions on the boundaries of such microstructures yield upper and lower bounds, respectively, for periodic constraints with regard to the stiffness of the material. On the micromechanical side, elliptical and circular two dimensional and spherical three dimensional particles are used. Their computational treatment is outlined with special regard to classical formulations available in literature. Finally, for the first time true two scale analyses of granular structures are performed and provided at large strains. Therein, the continuum approach of choice on the coarse scale is the finite element method which serves as nothing more than as a numerical tool without any constitutive assumptions. The physical behavior under deformation is solely governed by that of granular microstructures which are attached and invoked at every sampling point of every finite element in each integration loop. History variables of all interparticle contacts are stored throughout the simulation. Thus, the constitutive input is solely done on the microscopic scale by assuming constitutive laws that govern the mechanical behavior of the interparticle contact in both pressure and friction. In such implementations, the accuracy and physical relevance of the simulation are primarily determined by the constitutive model on the microscopic scale. Thus, in order to achieve a higher degree of accuracy, the micromechanical model could be extended such that other physical phenomena like pore water pressure could be included. Moreover, the link between the model parameters that govern the constitutive model and laboratory tests should be established such that the parameters are experimentally verified. In particular, the homogenization technique in three dimensions presented could serve as a numerical laboratory for the identification of material parameters which will find input in constitutive equations for use in phenomenological simulations of geomaterials. On the other hand, numerically a parallel implementation could be favored in order to reduce computing time and to provide for larger simulations on both the micro- and macroscopic scales. Also, a fully dynamic implementation circumventing the relaxation towards qua-

sistatic states should be done and comparative simulations with the quasistatic approach of the present work be performed. For two scale simulations, the development of shear bands in biaxial simulations could further be investigated. Also, a nonlocal extension of the homogenization technique to the so-called gradient theory could be tackled to account for the local macroscopic environment.

The second part of the work covers *dynamic* homogenization techniques for atomistic solids on the nano scale and also at large strains. The classical molecular dynamics technique is outlined and used for the simulation of the evolution of atoms in a nanostructure. The interatomic behavior is governed by empirical potentials. Several types of boundary constraints used in literature are described. A new uniform traction constraint is presented which yields a homogeneous stress state only on the surface of the nanosystem. It is followed that this formulation is the only suitable choice since it allows for a computational modeling of defects and cracks that propagate through the nanosystem. Other constraints, for example periodic definitions, do not allow for such simulations. This uniform stress constraint is implemented in a deformation-controlled scenario that allows for a computational treatment in coarse scale continuum methods. The homogenization procedure of nanoscopic quantities is given in a fully dynamic sense that not only considers the atomic penalty forces on the boundary, but also the kinetics of all atoms in such aggregates. The link to statistical mechanics is also provided, because when dealing with dynamic averaging procedures, the equivalence between time and ensemble averages need to be motivated. In a next step, nanosystems with atoms of more than one type of material as well as polycrystal structures could be investigated. In a further step, a parallel implementation, as previously suggested, could also be performed to provide for computations of (i) larger crystalline nanosystem, (ii) polycrystal structures and (iii) atomistic simulations on multiple scales, similar to those done with the granular structures. In the latter case, the embedding into a higher scale dynamic finite element formulation seems to be an interesting extension and should be viewed as a next step towards predictive simulations of materials through all time and length scales, which in the end should be based on ab initio calculations only.

References

[1] F. F. Abraham, R. Walkup, H. Gao, M. Duchaineau, T. Diaz De La Rubia, and M. Seager. Simulating materials failure by using up to one billion atoms and the world's fastest computer: work-hardening. *Proceedings of the National Academy of Sciences*, 99 (9):5783–5787, 2002.

[2] M. P. Allen and D. J. Tildesley. *Computer Simulation of Liquids*. Oxford University Press, 1987.

[3] H. C. Andersen. Molecular dynamics simulations at constant pressure and/or temperature. *Journal of Chemical Physics*, 72 (4):2384–2393, 1980.

[4] A. Anthoine. Derivation of in-plane characteristics of masonry through homogenization theory. *International Journal of Solids and Structures*, 32:137–163, 1995.

[5] W. T. Ashurst and W. G. Hoover. Microscopic fracture studies in the two-dimensional triangular lattice. *Physical Review B*, 14 (4):1465–1474, 1976.

[6] K. Bagi. Stress and strain in granular assemblies. *Mechanics of Materials*, 22:165–177, 1996.

[7] J. P. Bardet. Introduction to computational granular mechanics. In B. Cambou, editor, *Behaviour of Granular Materials, CISM Courses and Lectures No. 385*, pages 99–169. International Centre for Mechanical Sciences, Springer-Verlag, Wien, New York, 1998.

[8] J. P. Bardet and J. Proubet. Adaptative dynamic relaxation for statics of granular materials. *Computers & Structures*, 39:221–229, 1991.

[9] J. P. Bardet and I. Vardoulakis. The asymmetry of stress in granular media. *International Journal of Solids and Structures*, 38:353–367, 2001.

[10] Z. S. Basinski, M. S. Duesbery, and R. Taylor. Influence of shear stress on screw dislocations in a model sodium lattice. *Canadian Journal of Physics*, 49:2160–2180, 1971.

[11] R. J. Bathurst and L. Rothenburg. Micromechanical aspects of isotropic granular assemblies with linear contact interactions. *Journal of Applied Mechanics*, 55:17–23, 1988.

[12] C. G. Bayreuther. *Mehrskalenmodelle in der Festkörpermechanik und Kopplung von Mehrgittermethoden mit Homogenisierungsverfahren*. No. I-16, Institut für Mechanik (Bauwesen), Universität Stuttgart, 2005.

[13] D. Beeman. Some multistep methods for use in molecular dynamics calculations. *Journal of Computational Physics*, 20 (2):130–139, 1976.

[14] J. Bonet and J. Peraire. An alternating digital tree (ADT) algorithm for 3D geometric searching and intersection problems. *International Journal for Numerical Methods in Engineering*, 31:1–17, 1991.

[15] J. Bonet and R. D. Wood. *Nonlinear continuum mechanics for finite element analysis*. Cambridge University Press, 1997.

[16] R. I. Borja and J. R. Wren. Micromechanics of granular media Part I: Generation of overall constitutive equation for assemblies of circular disks. *Computer Methods in Applied Mechanics and Engineering*, 127:13–36, 1995.

[17] J. Q. Broughton, F. F. Abraham, N. Bernstein, and E. Kaxiras. Concurrent coupling of length scales: Methodology and application. *Physical Review B*, 60 (4-15):2391–2403, 1999.

[18] M. J. Buehler. *Atomistic and Continuum Studies of Deformation and Failure in Brittle Solids and Thin Film Systems*. No. 147, Max-Planck-Institut für Metallforschung Stuttgart and Universität Stuttgart, 2004.

[19] B. Cambou. Micromechanical approach in granular materials. In B. Cambou, editor, *Behaviour of Granular Materials*, pages 171–216. International Centre for Mechanical Sciences, Springer-Verlag, Vienna, 1997.

[20] B. Cambou, P. Dubujet, F. Emeriault, and F. Sidoroff. Homogenization for granular materials. *European Journal of Mechanics A / Solids*, 14 (2):255–276, 1995.

[21] A. E. Carlsson. In H. Ehrenreich and D. Turnbull, editors, *Solid State Physics 43, Adv. in Research and Applications*, page 1. Academic, New York, 1990, 1990.

[22] C. Cattaneo. Sul contatto di due corpi elastici: distribuzione locale degli sforzi. *Rendiconti dell'Academia nazionale dei Lincei*, 27 (6):342, 434, 474, 1938.

[23] C. S. Chang and C. L. Liao. Constitutive relation for a particulate medium with the effect of particle rotation. *International Journal of Solids and Structures*, 26 (4):437–453, 1999.

[24] C. S. Chang and L. Ma. A micromechanical-based micropolar theory for deformation of granular solids. *International Journal of Solids and Structures*, 28 (1):67–86, 1991.

[25] J. Christoffersen, M. M. Mehrabadi, and S. Nemat-Nasser. A micromechanical description of granular material behavior. *Journal of Applied Mechanics*, 48:339–344, 1981.

[26] F. Cleri. Representation of mechanical loads in molecular dynamics simulations. *Physical Review B*, 65:014107(1)–014107(6), 2001.

[27] D. R. Cook, D. S. Malkus, and M. E. Plesha. *Concepts and applications of finite element analysis*. John Wiley & Sons, 3 edition, 1989.

[28] P. A. Cundall. Formulation of a three-dimensional distinct element model — Part I. A scheme to detect and represent contacts in a system composed of many polyhedreal blocks. *International Journal of Rock Mechanics and Mining Sciences and Geomechanics Abstracts*, 25 (3):107–116, 1988.

[29] P. A. Cundall and O. D. L. Strack. A discrete numerical model for granular assemblies. *Géotechnique*, 29 (1):47–65, 1979.

[30] M. S. Daw and M. I. Baskes. Embedded-atom method: Derivation and application to impurities, surfaces, and other defects in metals. *Physical Review B*, 29:6443–6453, 1984.

[31] M. S. Daw, S. M. Foiles, and M. I. Baskes. The embedded-atom method: a review of theory and applications. *Materials Science Reports*, 9:251–310, 1993.

[32] B. deCelis, A. S. Argon, and S. Yip. Molecular dynamics simulation of crack tip processes in alpha-iron and copper. *Journal of Applied Physics*, 54 (9):4864–4878, 1983.

[33] J. Delhommelle and P. Millie. Inadequacy of the Lorentz-Berthelot combining rules for accurate predictions of equilibrium properties by molecular simulation. *Molecular Physics*, 99 (8):619–625, 2001.

[34] H. Deresiewicz. Mechanics of granular matter. *Advances in Applied Mechanics*, V:233–306, 1958.

[35] J. Desrues and G. Viggiani. Strain localization in sand: an overview of the experimental results obtained in grenoble using stereophotogrammetry. *International Journal for Numerical and Analytical Methods in Geomechanics*, 28:279–321, 2004.

[36] J. Dettmar and C. Miehe. Alternative definitions of micro-to-macro transitions in particle aggregates of granular materials. *Proceedings in Applied Mathematics and Mechanics*, 3:264–265, 2003.

[37] J. Dettmar and C. Miehe. Macroscopic finite element analyses of discrete materials based on directly evaluated micro-macro transitions. *Proceedings in Applied Mathematics and Mechanics*, 4:306–307, 2004.

[38] W. Ehlers, E. Ramm, S. Diebels, and G. A. D'Addetta. From particle ensembles to cosserat continua: homogenization of contact forces towards stresses and couple stresses. *International Journal of Solids and Structures*, 40:6681–6702, 2003.

[39] Cambou B. Emeriault, F. and A. Mahboudi. Homogenization for granular materials: non reversible behaviour. *Mechanics of Cohesive-Frictional Materials*, 1:199–218, 1996.

[40] F. F. F. F. Abraham, Broughton J. Q., Bernstein N., and Kaxiras E. Spanning the continuum to quantum length scales in a dynamic simulation of brittle fracture. *Europhysics Letters*, 44 (6):783–787, 1998.

[41] M. W. Finnis and J. E. Sinclair. A simple empirical N-body potential for transition metals. *Philosophical Magazine A*, 50:45–55, 1984.

[42] D. Frenkel and B. Smit. *Understanding molecular simulation: from algorithms to applications*. Academic Press, 1996.

[43] L. A. Girifalco and V. G. Weizer. Application of the morse potential function to cubic metals. *Physical Review*, 114 (3):687–690, 1959.

[44] E. Gürses, M. Lambrecht, and E. Miehe. Application of relaxation techniques to nonconvex isotropic damage model. *Proceedings in Applied Mathematics and Mechanics*, 3:222–223, 2003.

[45] P. K. Haff. Grain flow as a fluid-mechanical phenomenon. *Journal of Fluids Mechanics*, 134:401–430, 1983.

[46] J. M. Haile. *Molecular dynamics simulation: elementary methods*. John Wiley & Sons, 1997.

[47] H. J. Herrmann and S. Luding. Modeling granular media on the computer. *Continuum Mechanics and Thermodynamics*, 10:189–231, 1998.

[48] H. Hertz. Über die Berührung fester elastischer Körper. *Journal für die reine und angewandte Mathematik*, 92:156–171, 1882.

[49] G. A. Holzapfel. *Nonlinear solid mechanics. A continuum approach for engineering*. John Wiley & Sons, 1 edition, 2000.

[50] M. R. Horne. The behaviour of an assembly of rotund, rigid cohesionless particles – I, II. *Proceedings of the Royal Society London A*, 286:62–97, 1965.

[51] L. Hua, H. Rafii-Tabar, and M. Cross. Molecular dynamics simulation of fractures using an N-body potential. *Philosophical Magazine Letters*, 75 (5):237–244, 1997.

[52] R. Z. Huang, L. H. Zhang, M. L. Sui, and Y. M. Wang. Formation of disorder aluminium zones in an immiscible lead-aluminium system. *Journal of Physics: Condensed Matter*, 16:1131–1140, 2004.

[53] T. J. R. Hughes. *The finite element method. Linear static and dynamic finite element analysis*. Dover Publications Inc., 2 edition, 2000.

[54] J. T. Jenkins and S.B. Savage. A theory for the rapid flow of identical, smooth, nearly elastic, spherical particles. *Journal of Fluid Mechanics*, 130:187–202, 1983.

[55] Z. H. Jin, H. W. Sheng, and K. Lu. Melting of Pv clusters without free surfaces. *Physical Review B*, 60 (1):141–149, 1999.

[56] J. E. Jones. On the determination of molecular fields. I. From the variation of the viscosity of a gas with temperature. *Proceedings of the Royal Society London A*, 106:441–462, 1924.

[57] J. E. Jones. On the determination of molecular fields. II. From the equation of state of a gas. *Proceedings of the Royal Society London A*, 106:463–477, 1924.

[58] K. Kanatani. A micropolar continuum theory for the flow of granular materials. *International Journal of Engineering Science*, 17:419–432, 1979.

[59] K. Kaneko, K. Terada, T. Kyoya, and Y. Kishino. Global-local analysis of granular media in quasi-static equilibrium. *International Journal of Solids and Structures*, 40:4043–4069, 2003.

[60] C. L. Kelchner, S. J. Plimpton, and J. C. Hamilton. Dislocation nucleation and defect structure during surface indentation. *Physical Review B*, 58 (1):11085–11088, 1998.

[61] J. Konishi. Microscopic model studies on the mechanical behaviour of granular materials. In *Proceedings of the US-Japan seminar on: Continuum Mechanical and statistical Approaches in the Mechanics of Granular Materials*, pages 85–94. 1978.

[62] N. P. Kruyt and L. Rothenburg. Micromechanical definition of the strain tensor of granular assemblies. *Transactions of the ASME*, 118:706–711, 1996.

[63] N. P. Kruyt and L. Rothenburg. Statistical theories for the elastic moduli of two-dimensional assemblies of granular materials. *International Journal of Engineering Science*, 36:1127–1142, 1998.

[64] F. Kun and H. J. Herrmann. A study of fragmentation processes using a discrete element method. *Computer Methods in Applied Mechanics and Engineering*, 138:3–18, 1996.

[65] M. Lambrecht, C. Miehe, and J. Dettmar. Energy relaxation of non-convex incremental stress potentials in a strain-softening elastic-plastic bar. 40 (6):1369–1391, 2003.

[66] M. Lambrecht, C. Miehe, and E. Gürses. Relaxation analysis of material instabilities in damage mechanics based on incremental convexification techniques. In *Proc. of the VII International Conference on Computational Plasticity, COMPLAS 2003, Barcelona, Spain, 7-10 April 2003*, 2003.

[67] R. C. Lincoln, K. M. Koliwad, and P. B. Ghate. Morse-potential evaluation of second- and third-order elastic constants of some cubic metals. *Physical Review*, 157 (3):463–466, 1967.

[68] S. Luding. Collisions & contacts between two particles. In H. J. Herrmann, J.-P. Hovi, and S. Luding, editors, *Physics of dry granular Media*. Kluwer Academic Publishers, 1998.

[69] M. Lätzel, S. Luding, and H. J. Herrmann. Macroscopic material properties form quasi-static, microscopic simulations of a two-dimensional shear-cell. *Granular Materials*, 2 (3):123–135, 2000.

[70] R. A. MacDonald and W. M. MacDonald. Thermodynamic properties of fcc metals at high temperatures. *Physical Review B*, 24 (4):1715–1724, 1981.

[71] J. Marian, J. Knap, and M. Ortiz. Nanovoid deformation in aluminum under simple shear. *Acta Materialia*, 53:2893–2900, 2005.

[72] H. G. Matuttis and S. Luding. The effect of particle shape and friction on the stresses in heaps of granular media. In D. Wolf and P. Grassberger, editors, *Friction, Arching and Contact Dynamics*. 1998.

[73] M. M. Mehrabadi, B. Loret, and S. Nemat-Nasser. Incremental constitutive relations for granular materials based on micromechanics. *Proceedings of the Royal Society London A*, 441:433–463, 1993.

[74] C. Miehe. *Lectures on Computational Mechanics of Materials at Large Strains.* 2000-2004.

[75] C. Miehe. Computational micro-to-macro transitions for discretized microstructures of heterogeneous materials at large strains based on the minimization of averaged incremental energy. *Computer Methods in Applied Mechanics and Engineering*, 192:559–591, 2002.

[76] C. Miehe. Strain-driven homogenization of inelastic microstructures and composites based on an incremental variational formulation. *International Journal for Numerical Methods in Engineering*, 55:1285–1322, 2002.

[77] C. Miehe. Computational micro-to-macro transitions for discretized microstructures of heterogeneous materials at finite strains based on the minimization of averaged incremental energy. *Computer Methods in Applied Mechanics and Engineering*, 192 (5–6):559–591, 2003.

[78] C. Miehe and J. Dettmar. A framework for micro-macro transitions in periodic particle aggregates of granular materials. *Computer Methods in Applied Mechanics and Engineering*, 193 (3–5):225–256, 2004.

[79] C. Miehe and J. Dettmar. Static homogenization and multiple scale simulation of discrete granular materials at finite strains with directly evaluated micro-macro transition. *submitted to the International Journal of Solids and Structures*, 2005.

[80] C. Miehe, M. Lambrecht, and E. Gürses. Analysis of material instabilities in inelastic solids by incremental energy minimization and relaxation methods: evolving deformation microstructures in finite plasticity. *Journal of the Mechanics and Physics of Solids*, 52:2725–2769, 2004.

[81] C. Miehe and J. Schotte. Anisotropic finite elastoplastic analysis of shells: simulation of earing in deep-drawing of single- and polycrystalline sheets by taylor-type micro-to-macro transitions. *Computer Methods in Applied Mechanics and Engineering*, 193 (1-2):25–57, 2004.

[82] C. Miehe, J. Schotte, and M. Lambrecht. Homogenization of inelastic solid materials at finite strains based on incremental minimization principles. application to the texture analysis of polycrystals. *Journal of the Mechanics and Physics of Solids*, 50:2123–2167, 2002.

[83] C. Miehe, J. Schröder, and M. Becker. Computational homogenization analysis in finite elasticity. material and structural instabilities on the micro- and macro-scales of periodic composites and their interaction. *Computer Methods in Applied Mechanics and Engineering*, 191:4971–5005, 2002.

[84] C. Miehe, J. Schröder, and J. Schotte. Computational homogenization analysis in finite plasticity. simulation of texture development in polycrystalline materials. *Computer Methods in Applied Mechanics and Engineering*, 171:387–418, 1999.

[85] R. E. Miller and E. B. Tadmor. The quasicontinuum method: Overview, applications and current directions. *Journal of Computer-Aided Materials Design*, 9:203–239, 2002.

[86] M. J. Mills, M. S. Daw, and S. M. Foiles. High-resolution transmission electron microscopy studies of dislocation cores in metals and intermetallic compounds. *Ultramicroscopy*, 56:79–93, 1994.

[87] R. D. Mindlin. Compliance of elastic bodies in contact. *ASME Journal of Applied Mechanics*, 16:259–268, 1949.

[88] R. D. Mindlin and H. Deresiewicz. Elastic spheres in contact under varying oblique forces. *ASME Journal of Applied Mechanics*, 20:327–344, 1953.

[89] J. J. Moreau. Some numerical methods in multibody dynamics: application to granular materials. *European Journal of Mechanics A / Solids*, 13 (4):93–114, 1994.

[90] A. Munjiza and K. R. F. Andrews. NBS contact detection algorithm for bodies of similar size. *International Journal for Numerical Methods in Engineering*, 43:131–149, 1998.

[91] A. Munjiza, D. R. J. Owen, and N. Bićanić. A combined finite-discrete element method in transient dynamics of fracturing solids. *Engineering Computations*, 12:145–175, 1995.

[92] H.-B. Mühlhaus and I. Vardoulakis. The thickness of shear bands in granular materials. *Géotechnique*, 37 (3):271–283, 1987.

[93] S. Nemat-Nasser. *Plasticity : A Treatise on Finite Deformation of Heterogeneous Inelastic Materials*. Cambridge University Press, 2004.

[94] M. Oda, J. Konishi, and S. Nemat-Nasser. Experimental micromechanical evaluation of strength of granular materials: effects of particle rolling. *Mechanics of Materials*, 1:269–283, 1982.

[95] M. Ortiz and E. A. Repetto. Nonconvex energy minimization and dislocation structure in ductile single crystals. *Journal of the Mechanics and Physics of Solids*, 47:397–462, 1999.

[96] M. Papadrakakis. A method for the automatic evaluation of the dynamic relaxation parameters. *Computer Methods In Applied Mechanics and Engineering*, 25:35–48, 1981.

[97] H. S. Park and W. K. Liu. An introduction and tutorial on multiple-scale analysis in solids. *Computer Methods in Applied Mechanics and Engineering*, 193:1733–1772, 2004.

[98] K. C. Park. A family of solution algorithms for nonlinear structural analysis based on relaxation equations. *International Journal for Numerical Methods in Engineering*, 18:1337–1347, 1982.

[99] M. Parrinello and A. Rahman. Crystal structure and pair potentials : A molecular-dynamics study. *Physical Review Letters*, 45 (14):1196–1199, 1980.

[100] M. Parrinello and A. Rahman. Polymorphic transitions in single crystals: A new molecular dynamics method. *Journal of Applied Physics*, 52 (12):7182–7190, 1981.

[101] A. Patrascioiu. The ergodic hypothesis: A complicated problem in mathematics and physics. *Los Alamos Science*, pages 263–279, 1987.

[102] H. Rafii-Tabar and A. P. Sutton. Long-range Finnis-Sinclair potentials for fcc metallic alloys. *Philosophical Magazine Letters*, 63 (4):217–224, 1991.

[103] A. Rahman. Correlations in the motion of atoms in liquid argon. *Physical Review*, 136 (A2):A405–A411, 1964.

[104] L. Rothenburg and R. J. Bathurst. Micromechanical features of granular assemblies with planar elliptical particles. *Géotechnique*, 42 (1):79–95, 1992.

[105] J. Schröder. *Homogenisierungsmethoden der nichtlinearen Kontinuumsmechanik unter Beachtung von Stabilitätsproblemen.* No. I-7, Institut für Mechanik (Bauwesen), Universität Stuttgart, 2000.

[106] G. Skeie, O. C. Astrup, and P. G. Bergan. Applications of adapted, nonlinear solution strategies. In N.-E. Wiberg, editor, *Advances in finite element technology*, pages 212–236. CIMNE, Barcelona, 1995.

[107] S. W. Sloan. A fast algorithm for constructing Delaunay triangulations in the plane. *Advances in Engineering Software*, 9 (1):34–55, 1987.

[108] S. W. Sloan. A fast algorithm for generating constrained Delaunay triangulations. *Computers & Structures*, 47 (3):441–450, 1993.

[109] A. P. Sutton and J. Chen. Long-range Finnis-Sinclair potentials. *Philosophical Magazine Letters*, 61 (3):139–146, 1990.

[110] E. B. Tadmor. *The quasicontinuum method. Modeling microstructure on multiple length scales: A mixed Continuum and Atomistics Approach.* PhD thesis, Division of Engineering, Brown University, 1996.

[111] E. B. Tadmor, M. Ortiz, and R. Phillips. Quasicontinuum analysis of defects in solids. *Philosophical Magazine A*, 73:1529–1563, 1996.

[112] C. Thornton. The conditions of failure of a face-centered cubic array of uniform rigid spheres. *Géotechnique*, 29:441–459, 1979.

[113] C. Thornton. Coefficient of restitution for collinear collisions of elastic perfectly plastic spheres. *ASME Journal of Applied Mechanics*, 64:383–386, 1997.

[114] H. J. Tillemans and H. J. Herrmann. Simulating deformations of granular solids under shear. *Physica A*, 217:261–288, 1995.

[115] J. M. Ting, M. Khwaja, L. R. Meachum, and J. D. Rowell. An ellipse-based discrete element model for granular materials. *International Journal for Numerical and Analytical Methods in Geomechanics*, 17:603–623, 1993.

[116] P. Underwood. Dynamic relaxation. In T. Belytschko and T.J.R. Hughes, editors, *Computational Methods For Transient Analysis*, pages 245–265. Elsevier Science Publisher B.V., 1983.

[117] I. Vardoulakis and M. Goldscheider. Biaxialgerät zur Untersuchung der Festigkeit und Dilatanz von Scherfugen in Böden (a biaxial apparatus for testing of strength and dilatancy of shear bands in solids). *Geotechnik*, 3:19–31, 1980.

[118] A. F. Voter. The embedded-atom method. *Intermetallic Compounds*, 1:77–90, 1994.

[119] L. Vu-Quoc and X. Zhang. An accurate and efficient tangential force-displacement model for elastic frictional contact in particle-flow simulations. *Mechanics of Materials*, 31:235–269, 1999.

[120] L. Vu-Quoc and X. Zhang. An elastoplastic contact force-displacement model in the normal direction: displacement-driven version. *Proceedings of the Royal Society London A*, 455:4013–4044, 1999.

[121] O. R. Walton and R. L. Brown. Viscosity, granular temperature, and stress calculations for shearing assemblies of inelastic, frictional disks. *Journal of Rheology*, 30:949–980, 1986.

[122] J. R. Williams and R. O'Connor. Discrete element simulation and the contact problem. *Archives of Computational Methods in Engineering*, 6 (4):279–304, 1999.

[123] J. R. Williams, E. Perkins, and B. Cook. A contact algorithm for partitioning N arbitrary sized objects. *Engineering Computations: International Journal for Computer-Aided Engineering*, 21 (2-3):235–248, 2004.

[124] J. R. Wren and R. I. Borja. Micromechanics of granular media Part II: Overall tangential moduli and localization model for periodic assemblies of circular disks. *Computer Methods in Applied Mechanics and Engineering*, 141:221–246, 1997.

[125] M. Zhou. A new look at the atomic level virial stress: on continuum-molecular system equivalence. *Proceedings of the Royal Society London A*, 459:2347–2392, 2003.

List of Figures

1. Granular and metallic materials on different time and length scales 2
2. Granular aggregates of various particulate materials 3
3. Nanoscopic structures of various materials 4
4. Placement of the physical body into the Euclidean space 9
5. Reference and actual neighborhoods 11
6. Deformation gradient $\boldsymbol{F}$ 12
7. Tangent, normal and volume mappings 14
8. Reference and actual metric tensors defined as mappings 16
9. Right and left stretch tensors interpreted as mappings 17
10. Cut of a part of a body and replacement by tractions 20
11. Definition of stress tensors as mappings 22
12. Time and length scales associated with the modeling of granular materials 29
13. Continuous macrostructure with granular microstructures attached 29
14. Definition of periodic granular microstructures 30
15. Continuous and granular periodic microstructures 31
16. Equilibrium state of a particle aggregate 35
17. Deformation-driven boundary constraints for granular microstructures 39
18. Hertzian contact curvature of two particles in contact 46
19. Elastoplastic force-displacement law according to Walton & Brown 47
20. Elastic-perfectly plastic normal contact law according to Thornton 47
21. Contact interaction according to Mindlin & Deresiewicz 48
22. Slip, stick and tangential stress according to Mindlin & Deresiewicz 49
23. Configuration of two elliptically-shaped rigid particles in contact 50
24. Displacements of two elliptical particles that come into contact 51
25. Displacements of two rigid spherical particles that come into contact 54
26. Tangential plane at the contact point of two contacting spheres 55
27. Visualization of an exemplary Verlet neighbor list 58
28. Surface meshing of the granular microstructure 60
29. Velocity and acceleration in the context of the central difference method 62
30. Exemplary global relaxation function 62
31. Contact normal and tangential forces and particle contact force vector 64
32. Elliptical particle falling onto an inclined plane 67
33. Deformation of a heap of 433 elliptical particles under dead load 68
34. Deformation of an irregular package of 256 discs under compression and shear . . 70

35. Homogenized stresses of the granular structure of 256 particles during compression 71
36. Homogenized stresses of the granular structure of 256 particles during shear . . . 71
37. Relaxation of the rectangular granular microstructure with 256 particles 72
38. Rose diagrams of the granular microstructure with 256 particles 72
39. Assembly of eight deformed periodic granular microstructures 73
40. Homogenized stresses of a rectangular granular structure under cyclic shear . . . 74
41. Deformation of a circular granular package of 305 particles 74
42. Stress diagrams of the circular microstructures during compression and shear . . 75
43. Stress diagrams of the circular microstructures during shear 76
44. Deformation states of an irregular periodic package of 187 granules 77
45. Homogenized stresses for the aggregate of 187 particles during compression 77
46. Homogenized stresses for the aggregate of 187 particles during shear 78
47. Relaxation of the irregular aggregate of 187 particles 78
48. 3-D granular assemblies with 4076 and 513 spherical particles 79
49. Relaxation and mean kinetic energy of the 3-D microstructure with 513 granules 81
50. Deformation of the 3-D granular microstructure with 4076 particles 82
51. Cauchy stresses of the 3-D granular microstructure with 4076 particles 83
52. Deformation of the 3-D granular microstructure with 513 particles 84
53. Homogenized Cauchy stresses for the 3-D granular microstructures 84
54. Cauchy stresses of the 3-D granular microstructure with 513 particles 85
55. Coordination numbers and volume density for the 3-D granular microstructures 85
56. Quadratic triangular element with six nodes, a 92
57. Apportioning of body forces to the nodes of a quadratic triangular element 93
58. Coupling of micro- and macroscopic boundary value problems 94
59. Two-scale simulation of a macroscopically quadratic plane specimen 97
60. Load-displacement curve and relaxation of the two-scale simulation 97
61. Deformation of one granular microstructure during two-scale simulation 98
62. Macroscopic relaxation and kinetic energy during two-scale simulation 98
63. Description of the biaxial testing apparatus 99
64. Deformation of micro- and macroscopic structures of the two-scale simulation . . 100
65. Roscoe stress $\bar{t}/\bar{s}$ versus axial strain $\bar{\varepsilon}$ during two-scale simulation 101
66. Mobilized friction angle ϕ_m versus axial strain $\bar{\varepsilon}$ 102
67. Macroscopic kinetic energy development during granular two-scale simulation . . 102
68. Various simulation tools used on different time and length scales 105
69. Metals and metallic materials 113

70. Metallic bonding 113
71. Cutoff radius r_c and skin factor $f_c = \hat{f}_c(r)$ 115
72. Lennard-Jones 12-6 potential and derivative 116
73. Morse potential function and its derivative 117
74. EAM potential as a function of the interatomic distance and electron density . . 119
75. MD equilibration at free surface with EAM potential 121
76. Visualization of the ergodic hypothesis 127
77. Definition of a dynamically steady state 131
78. Nano- and meso scale mechanics 133
79. Inadequacy of periodic boundary conditions in atomistic systems 134
80. Elastic shearing of an fcc cube with 4631 atoms 138
81. Elastic stresses in the deformed fcc crystal 138
82. Slip planes and slip lines in metallic crystals 139
83. Dislocation movement of a point defect through 2D Al lattice 139
84. Stresses during 2D dislocation movement 140
85. Development of energies during atomistic deformation 140
86. Annihilation of two point defects in 2-D Al lattice 141
87. Initial 3D nanostructure with nanovoid 142
88. Incipient partial dislocation structures around the nanovoid 142
89. Shear stress of the 3D atomistic system with nanovoid 142
90. Potential energy and fluctuation distribution in atomistic cross section 143
91. Initial and final nanosystems with crack development 144
92. Magnification of the cracks of the atomistic nanosystem 144
93. Stresses and interatomic forces during deformation of a cracking nanosystem . . 145
94. Development of energies during atomistic fracture 145

Curriculum Vitae

Personal Data

Name:	Joachim Peter Dettmar
Date of Birth:	February 27, 1974
Place of Birth:	Cologne, Germany
Parents:	Dr. Peter Dettmar and Sabine Dettmar
Siblings:	Juliane Dettmar and Jasmin Dettmar

School Education

1980 – 1984	Wiehagen Elementary School, Werne an der Lippe, Germany
1984 – 1991	St. Christophorus High School, Werne an der Lippe, Germany
1994 – 1996	Evening Classes at High School of the City of Münster, Germany
May 1996	University Entrance Certificate (German Abitur)

Apprenticeship & University Education

1991 – 1994	Apprenticeship as Construction Drafter, Engineering Company M. Smulka in Bergkamen, Germany
1996 – 2001	Studies of Civil Engineering, Universität Stuttgart, Germany
1999 – 2000	Student Exchange, University of Calgary, Canada. Scholarship of the German Academic Exchange Service DAAD
January 2001	Graduation as Diplom-Ingenieur
July 2001	Artur-Fischer-Prize of the Faculty of Civil and Environmental Engineering, Universität Stuttgart, Germany

Professional Experience

1994 – 1996	Occupation as Construction Drafter, Engineering Company M. Smulka in Bergkamen, Germany
2001 – 2005	Research Associate and Lecturer, Institute of Applied Mechanics (Civil Engineering), Universität Stuttgart, Germany
since 2005	Management Consultant, L.E.K. Consulting, Munich, Germany

In dieser Schriftenreihe bisher erschienene Berichte:

I-1 (1996) *Theoretische und algorithmische Konzepte zur phänomenologischen Beschreibung anisotropen Materialverhaltens*, J. Schröder, Dissertation

I-2 (1996) *Zur Theorie und Numerik finiter elastoplastischer Deformationen von Schalentragwerken*, B. Seifert, Dissertation

I-3 (1996) *Zur Modellierung des künstlichen Infrarot-Dichroismus in Poymerfolien bei großen Deformationen*, J. Buhler, Dissertation

I-4 (1996) *Verfahren zur Ermittlung der Erdbebenlasten mit Berücksichtigung des stochastischen Charakters des Bebens*, S. Zhang, Dissertation

I-5 (1998) *Zur Beschreibung finiter Deformationen von Polymeren: Experimente, Modellbildung, Parameteridentifikation und Finite-Elemente-Formulierung*, J. Keck, Dissertation

I-6 (1999) *Berechnungsverfahren instationär erregter Systeme im Frequenzbereich*, A. Jaworek, Dissertation

I-7 (2000) *Homogenisierungsmethoden der nichtlinearen Kontinuumsmechanik unter Beachtung von Stabilitätsproblemen*, J. Schröder, Habilitation

I-8 (2002) *Theorie und Numerik von Materialinstabilitäten elastoplastischer Festkörper auf der Grundlage inkrementeller Variationsformulierungen*, M. Lambrecht, Dissertation

I-9 (2002) *Mikromechanisch motivierte Modelle zur Beschreibung finiter Deformationen gummiartiger Polymere: physikalische Modellbildung und numerische Simulation*, F. Lulei, Dissertation

I-10 (2003) *Adaptive Finite-Elemente-Berechnungen der nichlinearen Festkörpermechanik bei kleinen und großen Verzerrungen*, A. Koch, Dissertation

I-11 (2003) *Theorie und Numerik der Parameteridentifikation von Materialmodellen der finiten Elastizität und Inelastizität auf der Grundlage optischer Feldmeßmethoden*, G. Scheday, Dissertation

I-12 (2004) *Approaches to the Description of Anisotropic Material Behaviour at Finite Elastic and Plastic Deformations, Theory and Numerics*, N. Apel, Dissertation

I-13 (2004) *Temperaturabhängige Beschreibung visko-elasto-plastischer Deformationen kurzglasfaserverstärkter Thermoplaste: Modellbildung, Numerik und Experimente*, S. Rieger, Dissertation

I-14 (2005) *Zur Parameteridentifikation komplexer Materialmodelle auf der Basis realer und virtueller Testdaten*, A. Rieger, Dissertation

I-15 (2005) *Viskoelastisches Verhalten von Elastomeren bei finiten Verzerrungen: Experimente, Modellierung und Simulationen*, H. Zecha, Dissertation

I-16 (2005) *Mehrskalenmodelle in der Festkörpermechanik und Kopplung von Mehrgittermethoden mit Homogenisierungsverfahren*, C. G. Bayreuther, Dissertation

I-17 (2005) *Static and Dynamic Homogenization Analyses of Discrete Granular and Atomistic Structures on Different Time and Length Scales*, J. P. Dettmar, Dissertation